UNIVERSIDADE ESTADUAL PAULISTA
"JÚLIO DE MESQUITA FILHO"
CAMPUS DE GUARATINGUETÁ

GUSTAVO OLIVEIRA MADEIRA

Exploring models of formation and dynamic evolution of satellites and rings of the Solar System

Phobos of Mars, Galilean satellites of Jupiter, Neptune arcs, and an object with a mass anomaly

Guaratinguetá

2023

Gustavo Oliveira Madeira

Exploring models of formation and dynamic evolution of satellites and rings of the Solar System

Phobos of Mars, Galilean satellites of Jupiter, Neptune arcs, and an object with a mass anomaly

PhD thesis presented to the School of Engineering of Guaratinguetá, São Paulo State University, as part of the requirements for achievement of the title: Doctor in Physics

Supervisor: Prof. Dr. Silvia M. Giuliatti Winter
Co-supervisor: Prof. Dr. André Izidoro

Guaratinguetá
2023

Madeira, Gustavo Oliveira
M181e Exploring models of formation and dynamic evolution of satellites and rings of the Solar System Phobos of Mars, Galilean satellites of Jupiter, Neptune arcs, and an object with a mass anomaly / Gustavo Oliveira Madeira – Guaratinguetá, 2023.
210 f : il.
Bibliography: f. 167-190

Thesis (Doctor in Physics) – Universidade Estadual Paulista, Faculdade de Engenharia e Ciências de Guaratinguetá, 2023.
Supervisor: Profª. Drª. Silvia Maria Giuliatti Winter
Co-supervisor: Prof. Dr. André Izidoro

1. Satéllites. 2. Solar System. 3. Planets - Orbits. I. Títle.

CDU 629.783(043)

Luciana Máximo
Bibliotecária CRB-8/3595

unesp

UNIVERSIDADE ESTADUAL PAULISTA
CAMPUS DE GUARATINGUETÁ

GUSTAVO OLIVEIRA MADEIRA

ESTA TESE FOI JULGADA ADEQUADA PARA A OBTENÇÃO DO TÍTULO DE
"DOUTOR EM FÍSICA"

PROGRAMA: FÍSICA
CURSO: DOUTORADO

APROVADA EM SUA FORMA FINAL PELO PROGRAMA DE PÓS-GRADUAÇÃO

Prof. Dr. Ernesto Vieira Neto
Coordenador

B A N C A E X A M I N A D O R A:

PROFa. DRa. SILVIA MARIA GIULIATTI WINTER
Orientador / UNESP/FEG

participou por videoconferência

DR. ADRIAN RODRIGUEZ COLUCCI
UFRJ/Rio de Janeiro

participou por videoconferência

DR. MARIA PAULA RONCO
Instituto de Astrofísica de La Plata – CONICET UNLP – Argentina

participou por videoconferência

DR. MATTHEW M HEDMAN

University of Idaho

participou por videoconferência

DR. CRISTIÁN BEAUGÉ

Universidad Nacional de Córdoba

participou por videoconferência

Janeiro de 2023

CURRICULAR DATA

GUSTAVO OLIVEIRA MADEIRA

BORN 03.12.1994 - Cachoeira Paulista/SP - Brazil

FILIATION José Márcio Madeira
Liliam A. S. Oliveira Madeira

2012/2016 Bachelor in Physics
School of Engineering, Guaratinguetá
Universidade Estadual Paulista "Júlio de Mesquita Filho" (UNESP)

2016/2019 Master in Physics
School of Engineering, Guaratinguetá
Universidade Estadual Paulista "Júlio de Mesquita Filho" (UNESP)

2019/2023 Ph.D. in Physics
School of Engineering, Guaratinguetá
Universidade Estadual Paulista "Júlio de Mesquita Filho" (UNESP)

2021/2022 Sandwich Ph.D. in Physics
Cosmochemistry, Astrophysics and Experimental Geophysics team
Institut de Physique du Globe de Paris, France

I dedicate this thesis to Luis Inácio Lula da Silva, for giving back hope to Brazil

ACKNOWLEDGEMENTS

I would like to thank everyone who has supported me during academic journey so far. Thanks to everyone who laughed with me and made me laugh.

I sincerely thank the selected committee and substitute members for taking time to evaluate my thesis.

Thanks to FAPESP (Proc. 2018/23568-6, 2021/07181-7 and 2016/24561-0) for the financial support.

I would like to thank my professors for teaching me what I know about physics and astronomy. In particular, I would like to thank Prof. Othon Winter for all the support.

Thanks to my co-advisor André Izidoro for all the teaching on planetary formation. Thanks for helping me during code implementation, and for all the help while writing the Galilean's article.

My sincere thanks to Prof. Sebastién Charnoz for his company and all the learning and help during my stay in France. My thanks to my IPGP colleagues.

Thanks to Daniel Gallardo, Marco Muñoz-Gutiérez, Rafael Sfair, Taís Ribeiro, Paula Granados, Joseph A'Hearn, Ryuki Hyodo, Hidenori Genda, Patrick Michel, and Yun Zhang for all their contributions.

I thank my parents, Liliam and Márcio, my sister Luana, my grandparents Maria Reis and João Batista, and my aunt Fernanda for being there and supporting me during my studies.

I would like to thank all my friends for all the happy and crazy moments. Thanks to Rafael Ribeiro, Rodrigo Lima, Bárbara Camargo, my friends from Cortiço, Juan Carlos, Alana Oliveira, Joyce Vieira, Pedro Lourenço, and Sara Cristina. My special thanks to Cindy Evellyn for the amazing time in Paris. Thanks to my dear André Dimitri.

My most sincere thanks to my dear friends Luana Liberato, Tiago Francisco, and Victor Lattari for being always with me since the first year of undergraduation.

Finally, I would like to thank my mentor Prof. Silvia Giuliatti Winter for always being by my side and for making me the professional I am today.

This work was financially supported by:
Fundação de Amparo à Pesquisa do Estado de São Paulo - Brasil (FAPESP) - Proc. 2018/23568-6, 2021/07181-7 and 2016/24561-0
Coordenação de Aperfeiçoamento de Pessoal de Nível Superior - Brasil (CAPES) - Finance Code 001

“Quero inventar o meu próprio pecado (I want to create my own sin)
Quero morrer do meu próprio veneno (I want to die from my own poison)”
Chico Buarque and Gilberto Gil

ABSTRACT

Accretion in a circumstellar disk is the main mechanism for the formation of planets, while the formation of satellites and rings can occur through different mechanisms around the central body. This thesis aims to study the formation and stability of different systems of satellites and rings, in different environments and epochs of the Solar System. For this, we employ different numerical techniques. The topics addressed in the thesis are: the formation of Galilean satellites of Jupiter in a circumplanetary disk, the formation of Phobos of Mars due to a material recycling mechanism, the stability of 1+N co-orbital satellites confining the Neptune arcs and their formation due to the disruption of a satellite, and stability around spherical objects with a mass anomaly. We study the Galilean satellites using N-body numerical simulations and assuming that they formed in a circumplanetary disk during the last stages of Jupiter's formation. The model assumes impacts between satellitesimals, pebble accretion, and includes gas-driven migration, gas tidal damping, and drag. Under these effects, satellites migrate inwards stopping their migration when reaching the disk's inner cavity or when captured in mean motion resonances. In the system that best matches the masses of the real Galilean system, pairs of adjacent satellites are obtained in 2:1 mean motion resonances. We propose that the Galilean satellites system is a primordial resonant chain and that Callisto left the resonance without breaking the Laplacian resonance via divergent migration due to tidal interactions. The formation of Phobos was analyzed using 1D simulations of disk/satellite interactions. The model assumes that Phobos is a low-cohesion satellite formed through a cascade of disruptions and re-accretions of several parent bodies in a debris disk around Mars. We find that the recycling mechanism must, in fact, take place if the debris disk gives rise to low-cohesion objects. However, if Phobos were formed by this process, it would be accompanied today by a Roche-interior ring. So Phobos cannot be the outcome of such a recycling process. Turning attention to stability of rings, we study the equilibrium configurations for 1+N co-orbital satellites confining the Neptune rings. We use N-body simulations and obtain distinct configurations of satellites, with different numbers and sizes of moonlets, capable of confining arcs. Then, the formation of these possible co-orbital satellites is analyzed assuming the disruption of an ancient body at a Lagrangian point of a moon. The disruption fragments spread out and collide to form the co-orbital system. In such a scenario, the arcs likely formed through a mixture of different processes, with impacts between fragments and meteoroid impacts with the formed moonlets being attractive possibilities. Finally, we use the Poincaré surface of section technique to analyze the stability around a spherical body with a mass anomaly at its equator. Varying the parameters of the central object, we verify the existence of two distinct regions around the body, a chaotic inner region where particles are lost and a stable outer region. In the stable region, spin-orbit resonances are identified, and we obtain that periodic orbits in 1:1+p resonances are asymmetric. Modeling Chariklo as an object with a mass anomaly, we conclude that its rings are in the stable region, but not involved in the 1:3 spin-orbit resonance, as proposed in the literature. The results presented here aim to shed light on the processes involved in the formation of satellites and ring systems, as well as understanding their stability. We also tried to underline the symbiotic relationship between rings and satellites. The different methodologies employed in this thesis can be adapted to other systems in order to bring better

knowledge about the origin and fate of other satellites and rings of the Solar System.

KEYWORDS: satellite formation. ring formation. circumplanetary disk. debris disk. numerical simulations. Galilean satellites. Phobos. Neptune arcs. Chariklo.

RESUMO

A acreção em discos circumestelares é o principal mecanismo para a formação de planetas, enquanto a formação de satélites e anéis pode ocorrer por meio de diferentes mecanismos ao redor do corpo central. O objetivo desta tese é estudar a formação e estabilidade de diferentes sistemas de satélites e anéis, em diferentes ambientes e épocas do Sistema Solar. Para isto, fiz o uso de diferentes técnicas numéricas. Os tópicos abordados na tese são: a formação dos satélites Galileanos de Júpiter em um disco circum-planetário, a formação de Fobos de Marte por meio de um mecanismo de reciclagem de material, a estabilidade de 1+N satélites co-orbitais confinando os arcos de Netuno e suas formações por meio da destruição de um satélite e a estabilidade ao redor de corpos esféricos com uma anomalia de massa. Acredita-se que os satélites Galileanos tenham se formado durante os estágios finais da formação de Júpiter em um disco circumplanetário, sendo esta estudada por meio de simulações numéricas de N-corpos. O modelo assume impactos entre satelitesimais, acreção de seixos e inclui a migração devido ao gás, amortecimento e arrasto do gás. Sob esses efeitos, os satélites migrarão em direção ao planeta, sendo a migração freada quando os satélites atingem a cavidade interna do gás ou são capturados em uma ressonância de movimento médio. No melhor sistema análogo ao Galileano, obtém-se que os pares de satélites estão em ressonâncias de movimento médio 2:1. Eu proponho que o sistema de satélites Galileanos seja um corrente ressonante primordial e que Calisto deixou a ressonância de movimento médio, sem quebrar a ressonância Laplaciana, devido à uma migração divergente causada por interações de maré. A formação de Fobos foi estudada por meio de simulações unidimensionais das interações entre disco e satélite. O modelo assume ser Fobos um satélite com baixa coesão, formado através de uma cascata de destruições e recriações de satélites em um disco de detritos ao redor de Marte. Obtenho que o mecanismo de reciclagem deve de fato ocorrer se os satélites formados no disco possuírem baixa coesão. No entanto, um anel interior ao limite de Roche de Marte e coexistindo com Fobos é sempre obtido por meio deste mecanismo. Logo, Fobos não pode ter se formado por meio do processo de reciclagem. Atendo a estabilidade de anéis, eu analiso as configurações de equilíbrio de 1+N satélites co-orbitais confinando os arcos de Netuno e obtenho diferentes configurações, com diferentes massas e número de corpos. A formação desses satélites é estudada assumindo a ruptura de um corpo ancestral no ponto Lagrangiano de uma lua. Os fragmentos da ruptura se espalham e colidem, formando o sistema de satélites co-orbitais. Neste cenário, os arcos são formados por meio de diferentes processos, sendo as colisões entre fragmentos e impactos de corpos externos com as luas já formadas, os mais atrativos destes. Por fim, utilizo a técnica da seção de Poincaré para analisar a estabilidade ao redor de um corpo esférico com uma anomalia de massa em seu equador. Variando os parâmetros do corpo central, verifico a existência de duas regiões ao redor do corpo, uma região interna caótica, na qual as partículas são perdidas, e uma região externa estável. Nesta última são identificadas ressonâncias do tipo spin-órbita, sendo obtido que as órbitas periódicas associadas à ressonâncias 1:1+p são assimétricas. Modelando Cáriclo como um objeto esférico com uma anomalia de massa, concluo que seus anéis estão na região estável, porém não estão associados à ressonância 1:3 conforme proposto na literatura. Os resultados aqui apresentados buscam difundir os processos envolvidos na formação de satélites e anéis, assim como ajudar na compreensão da estabilidade destes. Em especial, tentei salientar a simbiótica relação existente entre os satélites e

anéis. As diferentes metodologias empregadas nesta tese podem ser adaptadas para outros sistemas de modo a ampliar o conhecimento a respeito da origem e destino de outros sistemas de satélites e anéis do Sistema Solar.

PALAVRAS-CHAVE: formação de satélites. formação de anéis. disco circumplanetário. disco de detritos. simulações numéricas. satélites Galileanos. Fobos. arcos de Netuno. Cáriclo.

LIST OF PUBLICATIONS

- Gaslac Gallardo DM, Giuliatti Winter SM, Madeira G, Muñoz-Gutiérrez MA. Analysing the region of the rings and small satellites of Neptune. Astrophysics and Space Science. 2020 Jan;365(1):1-0.
- Madeira G, Giuliatti Winter SM. Effects of immersed moonlets in the ring arc particles of Saturn. The European Physical Journal Special Topics. 2020 May;229(8):1527-43.
- Giuliatti Winter SM, Madeira G, Sfair R. Neptune's ring arcs confined by coorbital satellites: dust orbital evolution through solar radiation. Monthly Notices of the Royal Astronomical Society. 2020 Jul;496(1):590-7.
- Madeira G, Izidoro A, Giuliatti Winter SM. Building the Galilean moons system via pebble accretion and migration: a primordial resonant chain. Monthly Notices of the Royal Astronomical Society. 2021 Jun;504(2):1854-72.
- Madeira G, Giuliatti Winter SM, Ribeiro T, Winter OC. Dynamics around non-spherical symmetric bodies–I. The case of a spherical body with mass anomaly. Monthly Notices of the Royal Astronomical Society. 2022 Feb;510(1):1450-69.
- Muñoz-Gutiérrez MA, Granados Contreras AP, Madeira G, A'Hearn JA, Giuliatti Winter S. Long-term dynamical evolution of Pallene (Saturn XXXIII) and its diffuse, dusty ring. Monthly Notices of the Royal Astronomical Society. 2022 Apr;511(3):4202-22.
- Madeira G, Giuliatti Winter SM. Numerical analysis of processes for the formation of moonlets confining the arcs of Neptune. Monthly Notices of the Royal Astronomical Society. 2022 Jun;513(1):297-309.
- Madeira G, Charnoz S, Hyodo R. Dynamical origin of Dimorphos from fast spinning Didymos. Icarus. 2023 Jan 12:115428.
- Madeira G, Charnoz S, Zhang Y, Hyodo R, Michel P, Genda H, Giuliatti Winter SM. Exploring the recycling model of Phobos formation: rubble-pile satellites. The Astronomical Journal. In revision.
- Ribeiro T, Winter OC, Madeira G, Giuliatti Winter SM. Dynamics in Non-Spherical Symmetric Bodies: II. The case of a prolate body. Monthly Notices of the Royal Astronomical Society. In submission.
- Giuliatti Winter SM, Madeira G, Ribeiro T, Winter OC, Barbosa GO, Borderes-Motta G. On the stability around Chariklo and the confinement of its rings. Astronomy & Astrophysics. In submission.

LIST OF FIGURES

LIST OF TABLES

CONTENTS

1 INTRODUCTION

The question about the formation of the Solar System's planets and their satellites and rings is one of the oldest topics in science, remaining a topic of intense debate, fueled by the constant new data obtained by space missions. The first formal theory for the Solar System formation was proposed in the 18th century by Laplace (1798). According to this, a slowly spinning cloud would collapse forming the Sun and rings of gas and dust, from which planets would have formed. LAPLACE's theory fails to explain the solar angular momentum, however, its general idea was rescued by Safronov (1972) and Lynden-Bell e Pringle (1974), and today there is evidence pointing to the formation of the Solar System and others extra-solar planets from the collapse of a molecular cloud (KOOTEN et al., 2016).

After the collapse of the cloud that gives rise to a proto-Sun, a circumstellar disk is formed in the star's equatorial plane by angular momentum conservation, corresponding to the environment in which the planets, and later, the satellites and rings will form. In general, circumstellar disks have 1% of their material in the form of dust (monomers), the remainder being gas (KENYON; HARTMANN, 1987). Some of the monomers aggregate due to intermolecular forces forming objects with a radius of mm-cm called pebbles (BLUM; WURM, 2000). The gas drag is strong for such objects, inducing their radial deviation to the star (ADACHI; HAYASHI; NAKAZAWA, 1976) and also avoiding accretive collisions, which prevents the formation of larger bodies through impacts. However, under local specific conditions in the disk, a large concentration of pebbles can gravitationally collapse forming planetesimals (km-sized objects) through the streaming instability mechanism (YOUDIN; GOODMAN, 2005). The presence of a planetesimal population in the disk initiates a new growth regime, in which the gravitational force is dominant. In this regime, planetesimals grow due to impacts with other planetesimals or pebble accretion, giving birth to planets (KOKUBO; IDA, 1996).

Unlike pebbles and smaller objects that are coupled to the gas, planetesimals and larger bodies affect the structure of the gas disk by inducing the formation of spiral density waves that transport angular momentum. In response, these waves induce torques on the bodies, which will migrate because of this effect (TANAKA; TAKEUCHI; WARD, 2002). Planets formed in regions with an abundance of material (gas and dust) grow to large masses, opening gaps in the circumstellar disk, (LIN; PAPALOIZOU, 1986a; LIN; PAPALOIZOU, 1986b), and accreting gas in their envelopes. These planets will correspond to the gaseous planets (Jupiter, Saturn, Uranus, and Neptune).

When a gap is opened in the circumstellar disk, the material not yet accreted to the planet's envelope gives rise to a circumplanetary disk (ISELLA et al., 2019; TEAGUE; BAE; BERGIN, 2019). The latter is the birth environment of satellites and rings – it seems to be no coincidence the Solar System's gaseous planets are the ones that host planetary rings. The formation of satellites in a circumplanetary disk was proposed by Lunine e Stevenson (1982), being theorized that the Galilean satellites of Jupiter would have formed in a disk of gas and dust around the planet. The Galilean satellites – Io, Europa, Ganymede, and Callisto – were discovered by Galileo Galilei in the 17th century, corresponding to the first satellites discovered with the exception of our Moon. The main characteristics of the Galilean satellites are the fact that they are massive relative to the planet – their mass ratio to Jupiter is of the

same order as the mass ratio of Uranus and Neptune to the Sun – and the 1:2:4 Laplace resonance between Io, Europa, and Ganymede. Io completes four orbits around Jupiter at the same time as Europa and Ganymede complete two and one orbits, respectively.

Similar physical processes are expected to take place in protoplanetary and circumplanetary disks. However, they differ in that the circumstellar disk is essentially a closed system, while the circumplanetary disk is fed by the circumstellar disk due to meridional circulation of gas in the gap's vicinity (LUBOW; SEIBERT; ARTYMOWICZ, 1999; KLEY, 1999; BATYGIN; MORBIDELLI, 2020; SCHULIK et al., 2020). The circumplanetary disk can also capture pebbles, planetesimals, and fragments of the circumstellar disk (SUETSUGU; OHTSUKI; FUJITA, 2016; SUETSUGU; OHTSUKI, 2017). As the circumplanetary disk is an open system, the satellite formation can happen at different stages, having been proposed different and irreconcilable models of formation of the Galilean satellites. According to the minimum mass sub-nebula model (MOSQUEIRA; ESTRADA, 2003a; MOSQUEIRA; ESTRADA, 2003b; MIGUEL; IDA, 2016; MORAES; KLEY; NETO, 2018), the population of satelitesimals (the analogues of planetesimals in circumplanetary disks) is completely formed during the phase in which both disks are connected. Satellites would form through impacts after the dissipation of the circumstellar disk.

The gas-starved disk model (CANUP; WARD, 2002; CANUP; WARD, 2006; CANUP; WARD, 2009; SASAKI; STEWART; IDA, 2010; BATYGIN; MORBIDELLI, 2020), in turn, assumes a slow formation of the Galilean satellites during the last stages of Jupiter formation. In this scenario, the formation and growth of satellitesimals happen simultaneously in the disk, through the material deposited by the circumstellar disk. Finally, there is the capture model (SHIBAIKE et al., 2019), in which the circumplanetary disk would capture four satellitesimals of the circumstellar disk. These objects would grow by pebble accretion, forming the Galilean system. The caveats of these models are discussed in Section 2.1. Here, we invoke the gas-starved model and study the Galilean satellites' formation through impacts between satellitesimals and pebble accretion (Chapter 2).

Along with the Galilean satellites, Saturn's Titan (MOSQUEIRA; ESTRADA, 2003b; CANUP; WARD, 2006) and the larger regular satellites of Uranus and Neptune (MOSQUEIRA; ESTRADA, 2003b; CANUP; WARD, 2006; SZULÁGYI; CILIBRASI; MAYER, 2018) are also expected to have formed in circumplanetary disks. On the other hand, most regular mid-sized satellites of Saturn, Uranus, and Neptune are proposed to have formed from ancient rings (CHARNOZ; SALMON; CRIDA, 2010; CHARNOZ et al., 2011; CRIDA; CHARNOZ, 2012). The gas content of the circumplanetary disk dissipates in a few million years, leaving an ancient ring and satellites around the planet. Part of these satellites can be destroyed by tides, adding material to the ancient ring. Due to inter-particle collisions, the ring viscously spreads, releasing material outside the Roche limit that coagulates, possibly forming the mid-sized satellites of the Solar System (CRIDA; CHARNOZ, 2012). The formation of satellites from ancient rings is a demonstration of the strong interconnection observed between satellites and planetary rings (CHARNOZ et al., 2017).

Satellites are also observed around planets that are not expected to have opened a gap in the circumstellar disk. Therefore, a mechanism different from those mentioned needs to be invoked to explain the formation of these satellites. Our Moon orbits Earth while the small satellites Phobos

and Deimos orbit Mars; these were discovered at the end of 19th century (HALL, 1878). One could propose that these satellites are celestial bodies captured by the planet, however, their relatively low eccentricity and inclination and their chemical composition are inconsistent with such a hypothesis (SZETO, 1983).

The most plausible hypothesis for the origin of Earth and Mars satellites is their formation in a debris disk which is generated after a giant impact of an exterior body with the planet. In the case of Mars, the current spin rate of the planet can only be explained by an impact (DONES; TREMAINE, 1993; CRADDOCK, 1994; CRADDOCK, 2011), the same impact that is believed to form the Borealis basin, responsible for covering almost 40% of Mars' surface (MARINOVA; AHARONSON; ASPHAUG, 2008). Several works such as Citron, Genda e Ida (2015), Rosenblatt et al. (2016), Hyodo et al. (2017) and Canup e Salmon (2018) recreate the impact, obtaining that, in fact, it must give rise to a debris ring. Such a ring is expected to spread viscously, forming Phobos and Deimos (ROSENBLATT; CHARNOZ, 2012).

An important peculiarity of the martian system is the fact that Phobos and the Roche limit lie within the synchronous orbit, while Deimos lies beyond it. Assuming the formation from the debris ring spreading, we have that the newly formed satellites will feel opposing torques: ring torques that push them outside the planet and tidal torques that push them inside, and as consequence, there is a maximum distance at which a moon can migrate beyond the Roche limit, well inside the synchronous orbit. In the case of the giant planets, the Roche limits are beyond the synchronous orbit and all torques will push the satellites outward.

Seeing this peculiarity, we have three distinct models that intend to explain the formation of Phobos and Deimos: the splitting model, the stirred disk model, and the recycling model. The splitting model (BAGHERI et al., 2021) proposes the splitting of an ancient satellite formed in situ around Mars as the origin of the system. This satellite would have split at the synchronous orbit into two main fragments that migrated due to tides, forming Phobos and Deimos. However, studying the post-evolution of these fragments, it is obtained that they should collide with each other in less than Myr, forming a debris ring around the synchronous orbit (HYODO et al., 2022).

The stirred model assumes that the giant impact gives rise to the debris ring and also to a population of embryos beyond the Roche limit. A very cohesive satellite would form at the Roche limit and migrate outward due to ring torques. During migration, such a satellite would capture the embryos in 3:2 and 2:1 mean motion resonances, forming Phobos and Deimos, respectively. At some point, the resonances are broken and the satellite migrates inwards due to tides, pushing the ring towards the planet and then, falling itself onto Mars.

Finally, the recycling model proposes that Deimos is a direct fragment of the giant impact, while Phobos would have formed from the debris disk. A satellite formed at the Roche limit would first migrate outward due to ring torques. The ring continuously deposits material onto Mars, weakening the ring torques. At some point, the tidal torque overcomes those of the ring and the satellite begins to migrate inward. According to this model, the satellites are non-cohesive objects (rubble-pile satellites) being destroyed by tides at some position, forming a new ring that will restart the formation process.

Thus, material recycling cycles would take place around Mars. Each cycle would rise to a smaller

satellite than the one formed in the previous cycle, Phobos being the result of six of these cycles. The difference between the stirred disk and the recycling models is in the cohesion of the satellites, therefore, the data on Phobos composition that will be obtained by the MMX mission will be essential to distinguish between the models (HYODO; USUI, 2021). Additionally, the recycling model predicts the existence of a ring coexisting with Phobos, corresponding to a strong caveat of the model. In Chapter 3, we revisit the recycling model, focusing on the dynamics of the debris ring in order to find a good set of parameters capable of forming Phobos and a non-visible ring.

The formation of Phobos coexisting with a ring is another example of the intricate relation between rings and satellites, which are believed to be two aspects of the same geological system (CHARNOZ et al., 2017). Rings can give rise to satellites but satellites can also give rise to rings through processes such as tidal stripping in Uranus' rings (CANUP, 2010) and ejection of material due to impacts as in Pallene ringlet of Saturn (HEDMAN et al., 2009; MUÑOZ-GUTIÉRREZ et al., 2022). Satellites can confine rings as in Uranus' ϵ ring (PORCO; GOLDREICH, 1987) and can also be disrupted, forming new satellites. This is a possible origin for the Saturn's satellites Janus and Epimetheus (TREFFENSTÄDT; MOURÃO; WINTER, 2015).

An interesting ring system whose origin and dynamics are still not understood is that of the Neptune arcs. They were discovered in the 1980s (HUBBARD et al., 1986; SMITH et al., 1989; SICARDY; ROQUES; BRAHIC, 1991) and correspond to four bright segments of ring with well-defined azimuthal and radial widths, immersed in the Neptune's Adams ring (Fraternité, Egalité, Liberté, and Courage). As the differential Keplerian motion would completely spread the arcs in a few years (PATER et al., 2018), we have that nearby satellites must be holding the system.

For a long time, the satellite Galatea was believed to confine the arcs azimuthally due to a 84:86 corotation resonance and radially due to a 42:43 Lindblad resonance (PORCO, 1991; PORCO et al., 1995). However, observational data (SICARDY et al., 1999; DUMAS et al., 2002) show that the arcs are displaced from the corotation resonance location, leaving their confinement unexplained. Additionally, observational data show that the arcs have changed location and brightness since their discoveries (PATER et al., 2005; SHOWALTER et al., 2013; RENNER et al., 2014) and also that the arcs Liberté and Courage have disappeared (PATER et al., 2018). This evolution must be explained by any model that intends to explain the stability of the arcs.

The co-orbital family model (RENNER et al., 2014) proposes that the arcs are confined radially due to the 42:43 Lindblad resonance with Galatea and azimuthally due to 1+3 co-orbital satellites (i.e., one gravitationally dominant moon and three co-orbital moonlets). The satellites have their size and azimuthal location predicted by the original model (RENNER et al., 2014) so that the arcs are confined to the equilibrium positions of the system. The change in brightness and location of the arcs and the disappearance of two of the structures seem to be explained when the solar radiation pressure is included in the model, considering the arcs composed of particles with different typical sizes (GIULIATTI-WINTER; MADEIRA; SFAIR, 2020). Here, we study the stability of 1+N co-orbital satellites (YODER et al., 1983; RENNER; SICARDY, 2004) to verify if families of satellites different from the one proposed by Renner et al. (2014) can confine the Neptune arcs. We propose a scenario for the formation of co-orbital satellites and arcs through the disruption of an object (Chapter 4).

Recently, rings have been discovered around bodies other than planets, being observed around the centaurs Chariklo (BRAGA-RIBAS et al., 2014) and Chiron (ORTIZ et al., 2015), and the dwarf-planets Haumea (ORTIZ et al., 2017) and Quaoar (MORGADO et al., 2022). These objects have non-uniform and non-spherical shapes, which should strongly affect the dynamics of the rings. The dynamics around non-spherical bodies was studied for elongated bodies (MYSEN; OLSEN; AKSNES, 2006; MYSEN; AKSNES, 2007), contact binaries (LAGES; SHEPELYANSKY; SHEVCHENKO, 2017), and dumb-bell-shaped objects (LAGES; SHEVCHENKO; ROLLIN, 2018; ROLLIN; SHEVCHENKO; LAGES, 2021), being verified for all these classes of objects the existence of an essentially chaotic region in the vicinity of the central body. Thus, at first, it was not evident that non-uniform and non-spherical bodies could host rings.

Chariklo is a trans-Neptunian object that hosts two narrow rings (BRAGA-RIBAS et al., 2014), nicknamed Oiapoque and Chuí. The expected shape for the object is a triaxial ellipsoid (LEIVA et al., 2017; MORGADO et al., 2021), but observational data also suggest the presence of elevated topographic features on the object surface (SICARDY et al., 2019). Based on this, we study in Chapter 5 the stability around a spherical body with a mass anomaly at its equator, through the classic Poincaré surface of section technique. Afterwards, the obtained results are applied to the region of Chariklo rings.

In this thesis, we study the formation and dynamics of different ring and satellite systems, making use of different numerical techniques. The chapters are independent of each other and the physical quantities and variables and theoretical concepts involved in each system are presented in the same chapter in which they are used. Each chapter contains an abstract, an introduction, and a discussion of the results. The structure of the thesis is as follows:

- In Chapter 2, we study via N-body simulations the formation of the Galilean satellites in a circumplanetary disk around Jupiter. In Section 2.1, we present the system. In Section 2.2, we describe the methods used in the work. In Section 2.3, we describe my simulations, and in Section 2.4, we present the main results. In Section 2.5, we analyze the long-term evolution of my systems. We discuss my results and model in Section 2.6. Finally, we summarize my main findings in Section 2.7.

- In Chapter 3, we explore the recycling model for the formation of Phobos. In Section 3.1, there is the introduction of the chapter. In Section 3.2, we explain how we obtain the disruption distance depending on the mass and friction angle of a rubble-pile. In Section 3.3, we analyze the tidal evolution of Phobos and explore a tidal downsizing process of the satellite. In Section 3.4, we simulate the complete recycling mechanism and vary disk mass, debris size and friction angle. We detail the ring evolution over time in different scenarios. In Section 3.5, we discuss the implications of my results and perform analysis on the Yarkovsky effect and the effects of the recycling process on Deimos. We present my conclusions in Section 3.6.

- In Chapter 4, we study via N-body simulations equilibrium configurations for co-orbital satellites and a model for the formation of a set of arcs and co-orbital satellites. In Section 4.1, the system is introduced. In Section 4.2, we obtain the equilibrium positions of moonlets and particles in

an eccentric system of 1+N co-orbital satellites. The effects caused by Galatea are analysed in Section 4.3. In Section 4.4, we study the temporal evolution of fragments from the disruption of an ancient body. In Section 4.5, we discuss the implications of my model for the formation of the arcs. A general discussion is addressed in Section 4.6, and we present my conclusions in Section 4.7.

- In Chapter 5, we study the dynamics around a spherical body with a mass anomaly. In Section 5.1, we introduce the system. In Section 5.2, we present the disturbing function of my case of interest. In Section 5.3, we follow the pendulum model prescription to obtain an analytical recipe for the location and width of the spin-orbit resonances. Section 5.4 presents the Poincaré surface of section technique. In Section 5.5, we identify stable regions and give an overview of the system. In Sections 5.6 and 5.7, we use the Poincaré surface of section technique to confront my analytical model and study the spin-orbit resonances in detail. We apply my results to Chariklo in Section 5.8, exploring the dynamics around the object, in particular in the region of the rings. We address my final comments in Section 5.9.

- In Chapter 6, we address a general discussion of my results.

- In Appendix A, we study the dynamic evolution of the Pallene ring of Saturn.

2 BUILDING THE GALILEAN MOONS SYSTEM VIA PEBBLE ACCRETION AND MIGRATION

Due to their physical and orbital properties, it is believed that the Galilean satellites – Io, Europa, Ganymede, and Callisto – formed in a disk of dust and debris around Jupiter (LUNINE; STEVENSON, 1982), with different formation models being proposed during the last decades. One model is the gas-starved disk model (CANUP; WARD, 2002; CANUP; WARD, 2006; CANUP; WARD, 2009), in which it is assumed that the disk around Jupiter receives dust and gas, in a proportion of 1:100, from the circumstellar disk. Such material would coagulate forming satellitesimals that will give rise to the satellites. However, simulations data (LAMBRECHTS; JOHANSEN, 2014; BITSCH et al., 2018) show that the planet is responsible for gravitationally filtering the deposited material, preventing the injection of sufficiently large dust grains in the circumplanetary disk. For this reason, the formation of satellitesimals corresponds to a caveat of the classic gas-starved disk model. Here, we revisit the Galilean formation in the gas-starved disk including the pebble accretion effects in the disk, thus reducing the mass needed in the form of satellitesimals to form the system.

The content of this chapter was published as: Gustavo Madeira, André Izidoro, and Silvia M. Giuliatti Winter. "Building the Galilean moons system via pebble accretion and migration: a primordial resonant chain." Monthly Notices of the Royal Astronomical Society 504.2 (2021): 1854-1872 (MADEIRA; IZIDORO; GIULIATTI-WINTER, 2021).

2.1 INTRODUCTION

The Galilean satellites of Jupiter – namely, Io, Europa, Ganymede, and Callisto – were discovered by Galileo Galilei in the 17^{th} century. They were the first objects to be observed orbiting another body than the Earth and Sun. Historically, their importance lies in the fact that it was one of the first observational evidence supporting the Copernican view of the Solar System. Early mathematical studies of the Galilean satellites motion around Jupiter were also crucial to promote the development of celestial mechanics and our understanding of resonances in the Solar System and beyond it (JOHNSON, 1978). Today – 400 years after their discovery – the origins of the Galilean satellites remain an intense topic of debate.

Space-mission explorations, ground and space-based observations have provided a series of important constraints on Galilean satellites' formation models. The low orbital eccentricities and inclinations of these satellites and their common direction of rotation around Jupiter suggest formation in a thin common disk, in a process similar to the formation of planets around a star (LUNINE; STEVENSON, 1982). Indeed, observations (PINEDA et al., 2019; CHRISTIAENS et al., 2019) and numerical simulations (LUBOW; SEIBERT; ARTYMOWICZ, 1999; KLEY, 1999) suggest that the gas and dust not yet accreted to the envelope of a growing gas giant planet may give rise to a circumplanetary disk(hereafter referred as CPD). The formation of a circumplanetary disk is particularly possible if the temperature at the planet's envelope surface is not above a threshold ($\sim$ 2000 K) to prevent the planet's envelope from contracting and material in-falling into a fairly thin disk around its equator (WARD;

Table 1 – Physical and orbital parameters of the Galilean satellites. From left-to-right the columns are semi-major axis (a), eccentricity (e), inclination (I), mass (M), radius (R), the water-ice mass fraction (ice), and bulk density (d) of the Galilean satellites (SCHUBERT et al., 2004; OGIHARA; IDA, 2012)

	a ($\mathrm{R_J}$)	e (10^{-3})	I (deg)	M (10^{-5} $\mathrm{M_J}$)	R (km)	% ice	d (g/cm^3)
Io	5.9	4.1	0.04	4.70	1822	0	3.53
Europa	9.4	10.0	0.47	2.53	1565	8	2.99
Ganymede	15.0	1.5	0.19	7.80	2631	45	1.94
Callisto	26.4	7.0	0.28	5.69	2410	56	1.83

CANUP, 2010; SZULÁGYI et al., 2016).

A growing gas giant planet eventually opens a gap in the gaseous circumstellar disk (hereafter referred as CSD); (LIN; PAPALOIZOU, 1986a; LIN; PAPALOIZOU, 1986b). Numerical simulations show that the CPD is fed by a fraction of the gas from the CSD that enters the planet's Hill radius (LUBOW; SEIBERT; ARTYMOWICZ, 1999; KLEY, 1999) due to the meridional circulation of gas in the gap's vicinity (TANIGAWA; OHTSUKI; MACHIDA, 2012; MORBIDELLI et al., 2014; SZULÁGYI et al., 2014; SCHULIK et al., 2020). This theoretical result has been recently supported by observations of CPDs (ISELLA et al., 2019; TEAGUE; BAE; BERGIN, 2019). In this work, we use N-body numerical simulations to model the formation of the Galilean satellites in a gaseous circumplanetary disk around Jupiter. Our model includes the effects of pebble accretion, gas-driven migration, tidal damping of eccentricity and inclination, and gas drag. Before presenting the very details of our model and results, we briefly discuss the physical and orbital properties of the Galilean satellites and also review existing models accounting for the origins of the Galilean satellites.

2.1.1 Physical and orbital properties of the Galilean system

The Galilean satellites form a dynamically compact system. The innermost satellite – Io – orbits Jupiter at about $\sim$6 $\mathrm{R_J}$ while the outermost one – Callisto – is at $\sim$26 $\mathrm{R_J}$, where $\mathrm{R_J}$ is the physical radius of Jupiter. All these satellites have almost circular and coplanar orbits. Table 1 summarizes the physical and orbital parameters of the Galilean satellites.

The Galilean satellites system forms an intricate chain of orbital resonances. Io and Europa evolve in a 2:1 mean-motion resonance (MMR), where Io completes two orbits around Jupiter while Europa completes one. Europa and Ganymede are also in a 2:1 MMR. These resonances are associated with the characteristic resonant angles $2\lambda_E - \lambda_I - \varpi_I$, $2\lambda_E - \lambda_I - \varpi_E$, and $2\lambda_G - \lambda_E - \varpi_E$, where ϖ followed by a subscript label denotes a specific satellite (PEALE, 1999). These 2-body MMRs have low-amplitude libration, and they can be combined into an associated resonant angle $\phi_{I,E,G}$ that librates around 180° with a small amplitude of 0.03°. $\phi_{I,E,G}$ defines the so-called Laplace resonance and it is given as (GREENBERG, 1977)

$$\phi_{I,E,G} = 2\lambda_G - 3\lambda_E + \lambda_I, \tag{1}$$

where λ is the mean longitude, and the subscripts $_I$, $_E$, and $_G$ refer to the satellites Io, Europa, and Ganymede, respectively.

Unlike the three innermost Galilean satellites, Callisto is not locked in a first-order mean motion resonant configuration with any other satellite. This is an important constraint to formation and also dynamical evolution models.

Formation models are also constrained by the satellites' composition. Table 1 shows that the water-ice content (density) of these satellites increases (decreases) with their orbital distance to Jupiter. Io is virtually dry, Europa carries about 8% of its mass as water-ice, Ganymede and Callisto are water-ice rich bodies with ∼40-50% water-ice mass content.

The low water-ice contents of Io and Europa have been originally interpreted as evidence of formation in hot regions of the CPD disk, probably mostly inside the disk snowline – the location in the Jovian circumplanetary disk where water condensates as ice (LUNINE; STEVENSON, 1982). Their compositions have been used as strong constraints on several formation models (MOSQUEIRA; ESTRADA, 2003a; MOSQUEIRA; ESTRADA, 2003b; CANUP; WARD, 2009; RONNET; MOUSIS; VERNAZZA, 2017; SHIBAIKE et al., 2019). However, it has been more recently proposed that Io and Europa may have formed mostly from water-ice rich material (similar to Ganymede and Callisto) and lost (most of) their water. The energy deposited by the accretion of solids combined with warm temperatures in the inner parts of the CPD can lead to the formation of surface water oceans and rich water-vapor atmospheres. These water reservoirs are then rapidly lost via hydrodynamic escape, partially (or fully) drying the two innermost satellites (BIERSON; NIMMO, 2020). Additional water loss may be driven by giant impacts during their formation and enhanced tidal heating effects caused by the Laplace resonance (DWYER et al., 2013; HAY; TRINH; MATSUYAMA, 2020). Different from Io and Europa, the high concentrations of water-ice in Ganymede and Callisto suggest formation in cold and volatile-rich environments of the CPD (SCHUBERT et al., 2004), very likely outside the disk snowline where very limited water loss via hydrodynamic escape took place, if any at all.

Formation models have also attempted to account for expected differences in the internal structures of the Galilean satellites. Different levels of core-mantle segregation are typically associated to different accretion timescales (MOSQUEIRA; ESTRADA, 2003a; MOSQUEIRA; ESTRADA, 2003b; CANUP; WARD, 2002; CANUP; WARD, 2006; CANUP; WARD, 2009; SASAKI; STEWART; IDA, 2010; MIGUEL; IDA, 2016; RONNET; MOUSIS; VERNAZZA, 2017; SHIBAIKE et al., 2019). Io, Europa, and Ganymede are most likely fully differentiated bodies, with well distinct metallic cores and silicate mantles (SCHUBERT et al., 2004). Unlikely, Callisto has been thought to be at most only partially differentiated (SCHUBERT et al., 2004). The weak evidence of endogenic activity on Callisto's surface found by the Galileo mission in combination with frustrated detection of a core magnetic field by magnetic observations suggest limited differentiation (JOURNAUX et al., 2020). This implies that Callisto had a relatively late and protracted accretion phase, potentially completed after the extinction of short-lived radioactive nuclei (BARR; CANUP, 2008; BARR; CANUP, 2010) – the most likely source of heating to cause large scale ice melting and core segregation. In this school of thought, it has been proposed that Callisto formed no earlier than ∼3 Myr after the calcium–aluminum-rich inclusions (MCKINNON, 2006). Io, Europa, and Ganymede should have formed earlier than that to account for their differentiated state. However, the interior structure of Callisto is still debated. It has been more recently suggested that even in the scenario of late/protracted formation, it could be

very difficult to suppress differentiation of Callisto due to density gradients trapping heat generated by the decay of long-lived radioisotopes (O'ROURKE; STEVENSON, 2014) during the Solar System history. The presence of non-hydrostatic pressure gradients in Callisto could also allow a complete differentiated state (GAO; STEVENSON, 2013). So, if Callisto is (fully) differentiated or not remains unclear (RONNET; JOHANSEN, 2020).

Finally, it is also important to note in Table 1 that the masses of the Galilean satellites do not show any clear correlation with their orbital distance to Jupiter (e.g., no radial mass ranking), which is an important constraint to formation models (CRIDA; CHARNOZ, 2012). In the next section, we review Galilean satellite formation models to motivate this work.

2.1.2 The minimum mass sub-nebula model (MMSN model)

Based on the minimum mass solar nebula model for the Solar System (WEIDENSCHILLING, 1977; HAYASHI, 1981), Lunine e Stevenson (1982) and Mosqueira e Estrada (2003a), Mosqueira e Estrada (2003b) proposed a modified version of this scenario applied to the Galilean satellites system. In these models, solids in the CPD are assumed to be in form of km-sized satellitesimals (following Mosqueira e Estrada (2003a), Mosqueira e Estrada (2003b), we use the term "satellitesimals" to refer to km-sized objects, precursors of the satellites in the CPD) that grow by mutual collisions up to the Galilean satellites masses. In most of these simulations, satellites are formed in very short timescales, typically of about 10^2-10^3 years, which would suggest that they all should have differentiated interiors (or similar internal structure). This has been one of the issues raised against the MMSN model because several models considered that Callisto is at most only partially differentiated (CANUP; WARD, 2002). Regardless if Callisto is or not differentiated in reality, other inconsistencies between the model results and the real satellite system exist. In addition, the masses and orbits of the simulated satellites poorly match the Galilean ones (e.g. some simulations show satellite systems with radial mass ranking).

Miguel e Ida (2016) analyzed the formation of the Galilean satellites considering different MMSN model scenarios. They invoked a semi-analytical model to simulate migration and growth including also the effects of an inner cavity in the gas disk. This disk feature was mostly neglected in previous studies but it is crucial to avoid the dramatic loss of solids via gas drag and gas driven migration in the disk (MIGUEL; IDA, 2016). When a body reaches the inner disk cavity its drift and migration stop which allows other bodies migrating/drifting inwards to be captured in MMRs. This process tends to repeat and leads to the formation of a resonant chain anchored at the disk inner edge (IZIDORO et al., 2017; IZIDORO et al., 2021). The authors verified that the final period-ratio of adjacent satellites in their simulated systems better reproduce the Galilean system if the migration timescale is increased, relative to those used in Mosqueira e Estrada (2003a), Mosqueira e Estrada (2003b). However, by invoking longer migration timescales to avoid the mentioned issue, the masses of their simulated satellites did not provide a reasonable match to the Galilean satellites (MIGUEL; IDA, 2016). Finally, the semi-analytical treatment invoked in Miguel e Ida (2016) did not allow them to precisely model the secular and resonant interaction of adjacent satellite pairs neither their growth via giant impacts.

Moraes, Kley e Neto (2018) explored the MMSN model using N-body simulations starting from a population of satellites-embryos that are allowed to type-I migrate and grow via giant impacts. Some

of their simulations were successful in producing four satellites starting from a population of $\sim$20 satellite-embryos and many relatively smaller satellitesimals, but their simulations fail to match the final masses and orbital configuration of the Galilean satellites. In their best Galilean system analogue, the innermost satellite is at 17 R_J whereas Io is at 5.9 R_J (see Table 1). Their simulations also show that when several satellites reach the disk inner edge, forming a long-resonant chain, they all get engulfed by Jupiter. It is not clear why this phenomenon takes place in their simulations. If satellites are successively pushed inside the disk inner cavity and eventually collide with Jupiter one-by-one, one would expect that at least one satellite should survive anchored at the disk inner edge at the end of this process.

2.1.3 The classic gas-starved disk model (GSD model)

One of the major differences between the MMSN disk models and the gas-starved disk model (GSD model) is that the latter invokes CPDs that are orders of magnitude lower-mass than MMSN disks. The GSD model is probably one of the most successful early models for the origins of the Galilean satellites (CANUP; WARD, 2002; CANUP; WARD, 2006; CANUP; WARD, 2009). However, this model requires to be revisited because our paradigm of planet formation has evolved significantly in the last 10 years.

The GSD model is built on the assumption that a semi-steady gas flows from the circumstellar disk to Jupiter's circumplanetary disk simultaneously delivers gas and solid material to the CPD with roughly solar dust-to-gas ratio composition. The original GSD model invokes that all dust delivered to the CPD by gas in-fall coagulates and grows into satellitesimals of masses of about 5×10^{-7} M_J. Then, satellitesimals grow to satellites by mutual collisions (CANUP; WARD, 2002; CANUP; WARD, 2006; CANUP; WARD, 2009).

Although very appealing when initially proposed, this idea presents some conflicts with our current understanding of planet formation. Recent simulations show that a 10-20 Earth-mass planet, gravitationally interacting with the gas disk, creates a pressure bump outside its orbit (LAMBRECHTS; JOHANSEN, 2014; BITSCH et al., 2018) that prevents sufficiently large dust grains in CSD from being delivered to the planet's circumplanetary disk. So, in fact, the dust-to-gas ratio in Jupiter's CPD incoming gas is expected to be lower than that in the sun's CSD, perhaps several orders of magnitude lower than the solar value (RONNET et al., 2018; WEBER et al., 2018). This view is also supported by mass-independent isotopic anomalies measured in carbonaceous and non-carbonaceous meteorites. The isotopic differences between these two classes of meteorites have been interpreted as evidence of very efficient separation of the inner and outer Solar System pebble reservoirs, potentially caused by Jupiter's formation (KRUIJER et al., 2017; BRASSER; MOJZSIS, 2020). The filtering of pebbles promoted by Jupiter would have also affected the abundance of pebbles in its own CPD (RONNET; JOHANSEN, 2020). This is a critical issue because it challenges the in-situ formation of satellites(imals) in the CPD. Satellitesimal formation via streaming instability (YOUDIN; LITHWICK, 2007; SIMON et al., 2016a; ARMITAGE; EISNER; SIMON, 2016; DRAŻKOWSKA; SZULÁGYI, 2018) – the favorite scenario to explain how mm-cm size dust grains grow to km-sized objects – requires dust-to-gas ratio of at least a few percent (YANG; JOHANSEN; CARRERA, 2017).

Finally, the origins of satellitesimals in the CPD is probably more easily explained via capture of planetesimals or fragments (produced in planetesimal-planetesimal collisions) from the CSD. Planetesimals or fragments on eccentric orbits around the Sun may eventually cross the orbit of the growing Jupiter (RAYMOND; IZIDORO, 2017) and get temporarily or even permanently captured in the CPD (ESTRADA; MOSQUEIRA, 2006; CANUP; WARD, 2009). This is possible because gas drag dissipative effects act to damp the orbits of these objects when they travel across the CPD (ADACHI; HAYASHI; NAKAZAWA, 1976; ESTRADA; MOSQUEIRA, 2006; MOSQUEIRA; ESTRADA; TURRINI, 2010; FUJITA et al., 2013; D'ANGELO; PODOLAK, 2015; SUETSUGU; OHTSUKI; FUJITA, 2016; SUETSUGU; OHTSUKI, 2017). Planetesimals traveling across the CPD are also ablated and this mechanism is probably the main source of pebbles (mm-cm-sized dust grains) to the CPD (ESTRADA; MOSQUEIRA, 2006; ESTRADA et al., 2009; MOSQUEIRA; ESTRADA; TURRINI, 2010; FUJITA et al., 2013; D'ANGELO; PODOLAK, 2015; SUETSUGU; OHTSUKI; FUJITA, 2016; SUETSUGU; OHTSUKI, 2017; RONNET; JOHANSEN, 2020). The total mass in planetesimals/fragments captured and pebbles created via this process depends on planetesimals/fragments sizes, the total mass in planetesimals/fragments, and gas density in the giant's planet region which are not strongly constrained (RAYMOND; IZIDORO, 2017; RONNET; JOHANSEN, 2020). Nevertheless, this scenario is very appealing because it invokes a single mechanism to explain the origins of pebbles and satellitesimals in the CPD.

2.1.4 More Recent Models

Galilean satellites' formation models have also invoked gas-drag assisted accretion of millimeter and centimeter size pebbles to account for their origin (RONNET; MOUSIS; VERNAZZA, 2017; SHIBAIKE et al., 2019; RONNET; JOHANSEN, 2020). This regime of growth is popularly known as pebble accretion (ORMEL; KLAHR, 2010; LAMBRECHTS; JOHANSEN, 2012; LAMBRECHTS; JOHANSEN, 2014; MORBIDELLI et al., 2015; LEVISON; KRETKE; DUNCAN, 2015a; BITSCH et al., 2018).

One of the key advantages of invoking pebble accretion to explain the formation of the Galilean system is that the growth of satellitesimals up to the masses of these satellites does not necessarily require a large (N>500-1000) population of satellitesimals to exist in the CPD – as assumed in traditional models (MOSQUEIRA; ESTRADA, 2003a; MOSQUEIRA; ESTRADA, 2003b; CANUP; WARD, 2002; CANUP; WARD, 2006; CANUP; WARD, 2009). As already discussed, the in-situ formation of satellitesimals in the CPD may be problematic. However, if at least a handful of sufficiently massive satellitesimals exist in the CPD, pebble accretion may be efficient in forming a system with a few relatively massive final satellites.

Shibaike et al. (2019) studied the growth of the Galilean satellites via pebble accretion. Their simulations include the effects of gas drag and type-I migration. They invoke integrated pebble fluxes in the CPD of about 1.5×10^{-3} $\mathrm{M_J}$. Shibaike et al. (2019) set the CPD's inner edge at Io's current position (but see also Sasaki, Stewart e Ida (2010), Miguel e Ida (2016), Moraes, Kley e Neto (2018)). Shibaike et al. (2019) performed simulations considering initially 4 satellitesimals in the CPD. Satellitesimals are individually inserted in the CPD at different times, to mimic planetesimal capture from the CSD.

They admittedly fine-tuned their simulations to produce systems that match well the masses, orbits, and water ice fractions of the Galilean satellites. Although this is an interesting approach, giving the large number of free parameters in the model, one of the key caveats of their scenario is that it is built on semi-analytical calculations rather than in N-body numerical simulations. Their simulations do not account for the gravitational interaction between satellites as they accrete pebbles and migrate (CILIBRASI et al., 2018). The efficiency of pebble accretion is strongly dependent on the orbital parameters of the growing satellites (LEVISON; KRETKE; DUNCAN, 2015b). Thus, they can not precisely assess the final architecture of their systems. One of the questions that remains unanswered is whether or not an initial number of satellitesimals larger than four is also successful in reproducing the Galilean system. This is one of the questions we try to answer in this paper. We also advance to the reader that all our simulations starting initially with 4 satellitesimals produced less than 4 satellites at the end.

In a recent study, Batygin e Morbidelli (2020) proposed that the Galilean satellites' formation occurred in a vertically-fed CPD disk that spreads viscously outwards (the vertically averaged radial gas velocity is $v_r > 0$ everywhere in the CPD). In their model, satellitesimals in the CPD grow to satellites in an oligarchic growth fashion – via satellitesimal-satellitesimal collisions – rather than via pebble accretion. Numerical simulations in Batygin e Morbidelli (2020) start from planetesimals with masses of 4×10^{-7} $\mathrm{M_J}$ (4 times more massive than the initial masses considered in this paper). The authors find that in their disk model pebble accretion can be simply neglected, which is not necessarily the case for other disk models (RONNET; MOUSIS; VERNAZZA, 2017; RONNET; JOHANSEN, 2020). Their model successfully explains some characteristics of the Galilean system, as the overall masses of the Galilean satellites and the Laplace resonance, however, it remains to be demonstrated that the total dust reservoir assumed in their model can in fact settle into the CPD disk mid-plane to promote efficient satellitesimal formation via some sort of gravitational-hydrodynamic instability (BATYGIN; MORBIDELLI, 2020).

In this work, we use N-body numerical simulations to model the formation of the Galilean satellites in a GSD-style circumplanetary disk. Motivated by previous studies, the flux of pebbles assumed in our simulations is consistent with pebble fluxes estimated via ablation of planetesimals entering the circumplanetary disk (RONNET; JOHANSEN, 2020). The initial total number of satellitesimals in the CPD is not strongly constrained, so in our simulations, we test 4, 30, and 50 satellitesimals. Our study represents a further step towards the understanding of the origins of the Galilean satellites because previous studies modeling their formation via pebble accretion have typically invoked simple semi-analytical models that neglect the mutual interaction of the satellites when they grow and migrate in the disk. Here, we self-consistently model the growth and mutual dynamical interaction of satellitesimals allowing also for growth via giant collisions.

The model that we propose here has the very same basic ingredients invoked in models for the formation of the so-called close-in super-Earths and giant planets around other stars (IZIDORO et al., 2021; BITSCH et al., 2019; LAMBRECHTS et al., 2019) – namely pebble accretion and migration. Typical close-in super-Earths have masses of $\sim 10^{-5}$ $\mathrm{M_{star}}$. Interestingly, the mass ratio of individual Galilean satellites and Jupiter is also $\sim 10^{-5}$. The resonant dynamical architecture of the Galilean

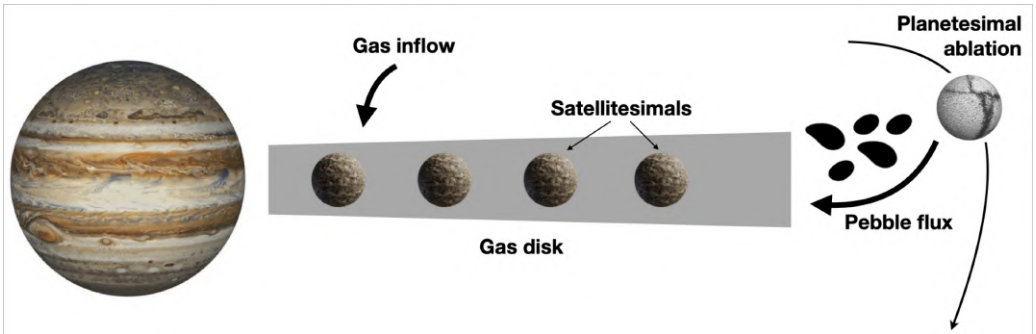

Figure 1 – Scheme of the satellite formation environment. Gas material from the CSD is deposited in the CPD due to meridional flows, while the ablation of planetesimals due to Jupiter gives rise to a population of satellitesimals and flux of pebbles in the disk. The satellitesimals grow by mutual collisions and pebble accretion, giving rise to the the Galilean satellites.

satellites also recalls that of some super-Earths systems (MIGUEL; IDA, 2016). So if one can explain the formation of these both types of systems via the same processes it would be reassuring. A scheme of our model is shown in Figure 1.

2.2 METHODS

Our numerical simulations were performed using an adapted version of the `MERCURY` package (CHAMBERS, 1999) including artificial forces to mimic the effects of the gas disk. These forces are: 1) gas drag; 2) type I migration, and eccentricity and inclination damping (Section 2.2.2). Our pebble accretion prescription is described in details in Section 2.2.3. Satellitesimals are allowed to grow via pebble accretion and collisions. Collisions are modeled as perfect merging events that conserve mass and linear momentum.

2.2.1 Circumplanetary disk model

We assume that as Jupiter grows via runaway gas accretion, opens a deep gap in the circumstellar disk, and a disk mostly composed by gas forms around its equator. The circumplanetary disk is continually supplied by the in-fall of material from the CSD. Assuming a semi-steady flow of gas and balance between the in-fall of material from the CSD and the mass accretion rate onto Jupiter, Canup e Ward (2002) obtained that the radial surface density of gas is given by

$$\Sigma_g(r) = \frac{\dot{\mathrm{M}}_\mathrm{g}}{3\pi\nu(r)} \begin{cases} 1 - \frac{4}{5}\sqrt{\frac{R_c}{R_d}} - \frac{1}{5}\left(\frac{r}{R_c}\right)^2 & \text{for } r \leq R_c \\ \frac{4}{5}\sqrt{\frac{R_c}{r}} - \frac{4}{5}\sqrt{\frac{R_c}{R_d}} & \text{for } r > R_c, \end{cases} \tag{2}$$

where R_c and R_d are the centrifugal and outer radius of the disk, respectively, $\dot{M}_g$ the mass in-fall rate, and ν the turbulent viscosity. Note that our disk model is qualitatively consistent with the delivery of gas to the CPD via meridional circulation of gas near the planet's gap (TANIGAWA; OHTSUKI; MACHIDA, 2012; MORBIDELLI et al., 2014; SZULÁGYI et al., 2014; SCHULIK et al., 2020; BATYGIN; MORBIDELLI, 2020). In our model, we assume that the gas is deposited into the CPD midplane at around the centrifugal radius (R_c), and then spreads viscously (CANUP; WARD, 2002).

R_c corresponds to the location in the CPD where the angular momentum of the inflowing material is equal to the Keplerian angular momentum. R_c is treated as a free parameter in our model (BATYGIN; MORBIDELLI, 2020).

The mass in-fall rate from the CSD on the CPD in our simulations was set as (SASAKI; STEWART; IDA, 2010; RONNET; MOUSIS; VERNAZZA, 2017)

$$\dot{\mathrm{M}}_{\mathrm{g}} = 10^{-7} e^{-\frac{t}{\tau_d}} \ \mathrm{M_J/yr}, \tag{3}$$

where t is the time and $\tau_d = 1.0$ Myr is the disk decay timescale (CANUP; WARD, 2002). For simplicity, in all our simulations, we neglect Jupiter's growth via gas accretion and set its mass as the current one.

We set the centrifugal radius at the fixed distance $R_c = 26\ \mathrm{R_J}$ (RONNET; MOUSIS; VERNAZZA, 2017) and the outer edge of the disk at $R_d = 150\ \mathrm{R_J}$, based on the results of hydrodynamic simulations (TANIGAWA; OHTSUKI; MACHIDA, 2012). The interaction of the CPD with Jupiter's magnetic field tends to slow down the planet's rotation and promotes the formation of an inner disk cavity. Batygin (2018) found that magnetic effects dominate the gas dynamics in the inner regions of the CPD up to $4 - 5\ \mathrm{R_J}$. Motivated by this result, we follow Izidoro et al. (2017) and impose a disk inner edge at $R_i = 5\ \mathrm{R_J}$ (BATYGIN; MORBIDELLI, 2020) in our CPD by re-scaling the gas surface density by

$$\mathcal{R} = \tanh\left(\frac{r - R_i}{0.05 R_i}\right) \tag{4}$$

We assumed the standard α-viscosity prescription to represent the disk viscosity (SHAKURA; SUNYAEV, 1973)

$$\nu = \alpha_z c_s H_g, \tag{5}$$

where $\alpha_z = 10^{-3}$ (RONNET; MOUSIS; VERNAZZA, 2017) is the coefficient of turbulent viscosity, c_s is the isothermal sound speed and H_g the gas scale height ($H_g = c_s/\Omega_k$, where Ω_k is the keplerian orbital frequency). For a CPD in hydrostatic equilibrium, the sound speed relates to the disk temperature $T(r)$ as $c_s^2 = 2.56 \times 10^{23}\ g^{-1}\ k_b T$, where k_b is the Boltzmann constant (HAYASHI, 1981). The snowline is initially located at $r \sim 14.5\ \mathrm{R_J}$ and the radial temperature profile is given by (RONNET; MOUSIS; VERNAZZA, 2017)

$$T = 225 \left(\frac{r}{10\ \mathrm{R_J}}\right)^{-3/4} K \tag{6}$$

Figure 2a shows the CPD aspect ratio ($h_g = H_g/r$, solid line) and ratio between the vertically averaged gas radial and keplerian velocities (v_r/v_k, dotted line). In our disk model, the gas inside $\sim R_c$ flows inwards whereas gas outside $\sim R_c$ flows outwards (BATYGIN; MORBIDELLI, 2020), as one can note in Figure 2a.

2.2.2 Gas effects

Our simulations start with satellitesimals of masses of $m \sim 10^{-7}\ \mathrm{M_J}$ and bulk density of $2\ \mathrm{g/cm^3}$. We have verified that in our disk setup gas-drag plays an important role in the dynamics of satellitesimals

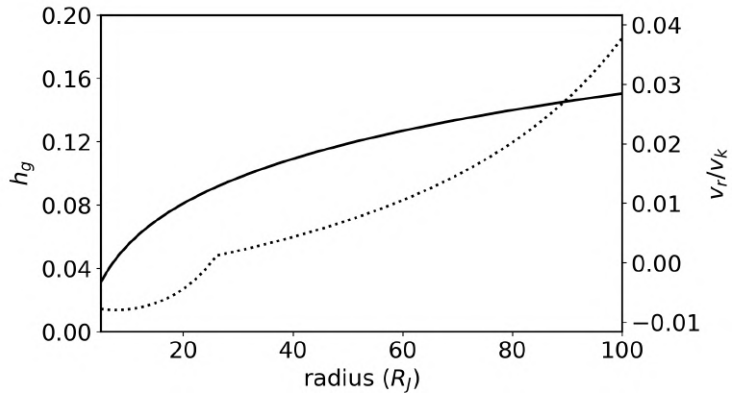

(a)

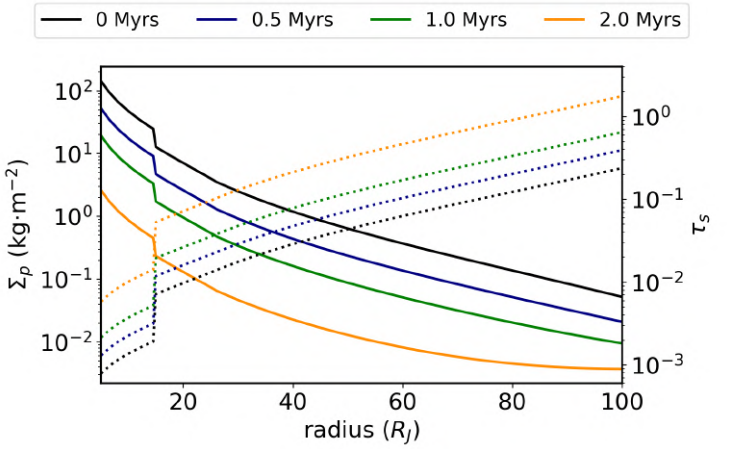

(b)

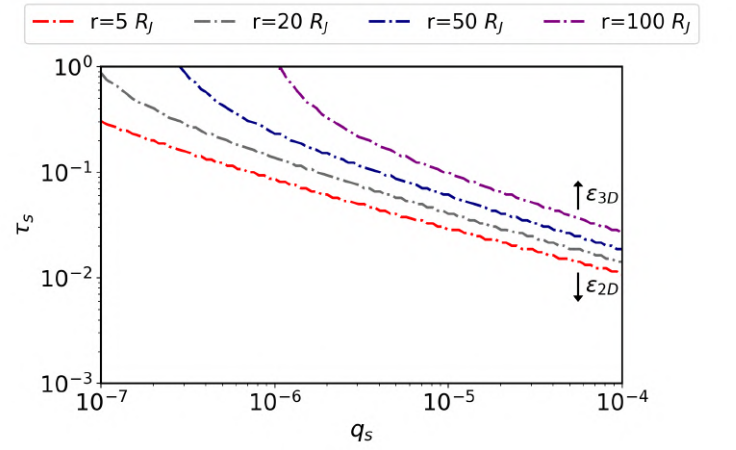

(c)

Figure 2 – (a) CPD aspect ratio ($h_g = H_g/r$, solid line) and vertically averaged gas radial velocity normalized by the keplerian velocity (v_r/v_k, dotted line); (b) pebble surface density (solid lines) and Stokes number (dotted lines) as a function of the distance to the planet. Each color shows different times: 0 Myr (black), 0.5 Myr (blue), 1.0 Myr (green), and 2.0 Myr (orange); (c) Threshold curves of 2D and 3D pebble accretion regimes for different satellite masses and Stokes numbers. The different colored lines correspond to different locations of the disk: 5 $\mathrm{R_J}$ (red), 20 $\mathrm{R_J}$ (gray), 50 $\mathrm{R_J}$ (navy blue), and 100 $\mathrm{R_J}$ (purple). The region above (below) of each curve corresponds to the region where the 3D (2D) accretion efficiency is higher than the 2D (3D) one (see Eq. 53). The initial pebble flux is $\dot{\mathrm{M}}_{\mathrm{p0}} = 1.5 \times 10^{-9}$ $\mathrm{M_J}$/yr. The integrated pebble flux over time is 10^{-3} $\mathrm{M_J}$.

of these sizes (MIGUEL; IDA, 2016). Thus, our model includes both the effects of gas drag and satellitesimal-disk gravitational interactions. We now describe how we model these effects.

2.2.2.1 Gas Drag

The CPD around Jupiter rotates at sub-Keplerian speed because it is pressure supported. Small satellitesimals in the CPD orbiting at keplerian speed feel an strong headwind, lose energy, and tend to spiral inwards. The azimuthal gas disk velocity is given by

$$v_g = (1 - \eta)v_k, \tag{7}$$

where $v_k = \Omega_k r$ is the Keplerian velocity and η characterizes the sub-Keplerian velocity of the gas disk. It is given by

$$\eta = -\frac{h_g^2}{2}\frac{\partial \ln c_s^2 \rho_g}{\partial \ln r}, \tag{8}$$

Setting $\rho_g = \int_{-\infty}^{\infty} \Sigma_g dz$, the gas volumetric density ρ_g is given by (WEIDENSCHILLING, 1977)

$$\rho_g = \frac{1}{\sqrt{2\pi}}\frac{\Sigma_g}{H_g} e^{-z^2/2H_g^2} \tag{9}$$

where z is the reference-frame vertical component.

The gas-drag acceleration on a body of radius R_s and bulk density ρ_s is given by (ADACHI; HAYASHI; NAKAZAWA, 1976)

$$\vec{a}_{gd} = -\frac{3}{8}\frac{C_d \rho_g v_{rel}}{\rho_s R_s}\vec{v}_{rel} \tag{10}$$

where C_d is the drag coefficient, $\vec{v}_{rel}$ is velocity of the body with respect to the gas.

The drag coefficient computes the intensity of the interaction between the gas and satellitesimal, and it is given by (BRASSER; DUNCAN; LEVISON, 2007)

$$C_d = \begin{cases} 2 & \mathcal{M} \geq 1 \\ 0.44 + 1.56\mathcal{M}^2 & \mathcal{M} < 1,\ Re \geq 10^3 \\ \frac{24(1+0.15Re^{0.687})}{Re} & \mathcal{M} < 1,\ Re < 10^3, \end{cases} \tag{11}$$

where $\mathcal{M} = v_{rel}/c_s$ is the Mach number and Re the Reynolds number written as

$$Re \approx 2.66 \times 10^8 \rho_g R_s \mathcal{M}. \tag{12}$$

2.2.2.2 Type-I migration

Sufficiently large satellitesimals interact gravitationally with the CPD launching spiral density waves that transport angular momentum. This interaction tends to promote eccentricity and inclination damping of orbits and radial migration. Satellites with masses of the order of the Galilean satellites ($m \sim 10^{-5}$ M_J) or lower mass are not expected to open gaps in our CPD disk and migrate in the type-I regime (CANUP; WARD, 2006). The total type-I migration torque consists of contributions

from the Lindblad and Co-rotational torques (PAARDEKOOPER et al., 2010; PAARDEKOOPER; BARUTEAU; KLEY, 2011).

The surface density and temperature gradient profiles, x and β, respectively, are given by

$$x = -\frac{\partial \ln \Sigma_g}{\partial \ln r} \tag{13}$$

and

$$\beta = -\frac{\partial \ln T}{\partial \ln r}. \tag{14}$$

The scaling torque at the satellite's location is given by (CRESSWELL; NELSON, 2008)

$$\Gamma_0 = \left(\frac{q_s}{h_g}\right)^2 \Sigma_g r^4 \Omega_k^2, \tag{15}$$

where $q_s = m/\mathrm{M_J}$ is the satellite-Jupiter mass ratio.

The Lindblad torque felt by a satellite on circular and coplanar orbit is parameterized as (PAARDEKOOPER et al., 2010; PAARDEKOOPER; BARUTEAU; KLEY, 2011)

$$\Gamma_L = (-2.5 - 1.5\beta + 0.1x)\frac{\Gamma_0}{\gamma_{\text{eff}}}, \tag{16}$$

where γ_{eff} is the effective adiabatic index defined by (PAARDEKOOPER et al., 2010; PAARDEKOOPER; BARUTEAU; KLEY, 2011)

$$\gamma_{\text{eff}} = \frac{2\gamma Q}{\gamma Q + \frac{1}{2}\sqrt{2\psi + 2\gamma^2 Q^2 - 2}}, \tag{17}$$

$$\psi = \sqrt{(\gamma^2 Q^2 + 1)^2 - 16Q^2(\gamma - 1)}, \tag{18}$$

and

$$Q = \frac{2\chi}{3h_g^3 r^2 \Omega_k} \tag{19}$$

where γ is the adiabatic index assumed as $\gamma = 1.4$ in this work. The thermal diffusion coefficient χ depends on the opacity κ and is given by (PAARDEKOOPER et al., 2010; PAARDEKOOPER; BARUTEAU; KLEY, 2011)

$$\chi = \frac{16\gamma(\gamma - 1)k_B T^4}{3\kappa\rho_g^2 (h_g r)^2 \Omega_k^2}. \tag{20}$$

The CPD disk opacity is calculated as in Bell et al. (1995).

A satellite on circular and coplanar orbit experiences a corotation torque that reads as (PAARDEKOOPER et al., 2010; PAARDEKOOPER; BARUTEAU; KLEY, 2011)

$$\begin{aligned}\Gamma_C = \Bigg[1.1\left(\frac{3}{2} - x\right)F(p_\nu)G(p_\nu) + \frac{7.9\xi}{\gamma_{\text{eff}}}F(p_\nu)F(p_\chi)\sqrt{G(p_\nu)G(p_\chi)} + \\ + 0.7\left(\frac{3}{2} - x\right)(1 - K(p_\nu)) + \left(2.2\xi - \frac{1.4\xi}{\gamma_{\text{eff}}}\right)\sqrt{(1 - K(p_\nu))(1 - K(p_\chi))}\Bigg]\frac{\Gamma_0}{\gamma_{\text{eff}}},\end{aligned} \tag{21}$$

where $\xi = \beta - (\gamma - 1)x$, and p_ν and p_χ are parameters that measure the viscous and thermal saturations of the co-orbital torque, respectively. F, G and K are functions of these parameters.

The parameters p_ν and p_χ are given by (PAARDEKOOPER et al., 2010; PAARDEKOOPER; BARUTEAU; KLEY, 2011)

$$p_\nu = \frac{2}{3}\sqrt{\frac{r^2\Omega_k}{2\pi\nu}\left(\frac{1.1}{\gamma_{\text{eff}}^{1/4}}\sqrt{\frac{q_s}{h_g}}\right)^3} \tag{22}$$

and

$$p_\chi = \frac{2}{3}\sqrt{\frac{r^2\Omega_k}{2\pi\chi}\left(\frac{1.1}{\gamma_{\text{eff}}^{1/4}}\sqrt{\frac{q_s}{h_g}}\right)^3} \tag{23}$$

The functions F, G e K are (PAARDEKOOPER et al., 2010; PAARDEKOOPER; BARUTEAU; KLEY, 2011)

$$F(p) = \frac{1}{1 + \left(\frac{p}{1.3}\right)^2}, \tag{24}$$

$$G(p) = \begin{cases} \frac{16}{25}\left(\frac{45\pi}{8}\right)^{3/4} p^{3/2} & \text{for } p < \sqrt{\frac{8}{45\pi}} \\ 1 - \frac{9}{25}\left(\frac{8}{45\pi}\right)^{4/3} p^{-8/3} & \text{for } p \geq \sqrt{\frac{8}{45\pi}} \end{cases}, \tag{25}$$

and

$$K(p) = \begin{cases} \frac{16}{25}\left(\frac{45\pi}{28}\right)^{3/4} p^{3/2} & \text{for } p < \sqrt{\frac{28}{45\pi}} \\ 1 - \frac{9}{25}\left(\frac{28}{45\pi}\right)^{4/3} p^{-8/3} & \text{for } p \geq \sqrt{\frac{28}{45\pi}} \end{cases} \tag{26}$$

The torques Γ_L and Γ_C need to be modified to account for satellitesimals/satellites on eccentric or inclined orbits. The Lindblad torque is reduced by factor Δ_L and the corotation torque by Δ_C (CRESSWELL; NELSON, 2008; COLEMAN; NELSON, 2014; FENDYKE; NELSON, 2014) given by

$$\Delta_L = \left\{ P_e + \frac{P_e}{|P_e|}\left[0.07\left(\frac{i_s}{h_g}\right) + 0.085\left(\frac{i_s}{h_g}\right)^4 - 0.08\left(\frac{e_s}{h_g}\right)\left(\frac{i_s}{h_g}\right)^2 \right] \right\}^{-1} \tag{27}$$

and

$$\Delta_C = \exp\left(-\frac{e_s}{0.5h_g + 0.01}\right)\left[1 - \tanh\left(\frac{i_s}{h_g}\right)\right] \tag{28}$$

where

$$P_e = \frac{1 + \left(\frac{e_s}{2.25h_g}\right)^{1.2} + \left(\frac{e_s}{2.84h_g}\right)^6}{1 - \left(\frac{e_s}{2.02h_g}\right)^4} \tag{29}$$

Finally, we can write the total torque associated to the type I migration as

$$\Gamma = \Delta_L\Gamma_L + \Delta_C\Gamma_C \tag{30}$$

and the acceleration $\vec{a}_m$ of a satellite with angular momentum L is (CRESSWELL; NELSON, 2008)

$$\vec{a}_m = \frac{\vec{v}}{L}\Gamma \tag{31}$$

The gas disk also damps eccentricity and inclination of sufficiently massive bodies on timescales given by (CRESSWELL; NELSON, 2008)

$$t_e = \frac{t_{wv}}{0.780}\left[1 - 0.14\left(\frac{e_s}{h_g}\right)^2 + 0.06\left(\frac{e_s}{h_g}\right)^3 + 0.18\left(\frac{e_s}{h_g}\right)\left(\frac{i_s}{h_g}\right)^2\right] \tag{32}$$

and

$$t_i = \frac{t_{wv}}{0.544}\left[1 - 0.30\left(\frac{i_s}{h_g}\right)^2 + 0.24\left(\frac{i_s}{h_g}\right)^3 + 0.14\left(\frac{e_s}{h_g}\right)^2\left(\frac{i_s}{h_g}\right)\right] \tag{33}$$

where $t_{\rm wv}$ is the wave timescale (CRESSWELL; NELSON, 2008)

$$t_{\rm wv} = \left(\frac{M*}{q_s \Sigma_g a_s^2}\right)\frac{h_g^4}{\Omega_k}, \tag{34}$$

a_s is the satellite/satellitesimal semi-major axis.

The accelerations experienced by the bodies due to the eccentricity and inclination damping are (CRESSWELL; NELSON, 2008)

$$\vec{a}_e = -2\frac{(\vec{v}\cdot\vec{r})\vec{r}}{r^2 t_e} \tag{35}$$

and

$$\vec{a}_i = -2\frac{(\vec{v}\cdot\hat{z})\hat{z}}{t_i} \tag{36}$$

2.2.3 Pebble Accretion

The pebble surface density Σ_p in our model is (SHIBAIKE et al., 2019)

$$\Sigma_p = \frac{\dot{\rm M}_{\rm p}}{4\pi\tau_s\eta v_k r}(1+\tau_s^2), \tag{37}$$

where τ_s is the Stokes number and $\dot{\rm M}_{\rm p}$ is the pebble mass flux given by $\dot{\rm M}_{\rm p} = \dot{\rm M}_{\rm p0} e^{-\frac{t}{\tau_d}}$ where $\dot{\rm M}_{\rm p0}$ is a free scaling parameter that we take to vary between $\dot{\rm M}_{\rm p0} = 10^{-9}$ M$_{\rm J}$/yr and 5×10^{-9} M$_{\rm J}$/yr. Thus the integrated pebble fluxes in our simulations vary between 8×10^{-4} M$_{\rm J}$ and 4×10^{-3} M$_{\rm J}$. These values are consistent with the pebble fluxes estimated via ablation of planetesimals (RONNET; JOHANSEN, 2020).

The Stokes number of a pebble with a physical radius R and bulk density ρ is given by (LAMBRECHTS; JOHANSEN, 2012)

$$\tau_s = \frac{\sqrt{2\pi}\rho R}{\Sigma_g} \tag{38}$$

In this work, we assumed a bi-modal population of pebbles in the CPD.

In our CPD the snowline is at ~ 14.5 R$_{\rm J}$. Pebbles outside the snowline are assumed to have sizes of $R = 1.0$ cm and $\rho = 2.0$ g/cm^3. As pebbles drift inwards via gas drag they eventually cross the CPD snowline. At this location, we reduce the pebble flux by a factor of 2 to account for the sublimation of the ice-pebble component. Ice pebbles sublimate at the snowline releasing small silicate dust grains. To account for this effect, pebbles inside the snowline have sizes of $R = 0.1$ cm and $\rho = 5.5$ g/cm^3.

Figure 2b shows the pebble surface density evolution and the Stokes number in function of the radial distance, in units of $\mathrm{R_J}$.

The pebble accretion rate is a product of the pebble flux and the total accretion efficiency ϵ (IDA; GUILLOT; MORBIDELLI, 2016). Following Liu e Ormel (2018) and Ormel e Liu (2018), the 2D accretion efficiency in the settling regime is given by

$$\epsilon_{2d,set} = 0.32\sqrt{\frac{q_s}{\tau_s \eta^2}\left(\frac{\Delta V}{v_k}\right)} f_{\mathrm{set}} \tag{39}$$

where ΔV is the relative velocity between pebble and satellite and f_{set} is a function that fits well the transition between different accretion regimes.

The relative velocity of a satellitesimal on a circular orbit and a pebble is (LIU; ORMEL, 2018)

$$V_{\mathrm{cir}} = \left[1 + 5.7\left(\frac{q_s \tau_s}{\eta^3}\right)\right]^{-1} \eta v_k + 0.52(q_s\tau_s)^{1/3} v_k \tag{40}$$

while the relative velocity of satellite on a non-circular but coplanar orbit reads (LIU; ORMEL, 2018)

$$V_{\mathrm{ecc}} = 0.76 e_s v_k \tag{41}$$

One can write the relative velocity between a pebble and a satellite in both regimes as (LIU; ORMEL, 2018; ORMEL; LIU, 2018)

$$\Delta V_y = \max(V_{\mathrm{cir}}, V_{\mathrm{ecc}}) \tag{42}$$

The relative velocity between a pebble and a satellite on a slightly inclined orbit can be written as $\Delta V_z = 0.68 i_s v_k$. Finally, the total relative velocity becomes (LIU; ORMEL, 2018; ORMEL; LIU, 2018)

$$\Delta V = \sqrt{\Delta V_y^2 + \Delta V_z^2} \tag{43}$$

The transition function f_{set} is given by (ORMEL; LIU, 2018)

$$f_{\mathrm{set}} = \frac{V_*}{\sqrt{V_*^2 + 0.33\sigma_{pz}^2}} \exp\left[-0.5\left(\frac{\Delta V_y^2}{V_*^2} + \frac{\Delta V_z^2}{V_*^2 + 0.33\sigma_{pz}^2}\right)\right] \tag{44}$$

where V_* is the transition velocity

$$V_* = \sqrt[3]{\frac{q_s}{\tau_s}} v_k \tag{45}$$

and σ_{pz} is the turbulent velocity in the z-direction (YOUDIN; LITHWICK, 2007):

$$\sigma_{pz} = \sqrt{\frac{\alpha_z}{1+\tau_s}}\left(1 + \frac{\tau_s}{1+\tau_s}\right)^{-1/2} h_g v_k \tag{46}$$

The pebble disk aspect ratio is given by (YOUDIN; LITHWICK, 2007)

$$h_p = \sqrt{\frac{\alpha_z}{\alpha_z + \tau_s}}\left(1 + \frac{\tau_s}{1+\tau_s}\right)^{-1/2} h_g, \tag{47}$$

and the pebble volume density is (ORMEL; LIU, 2018)

$$\rho_p = \frac{\Sigma_p}{\sqrt{2\pi} r h_p} \tag{48}$$

According to Liu e Ormel (2018) and Ormel e Liu (2018), the tridimensional pebble accretion efficiency in the settling regime is

$$\epsilon_{\rm 3d,set} = 0.39 \frac{q_s}{\eta h_{\rm eff}} f_{\rm set}^2 \tag{49}$$

where $h_{\rm eff}$ is the effective aspect ratio of pebbles in relation to a satellite in inclined orbit (ORMEL; LIU, 2018)

$$h_{\rm eff} = \sqrt{h_p^2 + \frac{\pi i_s^2}{2}\left[1 - \exp\left(-\frac{i_s}{2h_p}\right)\right]} \tag{50}$$

The accretion efficiency in the 2D and 3D ballistic regimes are (LIU; ORMEL, 2018; ORMEL; LIU, 2018)

$$\epsilon_{\rm 2d,bal} = \frac{R_s}{2\pi\tau_s \eta r}\sqrt{\frac{2q_s r}{R_s}\left(\frac{\Delta V}{v_k}\right)^2}(1 - f_{\rm set}) \tag{51}$$

and

$$\epsilon_{\rm 3d,bal} = \frac{1}{4\sqrt{2\pi}\eta\tau_s h_p}\left(2q_s \frac{v_k}{\Delta V}\frac{R_s}{r} + \frac{R_s^2}{r^2}\frac{\Delta V}{v_k}\right)(1 - f_{\rm set}^2) \tag{52}$$

Finally, the total pebble accretion efficiency is

$$\epsilon = \frac{f_{\rm set}}{\sqrt{\epsilon_{\rm 2d,set}^{-2} + \epsilon_{\rm 3d,set}^{-2}}} + \frac{1 - f_{\rm set}}{\sqrt{\epsilon_{\rm 2d,bal}^{-2} + \epsilon_{\rm 3d,bal}^{-2}}} \tag{53}$$

Figure 2c shows the curves $\epsilon_{2d} = \epsilon_{3d}$ for different Stokes number and satellite's masses. Each curve samples the accretion regime at one specific location of the disk. Regions above each curve corresponds to regions where the 3D accretion rate is higher than the 2D rate. Below each curve, it is the opposite.

When a satellite reaches the isolation mass $\rm M_{iso}$, its Hill radius becomes greater than the disk height creating a pressure bump that deflects gas and pebbles. If the satellite reaches $\rm M_{iso}$ the pebble accretion breaks off and the satellite grow only by impacts. The pebble isolation mass in $\rm M_J$ is given by (ATAIEE et al., 2018)

$$\rm M_{iso} = h_g^3\sqrt{37.3\alpha_z + 0.01}\left\{1 + 0.2\left(\frac{\sqrt{\alpha_z}}{h_g}\sqrt{\frac{1}{\tau_s^2} + 4}\right)^{0.7}\right\} \tag{54}$$

2.3 SIMULATIONS

We have performed 120 simulations considering different pebble fluxes and the initial number of satellitesimals. The initial number of satellitesimals in the CPD is poorly constrained and it may also increase in time if additional planetesimals are captured from the CSD as the system evolves (MOSQUEIRA; ESTRADA; TURRINI, 2010; RONNET; JOHANSEN, 2020). We decided to neglect

the capture of new planetesimals after our simulation starts by assuming that only sufficiently early captured planetesimals would successively grow by pebble accretion. We have performed simulations starting with 4, 30, and 50 satellitesimals in the CPD. While it would be ideal to systematically test the effects of different initial number of satellitesimals in our model, our N-body simulations are computationally expensive what limits our approach. Our simulations starting with 4 satellitesimals are designed to test the scenario proposed by Shibaike et al. (2019) using self-consistent N-body simulations. Satellitesimals are initially distributed between 20 $\mathrm{R_J}$ and 120 $\mathrm{R_J}$. Their initial masses are set 10^{-7} $\mathrm{M_J}$ and bulk densities $\rho = 2.0$ g/cm^3 which are consistent with the typical masses/sizes of planetesimals formed via streaming instability (JOHANSEN et al., 2014; ARMITAGE; EISNER; SIMON, 2016; SIMON et al., 2016b). Satellitesimals are initially separated from each other by 5 to 10 mutual Hill radii R_H (KOKUBO; IDA, 2000; KRETKE; LEVISON, 2014)

$$R_H = \frac{a_i + a_j}{2} \left(\frac{2 \times 10^{-7}}{3} \right)^{1/3} \tag{55}$$

where a_i and a_j are the semi-major axes of a pair of adjacent satellitesimals. They are set initially on nearly circular and coplanar orbits ($e \leq 10^{-4}$ and $I \leq 10^{-4}$). Other angular orbital elements are randomly and uniformly selected between 0 and 360 deg.

Our simulations are numerically integrated for 2 Myr, considering the gas disk effects. In a few cases, to evaluate the long-term dynamical stability of our final systems, we extended our simulations up to $\sim$10 Myr, assuming that the gaseous circumplanetary disk dissipates at 2 Myr. For simplicity, we relate the pebble flux in our simulations to the gas accretion flow in the CPD (SHIBAIKE et al., 2019). We performed simulations with $\dot{\mathrm{M}}_{\mathrm{p0}} = 10^{-9}$ $\mathrm{M_J}$/yr, 1.5×10^{-9} $\mathrm{M_J}$/yr, 3×10^{-9} $\mathrm{M_J}$/yr, and 5×10^{-9} $\mathrm{M_J}$/yr. The integrated pebble flux from the lowest pebbles flux to the highest one are 8×10^{-4} $\mathrm{M_J}$, 10^{-3} $\mathrm{M_J}$, 3×10^{-3} $\mathrm{M_J}$, and 4×10^{-3} $\mathrm{M_J}$. In these simulations, we have neglected the evolution of the CPD's temperature, but the gas surface dissipates exponentially with an e-fold timescale of 1 Myr.

2.3.1 Constraining our model

Our model is strongly constrained by key features of the Galilean satellites system as the number of satellites, orbital configuration, final masses, and compositions. To evaluate how our simulations match the Galilean satellites system, we define a list of relatively generous constraints. A Galilean system analogue must satisfy the following conditions:

i) the final system must contain at least four satellites;

ii) the two innermost satellite-pairs must be locked in a 2:1 MMR;

iii) the individual masses of all satellites must be between $0.8\mathrm{M_E}$ and $1.2\mathrm{M_G}$, where $\mathrm{M_E}$ and $\mathrm{M_G}$ are the masses of Europa and Ganymede, respectively;

iv) the two outermost satellites must have water-ice rich compositions (>0.3 water mass fraction).

Although Io is extremely water-ice depleted today and Europa contains only $\sim$8% of its mass as water-ice (Table 1), we do not consider these estimates to be strong constraints to our model, because it is possible that these satellites formed with water richer compositions and lost all/most of their water (BIERSON; NIMMO, 2020). Also, we stress that Callisto is not locked in a first-order mean motion resonance with Ganymede today. We also do not consider this observation a critical constrain to our model because Callisto may have left the resonance chain via divergent migration due to Jupiter-satellites tidal interactions (FULLER; LUAN; QUATAERT, 2016; DOWNEY; NIMMO; MATSUYAMA, 2020). We will further discuss these two issues later in the paper.

2.4 RESULTS

We start by presenting the results of our sets of simulations considering initially 4 satellitesimals in the CPD, inspired by simulations of Shibaike et al. (2019). In Shibaike et al. (2019), satellitesimals are assumed to "appear" in the CPD successively, at very specific times. In our simulations, they are assumed to appear simultaneously at the beginning of the simulation in arbitrarily selected positions. Note that, in our case, the four satellitesimals start about 20 $\mathrm{R_J}$ from each other, which roughly mimics their approach. By disposing our 4 satellitesimals initially fairly apart from each other, we avoid early collisions and allow them to grow at least one order of magnitude in mass before they start to strongly interact with each other (which may affect the efficiency of pebble accretion).

Figure 3 shows the evolution of one of our representative systems. In this simulation, we set $\dot{\mathrm{M}}_{\mathrm{p0}} = 10^{-9}$ $\mathrm{M_J}$/yr. Figure 3 shows that satellitesimals first grow by pebble accretion and start to migrate inwards. When they reach the inner edge of the disk a dynamical instability takes place and leads to a collision. At the end of this simulation, at 2 Myr, 3 satellites survive with individual masses of the order of 10^{-5} $\mathrm{M_J}$. The innermost and outermost satellite pairs are locked in a compact 5:4 and 3:2 MMR, respectively. The orbital eccentricities of satellites at the end of our simulations are between 0.02 and 0.05, which are larger than those of the Galilean satellites.

We verified that each one of our 40 numerical simulations starting with 4 satellitesimals shows at least one collision during the gas disk phase, typically when satellites approach the disk inner edge. This suggests that more than four satellitesimals are required to explain the Galilean system. This is in conflict with the results of Shibaike et al. (2019), and these simulations violate our constraint i). In fact, even the final period ratio of the satellites in our simulations does not agree with those Shibaike et al. (2019) have found. They have assumed that migrating satellites are successively captured in the 2:1 MMR when the migration timescale is longer than a critical timescale (OGIHARA; KOBAYASHI, 2013). The critical timescale criteria used in the semi-analytical model of Shibaike et al. (2019) does not fully account for the eccentricity/inclination evolution of the satellites due to secular and resonant interactions. The capture in MMR also depends on the resonance order and mass-ratio of the migrating satellites (BATYGIN, 2015). For instance, when the inner satellite is less massive than the outer one (e.g. Europa and Ganymede), the 2:1 MMR can be skipped even when the adiabatic criteria for capture is attended (BATYGIN, 2015). Thus, the criteria for capture in resonance assumed by Shibaike et al. (2019) is in fact too simplistic. It is just a good proxy to infer (non-)capture in mean motion resonance if the eccentricities of the satellites can be neglected (OGIHARA; KOBAYASHI, 2013), which we

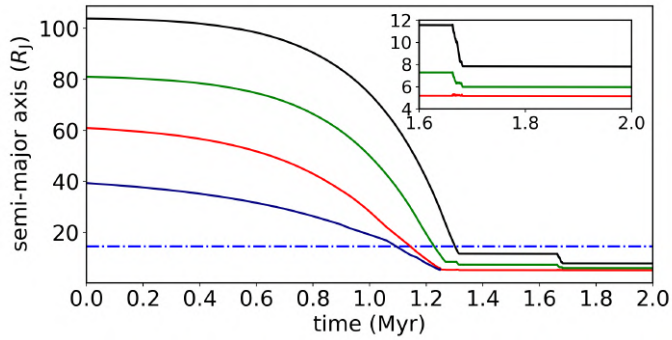

(a)

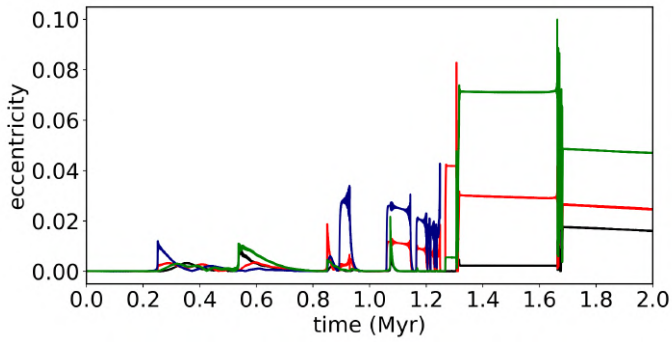

(b)

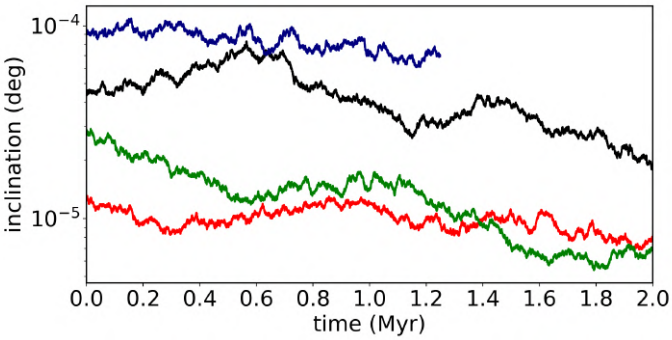

(c)

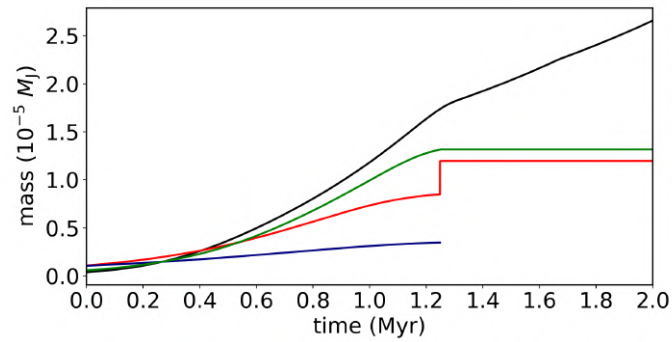

(d)

Figure 3 – Evolution of a) semi-major axes, b) orbital eccentricities, c) inclinations, and d) mass of satellitesimals in a simulation starting with four satellitesimals and $\dot{\mathrm{M}}_{\mathrm{p0}} = 10^{-9}$ $\mathrm{M_J}$/yr. Satellitesimals initially grow via pebble accretion and migrate inwards. When they reach the inner edge of the disk locate at about 5 $\mathrm{R_J}$, the innermost satellite pair collides at ~ 1.2 Myr forming a system with only three final satellites. The blue dot-dashed line in panel (a) shows the evolution of the snowline location in the disk.

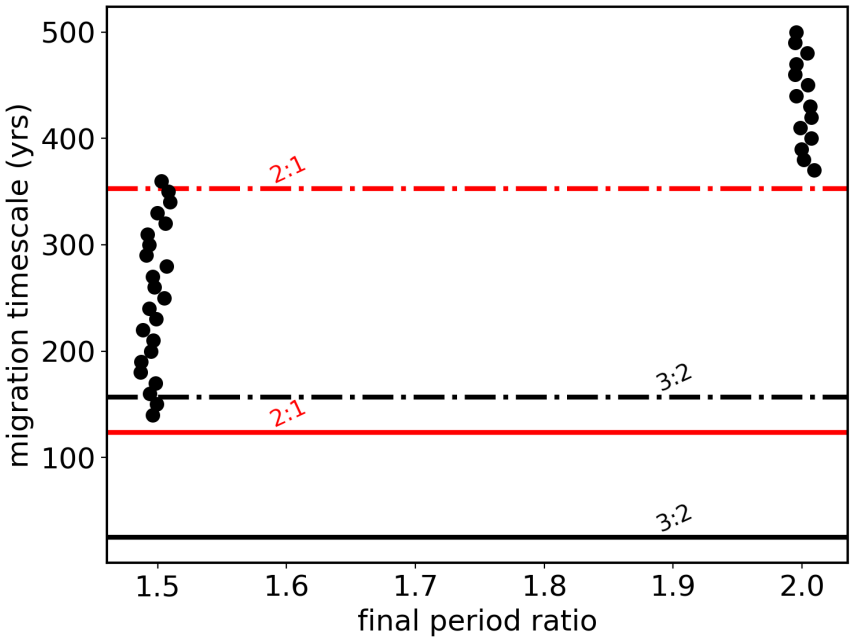

Figure 4 – Correlation between final period ratio and migration timescale in simulations considering only two satellites with masses analogues of those of Io and Europa. The black dots represent the results of our numerical simulations, and horizontal lines are estimated critical timescales that lead to capture into 3:2 MMR (black line) and 2:1 MMR (red lines). The solid lines show the critical timescales inferred by Ogihara e Kobayashi (2013) and the dashed lines show the critical timescales given by Goldreich e Schlichting (2014). We have found that migration timescales shorter than ∼130 yrs tend to lead to dynamical instabilities and collisions of the satellites.

show here to not be the case.

We performed some simple simulations considering the very disk model of Shibaike et al. (2019). This specific set of simulations starts with an Io-mass satellite fully formed and residing slightly outside the disk inner cavity, and an Europa-mass satellite initially placed at 15 R_J. These satellites are released to migrate inwards – but they are not allowed to accrete pebbles. Our goal here is just compare the final resonant architecture of these satellites in our simulations and that predicted by the approach invoked in Shibaike et al. (2019). To conduct this set of experiments, we assume that satellites migrate with constant migration timescales, that do not vary with the distance to Jupiter. Figure 4 shows these results. In the vertical axis of Figure 4, we show the migration timescale and in the horizontal axis the final period ratio of the satellites. Critical migration timescales that lead to capture in 2:1 and 3:2 MMR used in Shibaike et al. (2019) are shown as solid black and red lines, respectively. The dot-dashed black and red lines show the migration timescales that lead to capture in 2:1 and 3:2 MMR when orbital eccentricities are taken into account (GOLDREICH; SCHLICHTING, 2014). We use the eccentricity of the satellites in our simulations as input to calculate the latter timescales. The black dots show the results of our numerical simulations which agree very well with those of Goldreich e Schlichting (2014). The difference observed between our results and those of Shibaike et al. (2019) is caused by the increase in the eccentricity of the satellites when they approach each other, which breaks down the validity of their criteria for capture in resonance. We have found that the timescale predicted to lead to capture in 2:1 MMR in simulations of Shibaike et al. (2019) in fact tends to lead to collisions.

2.4.1 Effects of the pebble flux

In this section, we present the results of our simulations starting with 30 and 50 satellitesimals and compare the effects of different pebble fluxes. Figure 5 shows the final satellite systems produced in our simulations at the end of the gas disk phase ($\sim$2 Myr). Simulations starting with 30 satellitesimals are shown on the left panels, and simulations starting with 50 satellitesimals are presented on the right panels. The horizontal axis of each panel shows the final semi-major axis and the vertical axis shows the mass of satellites. Each panel shows the results of 10 different simulations, where in each simulation, satellitesimals start with slightly different orbital parameters. Colorful dot-dashed lines connecting different points (symbols) show different satellite systems. The black filled circles show the real Galilean satellite system for reference. For presentation purposes, in Figure 5, we have re-scaled the position of the satellites by a factor of order of unity to make the position of the innermost satellite in our simulations to correspond to the distance of Io to Jupiter ($a_{\rm in}$). At the top of each panel, we show the fraction of systems that produced a given final number of satellites.

Figure 5 shows that when the pebble flux decreases, from top to bottom, the final masses of the satellites also decrease. Final masses of satellites in simulations starting with 30 and 50 satellitesimals, and same pebble fluxes, are not dramatically different from each other. Both sets of simulations show that an increase in the pebble flux by a factor of $\gtrsim$2 (from $\dot{\rm M}_{\rm p0} = 1.5 \times 10^{-9}$ M$_{\rm J}$/yr to $\dot{\rm M}_{\rm p0} = 5 \times 10^{-9}$ M$_{\rm J}$/yr) is enough to change the final structure of our satellite systems from systems where satellites have masses fairly similar to those of the Galilean satellites to systems where satellites have systematically larger masses. Our overall best match to masses Galilean satellite system comes from simulations with $\dot{\rm M}_{\rm p0} = 1.5 \times 10^{-9}$ M$_{\rm J}$/yr. The time-integrated pebble flux in this latter case corresponds to $\sim 10^{-3}$M$_{\rm J}$. Lower pebble fluxes ($\dot{\rm M}_{\rm p0} = 10^{-9}$ M$_{\rm J}$/yr) produce too low-mass satellites, also inconsistent with the real system. Our simulations that best reproduce the mass of the Galilean satellites typically produce between 3 and 5 satellites. The efficiency of pebbles accretion in these systems is about 9%, which is similar to efficiencies calculated by Ronnet e Johansen (2020) ($\sim$10%).

Figure 6 shows the final period ratio distribution of adjacent satellites in our simulations. Again, the left and right panels show the results of simulations starting with 30 and 50 satellitesimals, respectively. The two top panels in this figure a) and b) – which correspond to the highest pebble flux – show that systems with more massive satellites tend to have dynamically less compact systems (e.g. a larger fraction of pairs with period ratio $\geq$ 2). Our sets of simulations that better match the masses of the Galilean satellites (Figure 6; panels e) and f)) typically produce $\sim$10-20% of satellite pairs locked in 2:1 MMR. The majority of satellite pairs in our systems is locked in more compact resonant configurations.

Figure 7 shows the final semi-major axis versus the mass of satellites in selected systems that satisfy all constraints defined in Section 2.3.1. As in Figure 5, each satellite is shown by a colorful point (symbol) – where lines connect satellites in a same system. The system shown in red represents our nominal analogue that will be further discussed later in the paper. The real Galilean system is shown in black. The three innermost vertical dotted lines mark the respective positions of the three innermost Galilean satellites. The outermost vertical dotted line shows the location of Callisto if it was also locked in a 2:1 mean motion resonance with Ganymede. The horizontal pink lines show

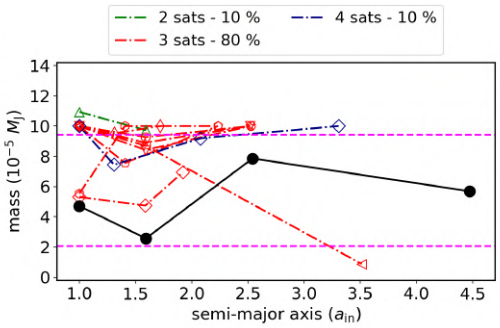

(a) $\dot{M}_{p0} = 5 \times 10^{-9}$ M_J/yr and 30 satellitesimals

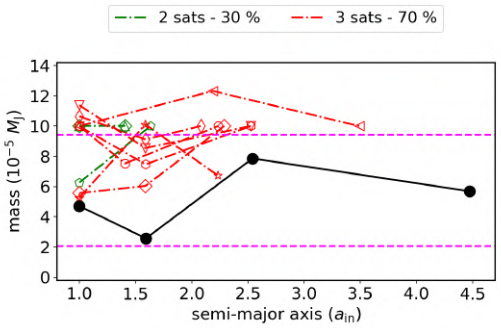

(b) $\dot{M}_{p0} = 5 \times 10^{-9}$ M_J/yr and 50 satellitesimals

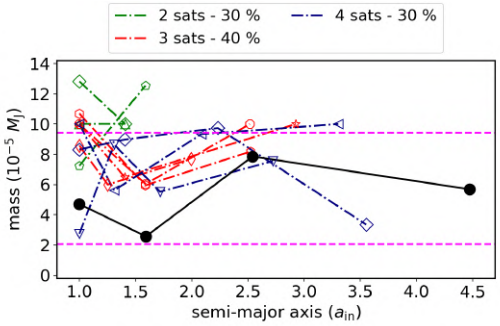

(c) $\dot{M}_{p0} = 3 \times 10^{-9}$ M_J/yr and 30 satellitesimals

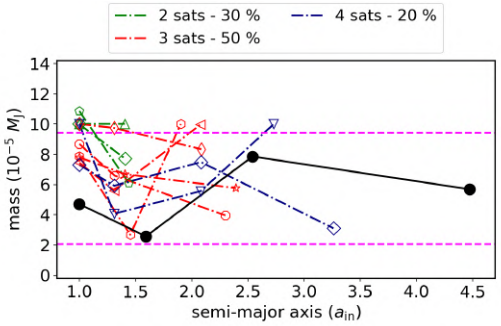

(d) $\dot{M}_{p0} = 3 \times 10^{-9}$ M_J/yr and 50 satellitesimals

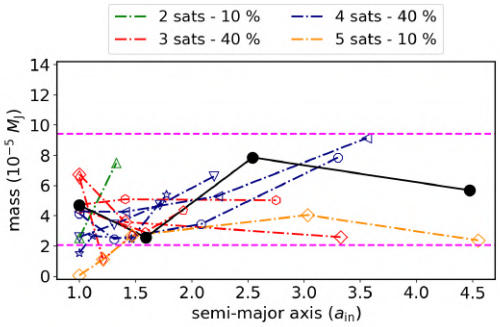

(e) $\dot{M}_{p0} = 1.5 \times 10^{-9}$ M_J/yr and 30 satellitesimals

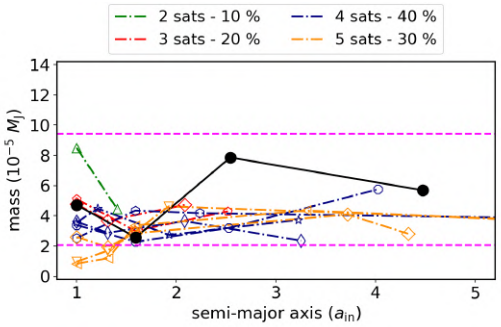

(f) $\dot{M}_{p0} = 1.5 \times 10^{-9}$ M_J/yr and 50 satellitesimals

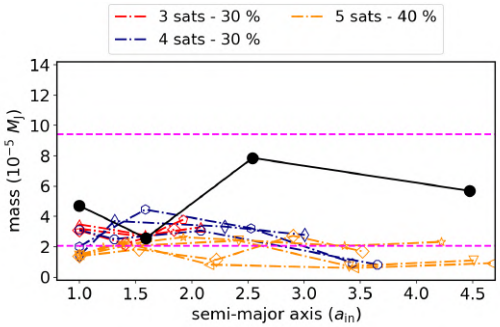

(g) $\dot{M}_{p0} = 10^{-9}$ M_J/yr and 30 satellitesimals

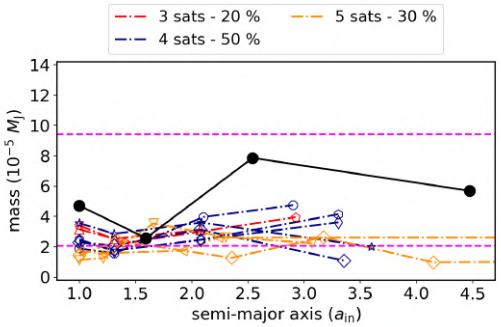

(h) $\dot{M}_{p0} = 10^{-9}$ M_J/yr and 50 satellitesimals

Figure 5 – Final satellite systems produced in simulations starting with different initial number of satellitesimals and pebble fluxes. The left and right side panels show the results of simulations starting with 30 and 50 satellitesimals, respectively. The panels show the results of simulations with different pebble fluxes: a) and b) $\dot{M}_{p0} = 5 \times 10^{-9}$ M_J/yr, c) and d) $\dot{M}_{p0} = 3 \times 10^{-9}$ M_J/yr, e) and f) $\dot{M}_{p0} = 1.5 \times 10^{-9}$ M_J/yr, and g) and h) $\dot{M}_{p0} = 10^{-9}$ M_J/yr. The lines connecting different points (symbols) show satellites in a same system. The fraction of simulations that produce two (green dot-dash lines), three (red dot-dash), four (blue dot-dash), and five satellites (orange dot-dash) are given at the top of each panel. The black solid line shows the real Galilean system. The horizontal pink lines correspond to $0.8M_E$ and $1.2M_G$ (see constraint iii)).

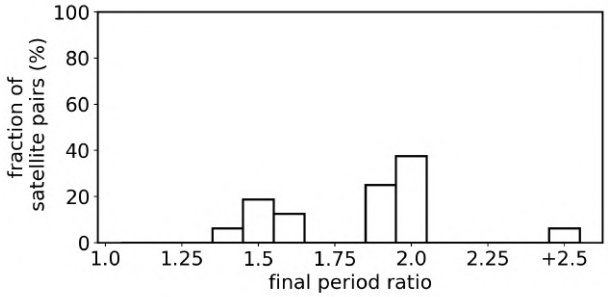

(a) $\dot{M}_{p0} = 5 \times 10^{-9}$ M_J/yr and 30 satellitesimals

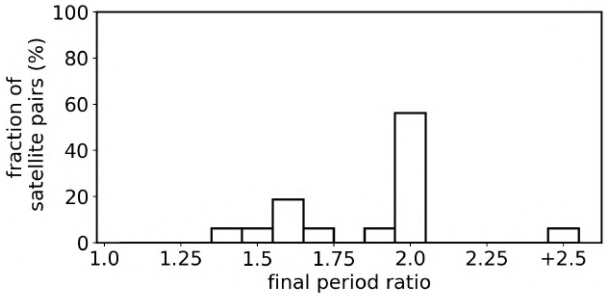

(b) $\dot{M}_{p0} = 5 \times 10^{-9}$ M_J/yr and 50 satellitesimals

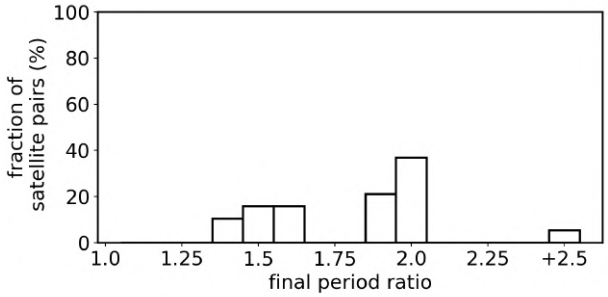

(c) $\dot{M}_{p0} = 3 \times 10^{-9}$ M_J/yr and 30 satellitesimals

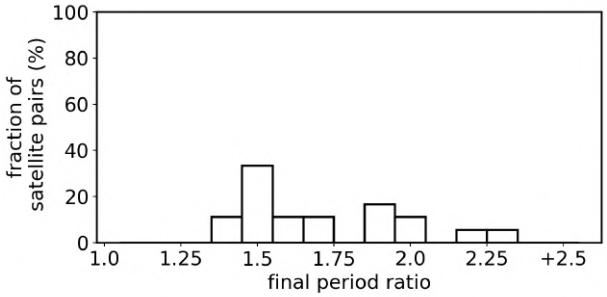

(d) $\dot{M}_{p0} = 3 \times 10^{-9}$ M_J/yr and 50 satellitesimals

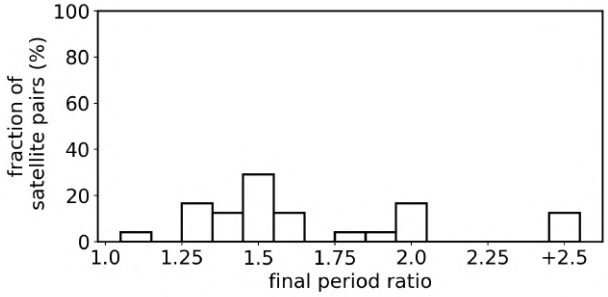

(e) $\dot{M}_{p0} = 1.5 \times 10^{-9}$ M_J/yr and 30 satellitesimals

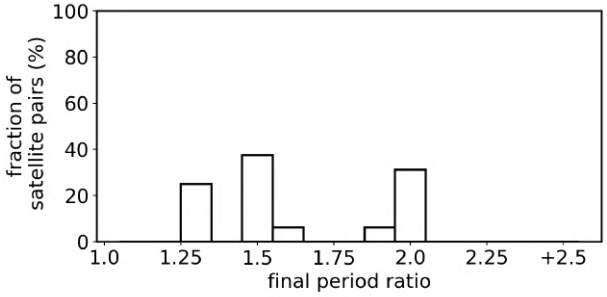

(f) $\dot{M}_{p0} = 1.5 \times 10^{-9}$ M_J/yr and 50 satellitesimals

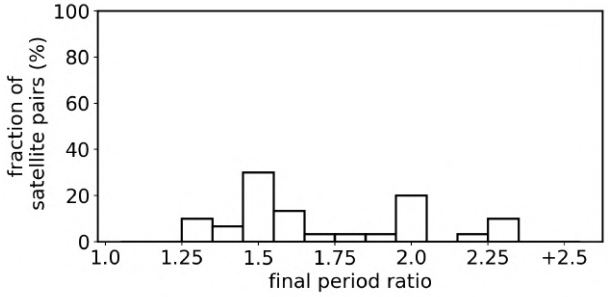

(g) $\dot{M}_{p0} = 10^{-9}$ M_J/yr and 30 satellitesimals

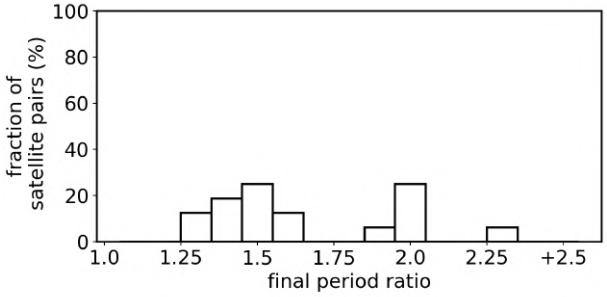

(h) $\dot{M}_{p0} = 10^{-9}$ M_J/yr and 50 satellitesimals

Figure 6 – Period ratio distribution of adjacent satellite-pairs. Each panel shows the results of 10 simulations. The left and right side panels show the results of simulations starting with 30 and 50 satellitesimals, respectively. The panels show the results of simulations with different pebble fluxes: a) and b) $\dot{M}_{p0} = 5 \times 10^{-9}$ M_J/yr, c) and d) $\dot{M}_{p0} = 3 \times 10^{-9}$ M_J/yr, e) and f) $\dot{M}_{p0} = 1.5 \times 10^{-9}$ M_J/yr, and g) and h) $\dot{M}_{p0} = 10^{-9}$ M_J/yr.

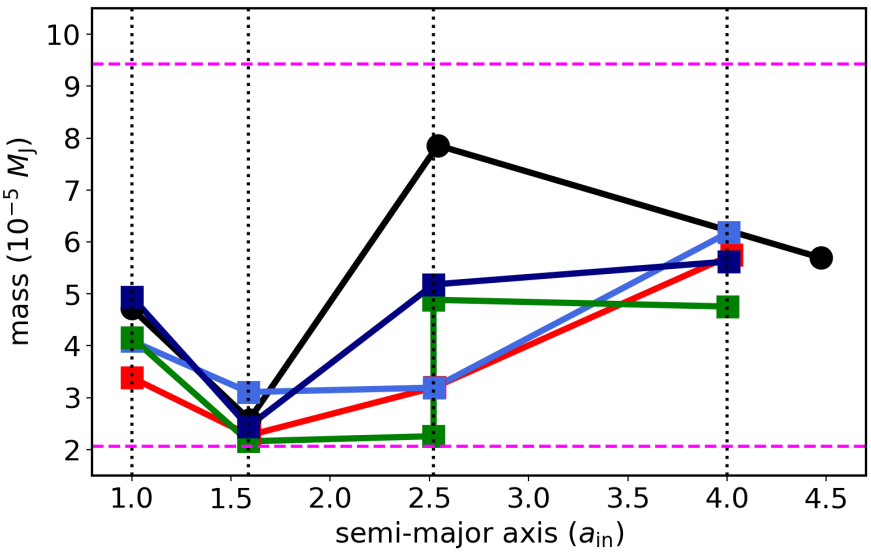

Figure 7 – Final masses and semi-major axes of satellites produced in our best-case simulations. For presentation purposes, we have re-scaled the position of the satellites by a factor of order of unity to make the position of the innermost satellite in our simulations to coincide with the distance of Io to Jupiter ($a_{\rm in}$). The real Galilean system is given by the black line with a circle and the vertical dotted lines give the location of the 8:4:2:1 resonant chain and the pink vertical lines give the limits on mass of our third constraint ($0.8{\rm M_E}$ and $1.2{\rm M_G}$). Our final systems show no radial mass ranking. The system represented by the green solid line shows a co-orbital satellite with the third innermost satellite.

the limiting masses defined in constraint iii) of Section 2.3.1. These systems match fairly well the masses and resonant configurations of the Galilean satellite system. However, the outermost satellite in our simulations is always locked in a 2:1 MMR with the second outermost one. As discussed before, Callisto is not locked in resonance with Ganymede. We do not consider this to be a critical issue for our model because Callisto may have left the resonance chain via divergent migration due to tidal-interaction of satellites with Jupiter (FULLER; LUAN; QUATAERT, 2016; DOWNEY; NIMMO; MATSUYAMA, 2020).

Figure 7 also shows that in our best analogues, the mass of the innermost satellite is typically larger than that of the second innermost one, which is also true in the Galilean system. However, the masses of our Ganymede-analogues are typically lower than that of the real satellite. Finally, one of the important result of our model is that the radial-mass distribution of our satellites do not present any radial mass-ranking (e.g. satellites' mass increases with their distance to Jupiter) or triangular-mass distribution (e.g. the innermost and outermost satellites are the less massive). These are typical issues found in previous models (**??**, e.g.)]Mosqueira2003a,Mosqueira2003b,Crida2012.

2.4.2 The Dynamical Architecture of our Systems

In this section, we present the dynamical evolution of some of our best Galilean system analogues. Figure 8 shows a simulation with $\dot{\rm M}_{\rm p0} = 1.5 \times 10^{-9}$ ${\rm M_J}$/yr, and starting with 50 satellitesimals. The panels show the temporal evolution of semi-major axis, orbital eccentricity, orbital inclination, and masses of satellitesimals/satellites. The colorful horizontal dotted lines in panel (d) match the color of one of the analogues, and they show the mass that each analogue should have to exactly match the mass of its corresponding Galilean satellite. Satellitesimals first grow by pebble accretion and start to

migrate inwards. The innermost satellitesimal reaches the inner edge and stop migrating. As additional satellitesimals converge to the inner edge of the disk, orbital eccentricities and inclinations start to increase, which leads to scattering events and collisions. Finally, the satellitesimals converge into a resonant configuration anchored at the disk inner edge. In this case, all adjacent satellite pairs are evolving in a 2:1 MMR. Their final orbits typically exhibit very low orbital inclinations ($\sim$0.01 deg). However, the final orbital eccentricities of our satellites are modestly high ($\sim$0.05-0.2). Table 1 shows that the orbital eccentricities of the Galilean satellites are much lower than those of analogues in Figure 8. More importantly, this is a trend present in all our best analogues. In the next section, we attempt to address this issue by slightly changing our disk model.

2.4.3 Simulations with a more realistic cooling CPD

In all our previous simulations, we have neglected the evolution of the disk temperature. However, as the disk evolves, it looses masses and gets colder and thin (SZULÁGYI et al., 2016). In this section we replace Eq. 6, representing our original CPD temperature profile, by the following new temperature profile (SASAKI; STEWART; IDA, 2010; RONNET; MOUSIS; VERNAZZA, 2017)

$$T_{\rm new} = 225 \left(\frac{r}{10\ {\rm R_J}} \right)^{-3/4} e^{-\frac{t}{4\tau_d}}\ K, \tag{56}$$

where t represents the time, and τ_d=1 Myr.

In our simulations where the disk temperature does not evolve in time, the CPD aspect ratio at 15 R_J (Ganymede's distance to Jupiter) is $\sim 0.06 - 0.07$. In our new disk setup, the disk aspect ratio at 15 R_J also at the end of the gas disk phase is ~ 0.04. We have conducted 40 new simulations, considering that the CPD temperature decays in time as Eq. 56.

Figure 9 shows the dynamical evolution of one of our good analogues (see Section 2.3.1). The gas in the CPD dissipates at 2 Myr and we follow the long-term dynamical evolution of these satellites up to 10 Myr. Figure 9 shows the evolution of semi-major axis, eccentricity, inclination, and masses of the satellitesimals. This simulation starts with 50 satellitesimals. The evolution of satellitesimals in this case is remarkably similar to that of simulations where the disk temperature is kept fixed in time. The combined pebble accretion efficiency of the system is about 13%, which is also similar to our other simulations with the exponential decay of the disk temperature. At the end of the gas disk phase, at 2 Myr, the satellites form a resonant chain anchored at the disk inner edge with all-three satellite pairs evolving in a 2:1 MMR. The final orbital eccentricities of satellites are lower than those observed in Figure 8, as expected. However, the orbital eccentricities of our analogues are still too high compared to those of the Galilean system.

We have found that the orbital eccentricities of satellites in simulations where the disk cools down in time are overall lower than those where the disk temperature is kept constant. This is not a surprising result because the equilibrium eccentricity of capture in resonance scales as $e_{\rm eq} \sim h_g$ (GOLDREICH; SCHLICHTING, 2014; DECK; BATYGIN, 2015; PICHIERRI; MORBIDELLI; CRIDA, 2018). This is in agreement with the results of our simulations (see Figure 3 and Figure 8). However, the observed eccentricities of our final satellites are still too high compared to those of the real satellites today

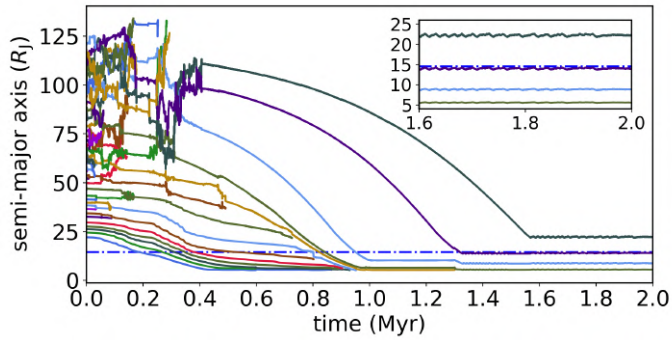

(a)

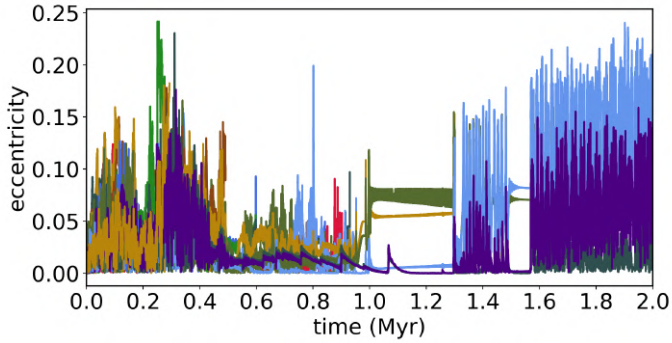

(b)

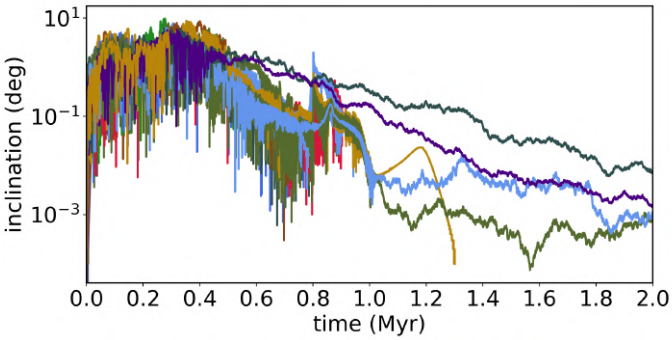

(c)

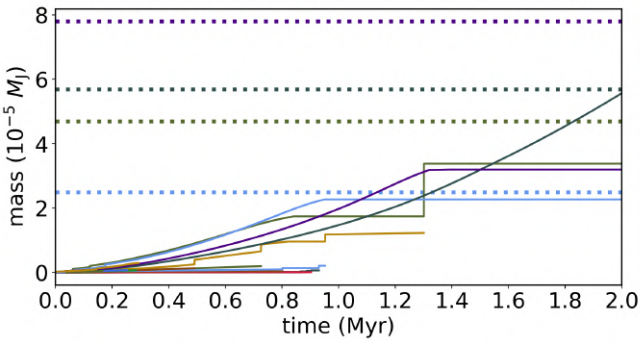

(d)

Figure 8 – Evolution of a) semi-major axes, b) orbital eccentricities, c) orbital inclinations, and d) masses of satellites in a simulation with $\dot{M}_{p0} = 1.5 \times 10^{-9}$ M_J/yr and starting with 50 satellitesimals. The dot-dashed line in panel (a) shows the snowline location, and horizontal lines in panel (d) show the masses of the real Galilean satellites. These horizontal line matches the color of the analogues to indicate the mass they should have to be a perfect match. All satellite pairs evolve in a 2:1 MMR.

(Figure 10). One could conjecture that this is because the disk aspect ratio of our new disk is still not low enough. However, in order to have a disk aspect ratio of $\leq$0.01-0.001 at $<$15 $R_{\rm J}$ – which could more easily lead to final satellites with eccentricities similar to those of Galilean satellites – it would require a CPD with gas temperature of about $\leq$5 K at 15 $R_{\rm J}$, which is unrealistic (SZULÁGYI et al., 2016). So we suggest that in order to damp the orbital eccentricities of our analogues down to the level of the Galilean satellites, a different mechanism should be invoked. We will conduct new simulations and discuss a possible solution to this issue in Section 2.5.

2.4.4 The Water-Ice mass fraction of our satellites

In this section, we analyze the water mass fraction of the satellites in our best Galilean system analogues. Figure 11 shows three of our best analogues. Each line shows one satellite system and the horizontal axis shows its distance from Jupiter. The color-coded dots show individual satellites, where the color represents their water-ice fraction and dot sizes scale linearly with mass. The real Galilean system is shown at the bottom, for reference. The orbital eccentricity of each satellite is represented by the horizontal red bars showing the variation in the planetocentric distance over the semi-major axis ($R_{\rm J}$). In all these systems, adjacent satellite pairs evolve in a 2:1 MMR.

It is clear in Figure 11 that the water-ice fraction of the innermost satellites in our simulations are significantly higher than those of Io and Europa. However, in all our systems the two outermost satellites have water-ice rich compositions similar to those of Ganymede and Callisto. This is a trend observed in all our simulations. In this work, we assume that pebbles inside the snowline are 0.1 cm size silicate particles and those outside are larger, 1 cm size icy-particles. Therefore, pebbles outside the snowline are far more efficiently accreted by the satellitesimals than those inside it. Consequently, satellitesimals beyond the snowline grow faster than those inside it and tend to starve the innermost satellitesimals by reducing the flux of pebbles that they receive. As distant more massive objects migrate inwards they collide with lower-mass satellites growing by the accretion of silicate pebbles. Typically, the innermost satellite in our simulations is a satellitesimal that – on its way to the inner edge of the disk – has collided with several satellitesimals growing inside the snowline. This tends to affect its final water-mass-fraction as observed in Figure 11. However, in none of our simulations, our innermost analogue is as dry as Io or Europa. We have performed a limited number of simulations where we increase the sizes of the pebbles inside the snowline by a factor of 3, to attempt to accelerate the growth of the innermost satellites, but none of these simulations produce good analogues satisfying the i)-iv) conditions of Section 2.3.1.

As discussed before, it is not clear if Io and Europa were born with water-ice poor compositions and then lost (most/all) their water-content after formation (BIERSON; NIMMO, 2020) or formed with their current compositions. So if Io and Europa formed by pebble accretion and with water-poor compositions they must have formed very early, probably much earlier than Ganymede and Callisto, and at a time where satellitesimals existed (or were able to efficiently grow via pebble accretion) only well inside the disk snowline.

On the other hand, if Io and Europa lost their water via hydrodynamic escape (BIERSON; NIMMO, 2020) the masses of the innermost satellites in our simulations should be reduced by a factor of 1.2-1.7

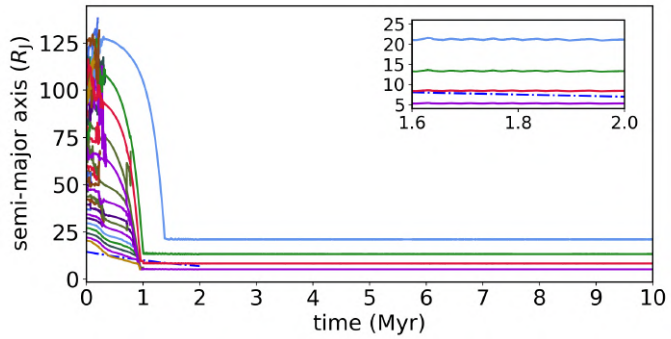

(a)

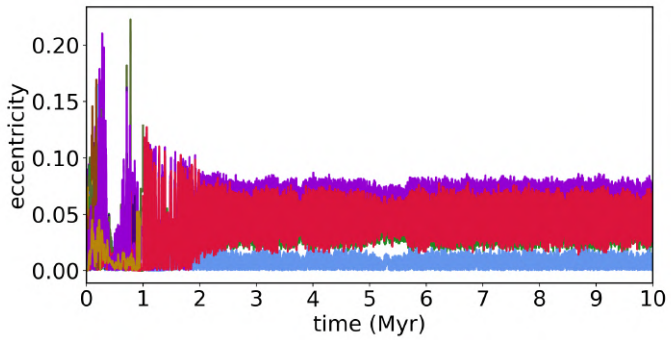

(b)

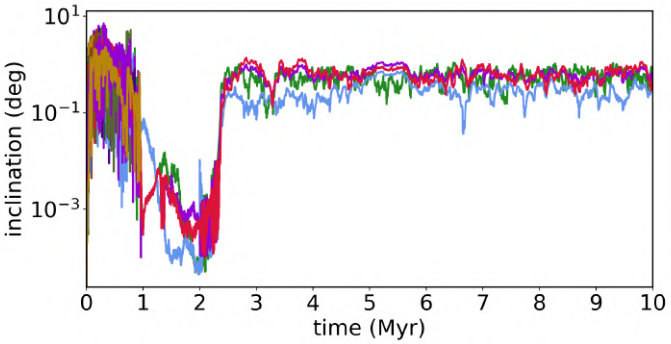

(c)

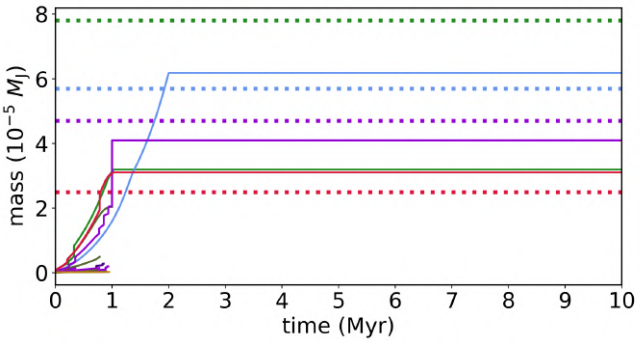

(d)

Figure 9 – Temporal evolution of a) semi-major axis, b) orbital eccentricity, c) inclination, and d) mass of satellitesimals in a simulation starting with 50 satellitesimals. As the disk cools down, the snowline moves inwards as shown by the blue dotted line in panel (a). The horizontal lines in panel (d) show the masses of the real Galilean satellites. These horizontal line matches the color of the analogues to indicate the mass they should have to be a perfect match. All satellite adjacent pairs are involved in a 2:1 MMR, forming a resonant chain. The gas disk dissipates at 2 Myr and the system remains dynamically stable up to 10 Myr.

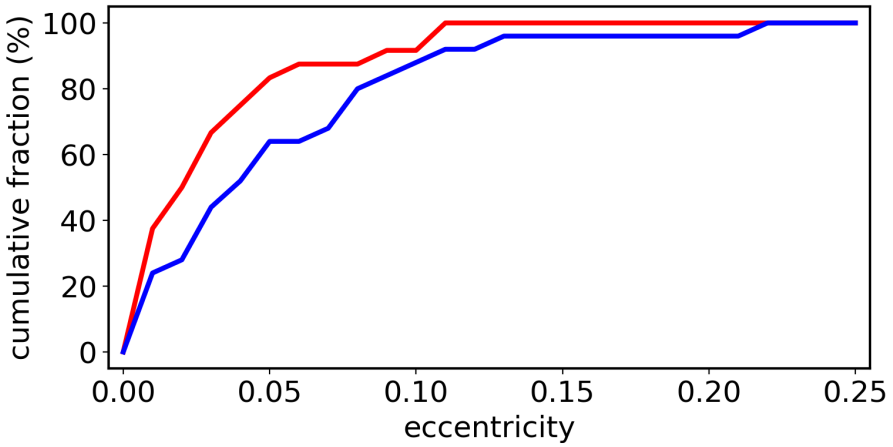

Figure 10 – Eccentricity distribution of our final satellites in simulations with $\dot{M}_{p0} = 1.5 \times 10^{-9}$ M_J/yr and 50 satellitesimals. The blue curve shows the case where the disk temperature is kept constant during the gas disk phase. The red line shows the case where the disk temperature decays exponentially in time (see Eq. 56).

to account for the water-ice component loss. We do not simulate this effect here, but if this is the case our innermost satellite would still have mass satisfying constraint iii) in most of our analogues. This is not true for the second innermost satellites in our analogues (Figure 11). But, as some of our simulations do produce Europa analogues twice as massive as the current Europa (Figure 11) our lack of a good match in our analogues' sample is probably a consequence of the stochasticity of these simulations and small number statistics.

Finally, the top system in Figure 11 shows that the third innermost analogue shares its orbit with a co-orbital satellite. Note that in our system analogues, Ganymede analogues are typically not as massive as the real Ganymede (but masses typically agree within a factor of $\sim$2). A potential future collision of these co-orbital satellites could result in a satellite with final mass even closer to that of Ganymede.

2.5 MIMICKING THE LONG-TERM DYNAMICAL EVOLUTION OF OUR GALILEAN SYSTEM ANALOGUES

In our simulations, when the gas in the CPD dissipates, at 2 Myr, orbital eccentricity damping and gas-driven migration cease. Our simulations are numerically integrated at most for additional 8 Myr in a gas-free environment where satellites and Jupiter gravitationally interact as point-mass particles. However, in reality, the long-term dynamical evolution of the Galilean satellites is also modulated by tidal interactions with Jupiter and other satellites (PEALE; LEE, 2002; FULLER; LUAN; QUATAERT, 2016; LARI; SAILLENFEST; FENUCCI, 2020). Tidal effects tend to increase the angular momentum of the satellites – that migrate outwards because the Galilean satellites are outside the centrifugal radius of Jupiter – and decrease their orbital eccentricities (GREENBERG, 1973). The resonant configuration of the Galilean satellites is expected to enhance the effects of planet-satellite tidal dissipation (LARI; SAILLENFEST; FENUCCI, 2020).

In the theory of dynamical tides, if each satellite feels a different effective Jovian tidal quality

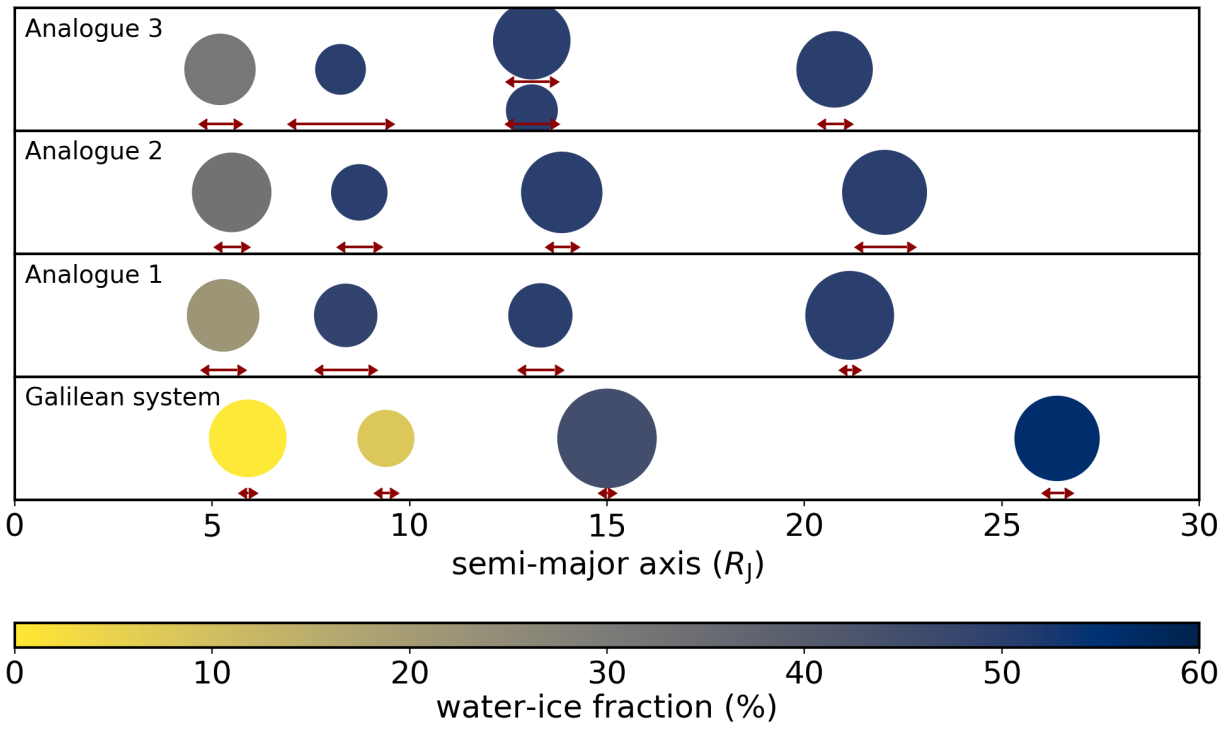

Figure 11 – Galilean system analogues at the end of the gas disk phase (2 Myr). Each line shows a satellite system produced in our simulations. Individual satellites are represented by color-coded dots. Dot's size scales linearly with the satellite's mass and color represents its water-ice fraction. The horizontal axis shows satellites' orbital semi-major axis. Orbital eccentricities are represented by the horizontal red bars showing the variation in heliocentric distance over semi-major axis (R_J). The three systems presented here are also shown in Figure 7.

factor Q due to resonance locking between moons and internal oscillation modes of Jupiter (see Eqs. 57 and 58), tidal migration can be divergent (FULLER; LUAN; QUATAERT, 2016). To estimate the potential effects of the resonance locking on the long-term dynamical evolution of our system analogues, we conduct some additional numerical simulations where we use a simple prescription to crudely mimic the effects of tides on our satellite systems. Our main goal here is to test if the three innermost satellites remain in resonance when subject to tidal dissipation forces and to infer the level of dynamical excitation of our final systems.

The migration timescale of a satellite via dynamical tides is given by (FULLER; LUAN; QUATAERT, 2016; NIMMO et al., 2018; DOWNEY; NIMMO; MATSUYAMA, 2020):

$$\frac{1}{t_a} = \frac{|\dot{a}|}{a} = \frac{2}{3}\frac{1}{t_\alpha}\left(\frac{\Omega}{n} - 1\right), \tag{57}$$

with

$$\frac{k_2}{Q} = \frac{1}{3nq_s}\left(\frac{a}{\mathrm{R_J}}\right)^5 \frac{1}{t_a}, \tag{58}$$

where Ω and t_α are Jupiter's rotation frequency and internal oscillation modes timescale and k_2 is Jupiter's Love number. Astrometric observations (LAINEY et al., 2009) suggest that three innermost Galilean satellites migrate outwards with timescales of 20 Gyr, which translates to t_α equal to 44, 101, and 217 Gyr, from the Io to Ganymede (DOWNEY; NIMMO; MATSUYAMA, 2020). There is no

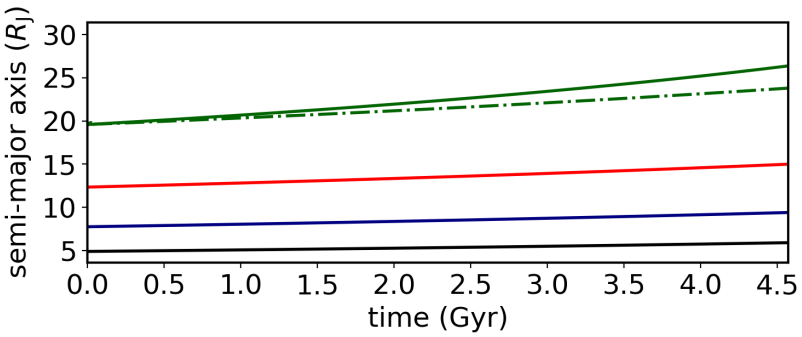

Figure 12 – Temporal evolution of the semimajor axis of the Galilean satellites over the Solar System age as estimated via resonance locking theory (FULLER; LUAN; QUATAERT, 2016). The values of t_α for Io, Europa, Ganymede, and Callisto are 44, 101, 217, and 318 Gyr, respectively. The dot-dashed line corresponds to the evolution of the 2:1 MMR with Ganymede.

estimate of the current tidal migration timescale of Callisto via astrometric observations (DOWNEY; NIMMO; MATSUYAMA, 2020). So we use equation 57 to estimate Callisto's current tidal migration timescale assuming that: i) Callisto is initially locked in a 2:1 MMR with Ganymede; ii) Ganymede is initially at 13 R_J (consistent with our Analogue 1); iii) Callisto migrates to its current position over the age of the Solar System; iv) the three innermost satellites remain locked in the Laplace resonance. We obtained for Callisto a $t_a = 12$ Gyr ($t_\alpha = 318$ Gyr). Figure 12 shows the estimated position of the satellites as a function of time, given by equation 57. The solid lines show the semi-major axis evolution of each satellite. The green dot-dashed line shows the position of the 2:1 MMR with Ganymede (red solid line). As one can see, at the end of the simulation at 4.57 Gyr, Callisto migrates outwards faster than the 2:1 MMR with Ganymede moves outwards, leaving the resonance configuration. The three innermost satellites, on the other hand, remain locked in the Laplace resonance as we will show later. With the migration timescales of all satellites in hand, we can now perform N-body numerical simulations to probe the long-term dynamical evolution of our analogues.

To perform our simulations mimicking the effects of dynamical tides, we use the final orbital configuration of the system at the end of the gas disk phase (Analogue 1) and we consider the subsequent evolution of the system in a gas-free scenario. Due to the high computational cost of these simulations, we do not numerically integrate our system for the entire age of the Solar System, but only for 20 Myr (which requires 3 weeks of CPU-time in a regular desktop). We have assumed for the three innermost satellites $t_a = 20$ Gyr, as suggested by observations (LAINEY et al., 2009), and $t_a = 12$ Gyr for Callisto as discussed before. When performing our N-body simulations we also apply eccentricity damping to the satellites, which is assumed to correlate with the tidal migration timescale via the factor S given as :

$$S = \frac{1/t_e}{1/t_a} = \frac{|\dot{e}/e|}{|\dot{a}/a|} \tag{59}$$

here we test $S = 10^5$ and $S = 10^6$. These values are based on the ratio between semimajor axis and eccentricity variation timescales for Galilean satellites in classical tidal theory (GOLDREICH; SOTER, 1966; ZHANG; ZHANG, 2004; LAINEY et al., 2017).

Figure 13 shows the semi-major axes and orbital eccentricities' evolution of satellites in Analogue 1 during 20 Myr. Our analogue satellites migrate outwards very slowly and the system remains dynami-

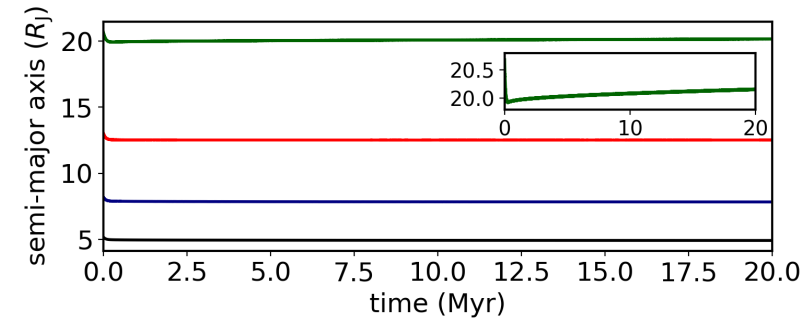

(a)

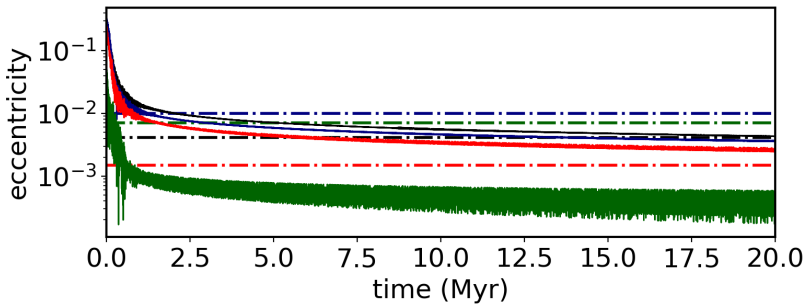

(b)

Figure 13 – a) Semi-major axis and b) eccentricity of the satellites in Analogue 1 for $S = 10^5$. Each solid line shows the evolution of one satellite. Dot-dashed horizontal lines show the orbital eccentricities of the Galilean satellites for reference.

cally stable. The bottom panel of Figure 13 shows that the orbital eccentricities of our analogues are damped to values consistent with those of the real Galilean satellites in a relatively short timescale. The Figure 13 corresponds to $S = 10^5$. Our simulation where $S = 10^6$ resulted in an even lower level of orbital excitation at 20 Myr.

Finally, in Figure 14, we analyze the behavior of the resonant angles characterizing our resonant chain in the same simulation of Figure 13. The panels (a), (b), and (c) show the resonant angles associated with the 2:1 MMR. These plots show that the innermost and second innermost satellite pairs remain locked in a 2:1 MMR when we mimic the tidal dissipation effects on eccentricity. This is indicated by the reduction – relative to the beginning of the simulation – in the libration amplitudes of the resonant angles (ϕ) which librate around zero with small amplitude after the simulation timespan. However, in the case of the outermost satellite pair, the amplitudes of libration of the associated resonance angles gradually increase until they start to circulate, dissolving the resonant configuration, without breaking the resonant configuration of the other pairs. The bottom panel shows that the amplitude of the resonant angle associated with the Laplace resonant slightly increases at ~ 8 Myr – the moment when the outermost satellite leaves the resonance with the second outermost satellite – but the three innermost satellites remain locked in this configuration. Therefore, our results also suggest that the Galilean satellite system is a primordial resonant chain, where Callisto was once in resonance with Ganymede but left this configuration via divergent migration due to dynamical tides (FULLER; LUAN; QUATAERT, 2016; DOWNEY; NIMMO; MATSUYAMA, 2020; LARI; SAILLENFEST; FENUCCI, 2020; HAY; TRINH; MATSUYAMA, 2020; DURANTE et al., 2020; IDINI; STEVENSON, 2021). Of course, a complete validation of this result may require self-consistent

simulations modeling tidal planet-satellite dissipation effects but this is beyond the scope of this paper.

2.6 DISCUSSION

We have assumed a fully formed Jupiter from the beginning of our simulations. We believe this is a fair approximation because Jupiter's CPD and the Galilean satellites mostly likely started to form during the final phase of Jupiter's growth. Szulágyi et al. (2016) showed that the characteristics of a circumplanetary disk are mainly determined by the temperature at the planet's location – which is driven by the gas accretion rate onto the planet – and have a weak dependency on the planet mass. In our model, the total flux of gas from the CSD to the CPD is about ~ 0.1 $\mathrm{M_J}$. So, even if one assumes that all gas entering the CPD is accreted by Jupiter, it should have no less than 90% of its current mass at the beginning of our simulations. Thus, we do not expect this small difference in the planet's mass than we have considered here to change the quality of our results. One potential impact could be seen in the migration timescale of the satellites. However, the migration timescale depends also on CPD's model, as surface density and aspect ratio. As we have performed simulations considering different dissipation modes for the gas disk we consider our main findings to be fairly robust against this issue.

Our treatment of collisions is also simplistic. All of our collisions are modeled as perfect merging events that conserve mass and linear momentum. To evaluate whether or not our assumption is adequate, we have analyzed the expected outcome of collisions in our simulations following Kokubo e Genda (2010) and Genda, Kokubo e Ida (2011). We have found that about 85% of our collisions qualify as perfect merging events, and only 15% of our simulations fall into the hit-and-run regime (see Figure 15). Impact velocities in our simulations are very low because collisions happen during the gas disk phase when satellites have low orbital eccentricities and inclinations due to gas-tidal damping and drag. These results show that our treatment of impacts is fairly appropriate to study the formation of the Galilean satellites.

For simplicity, our simulations started with satellitesimals distributed initially between 20 and 120 $\mathrm{R_J}$. We have argued that these objects were most likely captured from the CSD (ZHU et al., 2012) rather than having been born in-situ. However, we do not model the capture of planetesimals from the CSD in the CPD in this work. The CPD's location where planetesimals from the CSD are preferentially captured depends on planetesimals sizes, orbits, gas surface density, and ablation degree when they enter the CPD (FUJITA et al., 2013; RONNET; JOHANSEN, 2020). Simulations from Ronnet e Johansen (2020) suggest the total time necessary to Jupiter capture the total mass in satellitesimals assumed at the beginning of our simulations would be only $\sim 10^3 - 10^4$ years.

Our best Galilean satellite analogues have typically four satellites as the real Galilean system. However, Jupiter hosts a complex system of moons. Jupiter hosts four satellites with sizes of tens of kilometers inside Io's orbit and a large set of regular satellites of a few kilometers in size outside Callisto's orbit. Here we speculate that these two populations of objects represent fragments, late captured, or leftover satellitesimals that were too small to efficiently grow by pebble accretion. This hypothesis is under investigation.

Our model is honestly simplified and we do not plead to definitively explain the formation of the Galilean satellites. However, it is astonishing that using the same physical processes invo-

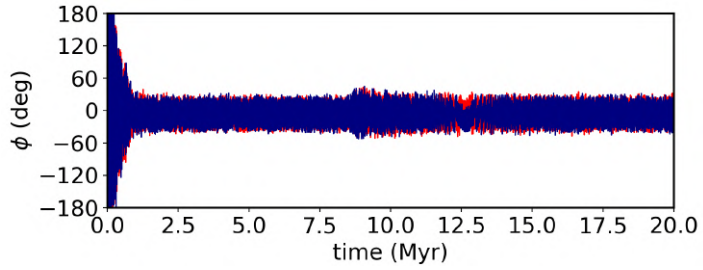

(a) $\phi = 2\lambda_2 - \lambda_1 - \varpi_1 - 180^\circ$ (red line) and $\phi = 2\lambda_2 - \lambda_1 - \varpi_2$ (blue line)

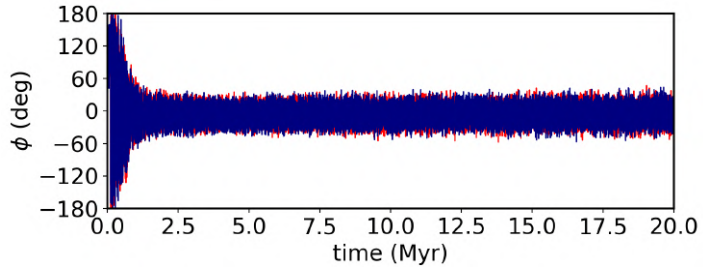

(b) $\phi = 2\lambda_3 - \lambda_2 - \varpi_2 - 180^\circ$ (red line) and $\phi = 2\lambda_3 - \lambda_2 - \varpi_3$ (blue line)

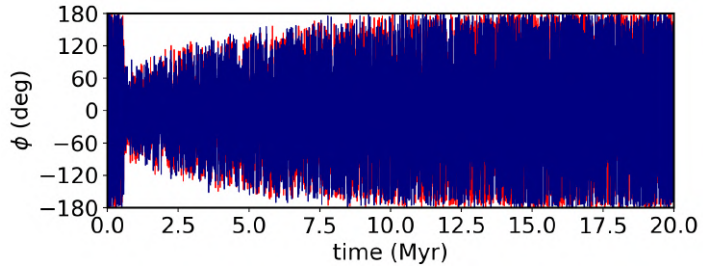

(c) $\phi = 2\lambda_4 - \lambda_3 - \varpi_3 - 180^\circ$ (red line) and $\phi = 2\lambda_4 - \lambda_3 - \varpi_4$ (blue line)

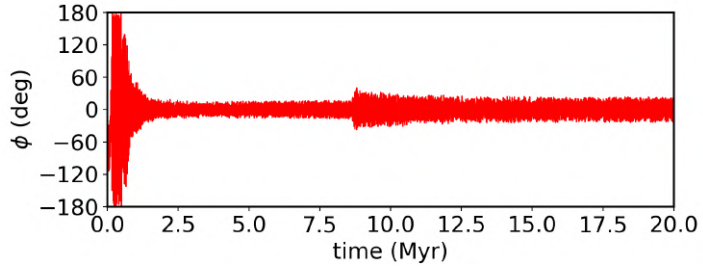

(d) $\phi = 2\lambda_3 - 3\lambda_2 + \lambda_1$

Figure 14 – Panels (a), (b), and (c) show the evolution of resonant angles associated with the 2:1 MMR of different satellite pairs. The bottom panels shows the resonant angle associated with the Laplace resonance characterized by the three innermost satellites. The labels 1, 2, 3, and 4 corresponds to the innermost, second innermost, third innermost, and outermost satellite in our simulation, respectively. All these resonant angles librate at the beginning of the simulation, which corresponds to the the end of the gas disk phase. The orbital eccentricity of the innermost satellite is damped in a timescale $t_e = t_a/S$, where $S = 10^5$ (see Figure 13), to mimic the effects of tidal dissipation.

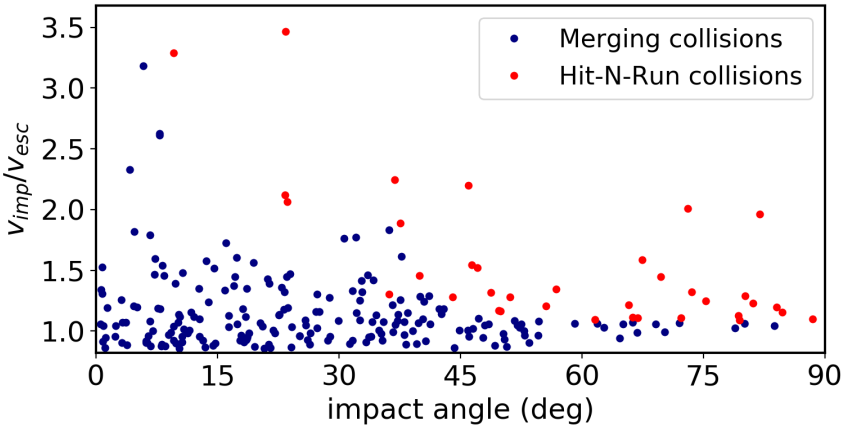

Figure 15 – Normalized impact velocity (v_{imp}/v_{esc}) as a function of the impact angle in simulations that produced Galilean satellite analogues. The color-coding shows the predicted outcome following Kokubo e Genda (2010) and Genda, Kokubo e Ida (2011). Blue (red) dots correspond to the impacts that fall in the merging (hit-and-run) regime. 85% of the impacts in these selected simulation qualify as perfect merging events.

ked in models to explain the formation of planets in the Solar System and around other stars (**??**, e.g.)]Levison2015b,Izidoro2019, our simulations can still form satellites systems that resemble fairly well the Galilean moons. Our results also show the importance of future studies to provide firmer constraints on the original composition of Io and Europa. Were they born with water-rich compositions or not?

2.7 CONCLUSIONS

We have performed a suite of N-body numerical simulations to study the formation of the Galilean satellites in a gas-starved disk scenario (CANUP; WARD, 2002; CANUP; WARD, 2006; CANUP; WARD, 2009; SASAKI; STEWART; IDA, 2010) invoking pebble accretion and migration. Our simulations start considering an initial population of ∼200 km-size satellitesimals in the circumplanetary disk that are envisioned to be planetesimals captured from the sun's natal disk. We have performed simulations testing different initial number of satellitesimals in the CPD and pebble fluxes. Our pebbles fluxes are consistent with those estimated via the ablation of planetesimals in the circumplanetary disk (RONNET; JOHANSEN, 2020). Our best Galilean system analogues were produced in simulations where the time-integrated pebble flux is about 10^{-3} M_J. In these simulations, satellitesimals grow via pebble accretion and migrate to the disk inner edge where they stop migrating at the inner edge trap. When they approach this location, dynamical instabilities and orbital crossing promote further growth via impacts. Our simulations typically produced between 3 and 5 final satellites anchored at the disk inner edge, forming a resonant chain. Their masses match relatively well those of the Galilean satellites. All our system analogues show 3 pairs of satellites locked in a 2:1 mean motion resonance. Thus, we propose that Callisto – the outermost Galilean satellite – was originally locked in resonance with Ganymede but left this primordial configuration via divergent migration due to tidal dissipative effects (FULLER; LUAN; QUATAERT, 2016; DOWNEY; NIMMO; MATSUYAMA, 2020). We also proposed that the orbital eccentricities of the Galilean satellites were much higher in the past and were

damped to their current values via tidal dissipation without destroying the resonant configuration of the innermost satellites (FULLER; LUAN; QUATAERT, 2016; DOWNEY; NIMMO; MATSUYAMA, 2020; LARI; SAILLENFEST; FENUCCI, 2020; HAY; TRINH; MATSUYAMA, 2020; DURANTE et al., 2020; IDINI; STEVENSON, 2021). Finally, we proposed that the Galilean system represents a primordial resonant chain that did not become unstable after the circumplanetary gas disk dispersal. Thus the formation path of the Galilean system is probably similar to that of systems of close-in super-Earths around stars, as the Kepler-223 (MILLS et al., 2016), TRAPPIST-1 (GILLON et al., 2017), and TOI-178 (LELEU et al., 2021) systems (IZIDORO et al., 2017; IZIDORO et al., 2021).

Our simulations do not reproduce the current low water-ice fractions of Io and Europa, and require efficient water loss via hydrodynamic escape (BIERSON; NIMMO, 2020) to occur to match their current bulk compositions. If efficient water loss via hydrodynamic took place it is expected that Europa should have developed a higher deuterium-to-hydrogen ratio compared with Ganymede and Callisto (BIERSON; NIMMO, 2020). This prediction may be tested in the future via in-situ measurements by the Europa Clipper spacecraft or infrared spectroscopic observations (BIERSON; NIMMO, 2020). In all our simulations, the two outermost satellites have water-ice rich compositions similar to Ganymede and Callisto. Our results suggest that if Io and Europa were born water-ice depleted, they should have formed much earlier than Ganymede and Callisto and well inside the CPD's snowline. Additional constraints on Io and Europa are now crucial to constrain Galilean satellites' formation models.

3 EXPLORING THE RECYCLING MODEL OF PHOBOS FORMATION

Phobos is the target of the return sample mission Martian Moons eXploration by JAXA, which will analyze in great detail the physical and compositional properties of the satellite from orbit, from the surface and in terrestrial laboratories, giving clues about its formation. Some models propose that Phobos and Deimos were formed after a giant impact giving rise to an extended debris disk (CITRON; GENDA; IDA, 2015). One of these models is the recycling model, which proposes that Phobos formed from a cascade of disruptions and re-accretions of several parent bodies in this disk (HESSELBROCK; MINTON, 2017). The central point of the recycling model is the assumption that the satellites accreted in the disk are gravitational aggregates, and, therefore, can be destroyed by tides, giving rise to material cycles. Given the context of the Martian Moons eXploration mission, we explore in detail the recycling model in order to obtain constrains about the properties of Phobos.

The content of this chapter is in revision as: G. Madeira, S. Charnoz, Y. Zhang, R. Hyodo, P. Michel, H. Genda, S.M. Giuliatti Winter. Exploring the recycling model of Phobos formation: rubble-pile satellites. The Astronomical Journal.

3.1 INTRODUCTION

Discovered in 1878 (HALL, 1878), Phobos and Deimos are the two natural satellites of Mars and target bodies of the return sample mission Martian Moons eXploration (MMX), from the Japan Aerospace eXploration Agency (JAXA) (KURAMOTO et al., 2022). The satellites are relatively small with low bulk density (probably high porosity), irregular shape, and cratered surface. Phobos' radius is $\sim$11 km, while Deimos has a radius of $\sim$6 km (THOMAS, 1993; WILLNER; SHI; OBERST, 2014). The latter is located at about 6.92 Mars' radius, $\mathrm{R_M} = 3389.5$ km (PEALE, 1999; ABALAKIN et al., 2002), presenting a weak tidal interaction with the planet. Because of this, the satellite moves very slowly away from Mars. Phobos, in turn, is close to the planet ($\sim 2.77\ \mathrm{R_M}$) (PEALE, 1999), felling a tidal torque responsible for its orbital decay. The difference in direction of migration of the satellites is because Phobos resides inside Mars' synchronous orbit (at about $6.03\ \mathrm{R_M}$) while Deimos resides beyond it. Tidal evolution studies show that Phobos would fall to Mars in less than 40 Myr (SHARPLESS, 1945; SAMUEL et al., 2019; BAGHERI et al., 2021). The most likely scenario, however, is the destruction of Phobos by tides before reaching Mars surface, between $1.0\ \mathrm{R_M}$ and $2.0\ \mathrm{R_M}$. A significant fraction of the satellite is believed to be heavily damaged (BLACK; MITTAL, 2015) and, as a consequence, Phobos must either be fully destroyed in a cloud of particles or fragmented into several large fragment accompanied by a cluster of debris (BLACK; MITTAL, 2015). This leaves the question: Are we in a privileged time, in which we can observe Phobos just before its end?

Early models (PANG et al., 1978; BURNS, 1992; PAJOLA et al., 2012; PAJOLA et al., 2013) proposed that Phobos and Deimos were asteroids captured by Mars. This hypothesis was motivated by data obtained by spacecraft, such as Mariner 9, Viking 1 and 2, and Phobos 2, which show that martian moons has low albedo and spectra resembling carbonaceous asteroids (FRAEMAN et al., 2012; WITASSE et al., 2014). However, the capture model is not consistent with dynamical constraints,

as tidal dissipation is not strong enough to change Deimos' orbit from highly inclined and eccentric – as expected for a captured object – to near-equatorial and near-circular in a shorter time than the Solar System age (SZETO, 1983). Some modified mechanisms have been proposed, such as a three-body capture (HANSEN, 2018). However, such a capture remains unlikely; in particular, it is unclear whether Phobos and Deimos would survive a capture by Mars if they have a rubble pile structure (ZHANG; MICHEL, 2020).

In opposition to the capture mechanism, it has been proposed that Phobos and Deimos formed in a debris disk around Mars, which would naturally explain their near-circular and near-equatorial orbits (CRADDOCK, 1994). Singer (2003) proposed that the debris disk around Mars would originate from an object captured and destroyed at the Mars' Roche limit due to tidal effects. The recent work of Bagheri et al. (2021) propose that Phobos and Deimos originated from the disruption of a progenitor moon, likely formed *in situ* around Mars. By performing backward tide simulations, they obtain that the orbits of Phobos and Deimos convert to a common position above the synchronous orbit in $\sim$1-3 Gyr, the possible time of destruction of the progenitor moon. After the destruction, Phobos and Deimos would be launched in highly eccentric orbits, feeling a strong satellite tidal dissipation, responsible for the damping of eccentricity and generating an inward migration. When the orbits are sufficiently circularized, the Martian tidal dissipation exceeds that of the satellite, and Deimos starts to migrate outward, while Phobos, now below the synchronous orbit, migrates inward toward its actual position. However, the post-evolution of Phobos and Deimos after the split was studied in detail by Hyodo et al. (2022), who obtained that the satellites collide with each other in less than 10^4 yr in most of the cases analysed, forming a debris ring around the synchronous radius. Therefore, Phobos and Deimos are unlikely to be the direct result of the splitting of an ancestor moon (HYODO et al., 2022).

As a matter of fact, the large basins seen on the surface of Mars seem to indicate past highly energetic impacts between the planet and ongoing objects. In particular, the impact responsible for the Borealis basin, which covers almost 40% of the Mars' surface (MARINOVA; AHARONSON; ASPHAUG, 2008), would provide enough energy for rock vaporization, resulting in the formation of a debris disk (CRADDOCK, 2011). Furthermore, Mars' current spin rate can only be explained by an impact with an external object (DONES; TREMAINE, 1993; CRADDOCK, 2011), placing a giant impact as the only mechanism capable of offering the appropriate environment for the formation of Phobos and Deimos.

Several works (CITRON; GENDA; IDA, 2015; ROSENBLATT et al., 2016; HYODO et al., 2017; CANUP; SALMON, 2018) have used impacts models relying on the Smoothed Particle Hydrodynamics (SPH) techniques to recreate the impact responsible for the Borealis basin and Mars' current spin rate. The ejecta produced by the impact – composed of material from Mars and the impactor – would reside right after the impact in highly elliptical and inclined orbits around the planet. Ejecta in the form of molten droplets due to their high temperature (HYODO et al., 2017; HYODO et al., 2018), then begin to solidify and collide with each other, inducing energy loss while angular momentum is conserved. As a consequence, the eccentricities and inclinations are quickly dampened, resulting in the formation of a flat and extended disk of debris with mass $\sim 10^{20}$ kg. Whereas most of the disk's mass is located inside the Roche limit of Mars, some debris from the impact extends up to the synchronous orbit (CITRON;

GENDA; IDA, 2015; ROSENBLATT et al., 2016; HYODO et al., 2017).

The debris disk is expected to viscously spread due to inter-particle collisions, and a mechanism similar to that proposed for the formation of Saturn's icy moons (CHARNOZ; SALMON; CRIDA, 2010; CHARNOZ et al., 2011) can be assumed to take place at the Martian Roche limit, located at about $3.2\ \mathrm{R_M}$. The ring located inside the Roche limit spreads viscously, releasing material outside the Roche limit. This material coagulates due to gravitational instabilities, generating the accretion of small-sized moonlets. In the case of Saturn – Roche limit outside the synchronous orbit – moonlets grow by mutual collisions and migrate outward due to disk-satellite torques and tidal effects, giving rise to the icy moons (CHARNOZ; SALMON; CRIDA, 2010; CHARNOZ et al., 2011). However, in the case of Mars, the Roche limit lies within the synchronous orbit, and the moonlets feel opposing forces: the disk-satellite torques push them outside the planet and tidal effects cause an inward migration of moonlets located within the synchronous orbit. As a consequence, there is a maximum distance at which a moon can migrate beyond the Roche limit, well inside the current orbit of Deimos. A satellite can be driven to Deimos' position only by resonant trains, in which inner moons slowly migrating outwards capture the outermost satellite into mean motion resonances (MMRs hereafter), pushing it towards outside the synchronous radius (SALMON; CANUP, 2017). Forming Deimos in such a scenario shows to be a trammel (ROSENBLATT; CHARNOZ, 2012), which spurred the development of more sophisticated mechanisms for the formation of Phobos and Deimos.

The stirred debris disk model proposed by Rosenblatt et al. (2016) assumes an initial outer disk – portion of the disk beyond the Roche limit – with a mass greater than that obtained by Citron, Genda e Ida (2015). The outer disk is assumed to be composed of a population of embryos located from $4.2\ \mathrm{R_M}$ to $7\ \mathrm{R_M}$. Due to viscous spreading and gravitational instabilities, moonlets are formed just outside the Roche limit. Eventually, all the moonlets result in a single massive moon that migrates outward due to disk-satellite torques. Embryos are trapped in the 2:1 and 3:2 MMR with the massive moon and migrate outward with it. Material is collected and accreted inside the massive moon's MMR. At some point, the system is composed only by a disk, massive moon and two moons formed near the 2:1 and 3:2 MMR with the massive moon. When the disk is sufficiently depleted, the tidal torque exceeds the disk-satellite torques and the massive moon migrates inward, pushing the disk towards and eventually falling onto the planet, leaving only the two satellites in the system. In the original ROSENBLATT et al. paper, the moons are assumed to be very cohesive, so they do not disrupt when they cross Mars' Roche Limit, and fall down to the planet's surface. This hypothesis is opposite to the one of the Hesselbrock e Minton (2017) that assume low-cohesion moons, and thus result in a "recycling" process (see below). In $\sim 1.4\%$ of their simulations, Rosenblatt et al. (2016) find innermost and outermost satellites with masses lying within 5% and 30% the current ones, respectively. The obtained location are equal to those expected for the satellites in the past.

The Roche limit is a theoretical distance at which a fluid body no longer has a tidal equilibrium shape, which means that the fluid object will be destroyed by tidal effects upon reaching this distance. For this reason, the Roche limit is also called the "Fluid Roche limit" (FRL hereafter), as it will be called from now on in this article. Solid bodies are stronger than fluids and can be destroyed at smaller distances (HOLSAPPLE; MICHEL, 2006; HOLSAPPLE; MICHEL, 2008), at the "Rigid Roche limit"

(RRL hereafter). Using this distinction between FRL and RRL, Hesselbrock e Minton (2017) propose another model for Phobos formation, the "recycling model", schematized in Figure 16. According to them, Deimos is a direct fragment from the giant impact, while Phobos formed from the debris disk initially confined within the FRL.

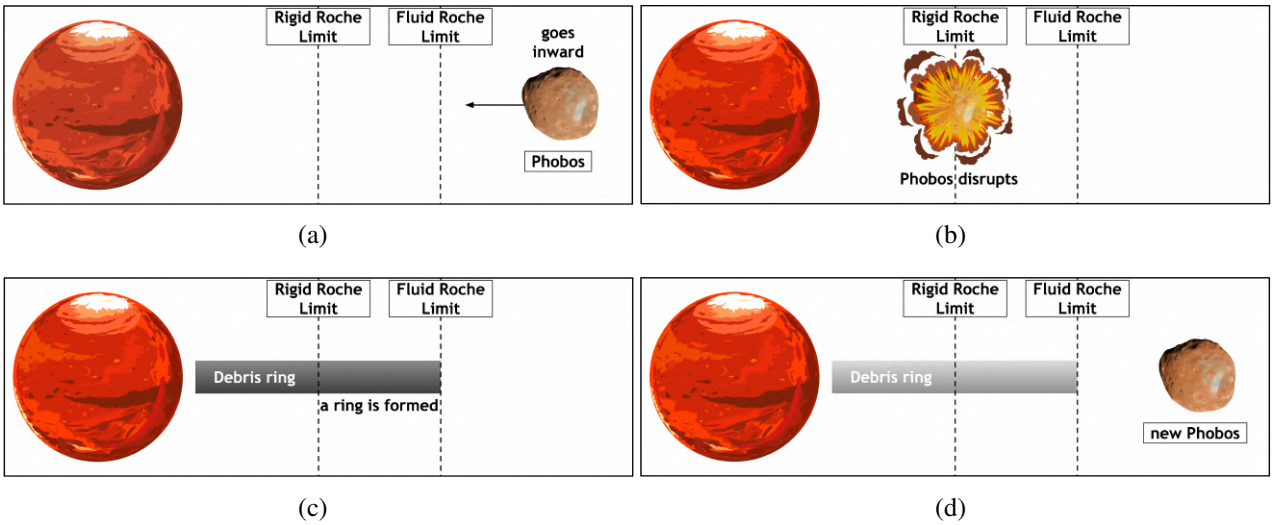

Figure 16 – Recycling model scheme. a) A Phobos is formed from the disk generated in the giant impact. b) Phobos is destroyed at the rigid Roche limit, and c) a debris ring is formed. d) A new Phobos is formed, restarting the process.

Through the aforementioned mechanism, moonlets form outside the FRL and collide with each other, giving rise to a moon (Figure 16a). This moon eventually begins to migrate inward, reaching the RRL. Assuming that the moon has low-cohesion, the moon breaks (Figure 16b) and forms a new ring (Figure 16c) that spreads, restarting the full process (Figure 16d). For each destruction/accretion cycle, the total mass of the system is divided by ≈ 5 in general. This factor is a direct consequence of how the viscous effects are handled, being susceptible to the system parameters. The mass of the largest moon in the oldest cycle depends on the initial width of the ring (HYODO; OHTSUKI; TAKEDA, 2015). The system evolution will also depend on the RRL location. It is expected that the closer to the planet the satellite is destroyed, more material will be deposited on Mars. HESSELBROCK; MINTON obtain in their representative simulation (RRL=$1.6\ \mathrm{R_M}$) that six of these recycling cycles are needed to form the current Phobos, meaning that there were five Phobos ancestors in the past. Now, if the RRL position is assumed to be $1.2\ \mathrm{R_M}$, e.g., they find that for each cycle, the mass of the system is divided by ≈ 17, taking 3 cycles to form Phobos.

An important aspect of the recycling model is the fact that Hesselbrock e Minton (2017) obtain a ring coexisting with Phobos with an optical depth $\tau \sim 0.03$. Observations of Mars' environment show that no ring is detectable around Mars with optical depth $\tau > 3 \times 10^{-5}$ (DUXBURY; OCAMPO, 1988) and no particle is detected around Mars down to a detection limit of 75 m (SHOWALTER; HAMILTON; NICHOLSON, 2006). Therefore, the ring obtained by Hesselbrock e Minton (2017) would be detectable, which can be assumed to be a strong enough caveat to rule out the model. In the original Hesselbrock e Minton (2017) paper, only one disk case was investigated, and due to computer limitation the full cycle could not be computed over 4.5 Gyr evolution. The model from Hesselbrock e

Minton (2017) is mostly the same as presented in Salmon et al. (2010) and Charnoz, Salmon e Crida (2010), but using a different version of the code. In this work, we revisit the recycling model, searching for a good set of parameters capable of forming Phobos and a non-visible ring. We emphasize that we use the original `HYDRORINGS` code (SALMON et al., 2010; CHARNOZ; SALMON; CRIDA, 2010), which is able to compute the ring's evolution over the full history of the Solar System.

In this work, we focus on the recycling model, analyzing the evolution of the satellites and studying the properties of the residual ring obtained by the process. The existence of different cycles relies on the important assumption that satellites are destroyed by tidal forces before falling onto the planet. This assumption distinguishes the recycling model from the stirred debris disk model. If we assume that the massive moon in the stirred debris disk is also destroyed by tidal forces, the formation of a ring of debris occurs and, consequently, material recycles occur as well.

What defines whether an object will fall entirely onto Mars or not is its constitutive characteristics. Weakly cohesive objects are expected to be disrupted, while strongly cohesive objects can survive (BLACK; MITTAL, 2015). MMX plans to collect and return samples from Phobos surface, which will allow constraining the satellite's strength (HYODO et al., 2019; HYODO; USUI, 2021) and obtaining evidence supporting one of the models for Phobos' formation. Although this is never mentioned by Rosenblatt et al. (2016) and Hesselbrock e Minton (2017), they are assuming different strengths for objects accreted in the debris disk. Here, we explore the case of rubble-pile satellites.

3.2 DISRUPTION LOCATION OF A RUBBLE-PILE SATELLITE

In this section we compute the distance from Mars, at which a rubble-pile satellite would be disrupted depending on its material properties and shape.

Close to the Roche limit, the planet's tidal forces tend to stretch satellites, making their equilibrium shape non-spherical. Effects such as rotation and tidal forces induce the redistribution of the satellite material. In the hypothetical case of a fluid satellite, planet's tidal forces deform the satellite until it reaches an equilibrium shape: a Roche or Jean ellipsoid (CHANDRASEKHAR, 1969). Satellites very close to the planet are not able to reach an equilibrium shape and are torn apart by tidal torques. The distance, from the planet's center, at which a fluid satellite no longer has an equilibrium shape is the "Fluid Roche Limit"(FRL).

The fluid model is mostly relevant for large objects, typically > 100 km, whose cohesion is negligible compared to their self-gravity. Conversely, small objects may be partially or mostly sustained by their internal strength. In solid bodies, strength is defined as the object's ability to withstand stresses. There are three strengths that define the total strength of an object: the tensile strength, cohesion (the shear strength at zero pressure), and compressive strength, see e.g. Dobrovolskis (1990), Sridhar e Tremaine (1992), Holsapple e Michel (2006). In this way, solid satellites can withstand tidal forces at inner distances to the FRL.

Aiming to analyze whether a satellite can survive a certain distance without being torn apart, we start by evaluating the forces on the object: centrifugal force due to spin, self-gravity, and tidal force from the planet. We assume that the satellite has an ellipsoidal shape (with semi-axes $a_1 \geq a_2 \geq a_3$), mass-to-planet ratio p, and uniform bulk density ρ. The satellite is in a circular and equatorial orbit

in the x_1x_2-plane, where d is the planet-satellite distance. It is also spinning around the x_3 axis with synchronous rotation.

The force on the body, per unit of mass, is (HOLSAPPLE; MICHEL, 2006):

$$b_i = \left[-2\pi\rho G A_i + \frac{GM}{d^3} S_i\right] x_i \tag{1}$$

where G is the gravitational constant, M is the planet mass, and the coefficients S_i are: $S_1 = 3 + p$, $S_2 = p$, and $S_3 = -1$. The self-gravity coefficients A_i are given by (HOLSAPPLE; MICHEL, 2006):

$$A_i = a_1 a_2 a_3 \int_0^\infty \frac{du}{(a_i^2 + u)(a_1^2 + u)^{1/2}(a_2^2 + u)^{1/2}(a_3^2 + u)^{1/2}} \tag{2}$$

The equilibrium equation, relating the stress tensor components σ_{ij} and the force on the body (HOLSAPPLE, 2001) is :

$$\frac{\partial}{\partial x_j}\sigma_{ij} + \rho b_i = 0 \tag{3}$$

Using Equation 3 and averaging over the body volume, we find that (HOLSAPPLE; MICHEL, 2008)

$$\overline{\sigma}_{ii} = \left[-2\pi\rho G A_i + \frac{GM}{d^3} S_i\right] \frac{\rho a_i^2}{5} \tag{4}$$

while the non-diagonal components are equal to zero.

Once we know the average stress on the satellite ($\overline{\sigma}_{ij}$), we can compare it to the satellite strength. For this, we assume the Drucker-Prager criterion, a failure criterion for geological materials given by (CHEN; HAN, 2007)

$$\sqrt{(\overline{\sigma}_{xx} - \overline{\sigma}_{yy})^2 + (\overline{\sigma}_{yy} - \overline{\sigma}_{zz})^2 + (\overline{\sigma}_{zz} - \overline{\sigma}_{xx})^2} \leq \sqrt{6}[k_{dp} - s_{dp}(\overline{\sigma}_{xx} + \overline{\sigma}_{yy} + \overline{\sigma}_{zz})] \tag{5}$$

where s_{dp} and k_{dp} are material constants related to cohesion Y and friction angle ϕ. These two parameters are related to inter-particle forces within the body, with cohesion giving the body's response to shear stress at zero normal stress, being related to inter-molecular forces. The friction angle is responsible for measuring the response of the body under shear stress and is related to the geometrical interlocking of the granular particles (SÁNCHEZ, 2015). The constants s_{dp} and k_{dp} are given by (CHEN; HAN, 2007)

$$s_{dp} = \frac{2\sin\phi}{\sqrt{3}(3 - \sin\phi)} \tag{6}$$

and

$$k_{dp} = \frac{6Y\cos\phi}{\sqrt{3}(3 - \sin\phi)} \tag{7}$$

In our numerical simulations, we assume the typical cohesion of a rubble-pile object, $Y = 0.025\rho^2/(a_1a_2a_3)^{1/6}$ (HOLSAPPLE; MICHEL, 2008; BLACK; MITTAL, 2015), and set three values of friction angle: $\phi = 25°$, approximately the friction angle of a close-packed rubble-pile composed by frictionless particles (ALBERT et al., 1997), $\phi = 40°$, a typical value for rocks (USOL'TSEVA et al., 2019), and $\phi = 80°$, corresponding to a hypothetical case of an extremely packed core since $\phi \gtrsim 60°$

are not generally found in nature (YANG; LUO, 2018; USOL'TSEVA et al., 2019).

We look for the disruption location of a rubble-pile object around Mars by using the following methodology: For a given mass, we find all possible combinations of semi-axes for the shape of the object. For this, we assume a_2 and a_3 in the ranges $0 < a_2/a_1 < 1$ ($\Delta(a_2/a_1) = 0.01$) and $0 < a_3/a_1 \leq a_2/a_1$ ($\Delta(a_3/a_1) = 0.01$), with a_1 calculated from the mass. Then we vary the semi-major axis of the object from 2.2 R_M to 1.0 R_M, with a step of 0.05 R_M (distances are counted from external to internal ones), and apply the Drucker-Prager criterion for all configurations. With this, we obtain which ellipsoidal shapes are stable at that location. Then, we assume as "Rigid Roche Limit" the distance below which none of the configurations is no longer stable. We do this calculation for 400 different values of mass, equally spaced in the range $10^{12} - 10^{18}$ kg, assuming the bulk density of Phobos $\rho = 1.845$ g/cm^3 (WILLNER; SHI; OBERST, 2014; DMITROVSKII et al., 2022). Figure 17 shows the disruption distance as a function of satellite's mass/equivalent spherical radius for $\phi = 25°$ (red line), 40° (black line), and 80° (blue line). The vertical line is set at the mass/radius of Phobos.

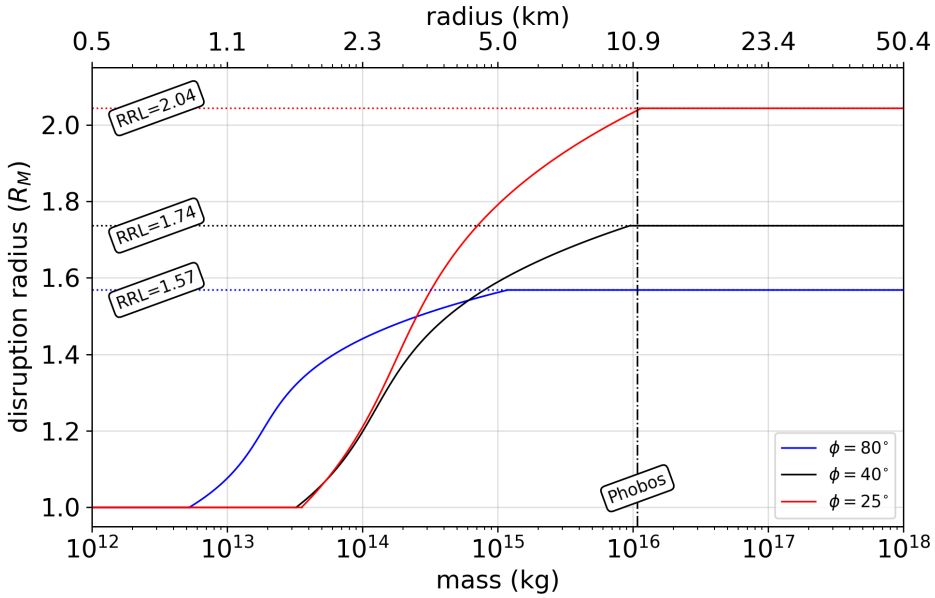

Figure 17 – Disruption location, in Mars radius (R_M), of a rubble-pile satellite as a function of its mass/equivalent spherical radius. The red, black, and blue lines correspond to the cases with friction angle $\phi = 25°$, 40°, and 80°, respectively. The dot-dashed vertical line shows the mass and radius of Phobos.

For each value of the friction angle, there is a critical body mass beyond which the RRL is constant (and thus mass independent, but depending on ϕ), and below which the RRL is an increasing function of the body mass. All solid bodies contain a distribution of incipient flaws and the size of the largest flaw increases with the object's size. Since the weakness of a body is defined by the size of the flaws (HOLSAPPLE; MICHEL, 2008), we have that large bodies are weaker than small ones. Small bodies behave in the "strength regime" and increasing in size, the strength decreases, and there is a threshold above which it doesn't matter and gravity takes the lead. This corresponds to the "gravity regime" in which the greater the friction angle, the closer to the planet the satellite disrupts, as can be seen in Figure 17.

Therefore, RRL=2.04 R_M, 1.74 R_M, and 1.57 R_M for $\phi = 25°$, 40°, and 80°, respectively. Hesselbrock e Minton (2017) set RRL=1.6 R_M, approaching our hypothetical case with $\phi = 80°$. In the

numerical simulations of Section 3.4, we assume that a satellite breaks up at the location given by Figure 17, which means that satellites in the strength regime will disrupt in different locations than those in the gravity regime.

3.3 EXPLORATION OF THE TIDAL DECAY AND EROSION OF ONE SINGLE MOON

In the previous section we computed the distance at which a rubble pile would be disrupted by tidal forces. We now focus on the coupling of the inward tidal migration of the moon with the change of its shape, as it falls down to the planet. Orbital tidal decay is dynamically a very slow process. For example, it will take about 15 Myr for Phobos to move from $2.5\ \mathrm{R_M}$ to $2\ \mathrm{R_M}$, that is about 19 billions of orbits (BLACK; MITTAL, 2015). As the object deforms, it may have time to re-organize its shape to the evolving tidal stress environment. So, we may expect that tidal forces result in a slow erosion of the object (a diminution of its average radius), as its upper layers are slowly tidally eroded. We call this process "tidal downsizing", being similar to the tidal stripping process obtained by Canup (2010) for differentiated satellites. According to CANUP's work, tides are responsible for stripping material from the outer layers of satellites within the Roche limit, since these layers have a lower density than the rest of the body. Previous studies (BLACK; MITTAL, 2015) have shown that Phobos would reach the planet's surface in about 30 Myr. However the mass and radius of Phobos were considered as a constant in this study. Here, we re-assess Phobos' evolution, taking into consideration the progressive tidal downsizing of the object below the Roche Limit.

Figure 18 shows the tidal evolution of Phobos. We assume $k_2/Q = 10^{-6}$ for Phobos (BAGHERI et al., 2021), where k_2 is the Love number and Q is the tidal quality factor. All other quantities are the same as assumed by Bagheri et al. (2021). The solid black line gives the evolution of Phobos until reaching the RRL ($\phi = 40°$, dotted line), where it would be completely destroyed according to theory (black point, "tidal destruction"). The RRL is reached in about 31 Myr. Assuming that the satellite is not destroyed, we show in dashed black line the case where Phobos maintains its original mass ("very cohesive Phobos") (BLACK; MITTAL, 2015). In this case, Phobos falls onto the surface in about 32 Myr. Finally, the red line corresponds to the hypothetical case in which Phobos does not disrupt upon reaching the RRL, but only loses its external layers in order to reach a tidal equilibrium shape ("tidal downsizing"). We follow Figure 17 to model the tidal downsizing effect. As Phobos migrates inward, we verify if its mass would allow it to be stable in that location. If not, we assume that Phobos loses the amount of mass necessary for the satellite to be marginally stable. E.g., Phobos with its current mass ($\sim 10^{16}$ kg) would not be stable at $\sim 2\ \mathrm{R_M}$ (case with $\phi = 25°$). Therefore, in our tidal downsizing simulations, we would assume that Phobos eroded to the maximum stable mass at that location, $\sim 6 \times 10^{15}$ kg. As can be seen, below the RRL, Phobos begins to shrink towards the planet, reaching the surface of Mars at about 60 Myr. When it reaches the planet's surface, its remaining radius is ~ 2 km only.

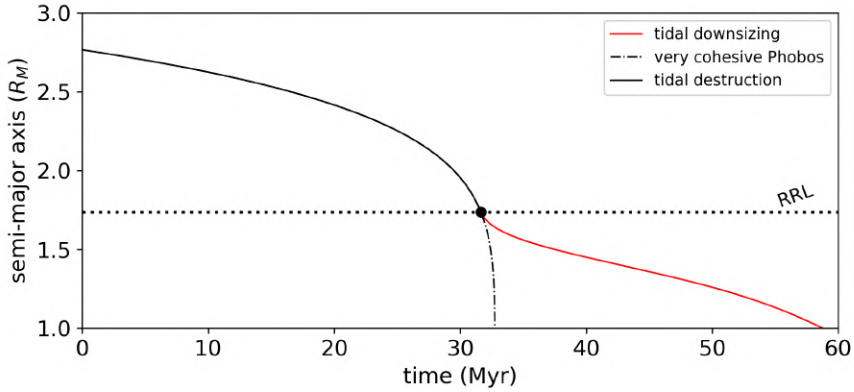

(a)

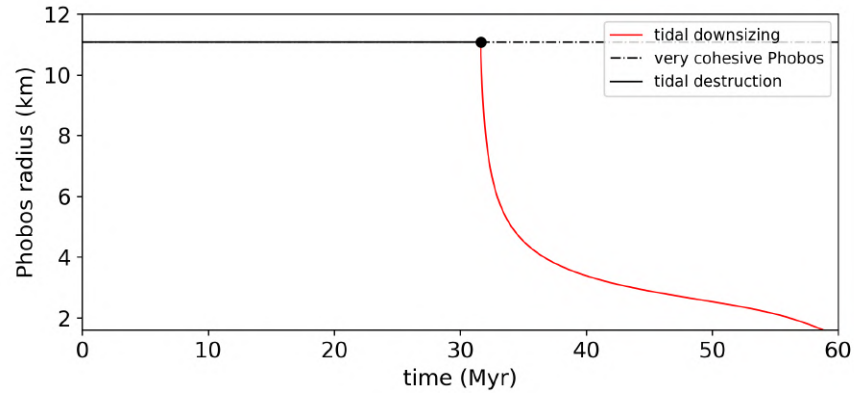

(b)

Figure 18 – Temporal evolution of (a) semimajor axis and (b) physical radius of Phobos ($k_2/Q = 10^{-6}$) under tidal effects. The evolution of the satellite before reaching the RRL (dotted horizontal line) is given by the solid black line, with the black dot showing the instant Phobos would be destroyed. The dash-dotted line shows what the evolution of the satellite would have been if it had not been torn apart by tidal forces. A hypothetical case in which Phobos shrinks due to tidal effects is shown by the solid red line.

3.4 EXPLORING THE RECYCLING MODEL

We now turn to Phobos formation, where we analyse both disk evolution and tidal evolution of the satellites, following an approach similar to Hesselbrock e Minton (2017). However, whereas only a few tens of Myr evolution could be numerically investigated in Hesselbrock e Minton (2017), we do perform simulations here on 4.5 Gyr evolution. Our study is mostly focused on the ring's evolution, which is only little discussed in Hesselbrock e Minton (2017) because of computer limitations.

We perform a set of numerical simulations varying the size of the particles in the debris disk, the friction angle of the rubble-pile (defining the disruption location, i.e., the RRL), and the initial mass of the debris disk. The values assumed by us are given in Table 2. The density of disk particles and satellites is assumed to be the bulk density of Phobos ($\rho = 1.845$ g/cm^3) and the initial disk surface density is defined following Hyodo et al. (2017), Hyodo et al. (2017), which is consistent with expectations for a debris disk formed after an impact on Mars forming the Borealis basin, as in Citron, Genda e Ida (2015).

The simulations are performed using the hybrid code `HYDRORINGS` (CHARNOZ; SALMON; CRIDA, 2010; SALMON et al., 2010) composed of two self-consistently coupled codes: an one-

dimensional finite volume code for tracking the viscous evolution of the disk (SALMON et al., 2010) and an analytical orbital integrator that follows the satellite evolution (CHARNOZ et al., 2011). The evolution of the disk surface density (Σ) is calculated on a regular grid composed of 200 uni-dimensional cells (HESSELBROCK; MINTON, 2017) extending from 1.0 $\mathrm{R_M}$ to 3.2 $\mathrm{R_M}$. The center of a cell has a radial location R while its width is $\Delta R = 0.011$ $\mathrm{R_M}$. At each time-step, the surface density variation is calculated using a second-order Range-Kutta scheme, being verified the material flux at the edges of each cell. Material falling onto Mars is removed while the material that spreads beyond the FRL (at 3.14 $\mathrm{R_M}$) is converted into one satellite per grid-cell. The number of cells defined by us ensures that mass and angular momentum are conserved down to machine precision when we form moons.

The temporal variation of the surface density is given by (BATH; PRINGLE, 1981):

$$\frac{\partial \Sigma}{\partial t} = \frac{3}{R}\frac{\partial}{\partial R}\left[\sqrt{R}\frac{\partial}{\partial R}(\nu\Sigma\sqrt{R})\right] \tag{8}$$

where t is time and ν is the total viscosity. We assume the total viscosity as the sum of the translational, collisional, and gravitational viscosities (SALMON et al., 2010).

Viscosity effects will occur differently if the disk is in the non-self-gravitating or gravitational regime. In the first, the disk is dense enough to be considered a fluid, while in the second, inter-particle interactions become important for the ring evolution. We determine the regime using the Toomre parameter (TOOMRE, 1964):

$$Q = \frac{\Omega\sigma_\nu}{3.36G\Sigma}, \tag{9}$$

where Ω is the keplerian frequency and σ_ν is the particle radial velocity dispersion. We have that $\sigma_\nu = 2s\Omega$ if $r_h < s$ and $\sigma_\nu = \sqrt{Gm/s}$ if $r_h \geq s$, where m is the mass of the ring particle and $r_h = (2m/3M_M)^{1/3}R$ the particle Hill radius (DAISAKA; TANAKA; IDA, 2001).

For the non-self-gravitating regime ($Q > 2$), the total viscosity is (SALMON et al., 2010)

$$\nu = 2.76\frac{\sigma_\nu^2}{\Omega}\left(\frac{s\rho\Sigma}{16s^2\rho^2 + 9\Sigma^2}\right) + 0.75\frac{s\Omega\Sigma}{\rho} \tag{10}$$

while for the self-gravitating regime ($Q < 2$), it is (SALMON et al., 2010)

$$\nu = 0.81\frac{r_h^5\mathrm{G}^2\Sigma^2}{s^5\Omega^3} + 0.75\frac{s\Omega\Sigma}{\rho} \tag{11}$$

We have that the viscous spreading timescale in our system in a crude approximation, will be given by (BRAHIC, 1977; SALMON et al., 2010):

$$\tau_{\mathrm{vis}} = (2.14\ R_M)^2\frac{1}{\nu} \sim (2.14\ R_M)^2\frac{\zeta\Omega^3}{\Sigma^2} \tag{12}$$

where ζ is a function approximately linearly proportional to the particle size s.

The semi-major axis a and eccentricity e of the satellites evolve under tidal effects and disk-satellite torques (Γ_s), and their temporal evolution are given by (KAULA, 1964; PEALE; CASSEN, 1978;

Table 2 – Parameter values assumed in the simulations of Section 3.4. M_P corresponds to the mass of Phobos, $M_P = 1.059 \times 10^{16}$ (PÄTZOLD et al., 2014).

Parameter	Symbol	Unit	Values
Particle size	s	m	0.1, 1, 10, and 100
Initial disk mass	M_{disk}	10^{20} kg	1, 1.2, 2, 3, and 5
		10^4 M_P	0.9, 1.1, 1.9, 2.8, and 4.6
Friction angle	ϕ	deg	25, 40, and 80

CHARNOZ; SALMON; CRIDA, 2010)

$$\frac{da}{dt} = \frac{3k_2 M_s G^{1/2} R_M^5}{Q M_M^{1/2} a^{11/2}} \left[1 + \frac{51e^2}{4}\right] + \frac{2a^{1/2}\Gamma_s}{M_s \left(GM_M\right)^{1/2}} \tag{13}$$

$$\frac{de}{dt} = \frac{57k_2 \Omega M_s R_M^5}{Q M_M a^5} e + F_{me} \tag{14}$$

where M_s is the satellite mass and tidal parameter is $k_2/Q = 0.00178$ (BAGHERI et al., 2021). We use the formalism described in Meyer-Vernet e Sicardy (1987) to estimate the disk-satellite interactions and the toy model described in Charnoz et al. (2011) to estimate the eccentricity kicks due to mutual encounters between the satellites (F_{me}). Two satellites are considered to merge when the distance between them is less than twice the mutual Hill radius. When immersed in the disk, the satellite accretes material following the recipe given by Thommes, Duncan e Levison (2003). Once the RRL is reached, the total satellite's mass is transferred in the ring-cell in which it is located, and the satellite is removed from the simulation (case without downsizing).

3.4.1 Dynamic evolution of an example system

Figure 19 shows the first cycle (Cycle #1) of a simulation with $M_{disk} = 1.1 \times 10^4$ M_P (HESSELBROCK; MINTON, 2017), $s = 10$ m, and $\phi = 40°$ (standard model). The left scale of the panels gives the disk surface density (Σ, solid blue line), while the right scale gives the satellite mass (black dots), as a function of distance to Mars.

The disk is initially confined within the FRL. Due to its own viscosity, the disk spreads inward and outward (Figure 19a). Some disk material is deposited at Mars equator and some spreads beyond the FRL (SALMON et al., 2010). Beyond the FRL, gravitational instabilities promote rapid accretion of material into aggregates (KARJALAINEN, 2007; CHARNOZ; SALMON; CRIDA, 2010; CHARNOZ et al., 2011), giving rise to Lagrangian moons (ROSENBLATT; CHARNOZ, 2012; HESSELBROCK; MINTON, 2017). Satellites capture all disk material and neighboring satellites present within their Hill sphere, which depends on both the semi-major axis and planet mass. The satellite is expected to be porous if the bulk density of disk particles is significantly greater than a critical Hill density defined as $\rho_c = M_M/(1.59a^3)$ (PORCO et al., 2007). This is our case ($\rho_c = 0.334$ g/cm^3), which indicates that our assumption of satellites as gravitational aggregates is, in first approximation, applicable.

The moon grows from impacts with other newly formed moons, while migrating outward due to disk-satellite torques. Due to this mechanism, a population of satellites is formed with masses ordered by increasing semi-major axis as can be seen in Figure 19b. Satellite migration slows down as the

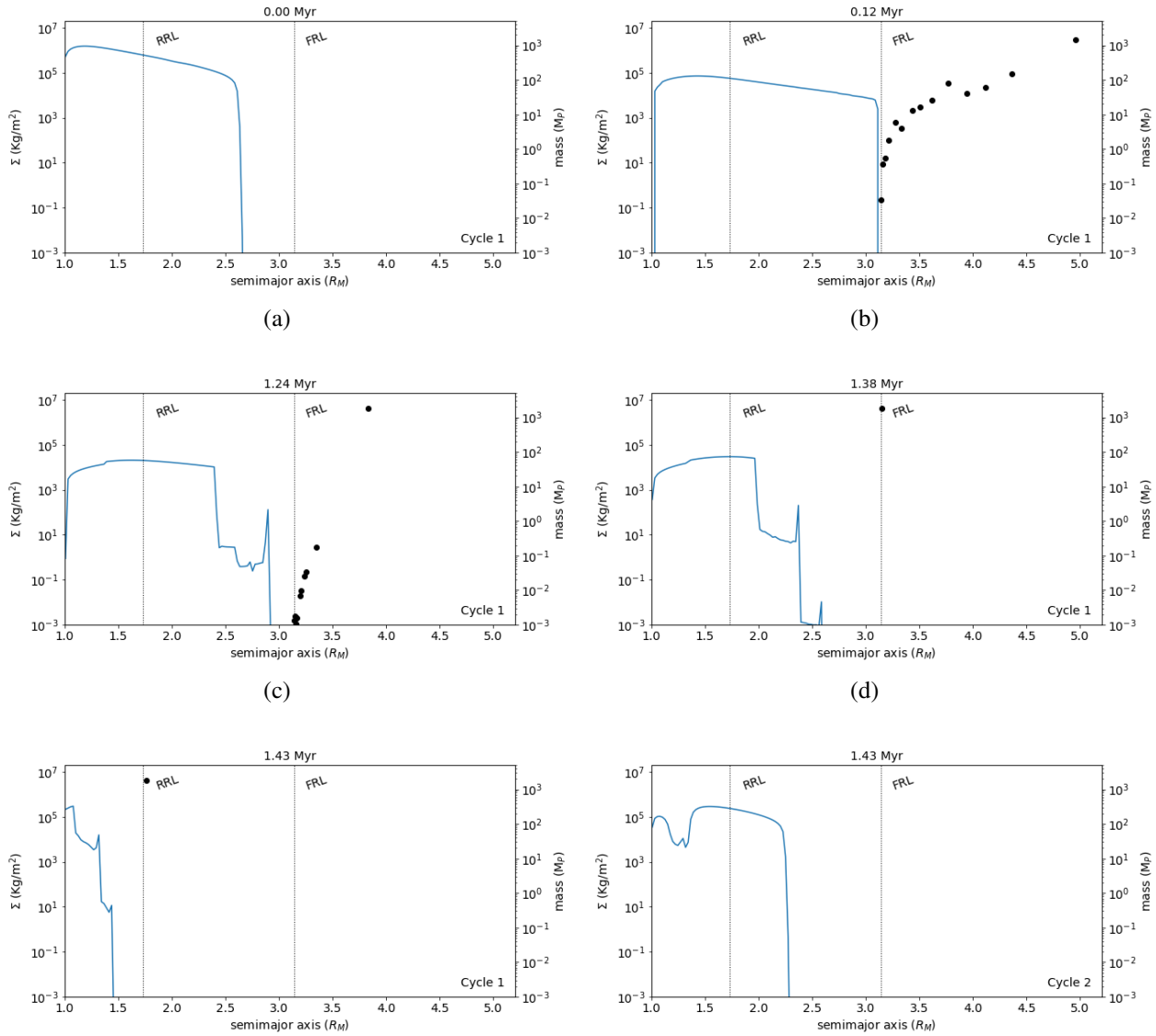

Figure 19 – Evolution of disk surface density (solid blue line, left scale) and satellite mass (black dots, right scale) as a function of distance to Mars (semimajor axis in $\mathrm{R_M}$). The simulation time is given at the top of each panel, and the vertical dashed lines show the location of RRL ($1.74\ \mathrm{R_M}$) and FRL ($3.14\ \mathrm{R_M}$). The panels only show the first cycle of the simulation, with initial disk mass being $1.1 \times 10^4\ \mathrm{M_P}$, particle size 10 m, and friction angle $40°$. An animation with the complete evolution of the system can be found at the link: <https://tinyurl.com/phobosanimations>.

distance increases, ceasing when the satellite's 2:1 inner Lindblad resonance (ILR) leaves the disk (CHARNOZ et al., 2011), which happens at $\mathrm{a}_{2:1}^{\mathrm{ILR}} = 4.98\ \mathrm{R_M}$. If the disk is sufficiently depleted, the tidal torque exceeds the disk-satellite torque and the satellite migrates inward. Otherwise, it will remain at around $4.98\ \mathrm{R_M}$.

After ~ 0.2 Myr, the torque balance on the outermost satellite results in inward migration, and the satellite accretes the inner satellites as it migrates toward the planet (Figure 19c). In Figure 19d, the outermost satellite (a Phobos ancestor) remains the only surviving satellite in the system. Here, we define as *Phobos ancestor*, the most massive satellite of the cycle (with a minimal mass of $2\ \mathrm{M_P}$, where $\mathrm{M_P}$ is Phobos' mass), the one that will migrate inward and reach the RRL. In most cycles, Phobos

ancestor is also the outermost satellite at any time. A satellite with these same characteristics, but masses in the range $0.5 - 2.0$ M_P will correspond to a *Phobos analogue*, according to our definition. This mass range corresponds to the narrowest range needed to ensure that all simulations will produce a satellite analogous to Phobos.

Disk and satellite interact mainly by IRL torques (MEYER-VERNET; SICARDY, 1987) and if the resonant torque exceeds the disk viscous torque, the satellite confines the disk. The minimum mass for the satellite to confine the disk is given by (LONGARETTI, 2018)

$$m_s = 1.58 \frac{\Sigma}{a_d \rho} \left| \frac{x_e}{a_d} \right| M_M \tag{15}$$

where x_e and a_d are the distances from the outer disk edge to the satellite and planet, respectively. In the first cycle, a minimum mass of $\sim 10^2$ M_P is needed to confine the disk. Such a condition is met by the Phobos ancestor. The Σ peaks on Figure 19c-e correspond to the locations of the 2:1, 3:2, and 4:3 ILRs, from left to right. By this mechanism, the satellite pushes the disk towards the planet as it migrates inward (Figure 19e), and material is deposited at Mars equator. The satellite enters in the region below the FRL but is not disrupted before it reaches its RRL (~ 1.74 R_M). Just before the satellite reaches its RRL, a residual ring still exists very close to Mars (Figure 19e). Finally, when the satellite crosses its RRL, it is disrupted by tides, and debris are transferred to the ring that spreads rapidly. Then a new cycle begins (Figure 19f). Note that here we have assumed that the satellite is fully destroyed in ring particles when it crosses the RRL, as in the case of Hesselbrock e Minton (2017). We have also studied the case when the satellite is downsized by tides (Section 3.4.2).

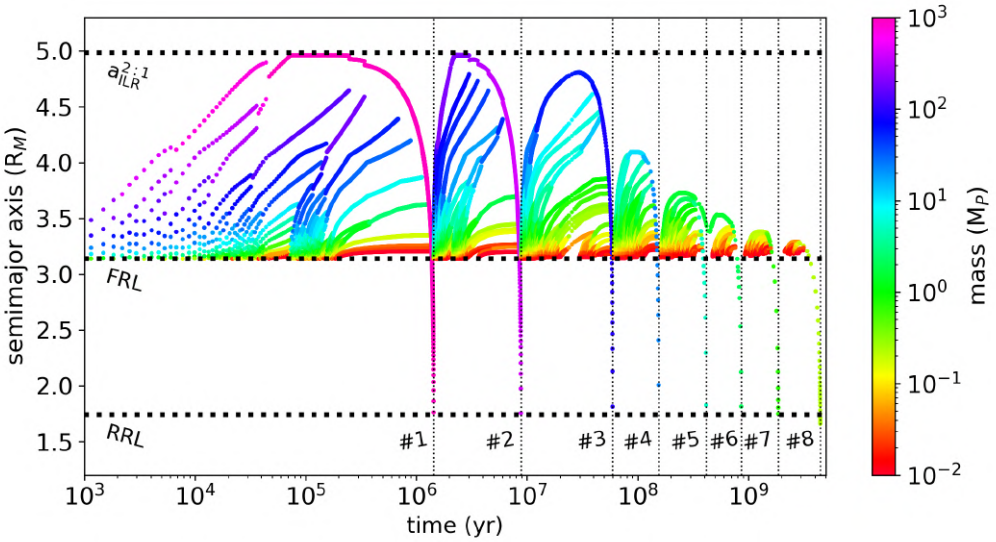

Figure 20 – Semi-major axis of satellites as a function of time, for the same simulation as in Figure 19. Each dot stands for a satellite obtained in the simulation, but at different times. The color represents the satellite's mass. Satellites with masses similar to Phobos are colored green. The horizontal dotted lines provide the location of RRL, FRL, and 2:1 ILR with FRL. The vertical dotted lines delimit the beginning and end of the cycles.

In general, we find that most cycles follow the same evolution as described above, with some notable exceptions that we describe hereafter. Figure 20 shows the position and masses of satellites,

as a function of time. As we can see, the maximum distance reached by Phobos ancestors decreases with the number of cycles. Indeed, since the disk mass is continuously decreasing, the most massive satellite that can accrete at each new cycle has its maximum mass decreasing with time. This effect was reported in Hesselbrock e Minton (2017).

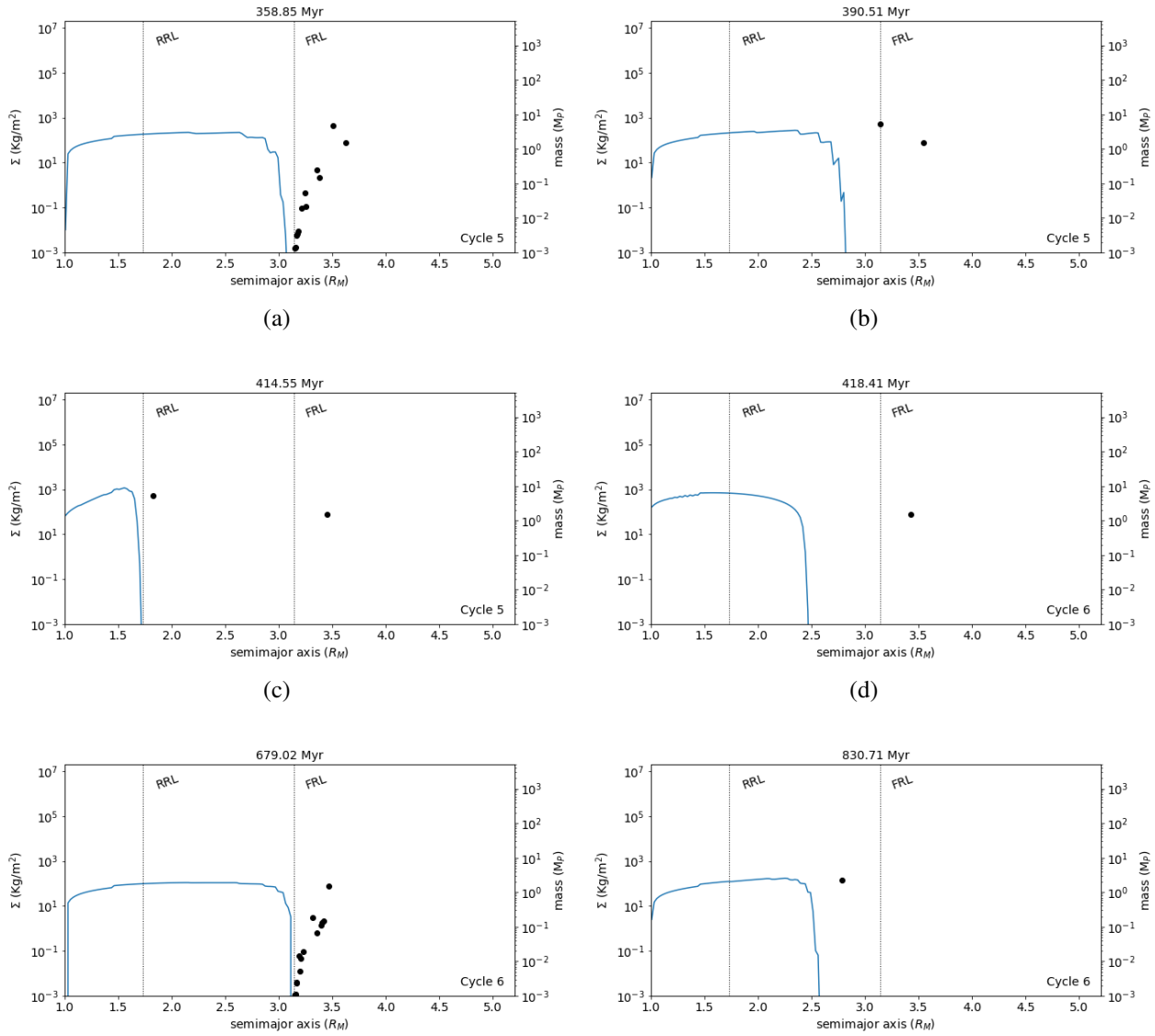

Figure 21 – Evolution of disk surface density and satellite mass, for the fifth and sixth cycles of our standard model. The disk is shown as a solid blue line, with surface density given on the left scale and satellites are given by black dots, with mass on right scale. The vertical dashed lines show the locations of RRL and FRL. An animation with the complete evolution of the system can be found at the link: <https://tinyurl.com/phobosanimations>.

In most observed cycles, the disk evolves into a system composed of one Phobos ancestor and a ring confined by the satellite. However, sometimes, a different evolution is observed, like in Cycle #5 of the standard model. Figure 21 shows the evolution of disk and satellites in cycles #5 and #6, for comparison. Cycle #6 (Figure 21d and e), is a "typical" cycle, where the most massive satellite is the most distant. In that case, the ring's outer edge is always in 2:1 resonance with the outermost satellite. Cycle #5 is peculiar because the most massive satellite ($\sim 10\ \mathrm{M_P}$) is not the most distant. The most

distant is ~ 3 M_P (Figure 21a and b). Because the most massive satellite feels a stronger planet's tidal torque it moves inward and pushes the ring down to the planet, leaving, temporarily a Roche Zone region almost empty and a satellite with ~ 3 M_P just beyond the Roche Limit. If the most massive satellite was very cohesive, it would completely eliminate the ring and would fall onto the planet, just leaving one satellite in the system. However in the current simulation, the object disrupts (Figure 21c) and Cycle #6 starts.

Cycle #5 is very similar to the scenario proposed by Rosenblatt et al. (2016), in which there is only one cycle, because satellites are assumed to be very cohesive, so are not destroyed at the RRL. This is why Rosenblatt et al. (2016) find only one remaining Phobos (and one Deimos) and no disk surviving at the end of their process.

In the seventh cycle, a Phobos analogue is obtained at ~ 1.8 Gyr after the start of the simulation (assumed to be the time of the giant impact that formed the circum-martian disk). When the satellite accretes the last moon at ~ 1.8 Gyr, it is located at ~ 3.2 R_M, taking additional ~ 0.2 Gyr to reach the actual position of Phobos (2.76 R_M). Such a value would be the "age" of Phobos according to this simulation, which is the time between today and the last major collision with another satellite. Interestingly, this age is close to the lowest age estimated by Ramsley e Head (2017) based on craters study. This places the giant impact that hit Mars and formed the Borealis Basin at $t_{gi} \sim 2.5$ Gyr after the formation of Mars, while several works suggest that the impact would have happened < 0.5 Gyr after the formation of the planet (see Section 3.5). Phobos' formation must have occurred on a longer timescale than that obtained in the simulation. Furthermore, we get a ring with optical depth of $\tau \sim 9 \times 10^{-4}$ coexisting with Phobos, i.e., a ring that would be detectable today.

3.4.2 Effect of tidal downsizing on Phobos formation

In Section 3.3 we theorize the possibility that the tidal force is responsible for satellite downsizing inside the RRL, in a process we called "tidal downsizing". Seen that, we also performed numerical simulations accounting for the tidal downsizing effect. Upon reaching the RRL, we assume that the satellite loses the amount of material necessary to be marginally stable at that location (Figure 17), and the mass is transferred to the ring-cell in which it is located. Then, at each time-step, the satellite mass is changed according to Figure 17 and the eroded mass is transferred to the ring.

Figure 22 shows a simulation with the same parameters as our standard model (Figure 20), including the tidal downsizing effect. Generally speaking, we find that the downsizing has a minor effect on Phobos formation, as can be seen by comparing Figure 22 and Figure 20. The maximum mass that can survive at the RRL (1.74 R_M) is about 10^{16} kg, a value at least two orders of magnitude smaller than the mass of Phobos ancestor in the first four cycles. In these cycles, Phobos ancestor loses more than 99% of its mass right at the RRL, which is very close to the extreme hypothesis of full destruction in Figure 20.

Small differences in the system can be noticed in the cycles prior to Phobos formation – cycles #5 and #6 in Figure 22. The differences, however, are not enough to significantly change the results regarding the formation time and optical depth (Section 3.4.6). In these cycles, more than 10% of the mass of the ancestor satellite survives when reaching RRL, but due to the rapid decay of mass

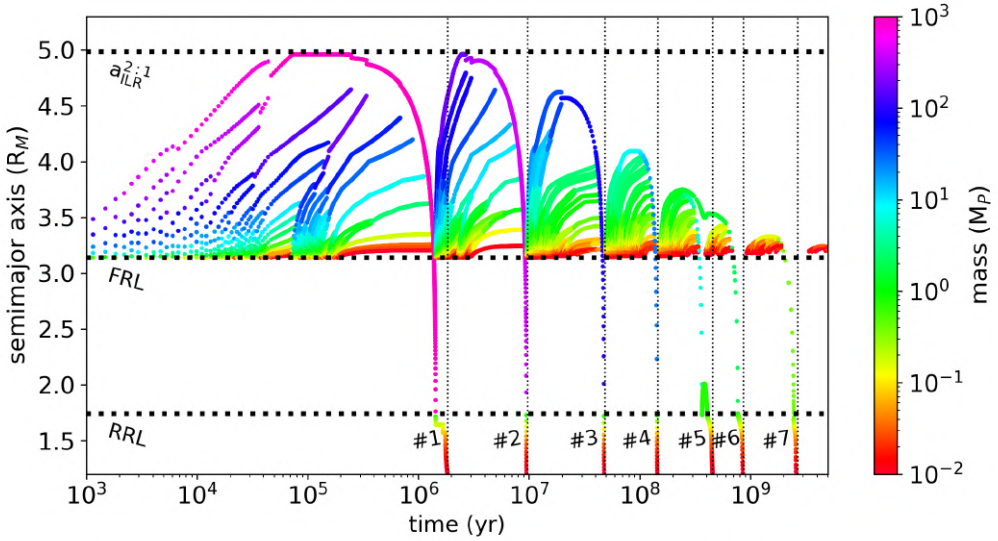

Figure 22 – Semi-major axis of satellites as a function of time, for a simulation with $\mathrm{M_{disk}} = 1.1 \times 10^4\ \mathrm{M_P}$, $s = 10$ m, and $\phi = 40°$, with tidal downsizing. Each dot stands for a satellite obtained in the simulation, but at different times. The color represents the satellite's mass. An animation with the complete evolution of the system can be found at the link: <https://tinyurl.com/phobosanimations>.

as a function of the semi-major axis in Figure 17, we have that the satellites lose more than 99% of their mass before reaching $\sim 1.6\ \mathrm{R_M}$. Physically, this means that tidal effects are responsible for rapid downsizing of the body when inside the RRL.

It is also seen that the surviving parts of the satellites are not massive enough to confine the ring, being immersed in it. The satellites don't promote a cleaning process by pushing material towards the planet, as one might think. Although tidal downsizing does not have a significant effect on the formation of Phobos, it might be important in the post-evolution of the satellite, as already pointed out in Section 3.3. Because of this, from now on we will only focus on the simulations with the full destruction of satellites. In the following sections, we explore the effects of the particle size, initial disk mass, and friction angle in such simulations.

3.4.3 On the particle size dependence

The typical size of the particles in the debris disk is a key parameter of the recycling model, as it defines the viscous evolution of the disk (Equation 12). Particles are also the building blocks of the rubble-piles. As this parameter is unconstrained, we performed simulations with sizes ranging from 0.1 m to 100 m.

Figure 23 summarizes the results of the simulations with $\mathrm{M_{disk}} = 1.1 \times 10^4\ \mathrm{M_P}$ and $\phi = 40°$. The top panel (Figure 23a) shows on the left scale (solid line) the time to obtain a Phobos analogue, and on the right scale (dotted line), the number of cycles required to form the satellite. The middle panel (Figure 23b) gives the fraction between the mass of the largest satellite formed in one cycle and the initial mass of the disk in the same cycle ($\mathrm{M_{sat}}/\mathrm{M_{disk}}$), as a function of the time when the largest satellite disrupts. Finally, the bottom panel (Figure 23c) provides data about the ring coexisting with Phobos analogue. The y-axis gives the average optical depth of the ring. Below the black curve is

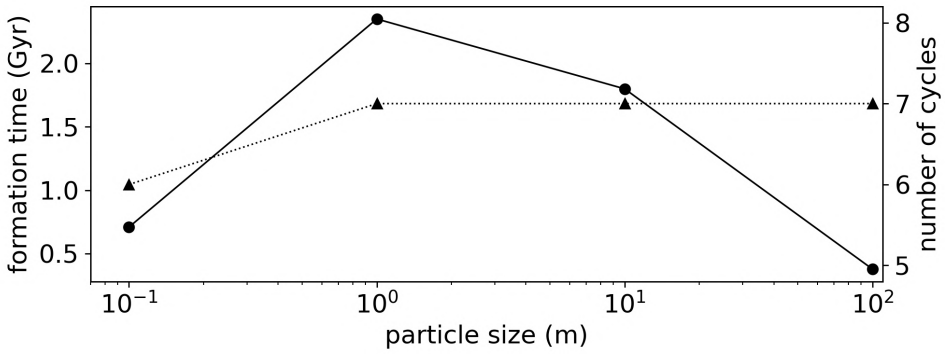

(a)

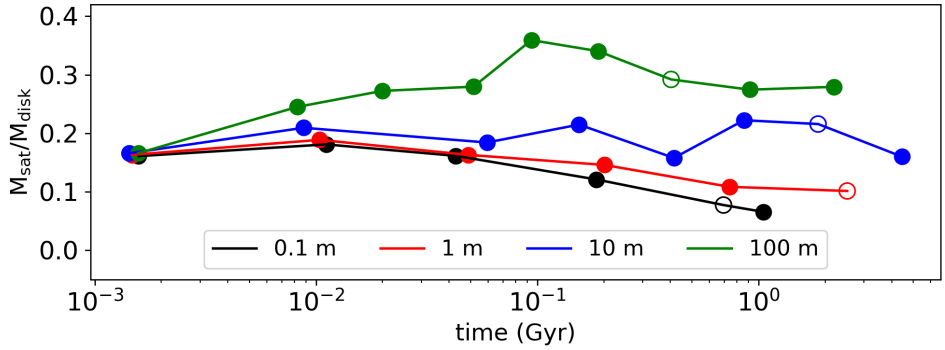

(b)

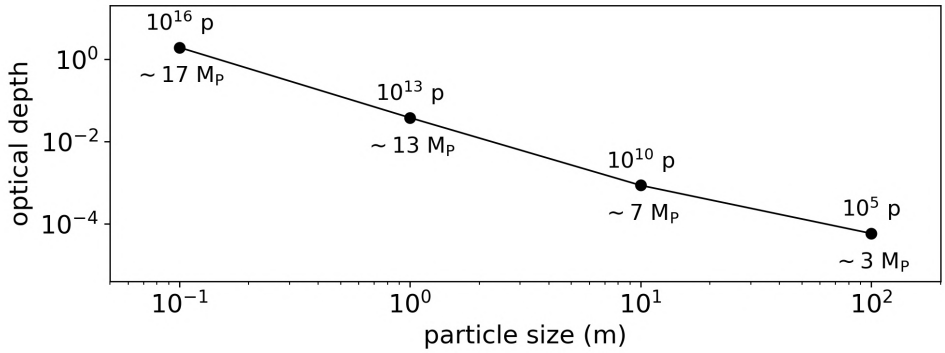

(c)

Figure 23 – (a) Timespan (left scale, solid line) and number of cycles (right scale, dotted line) to form a Phobos analogue as a function of the particle size. (b) Mass of the largest satellite in the cycle relative to the initial disk mass in the same cycle, with different colors corresponding to different particle sizes. The open points in the panel correspond to the cycles that form a Phobos analogue. (c) Average optical depth of the residual ring coexisting with Phobos as a function of the particle size. We set the initial disk mass as 1.1×10^4 M_P and friction angle equals to $40°$. The annotations below and above the black curve give the ring mass and number of particles in the ring, respectively.

given the mass of the ring, while above it we show the amount of particles that such a mass would represent. Here, we define the average optical depth as the ratio of the total cross-section of material in the ring and the total surface area of the ring, found as

$$\tau = \frac{3M_{\text{ring}}}{4\rho s A_{\text{ring}}} \tag{16}$$

where M_{ring} and A_{ring} are the mass and surface area of the ring extracted from the simulation.

The viscous evolution of the ring through the cycles is a very intricate problem. Although the ring spreads more slowly when the particles are smaller, at first depositing less material onto Mars, we have that for the same reason, satellites will grow more slowly and the cycles will last longer, depositing material on Mars for longer. In addition, the system is influenced by the residual ring obtained at the end of each cycle, affecting interactions with the satellite. Despite this, we obtain some clear relationships between our chosen parameters and the evolution of the system.

In general, we obtain an increase in the Phobos analogue formation time when decreasing the particle size. The exception is the case with $s = 0.1$ m, where Phobos analogue is formed faster than the cases with 1 and 10 m. This happens because it takes 6 cycles to form Phobos in the case with $s = 0.1$ m, while in the other cases, the satellite is formed after 7 cycles. If Phobos were a seventh generation satellite also in the case with $s = 0.1$ m, we would get a formation time of ~ 5 Gyr, a much longer time than for the case with $s = 1$ m. However, the satellite formed in the seventh cycle is too small to be considered a Phobos analogue ($0.4\ \mathrm{M_P}$), also coexisting with a visible ring of $\tau = 0.4$. We find that the number of cycles required to form Phobos increases with particle size. That's why the case with $s = 0.1$ m requires fewer cycles to form a satellite with mass close to Phobos. In a simulation with $s = 1000$ m, for example, we obtain that a Phobos analogue is formed only after 9 cycles.

Our definition of Phobos analogue is somewhat arbitrary and one might wonder whether this could affect our conclusions. The mass range $0.5 - 2.0\ \mathrm{M_P}$ is the narrowest one required to obtain at least one Phobos analogue in all our simulations. For narrower ranges, some simulations will not form a satellite analogous to Phobos. If we extend the lower/upper limit of the mass range, it takes a longer/shorter period to form Phobos. However, we verify that the main result of the article remains unchanged (Section 3.5.1). A visible ring coexisting with Phobos is always obtained, although we obtain a smaller optical depth in cases where Phobos is formed in a longer period (reductions of about 10 times).

In Figure 23b, we can see that $\mathrm{M_{sat}}/\mathrm{M_{disk}}$ decreases with time, because of the residual ring that accumulates mass from a cycle to another, reducing the value of the total fraction. If we calculate the ratio between the mass of the largest satellite formed in a cycle and the mass of the largest satellite formed in the previous one, we obtain values ~ 0.25, the same as those claimed by Hesselbrock e Minton (2017). This means that the accretion efficiency has a weak dependence on particle size and number of cycles (disk mass). Hesselbrock e Minton (2017) find that the accretion efficiency is mainly affected by the RRL location, a result also obtained by us. The residual ring mass, however, depends on the particle size, which results in the pattern seen in Figure 23b.

Finally, we obtain a clear relationship between particle size and average optical depth. For the same total mass, the cross-section covered by a set of particles is greater for smaller particles. This is, in part, an explanation for our results. Nonetheless, we also obtain an increase in residual ring mass with particle size, explaining the increase in average optical depth with particle size. The simulation with $s = 0.1$ m generates a ring with $\tau \sim 2$, of the same order as the denser broad rings of Saturn (rings A and B) (FRENCH et al., 2017). As we increase the particle size, the average optical depth drops to values of the same order as the C ring, another broad and dense ring of Saturn (NICHOLSON et al., 2014). For the largest particle size, $\tau = 6 \times 10^{-5}$ corresponding to a ring composed of $\sim 10^5$ particles of 100 meters of radius. Such material would certainly be detected by orbiters around Mars.

3.4.4 On the initial disk mass dependence

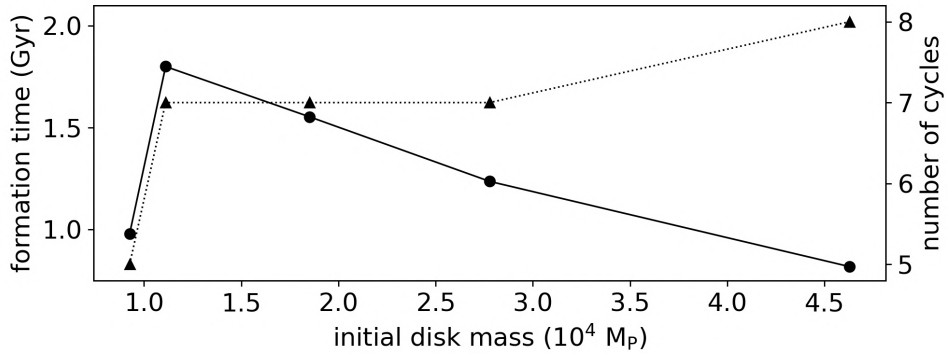

(a)

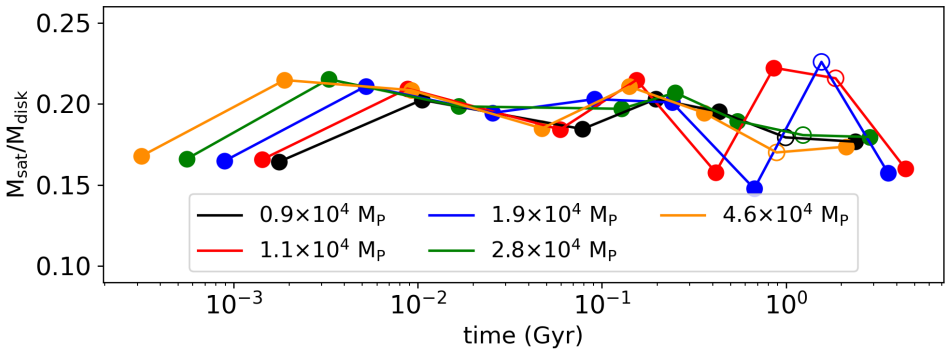

(b)

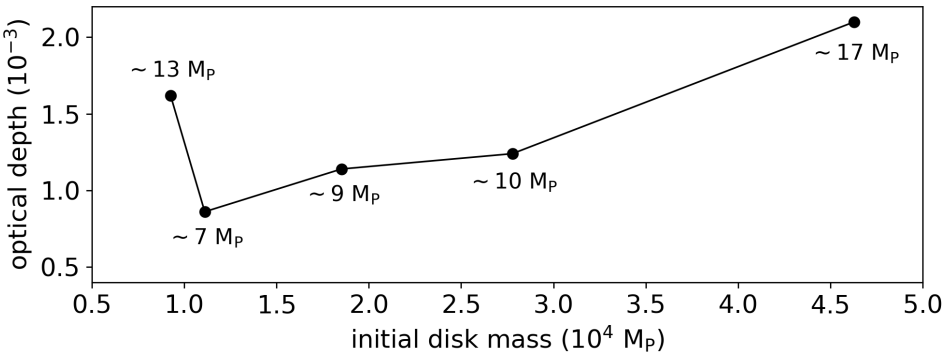

(c)

Figure 24 – (a) Timespan (left scale, solid line) and number of cycles (right scale, dotted line) to form a Phobos analogue as a function of the initial disk mass. (b) Mass of the largest satellite in the cycle relative to the initial disk mass in the same cycle, with different colors corresponding to different disk mass. (c) Average optical depth of the residual ring coexisting with Phobos. We assumed the particle size as 10 m and friction angle as $40°$. The open points in panel b correspond to the cycles that form a Phobos analogue. The annotations in panel c give the mass of the residual ring.

Figure 24 shows the same panels as Figure 23 for simulations with $s = 10$ m and $\phi = 40°$. The greater the mass of the disk, the faster the viscous spreading, being required more cycles to form Phobos. At the same time, we obtain that the formation time decreases with the initial disk mass. Some exceptions are obtained, as in the case with $M_{disk} = 0.9 \times 10^4$ M_P of Figure 24a. In this case, a Phobos analogue with mass of 1.5 M_P is obtained in the fifth cycle (~ 1 Gyr). The same cycle in the case with $M_{disk} = 1.1 \times 10^4$ M_P (~ 0.4 Gyr) gives rise to a satellite with a mass of 7 M_P, which is too

large to be considered a Phobos analogue, requiring two more cycles to form an object with mass close to that of Phobos. So the formation takes longer in the case with $M_{disk} = 1.1 \times 10^4$ M_P.

As can be seen in Figure 24b, there is no clear relationship between M_{sat}/M_{disk} and M_{disk}, with all points spreading around an average curve. This leads us to conclude that M_{sat}/M_{disk} has only a small dependence on the initial disk mass, meaning that the accretion efficiency and the residual ring mass fraction are almost invariant to M_{disk}. Finally, we get that increasing M_{disk}, we obtain more massive and brighter residual rings (Figure 24c). The same exceptions observed for formation time are obtained for the optical depth.

3.4.5 On the friction angle dependence

Now, we analyze the effect of the rubble-pile friction angle on the recycling process. The same panels shown in Figure 23 are given in Figure 25, for a case with $M_{disk} = 1.1 \times 10^4$ M_P and $s = 10$ m varying the friction angle. As discussed in Section 3.3, by increasing ϕ, we are decreasing the location to Mars where the satellite is torn apart by tides. Thus, the closer to Mars the satellite disrupts, the greater the amount of material deposited on the planet per cycle. The more depleted the disk in each cycle, and the slower the viscous spreading. As expected, the number of cycles and M_{sat}/M_{disk} decrease with decreasing disruption location (Figure 25a,b), a result also obtained by Hesselbrock e Minton (2017). In turn, the formation time increases with the friction angle (Figure 25a), while the optical depth decreases, since the residual ring is less massive when the satellite is closer to the planet (Figure 25c). In the next section, we summarize the results of our numerical simulations.

3.4.6 The ring coexisting with Phobos

In the previous section, we showed that disk accretion on satellites is not completely efficient, leaving a residual ring after the formation of the satellites. In all of our 60 numerical simulations with full destruction, we obtained a ring coexisting with the Phobos analogues. We then analyzed whether the recycling process would generate an extremely faint ring coexisting with Phobos, which would not be visible with the current observational instruments. Using data from Viking Orbiter 1, Duxbury e Ocampo (1988) looked for a ring in the region inside Phobos, ruling out the possibility of a ring with optical depth $\tau > 3 \times 10^{-5}$. More recently, Showalter, Hamilton e Nicholson (2006) using Hubble data, did not detect rings coorbital to Phobos and Deimos. They got the upper limit of 3×10^{-8} for a possible Phobos ring. They also ruled out the existence of objects larger than 75 m in radius around Mars. Such limits define a "forbidden region" in terms of optical depth and particle size for a ring around Mars.

Figure 26 shows in the top panel the average optical depth of the ring coexisting with Phobos, as a function of the particle size. In the bottom panel, we show the period the recycling process would begin after the formation of Mars. Here, we assume that Mars formed ~ 4.5 Gyr ago (NESVORNÝ et al., 2018; IZIDORO et al., 2022), while we extract from the numerical simulations the time for the formation of Phobos analogue and the time for Phobos to migrate to its current position ($\sim 0.1 - 0.5$ Gyr). Thus, the instant the recycling process began is given by the relation: 4.5 Gyr $-$ formation time $-$ migration time. The different lines and colors correspond to different sets of disk

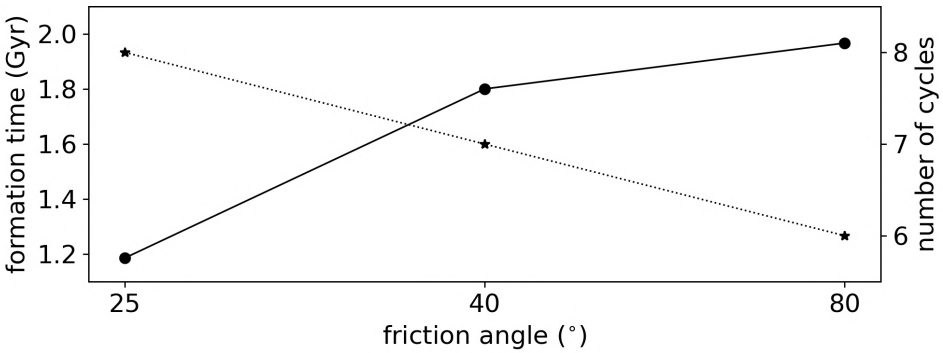

(a)

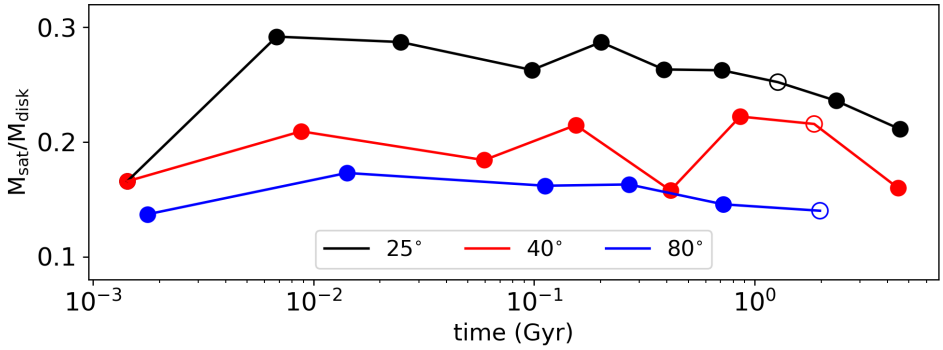

(b)

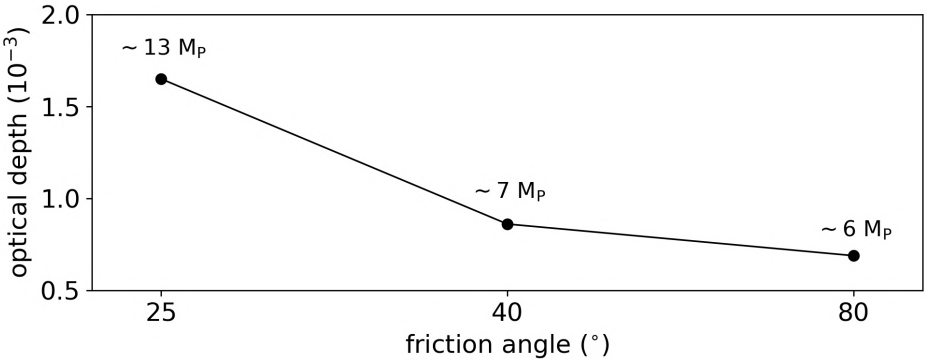

(c)

Figure 25 – (a) Timespan (left scale, solid line) and number of cycles (right scale, dotted line) to form a Phobos analogue, as a function of the friction angle. (b) Mass of the largest satellite in the cycle in relation to the initial disk mass in the same cycle. (c) Average optical depth of the residual ring coexisting with Phobos. We assumed the initial disk mass as 1.1×10^4 M_P and particle size as 10 m. The open points in panel b correspond to the cycles that form a Phobos analogue, while the annotations in panel c give the residual ring mass.

mass and friction angle, and the gray regions set the forbidden region. Here, we assume that ideally the recycling process began < 0.5 Gyr after the formation of the planet (see Section 3.5.1), defining the forbidden region in time (Figure 26b).

As a rule, we obtain that disks with larger particles (10 m and 100 m) generate a fainter ring and Phobos is formed quickly, while for smaller particles (0.1 m and 1 m), the time for Phobos formation is longer, but the residual ring is brighter. In all our numerical simulations, the optical depth is in the forbidden region. Also, most of our simulations require a very recent giant impact. Only in numerical simulations with $s = 1$ m and $\phi = 25°$, the giant impact would have happened in a time compatible

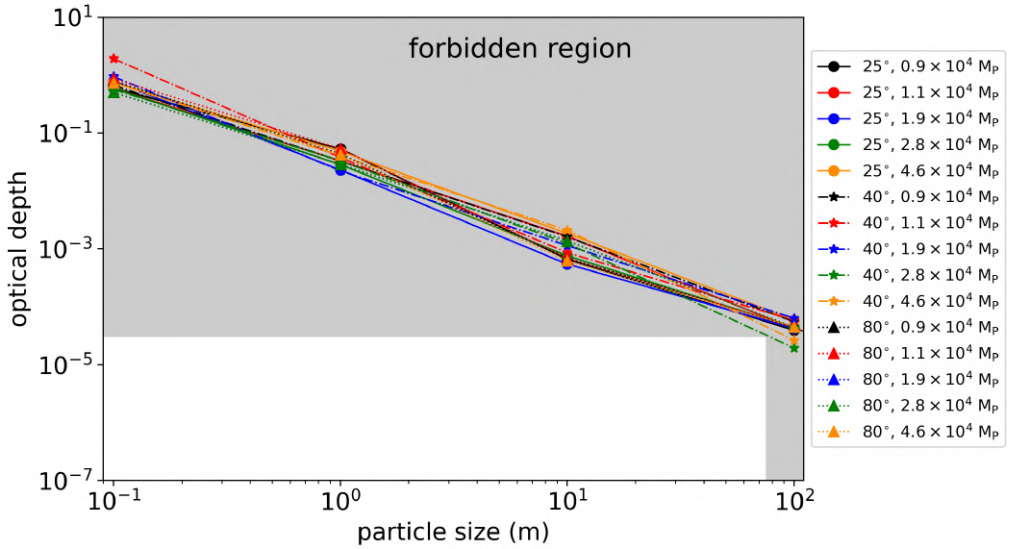

(a)

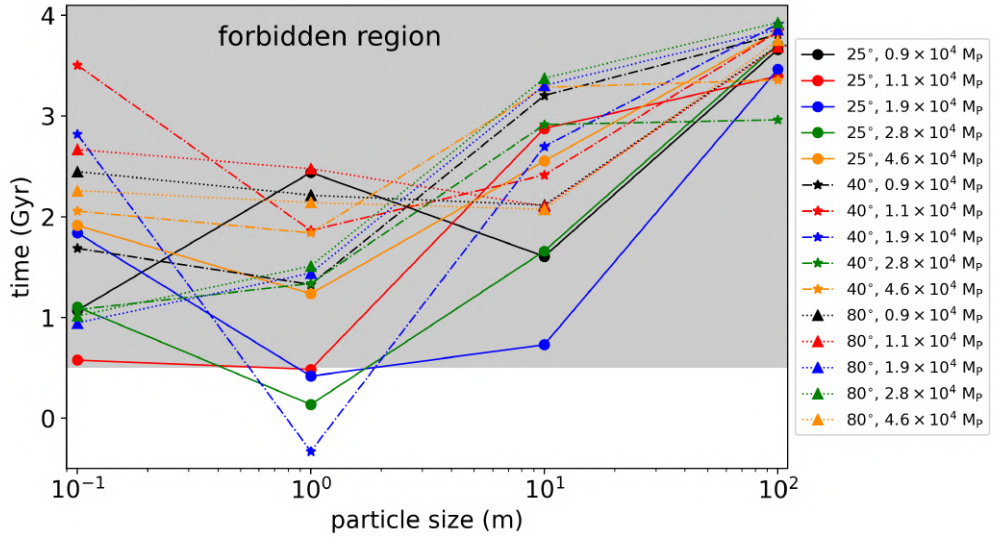

(b)

Figure 26 – a) Average optical depth of the ring coexisting with Phobos and b) instant of the beginning of the recycling process (after Mars formation), as a function of the particle size. The solid lines with circles, dashed lines with stars, and dotted lines with triangles give the cases with $\phi = 25°$, $40°$, and $80°$, respectively. The different colors correspond to different initial disk mass. The gray regions correspond to the forbidden region for the optical depth of the ring and instant of the giant impact.

with estimates given in the literature. In the simulation with $s = 1$, $\phi = 40°$, and $\mathrm{M_{disk}} = 1.9 \times 10^4\ \mathrm{M_P}$, the Phobos analogue is obtained at its current position in a period greater than the age of Mars. In the next section, we discuss additional processes and implications related to the recycling mechanism.

3.5 DISCUSSION

3.5.1 General Remarks

We explored the material recycling mechanism for the formation of Phobos, assuming that the satellites aggregated in the debris disk are rubble-piles. In our numerical simulations, the mechanism

is successful in forming a satellite with the mass and position of Phobos, however, there are two main caveats: the formation time and the ring coexisting with Phobos.

Regarding the formation time, we need to analyze two important variables: the age of Phobos and the time when the recycling process began. Some studies estimate the age of Phobos through the analysis of topographical structures on the surface of the satellite, but the results differ depending on the method applied. Schmedemann et al. (2014), by counting craters within the Stickney crater – the largest crater on Phobos' surface – and assuming that the craters are the result of external impactors, estimate an age of $\sim 2.8 - 4.2$ Gyr for the structure. In turn, Ramsley e Head (2017) assume the craters as a result of secondary impacts, estimating an age of $0.1 - 0.5$ Gyr for the Stickney crater. In our numerical simulations, we obtain that Phobos would have formed $\sim 0.1 - 0.5$ Gyr ago, corroborating the secondary impact crater hypothesis.

The caveat, in fact, resides on the time of the beginning of the recycling process. Works by, e.g., Citron, Genda e Ida (2015), Rosenblatt et al. (2016) and Canup e Salmon (2018) assume that the debris disk and Borealis basin originated from the same giant impact, which took place > 4 Gyr ago, according estimates by Nimmo et al. (2008), Andrews-Hanna, Zuber e Banerdt (2008) and Marinova, Aharonson e Asphaug (2008). The impacts responsible for the Hellas, Utopia, Isidis, and Argyre basins on Mars (SEARLS; BANERDT; PHILLIPS, 2006; SCHELLER; EHLMANN, 2020) could also give rise to disks of material, albeit less massive than that from the Borealis impact. In fact, it is likely that the disk that gave rise to Phobos was formed from the collection of these successive impacts. Bottke e Andrews-Hanna (2017) using topology analysis, narrow the epoch of the Borealis impact to around 4.5 Gyr ago, while finding that impacts responsible for the smaller basins occurred between 3.8 and 4.4 Gyr ago. Accounting for these studies, we set 0.5 Gyr after Mars formation as the a maximum fiducial value for the start of the recycling process, which is met only by the cases with $s = 1$ m and $\phi = 25°$.

The other caveat of the recycling model for rubble-pile satellites is the presence of a ring coexisting with Phobos. Duxbury e Ocampo (1988) and Showalter, Hamilton e Nicholson (2006) set an upper limit for the optical depth of a ring around Mars, but the most likely scenario is that there is not a ring inside Phobos' orbit. This statement is motivated by the presence of orbiters in low-orbits around Mars for long periods of time ($\sim$yrs) – such as Viking-2 (CHRISTENSEN; WILLIAMS, 1979), Mars Global Surveyor (ALBEE et al., 2001), 2001 Mars Odyssey (MASE et al., 2005), and Mars Reconnaissance Orbiter (GRAF et al., 2005). Such orbiters would likely be impacted by debris if there were a ring composed of metric particles around Mars.

Given this, we make a last effort and analyze whether external forces could be responsible for the removal of the ring. Various forces act on rings – plasma and atmospheric drag, Poynting-Robertson effect, Lorentz force, and Yarkovsky effect (HAMILTON; KRIVOV, 1996; MADEIRA; GIULIATTI-WINTER, 2020; LIU; SCHMIDT, 2021; LIANG; HYODO, 2023) – however, most are only relevant in the evolution of micrometer-sized particles, a size range not considered by us. This is because rubble-pile satellites are highly unlikely to be reduced to micrometer particles due to tidal forces. For the size range considered by us, the Yarkovsky effect could be the dominant perturbation. We consider this effect in the next section.

Table 3 – Assumed parameters for the Yarkovsky effect.

Parameter	Symbol	Value	Reference
Solar insolation on Mars	$F_{\rm sun}$	590.3 Wm^{-2}	Rubincam (2006)
Mars Bond albedo	A_M	0.248	Genio et al. (2019)
Average temperature	T_0	229 K	Rubincam (2014)
Specific heat	C_p	690.8 $\mathrm{Jkg}^{-1}\mathrm{K}^{-1}$	Rubincam (2014)
Thermal conductivity	K	2.54 $\mathrm{Wm}^{-1}\mathrm{K}^{-1}$	Rubincam (2014)
Infrared emissivity	ϵ_{IR}	0.9	Rubincam (2014)
Visible albedo	A_v	0.05	Rubincam (2014)
Infrared albedo	A_{IR}	0.1	Rubincam (2014)

3.5.2 Debris disk under the Yarkovsky effect

Yarkovsky effect is a composition of different effects that arise from the asymmetric illumination of particles. The particle side facing a heat source (Sun or Mars) gets hotter than the opposite side, resulting in a thrust in the motion of the particle (RUBINCAM, 1982). The strength of the Yarkovsky effect is mainly defined by the linkage of the spin and orbital motion of the particle with the insolation from the Sun or planet. It is the strongest only when the particle rotates with undisturbed principal axis rotation (BOTTKE et al., 2002). Considering a disk of material, we have that collisions are responsible for the tumbling of the particles, which weakens the Yarkovsky effect that can become insignificant if the tumbling timescale is smaller than the orbital period (RUBINCAM, 2014).

To assess whether the Yarkovsky effect is significant for the debris disk, a complete study of the spin variation of the particles would be necessary, which is beyond the scope of this work. However, for completeness, we study the case in which the tumbling of particles due to collisions is disregarded. The spin vector of the particles is assumed to be constant and perpendicular to the equatorial plane during the simulation. Although physically inconsistent – collisions between particles are what induces the disk viscous spreading – we can consider that the actual evolution of the disk is likely to be a scenario between this case and the one given in Section 3.4.

We have redone all the simulations of Section 3.4 including the Yarkovsky effect. For this, we computed the secular variation of the semi-major axis due to two different components: the Yarkovsky–Schach and the seasonal Yarkovsky. The Yarkovsky–Schach effect is related to Solar illumination, where one side of the particle absorbs sunlight and remits it in the infrared when in the planetary shadow, feeling a kick that increases its semi-major axis. The seasonal Yarkovsky effect results from the remission by the particle of photons from Mars illumination, this effect being responsible for the orbital decay.

The semimajor axis variation is (RUBINCAM, 2006)

$$\frac{da}{dt} = \frac{F_{\rm sun} B \sin\delta}{18nc\rho s}\left[2(1-A_v)b_1\sin\theta_{\rm sun} - \left(1.78 + \frac{2.06A_M}{1-A_M}\right)\left(\frac{R_M}{a}\right)^2(1-A_M)(1-A_{IR})\right] \tag{17}$$

where b_1, B, $\theta_{\rm sun}$, and δ are functions presented in Rubincam (2006). The parameters assumed in our calculations are given in Table 3.

We obtain that the Yarkovsky effect is responsible for the decay of the orbits for the set of parameters

assumed by us. For the largest particle sizes ($s = 10$ m and 100 m), the decay timescale due to the Yarkovsky effect $\tau_Y \sim 10^8$ yr. Such a value is greater than the viscous spreading timescale of the first cycles ($1 - 5$), which, therefore, show the same evolution obtained in Section 3.4. The timescale τ_Y is comparable to the viscous spreading timescale only for the cycle forming Phobos and the previous one. In these cycles, the amount of material that falls on Mars increases, reducing the average optical depth of the ring. The average optical depth reduction is $< 30\%$, and the ring coexisting with Phobos still remains in the forbidden region for all cases with $s = 10$ m and 100 m.

The picture is different for the cases with the smallest particles. $\tau_Y \sim 10^6$ yr and $\tau_Y \sim 10^7$ yr for particles of 0.1 m and 1 m, respectively. It implies that the Yarkovsky effect is relevant already in the third cycle. As the Yarkovsky effect removes material, the disk spreads more slowly, forming less massive satellites. Therefore, the cycles become slower, resulting in a more efficient action of the Yarkovsky effect, giving rise to a ripple effect. In the end, we get that the disk material is completely removed after 3-5 cycles.

In general, the results of our simulations with $s = 0.1$ m and 1 m fall into three different cases:

- In the cases with RRL closer to the planet ($\phi = 40°$ and $80°$) and less massive disk ($\mathrm{M_{disk}} = 0.9 - 2.8 \times 10^4$ $\mathrm{M_P}$), we find that the disk is quickly removed (∼50 Myr), with the last satellite formed being too massive to be considered a Phobos analogue. That is, the disk is completely removed before forming Phobos.

- In the cases with $\phi = 40°$ and $80°$ and more massive disk ($\mathrm{M_{disk}} = 2.8 - 4.6 \times 10^4$ $\mathrm{M_P}$) and in the cases with $\phi = 25°$ and $\mathrm{M_{disk}} = 0.9 - 1.9 \times 10^4$ $\mathrm{M_P}$, the disk is completely removed in $\sim 10^8 - 10^9$ Gyr and a Phobos analogue is obtained without the ring. That is, the disk is completely removed in the cycle that forms Phobos.

- For cases with $\phi = 25°$ and $\mathrm{M_{disk}} = 1.9 - 4.6 \times 10^4$ $\mathrm{M_P}$, the disk is also completely depleted in $\sim 10^8 - 10^9$ Gyr, but the last satellite formed is too small to be considered a Phobos analogue. The disk is completely removed in a cycle after the one that forms Phobos.

Figure 27 shows on the left scale the disk mass (solid line) and the satellite mass (dashed line), for a system with $\mathrm{M_{disk}} = 0.9 \times 10^4$ $\mathrm{M_P}$, $\phi = 25°$, and $s = 0.1$ m. The right scale gives the optical depth of the disk, and the horizontal dotted line places the mass of Phobos. We find that the evolution of the system in the first two cycles is almost the same as in the case without the Yarkovsky effect, which is due to the fact that the cycle timespan is shorter than τ_Y. However, for the third cycle, the timescales of viscous spreading and the Yarkovsky effect timescales are comparable, and we can see a more abrupt drop in the disk mass curve. In this case, we obtain a less massive Phobos ancestor than the one formed in the case without dissipation.

In the fourth cycle, τ_Y exceeds the spreading timescale and the disk is completely removed in ~ 46 Myr. When it occurs, there are 15 satellites with radial mass ranking. In the absence of the disk, satellites only migrate due to tidal effects, with the farthest one (at 3.3 R_M) migrating faster due to its greater mass. It accretes the internal ones. At 90 Myr, the Phobos analogue is formed (at 3.2 R_M) with a mass of M_p, reaching the current Phobos location at ~ 150 Myr. The satellite is destroyed in ~ 178 Myr, giving rise to a disk that is completely removed in a few Myr.

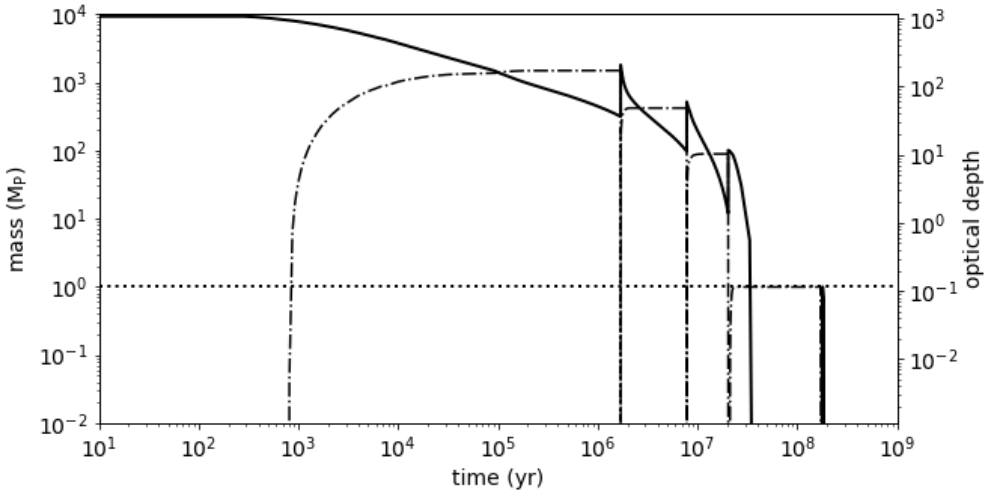

Figure 27 – Evolution of disk and satellite masses as a function of time for a simulation with $M_{disk} = 0.9 \times 10^4$ M_P, $\phi = 25°$, and $s = 0.1$ m, including the Yarkovsky effect. The left scale gives the mass, with the solid line corresponding to the mass of the disk and the dashed line to the mass of the satellites. The horizontal dotted line shows the mass of Phobos. The right scale gives the optical depth of the disk. An animation with the complete evolution of the system can be found at the link: <https://tinyurl.com/phobosanimations>.

In some simulations with Yarkovsky effect, Phobos is formed without a ring, but in these cases the satellite would be very young. For example, in the case of Figure 27, we get a Phobos that is only 60 Myr old. In fact, it is the presence of the disk in the simulations of Section 3.4 that delays satellite migration due to tides, allowing ages in the range constrained by Ramsley e Head (2017). The simulation of Figure 27 also requires the recycling process beginning 150 Myr ago.

As already discussed, we include the Yarkovsky effect assuming the extreme (and unrealistic) case where tumbling due to collisions can be disregarded. In the real case, collisions will generate tumbling of the particle spin, damping the Yarkovsky effect. Depending on the impact configuration, collisions can also result in fragmentation and grinding into smaller dust and the latter must be affected by external forces that do not play a role in the evolution of metric particles. For example, Liang e Hyodo (2023) study the effect of solar radiation and Poynting-Robertson force on the evolution of particles orbiting Mars, finding that particles with $s \lesssim 100$ μm have lifetimes of up to $\sim 10^4$ yr. Therefore, such effects can act over the cycles, removing material resulting from impacts between particles.

It seems general that by removing material from the system, Phobos can be formed without a ring, but in a short timespan, regardless of the external effect included. However, the viscous evolution of the debris disk over the cycles is an intricate problem and we do not rule out the possibility that a set of external forces combine a reasonable formation time for Phobos with the lack of a ring. A more appropriate study of the particulative evolution of the ring with Yarkovsky effects, including particle tumbling, collisional grinding, and other external forces is needed to verify this possibility.

3.5.3 Resonances with Deimos

Models that assume Phobos formation beyond the 2:1 MMR with Deimos (CRADDOCK, 2011; ROSENBLATT et al., 2016; CANUP; SALMON, 2018) obtain that Phobos would have gone through

such a resonance ~ 2 Gyr ago. Due to this, Deimos' eccentricity would be increased to values of ~ 0.002 (YODER, 1982), requiring an intense dissipation in the satellite, in order to dampen the eccentricity to its current value (2.7×10^{-4}) (JACOBSON; LAINEY, 2014). In turn, Hesselbrock e Minton (2017) obtain that only the oldest Phobos ancestor crosses the 2:1 MMR with Deimos (> 4 Gyr ago), which diminishes the value of dissipation factor k_2/Q required for Deimos.

In our simulations, because of the ring that remains in every cycle, Phobos ancestors migrate further comparing to the results of Hesselbrock e Minton (2017). As a consequence, the 2:1 MMR crossing no only happens in the first cycle, but also in the second and third – as can be seen in Figure 19. To analyze the effect of the resonance crossing, we performed some N-body numerical simulations with the Rebound code (REIN; LIU, 2012), using the MERCURIUS hybrid symplectic integrator. We include Mars, Deimos with its current semi-major axis, a Phobos ancestor initially at 4 R$_M$, tidal effect, and an artificial force to mimic the disk-satellite effect (ĆUK et al., 2020). Both satellites are initially in near circular and near equatorial orbits.

Figure 28 shows the case of a system with an artificial force responsible for approximately reproducing the evolution of Phobos ancestor in the first cycle of Figure 19. The top panel (Figure 28a) shows the temporal evolution of the semi-major axis of Phobos ancestor (at 4 R$_M$) and Deimos (at ~ 7 R$_M$), the middle panel (Figure 28b) shows Deimos' eccentricity and the bottom panel (Figure 28c) shows the following characteristic angles: $\phi_1 = 2\lambda_D - \lambda_P - \varpi_P$, $\phi_2 = 2\lambda_D - \lambda_P - \varpi_D$, and $\phi_2 - \phi_1 = \varpi_D - \varpi_P$. λ and ϖ are the mean longitude and the argument of pericenter, respectively, while the subscripts $_P$ and $_D$ refer to Phobos and Deimos, respectively.

Phobos ancestor crosses the 2:1 MMR location (~ 4.4 R$_M$) after ~ 0.03 Myr, capturing Deimos in an apsidal corotation resonance. This resonance occurs when both characteristic angles ϕ_1 and ϕ_2 librate, meaning that the satellite periapses are fixed relative to each other ($\phi_2 - \phi_1$) (FERRAZ-MELLO; TSUCHIDA; KLAFKE, 1993). When the inner migrating satellite is orders of magnitude more massive than the outer one – which is the case of all our simulations – capture will result in an asymmetric apsidal corotation, which means that the argument of pericenter of the satellites will not remain aligned or anti-aligned relative to each other (FERRAZ-MELLO; BEAUGE; MICHTCHENKO, 2003).

While migrating outward, the Phobos ancestor pushes Deimos outward and the eccentricity of both satellites increases (BEAUGÉ, 1994; BEAUGÉ; MICHTCHENKO; FERRAZ-MELLO, 2006), as can be seen in Figure 28. Upon reaching ~ 5 R$_\mathrm{M}$, in ~ 0.07 Myr, Phobos migration ceases and so does the growth of eccentricities, with the eccentricity of Deimos oscillating around 0.245 while Phobos' eccentricity reaches values up to 3×10^{-5}. At this point, Deimos is located at ~ 7.9 R$_M$. Asymmetric corotation is stable only for outward migration and eccentricities start to decrease when Phobos starts to migrate inward after 0.25 Myr. $\phi_2 - \phi_1$ begins to precess, and the resonance is broken when Deimos is again at 7 R$_M$, having eccentricity $\sim 10^{-4}$.

Analog dynamics is verified for the second and third cycle. At the end of the latter, Deimos is approximately restored to its initial position, while its eccentricity has been increased to $\sim 10^{-3}$. We find that for $k_2/Q = 1.2 \times 10^{-4}$, Deimos' eccentricity reaches a value compatible with the observed one. Such a value of k_2/Q corresponds to that estimated by Bagheri et al. (2021) for a loosely connected aggregate Deimos.

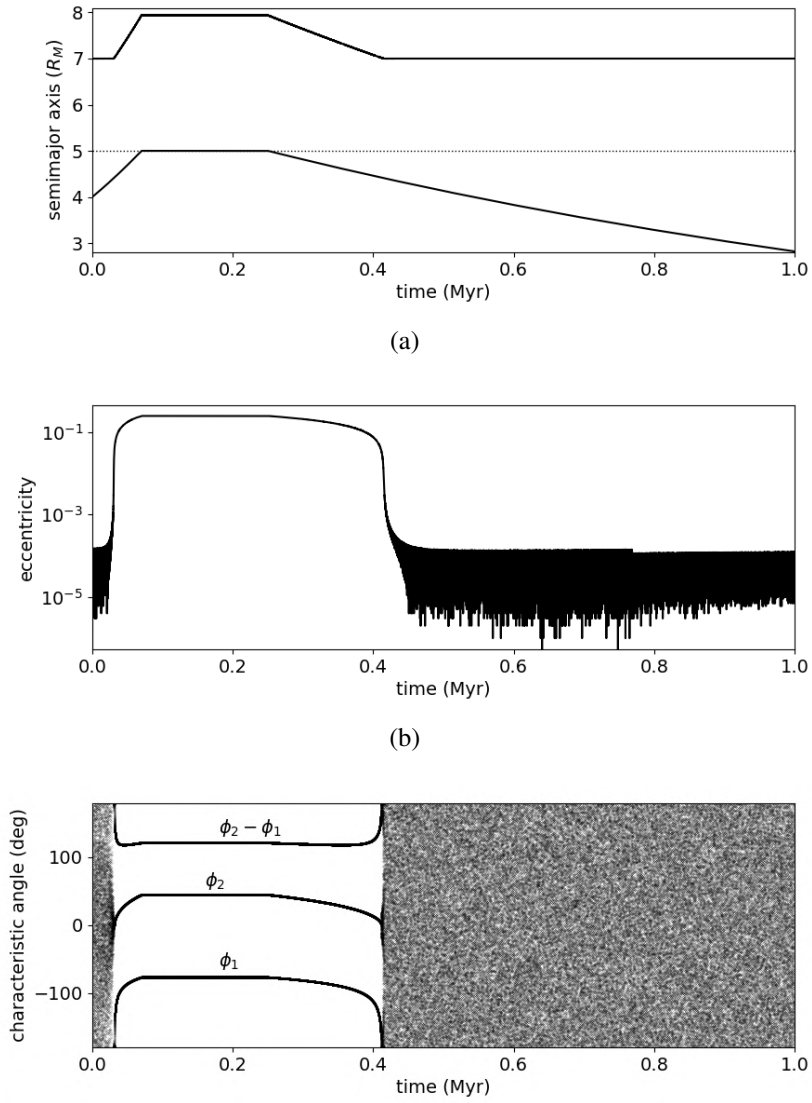

Figure 28 – Temporal evolution of a) semimajor axis of the Phobos ancestor and Deimos, b) eccentricity of Deimos, and c) characteristic angles associated with the 2:1 MMR (see text). Phobos ancestor is initially at 4 R_M and Deimos is at $\sim$ 7 R_M. The N-body simulation approximately reproduces part of the cycle 1 shown in Figure 19.

Similar results were obtained in all simulations, leading us to conclude that the recycling model is compatible with the hypothesis that Deimos is a direct fragment of the impact. Rosenblatt et al. (2016) assume that the impact gave rise to a population of embryos beyond the fluid Roche limit and that a massive innermost satellite migrating outward captured the embryos at 2:1 MMR, forming Deimos. We emphasize that in the recycling model, this may also be a possibility, with a Phobos ancestor acting as the innermost satellite proposed by Rosenblatt et al. (2016).

3.5.4 Limitation of the code

The HYDRORINGS code is extensively described in Salmon et al. (2010) and in Charnoz et al. (2011) and seems very similar to the code used in Hesselbrock e Minton (2017). The ring is described using an hydrodynamical approach (SALMON et al., 2010), adapted to compute long term evolution,

on timescales comparable to viscous spreading timescales. Particles in rings are assumed to have a single size in order to make the calculation tractable, and also because a hydrodynamic formalism with multiple sizes still does not exist (in a closed-form). The main limitations concern the orbital evolution of satellites. Satellites' semi-major axes evolve under the combined influence of planet's tides, and disk's torque (summed over all first order mean motion resonances implanted in the rings). Satellites mutual interactions are not considered. Including theses interactions would imply to integrate their motion over billions of years, representing 10 to 100 billions of orbits, which is beyond current computer capacities (if the disk must be tracked simultaneously). These limitations will be addressed in the future, but still, would imply significant theoretical and numerical developments. Therefore, the results presented in this paper should be considered as a first order study, like any previous study of this kind. To ensure the statistical validity of our results, we ran a large number of simulations and on different computers. Our tests show that the results are not affected by the resolution adopted in the simulation, demonstrating the robustness of the numerical results.

3.6 CONCLUSION

In this work, we have analyzed the material recycling model for the formation of Phobos, initially proposed by Hesselbrock e Minton (2017). We focused our study on the evolution of the debris disk and we have assumed that the parent moons of Phobos are rubble piles. Due to tidal forces, rubble-pile satellites are ground down to their constitutive particles or quickly tidally downsized. We have explored the effect of particle size and friction angle onto the evolution of the debris rings and satellite evolution, as well as the disk initial mass. As described in Hesselbrock e Minton (2017), Hesselbrock e Minton (2019) we do find that an ancient moon, heavier than Phobos, would experience multi-cycle recycling process when it crosses the Roche Limit. At each cycle, a new ring and a new satellite population is formed at the Roche limit. At every cycle the ring and moon mass diminishes consistently with Hesselbrock e Minton (2017).

Our main result is that the disk that is produced after the tidal destruction of the parent bodies of Phobos, never fully converts into satellites nor falls onto Mars. In every cycle, a remaining Roche-interior ring orbits around the planet, co-existing with one or several moonlets just exterior to the Fluid Roche Limit. By comparing our simulations to observational surveys of dust or ring around Mars (DUXBURY; OCAMPO, 1988; SHOWALTER; HAMILTON; NICHOLSON, 2006), we show that the debris ring resulting from the recycling process should have been already detected, if the recycling process did really happen. Indeed, when Phobos is formed, the resulting ring is either too bright or either its constituent particles are too big to be reconciled with observations. Whereas we varied many parameters of the simulation (particle size, angle of friction, initial mass), we never find a case where the final ring could be reconciled with observations.

This raises the question: why do we not see a ring around Mars today? One could argue that the Roche-interior debris ring could have been removed after the formation of Phobos. However, in the recycling model, Phobos is formed between 3.0 and 3.5 Mars radii, leading to tidal infall time < 0.5 Gyr, and no known process seems able to remove macroscopic particles (cm to m) on such a timescale. The only solution we found is to consider the Yarkovsky effect acting on macroscopic

particles. However, it would be only effective if the rotation state of particles does not change on Gyr timescales, which doesn't seem possible in a collisional system. Also, it would require the recycling process beginning a few Gyr after the formation of Mars, while there are no evidence of a giant impact in the recent history of Mars.

Therefore, we conclude that Phobos is unlikely to be the result of a recycling process. The impacts that gave rise to the basins seen on Mars surface certainly produced a Roche-interior disk of material in the few hundred thousand years after Mars formation (ANDREWS-HANNA; ZUBER; BANERDT, 2008; MARINOVA; AHARONSON; ASPHAUG, 2008). This disk may be responsible for the formation of satellites including Phobos, but Phobos is unlikely to have experienced recycling as in Hesselbrock e Minton (2017). Phobos would be older than predicted by the recycling model, perhaps in the range obtained by Schmedemann et al. (2014). Also, it would have formed far beyond the Fluid Roche Limit ($\sim 3.2\ \mathrm{R_M}$).

If the satellites formed from the Roche-interior disk were rubble-pile objects, the recycling mechanism would be expected to have happened, with the disk diminishing in mass at each cycle until its (almost) disappearance. Note that it is consistent with our results when we do not constrain an object with a mass similar to Phobos to be the real Phobos. Now, if the formed satellites were very cohesive, they would push the disk towards Mars and then fall entirely onto the planet (ROSENBLATT et al., 2016). So the recycling mechanism would not happen at all. Such a scenario is very similar to the stirred disk model and could be an explanation for the elongated craters seen on Mars.

Martian Moons eXploration (MMX), developed by the Japan Aerospace Exploration Agency (JAXA), is expected to be launched in 2024. The MMX mission plans to collect samples of > 10 g from the surface of Phobos and return them to Earth in 2029 with the aims of elucidating the origin of Martian moons (FUJIMOTO; TASKER, 2019), collecting geochemical information about the evolution of Martian surface environment (HYODO et al., 2019), and searching for traces of Martian life (HYODO; USUI, 2021). The MMX data will be decisive in constraining the physical properties of Phobos, allowing the distinction between the stirred disk and the recycling models.

4 NUMERICAL ANALYSIS OF PROCESSES FOR THE FORMATION OF MOONLETS CONFINING THE ARCS OF NEPTUNE

The arcs of Neptune – Fraternité, Egalité, Liberté, and Courage – are four incomplete rings immersed in the Adams ring. A recent confinement model for the arcs proposes that the structures are azimuthally confined by 1+3 co-orbital moonlets and radially confined by the satellite Galatea. The model proposes specific masses and locations for the satellites, being explored here if different configurations of moonlets in mass and number are able to confine and reproduce the location of the arcs. Furthermore, we propose a formation scenario for the family of moonlets and arcs. According to our proposal, the system may have formed from the disruption of an ancient body at a Lagrangian point of a moon.

The content of this chapter was published as: Gustavo Madeira, and Silvia M. Giuliatti Winter. "Numerical analysis of processes for the formation of moonlets confining the arcs of Neptune."Monthly Notices of the Royal Astronomical Society 513.1 (2022): 297-309 (MADEIRA; GIULIATTI-WINTER, 2022).

4.1 INTRODUCTION

In 1984, during a stellar occultation, an incomplete ring was detected around the planet Neptune (HUBBARD et al., 1986). Confirmed by ground-based observations (SICARDY; ROQUES; BRAHIC, 1991) and *Voyager* spacecraft images (SMITH et al., 1989), the four arcs of Neptune, known as Fraternité, Egalité, Liberté, and Courage, are indeed the densest parts of a complete ring, the Adams ring. They have individual angular widths ranging from 2 deg (Courage) to 9 deg (Fraternité) and radial width of 15 km (PORCO et al., 1995). Since differential Keplerian motion would completely spread the arcs in about three years (PATER et al., 2018), several confinement models were proposed over time to explain these structures' dimensions and stability.

The first known confinement model is present in Brown (1911), in which the author shows that Jupiter confines trojan asteroids in tadpole orbits around its triangular points (L_4 and L_5) in the Sun-Jupiter-trojans system. Based on this work, Lissauer (1985) proposed that a sizeable hypothetical satellite would azimuthally confine the Neptune arcs in its triangular points. At the same time, another hypothetical internal satellite would be responsible for the radial confinement of the arcs. Sicardy e Lissauer (1992) improved such model by proposing that a pair of co-orbital satellites azimuthally confine the structures, which allows the possible existence of smaller satellites. However, such models were ruled out since *Voyager* spacecraft did not observe satellites with the dimensions required by them.

A confinement model envisioned by Goldreich, Tremaine e Borderies (1986) and confirmed by the discovery of the satellite Galatea (SMITH et al., 1989) proposes that a single internal satellite would be responsible for the azimuthal and radial confinements of the arcs. Porco (1991) shows that the arcs are close to the 84:86 corotation inclined resonance (CIR, azimuthal confinement) and the 42:43 Lindblad resonance (LER, radial confinement) with Galatea. The author proposes that the arcs are trapped

in some of the 84 sites formed by the CIR, which could explain their radial and azimuthal widths (FORYTA; SICARDY, 1996). Similarly, the coupling between Lindblad and corotation resonances with Mimas is the mechanism that holds (at least, temporarily) the Aegaeon, Anthe, and Methone arcs of Saturn (HEDMAN et al., 2009; HEDMAN et al., 2010; MOUTAMID; SICARDY; RENNER, 2014; SUN et al., 2017; MADEIRA et al., 2018; MADEIRA; GIULIATTI-WINTER, 2020).

New evidence from ground-based observations shows that the semi-major axis of the arcs is displaced from the 84:86 CIR location (SICARDY et al., 1999; DUMAS et al., 2002), which leaves the arcs without azimuthal confinement. The arcs have changed location and decayed in intensity since their discovery (PATER et al., 2005; SHOWALTER et al., 2013; RENNER et al., 2014). In fact, data discussed in Pater et al. (2018) indicate the disappearance of the arcs Liberté and Courage.

Renner et al. (2014) rescue the confinement model based on co-orbital satellites, proposing that Galatea radially confines the arcs while several co-orbital moonlets (at least four) with diameters below the precision of *Voyager* spacecraft confine them azimuthally. The system was assumed to consist of four co-orbital moonlets and Galatea. A set of azimuthal locations and mass ratios is obtained for the co-orbital satellites to reproduce the arc widths. Next, a representative case is explored by the authors where the masses of the moonlets S_1, S_2, S_3 and S_4, are assumed to be 60.0, 0.54, 1.17 and 0.66×10^{13} kg, respectively. S_2, S_3 and S_4 are azimuthally located at longitudes $\theta = 48.31$ deg, 59.38 deg and 72.19 deg, respectively, with respect to S_1 ($\theta = \lambda - \lambda_{S_1}$, where λ is the mean longitude). All the system is in the 42:43 LER with Galatea.

Giuliatti-Winter, Madeira e Sfair (2020) explore the model proposed in Renner et al. (2014), including the effects of the solar radiation force and also accounting for the mass production rate of the moonlets. They found that micrometre particles are removed from the arcs due to solar radiation in less than 50 years. Part of these particles become transient between the arcs, being a possible explanation for the arcs' changes in longitude and intensity. In this work, we intend to approach some points related to the dynamics of these co-orbital satellites and propose a model for their formation.

The 1:1 resonance dynamics have been known for over a century in the planar restrict 3-body problem. It has been used to explain the dynamics of the trojan asteroids (BROWN, 1911), Helene and Polydeuces (LECACHEUX et al., 1980), – confined in the L_4 and L_5 points of Dione, respectively – and Telesto and Calypso (SMITH et al., 1980; PASCU; HARRINGTON; SEIDELMANN, 1980; OBERTI; VIENNE, 2003) – confined in the L_4 and L_5 points of Tethys, respectively. Another example is the Janus and Epimetheus system, in which both satellites have comparable masses and perform horseshoe fashion orbits in the rotating frame, as shown by Dermott e Murray (1981) and Yoder et al. (1983).

The study of systems with more than two co-orbital satellites became feasible with computational advances. Salo e Yoder (1988) carried out complete analytical and numerical studies of N co-orbital satellites with the same mass ($N \leq 9$) in circular orbits, identifying stable equilibrium configurations. Similar work was carried out by Renner e Sicardy (2004), where the authors solved analytically the case N=3 and proposed a numerical method to find the possible linearly stable solutions for any given set of masses and number of co-orbital satellites. More recently, A'Hearn, Hedman e Hamilton (2021) analysed the confinement of four D68 clumps by co-orbital satellites, obtaining a set of five moonlets

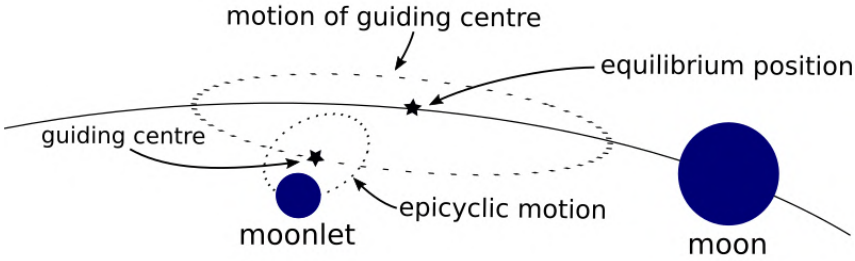

Figure 29 – Scheme of the trajectory in the rotating frame of a moonlet co-orbital to a larger moon. Based on figure 3.14 of Murray e Dermott (1999).

capable of confining them. However, the authors rule out this scenario as a likely explanation for the clumps, given the highly fragile stability shown by the co-orbital configuration.

Here, we based our analysis on the work of Renner e Sicardy (2004) to obtain the equilibrium configurations of 1+N co-orbital satellites. We evaluate the effects of Galatea in the co-orbital system and also propose different scenarios for the formation of the arcs. Treffenstädt, Mourão e Winter (2015) showed that the collisions of large fragments produced in the disruption of an ancient satellite might form Janus and Epimetheus. Following this work, we suggest the formation of co-orbital satellites through the disruption of an ancient body located at a triangular point of a satellite.

4.2 1+N CO-ORBITAL SATELLITE DYNAMICS

In this section, we revisit the work of Renner e Sicardy (2004) and investigate the dynamics of a system with a gravitationally dominant satellite sharing its orbit with N smaller satellites and a set of particles. We will assume the dominant satellite as the satellite S_1 proposed in Renner et al. (2014) in an eccentric orbit ($e = 3 \times 10^{-4}$, Table 4). All results will be given in the rotating frame with S_1.

For clarity, we will refer to the largest co-orbital as "moon" and the N smaller ones as "moonlets", keeping the "satellite" nomenclature for Galatea. Moonlets and particles differ from each other by the fact that the moonlets interact gravitationally with each other. In contrast, the particles feel the gravitational effect of the massive bodies but do not interact with each other. Consequently, each of these classes will have different stable equilibrium positions. Firstly, we analyse the equilibrium positions of the moonlets.

4.2.1 Moonlet stable equilibrium positions

Assuming a system composed only by the planet and the 1+N co-orbital satellites, we obtain tadpole-like trajectories for the N moonlets in the rotating frame. Such trajectories are composed of two distinct motions: an epicyclic motion and the guiding centre (or epicycle centre) motion (DERMOTT, 1984). Figure 29 shows a scheme with the trajectory of a moonlet in the rotating frame. The equilibrium positions are locations of maximum potential energy and depend on the mass distribution in the system. When all moonlets are precisely in the equilibrium positions, they remain stationary in relation to each other, and we say that the system is in an equilibrium configuration.

We obtain the equilibrium configurations of 1+N co-orbital satellites by performing numerical simulations with the `MERCURY` package, with the Bulirsch–Stoer algorithm (CHAMBERS, 1999). We

Table 4 – Orbital elements and masses of Galatea and the hypothetical moon S_1 (GIULIATTI-WINTER; MADEIRA; SFAIR, 2020).

	a (km)	e (10^{-4})	I (deg)	ϖ (deg)	Ω (deg)	λ (deg)	m (kg)
Galatea	61953.0	2.2	0.0231	225.81	196.94	351.114	1.94×10^{18}
S_1	62932.7	3.0	0.0	50.82	0.0	211.88	6.00×10^{14}

include Neptune with its gravitational coefficients (J_2 and J_4, the planet parameters were taken from Owen, Vaughan e Synnott (1991)), the moon S_1 and N moonlets. The initial orbital elements of S_1 and Galatea (later added to the system) are the same as those used in Giuliatti-Winter, Madeira e Sfair (2020), given in Table 4. Such values were obtained by GIULIATTI-WINTER; MADEIRA; SFAIR to reproduce the observational data (PORCO, 1991) and the results of Renner et al. (2014).

We have assumed moonlets with masses $m = 10^{-2} m_{S_1}$, where m_{S_1} is the mass of S_1, in the same orbit as the moon, but with different and randomly selected mean longitudes. We have also included a non-conservative term in the velocities to vary the system energy and carry the moonlets to the linearly stable equilibrium points (RENNER; SICARDY, 2004). The term, provided in Renner e Sicardy (2004) for circular orbits, is given by:

$$\dot{r} = -\nu(r - r_0) \tag{1}$$

where r is the orbital radius of the body, $\dot{r}$ its temporal derivative, r_0 is the average orbital radius and ν is a constant that defines the timespan for the system to reach an equilibrium configuration.

To demonstrate the effect of this non-conservative term, we present in Figure 30 the angular evolution of three moonlets initially at $\theta = 50$, 70, and 90 deg, for $\nu = 0$ and 10^{-6} yr^{-1}. The moonlets are initially close to the equilibrium positions at $\theta = 51.5$, 61.3, and 71.9 deg (vertical dotted lines). As we can see, without the non-conservative term (Figure 30a), the moonlets remain in a significant angular motion around the equilibrium positions of the system. Meanwhile, when we include the non-conservative term (Figure 30b), the amplitude of motion of the guiding centre decreases with time, and the moonlets spiral toward the equilibrium positions (RENNER; SICARDY, 2004). The system reaches the equilibrium configuration in approximately 3000 years. The rate at which the amplitude of motion decreases depends linearly on the value of ν. For example, for $\nu = 10^{-5}$ and 10^{-4} yr^{-1}, the system reaches the equilibrium configuration in 300, and 30 years, respectively.

The equilibrium configurations of the 1+N co-orbital satellite system for N=1, 2, 3, and 4 are presented in Figure 31, Figure 32, Figure 33, and Figure 34, respectively. Each system with N odd has $(N+1)/2$ equilibrium configurations asymmetric with respect to S_1, while systems with N even have $(N+2)/2$ equilibrium configurations, being one of them symmetric (RENNER; SICARDY, 2004). The large blue dot at θ=0 deg is the moon, and the smaller ones are the moonlets. The red crosses are the equilibrium positions of particles, obtained in Section 4.2.2, and the red lines are the trajectories of representative particles. The y-axis gives the radial variation of the trajectories. In the figures' upper right corner, we have the amplitude Δr of the trajectory with the largest radial variation (y-axis scale). For visual purposes, the moon/moonlets are not in scale. Just to be clear, the particle trajectory never crosses the satellite.

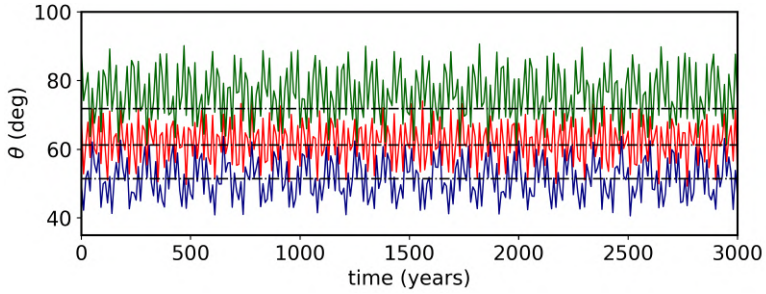

(a) $\nu = 0$

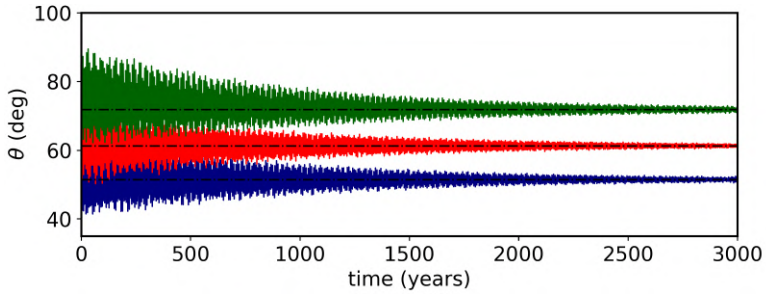

(b) $\nu = 10^{-6}$ yr^{-1}

Figure 30 – Azimuthal angle ($\theta = \lambda - \lambda_{S_1}$) of S_1 and three test moonlets initially at θ=50 deg (solid blue line), 70 deg (solid red line) and 90 deg (solid green line) for a) $\nu = 0$ and b) $\nu = 10^{-6}$ yr^{-1}. The dotted lines correspond to the equilibrium position associated with each moonlet.

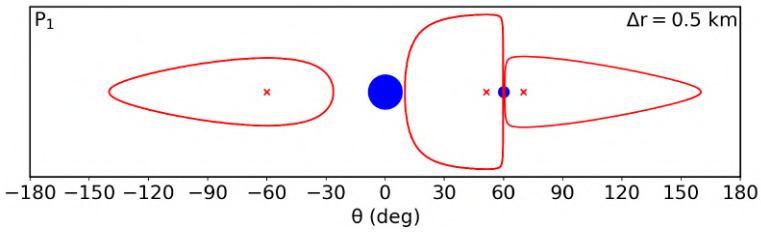

Figure 31 – Equilibrium positions of moonlets (small blue dots) and equilibrium positions of massless particles (red crosses) in a 1+1 co-orbital satellite system. The x-axis gives the longitude θ in relation to the moon (largest blue dot), and the y-axis shows the radial variation with scale Δr given in the upper right corner of the figure. The red lines show the trajectory of some representative particles.

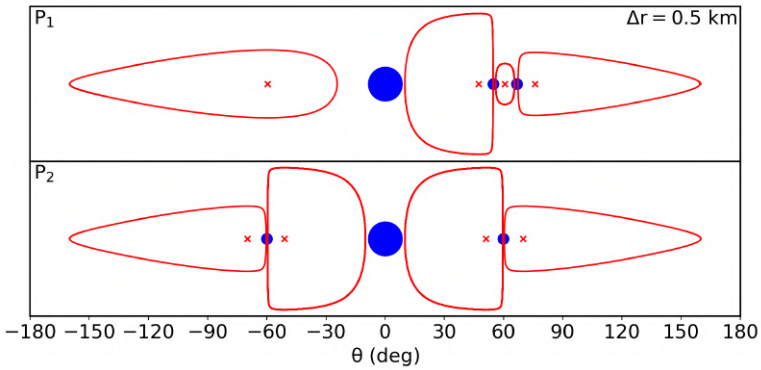

Figure 32 – Same as Figure 31 for 1+2 co-orbital satellite system.

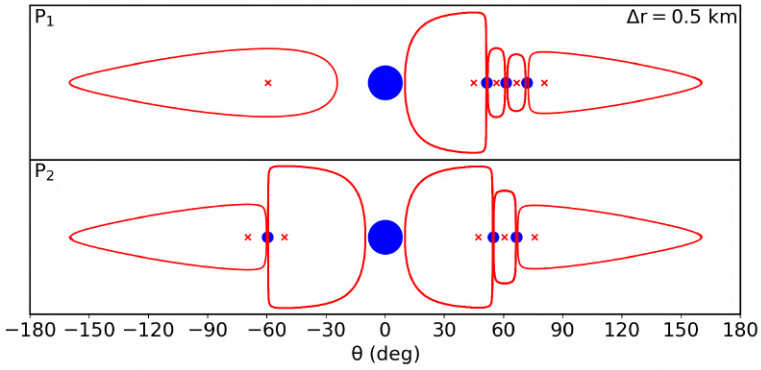

Figure 33 – Same as Figure 31 for 1+3 co-orbital satellite system.

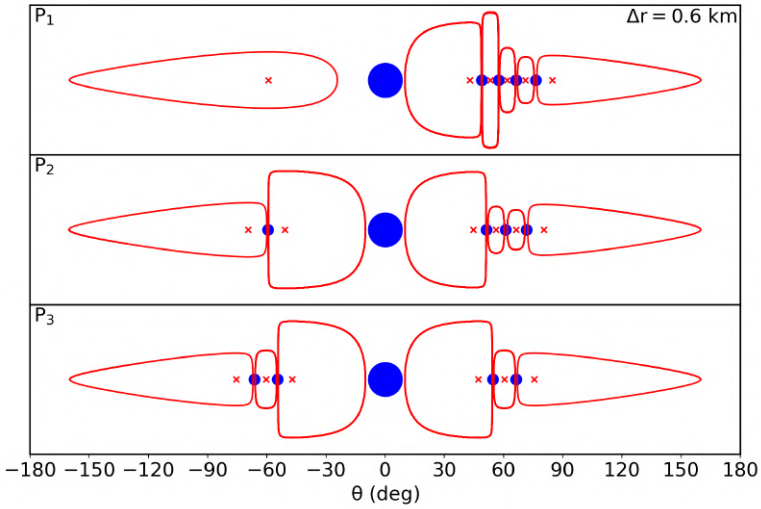

Figure 34 – Same as Figure 31 for 1+4 co-orbital satellite system.

The nomenclatures "$\mathrm{P_i}$" on each line correspond to the label we'll use to refer to each equilibrium configuration from now on. We start in the configurations with all moonlets grouped near the Lagrangian point L_4 and ends in the configurations with moonlets on either side of S_1, near L_4 and L_5. We point out that the mirror version of every asymmetric configuration is an equally possible solution. An example is L_5, corresponding to the mirrored version of L_4.

We obtain that the small eccentricity of the system does not significantly alter the equilibrium positions of the system in comparison to the circular case. The positions found by us are the same as those obtained by (RENNER; SICARDY, 2004). If we assume larger eccentricities ($e \sim 10^{-3}$), however, the locations of the equilibrium positions will change.

4.2.2 Particle stable equilibrium positions

We obtain the particle equilibrium positions in a 1+N co-orbital satellite system using a practical method, seeking the azimuthal location with maximum radial variation of particles, in a simulation with a set of randomly distributed co-orbital particles without the non-conservative term. The particle equilibrium positions are the maximum of the potential exerted by the co-orbital satellites, and for a 1+N co-orbital satellite system, there will be 2+N particle equilibrium positions. As a rule, the particles are confined at one of the moon's triangular points or azimuthally trapped between a pair of

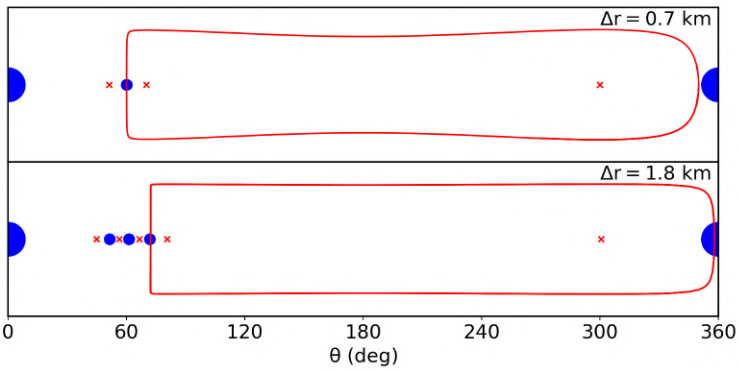

Figure 35 – Trajectory of a particle in horseshoe fashion orbit for a 1+1 (top panel) and 1+3 (bottom panel) co-orbital satellite system, both in P_1 configuration. The blue dots provide the location of moon/moonlets, and the red crosses are the particle equilibrium positions.

moonlets.

In Figure 31-Figure 34, the red crosses give the particle equilibrium positions, while the red lines are trajectories of some representative particles. All trajectories involve only one red cross and therefore correspond to tadpole-fashion orbits. This type of orbit is thought to be associated with the Neptune arcs, in the model of Renner et al. (2014). There are also orbits involving more than one particle equilibrium position, as shown in Figure 35 for a 1+1 and 1+3 co-orbital satellites, from top to bottom. They correspond to horseshoe-fashion orbits and are beyond the scope of this work. In the next section, we give a step further by including the internal satellite Galatea into the system.

4.3 EFFECTS OF GALATEA ON 1+N CO-ORBITAL SATELLITE SYSTEMS

Once we studied the equilibrium configurations in the co-orbital satellite system, we redid the simulations of Section 4.2 including the gravitational effects of Galatea with initial orbital elements given in Table 4. In this case, S_1 is involved in 42:43 LER with Galatea and displaced less than 1 km from 84:86 CIR (RENNER et al., 2014; GIULIATTI-WINTER; MADEIRA; SFAIR, 2020). The resonant angles associated with these resonances are shown in Figure 36. We used the algorithm presented in Renner e Sicardy (2006) to transform the state vector into geometric orbital elements.

When Galatea is included in the system, we see a slight shift in the moonlet's equilibrium locations. Figure 37 shows the longitudinal evolution of the moonlets in P_1 configuration with 1+3 co-orbital satellites, for cases with and without Galatea (in red and blue, respectively). The grey bands ("LER bands") correspond to the regions where the ϕ_{LER} of a particle librates. As can be seen, the equilibrium location of the orbits shifts to the nearest LER band and the moonlets remain in a libration motion around the equilibrium. In this way, the moonlets remain confined azimuthally and radially around these "new equilibrium positions".

Figure 38 gives the moonlet equilibrium positions (black dots) for the 1+3 co-orbital satellite system, under Galatea effects. The equilibrium positions for the case without the satellite are the unfilled blue dots. If we assume different conditions for the moon/Galatea, the initial condition in the resonance phase space will change, leading to slightly different effects on moonlets motion (FORYTA; SICARDY, 1996). As a consequence, the angular positions of the moonlets will differ by a few

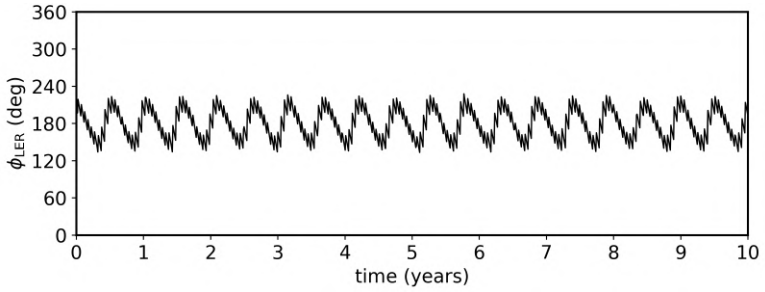

(a)

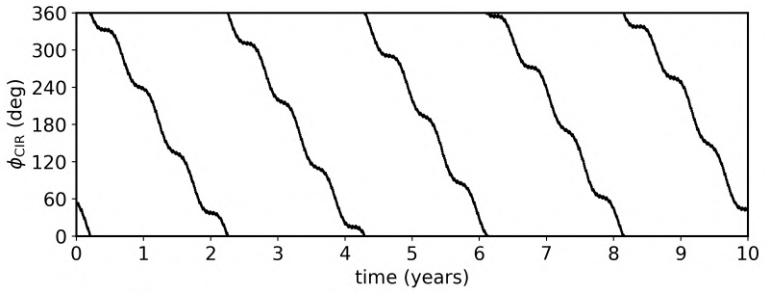

(b)

Figure 36 – Resonant angles a) of 42:43 LER ($\phi_{\rm LER}$) and b) 84:86 CIR ($\phi_{\rm CIR}$) between S_1 and Galatea. The angles are given by $\phi_{\rm LER} = 43\lambda - 42\lambda_{\rm G} - \varpi$ and $\phi_{\rm CIR} = 86\lambda - 84\lambda_{\rm G} - 2\Omega_{\rm G}$, where λ, ϖ, and Ω are mean longitude, longitude of pericentre, and argument of longitude node, respectively. The subscript $_{\rm G}$ refers to the satellite Galatea.

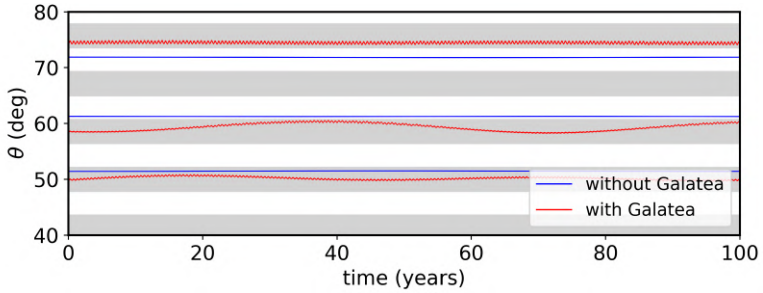

Figure 37 – Blue lines are the location of the equilibrium points for $\rm P_1$ configuration with 1+3 co-orbital satellites without Galatea's effects. Regions where one body remains in 42:43 LER with Galatea are shown as grey bands. The azimuthal evolution of the moonlets under the effects of Galatea is shown by the red lines.

degrees. The displacement of the equilibrium locations due to LER were also verified by Foryta e Sicardy (1996) and Moutamid, Sicardy e Renner (2014) in systems where the overlap of corotation and Lindblad resonances comes from the same satellite. In our work, a similar phenomenon occurs, with the difference that corotation and Lindblad resonances originate from different bodies.

Galatea also disturbs the orbital evolution of the particles, which oscillate around the equilibrium positions with larger radial variations. Figure 39 shows the radial variation (Figure 39a), semi-major axis (Figure 39b), and eccentricity (Figure 39c) of a representative particle in $\rm P_1$ configuration with 1+1 co-orbital satellites, for 100 years. The timespan of the zoom box in the top panel is of 50 days. Cases with and without Galatea are in black and red lines, respectively.

In Figure 39a, the black dot places the moonlet equilibrium position in the system with Galatea, and the unfilled blue dot places the position in the system without the satellite. As can be seen in the

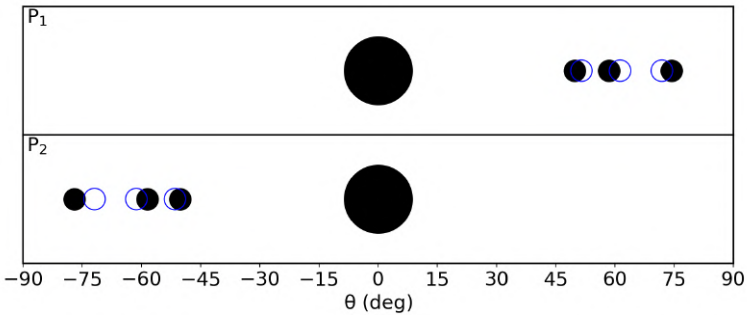

Figure 38 – Moonlet equilibrium positions in a 1+3 co-orbital satellite system. The black dots give the positions of the moonlets when we include Galatea. Unfilled blue dots correspond to the case without the satellite.

zoom, the particle shows an additional oscillation with Galatea in the system, which translates into larger radial and azimuthal variations in the particle motion. The satellite is also responsible for the larger variations in the semi-major axis and eccentricity of the particle. The peaks seen in the temporal evolution of the semimajor axis are due to closest approach between the particle and the co-orbital satellite.

To exemplify equilibrium configurations when Galatea is presented in the system, we show in the Figure 40, from top to bottom, the P_1 configuration with 1+3 co-orbital satellites and the P_1 and P_2 configurations with 1+4 co-orbital satellites. These cases are especially interesting because they can reproduce the angular distribution of the arcs Fraternité, Egalité, Liberté, and Courage. In the figure, the particles (in red) are azimuthally confined by the moonlets (in black). Solid lines correspond to the case with Galatea, and the dotted lines to the case without the satellite. In the next section, we simulate a set of fragments supposedly formed in the disruption of an old moon, analysing whether they can give rise to a system of 1+N co-orbital satellites.

4.4 TEMPORAL EVOLUTION OF FRAGMENTS FROM A MOON DISRUPTION

4.4.1 Impact between an ongoing object and a trojan moon

In light of the Janus/Epimetheus formation model proposed in Treffenstädt, Mourão e Winter (2015), we envision the following scenario for the formation of a 1+N co-orbital satellite system (Figure 41): Initially, we assume an ancient system composed of the moon S_1 ($R_{\mathrm{S}_1} = 5.2$ km) and an object located at one of its triangular points (trojan, Figure 41a). After an impact with an ongoing object, the trojan disrupts, forming fragments and debris (Figure 41b). The disruption outcomes perform horseshoe orbits with S_1 and collide with each other (Figure 41c), giving rise to moonlets. Finally, the moonlets settle into equilibrium positions of the system, confining the arc material (Figure 41d).

Keeping in mind the system proposed by Renner et al. (2014), we define the minimum trojan mass as $m_{\mathrm{tro}} = 4 \times 10^{-2} m_{S_1}$, corresponding to an object made of ice with physical radius of $R_{\mathrm{tro}} = 1.8$ km. m_{tro} is approximately the sum of the masses of the moonlets S_2, S_3 and S_4 proposed by Renner et al. (2014). For a fiducial impact of $3000\ \mathrm{m/s}$, the minimum incident kinetic energy per mass Q_* required

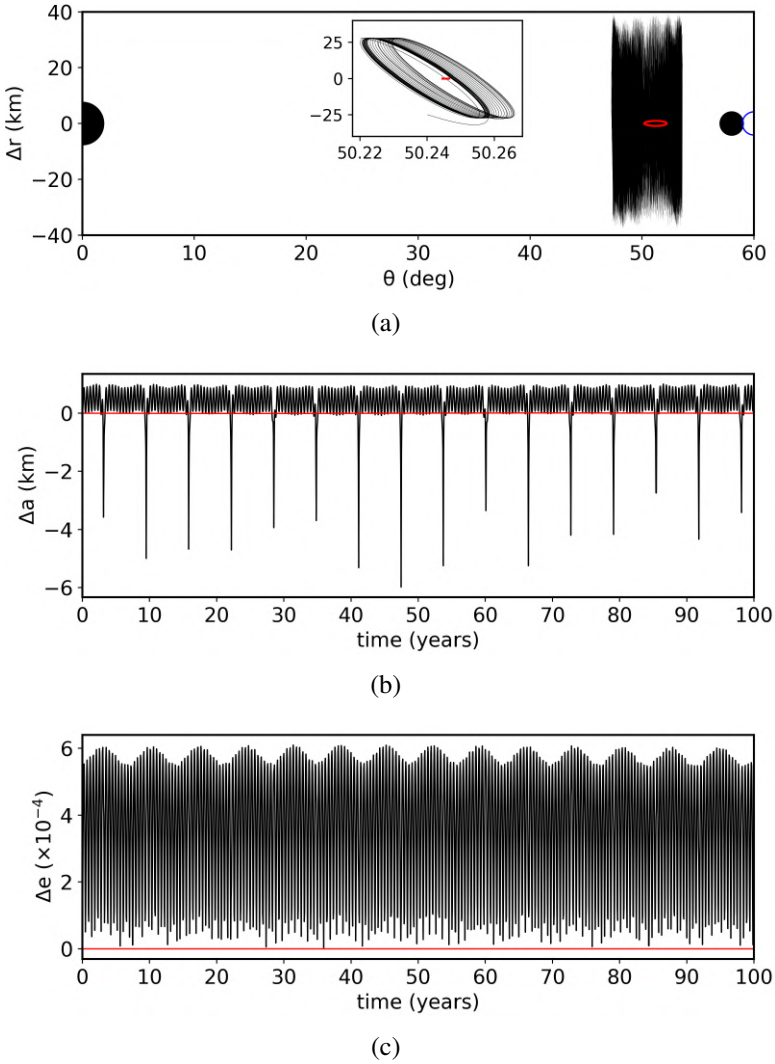

Figure 39 – a) Azimuthal and radial variation, b) semi-major axis, and c) eccentricity of a representative particle in a P_1 configuration with 1+1 co-orbital satellites. Solid black line provides the particle in the system under the effects of Galatea, and the red line is the case without the satellite. The simulation timespan is 100 years, with the first 50 days shown in the zoom. In the top panel, the moonlet confining the particle is in black and blue for the case with and without Galatea, respectively.

to disrupt the trojan is (BENZ; ASPHAUG, 1999)

$$Q_* = 2.7 \times 10^{-12} \left(\frac{R_{\rm tro}}{1\ {\rm m}}\right)^{-0.39} + 4 \times 10^{-2} \left(\frac{R_{\rm tro}}{1\ {\rm m}}\right)^{1.26} {\rm J/kg}. \quad (2)$$

The radius $R_{\rm imp}$ required for an ice impactor to disrupt the trojan can be estimated as (STEWART; LEINHARDT, 2012; MELITA et al., 2017)

$$R_{\rm imp} = \left(\frac{3}{2\pi(10^3\ {\rm kg/m^3})} \frac{Q m_{\rm tro}}{(3000\ {\rm m/s} + v_{\rm esc})^2}\right)^{1/3} \quad (3)$$

where $v_{\rm esc}$ is the escape velocity of the trojan and Q is the reduced kinetic energy of the system. For a disruption, $Q \geq Q_*$.

Benz e Asphaug (1999) shows that the mass of the largest remnant $m_{\rm lr}$ produced by the disruption

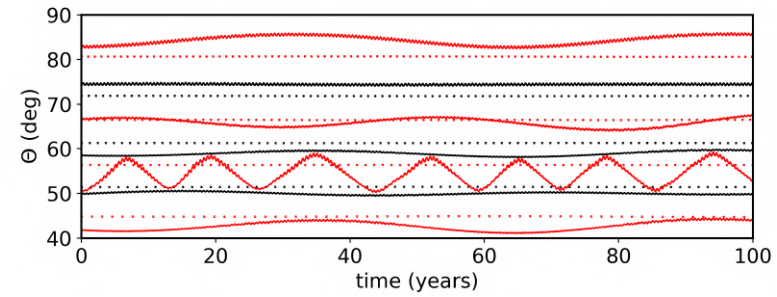

(a)

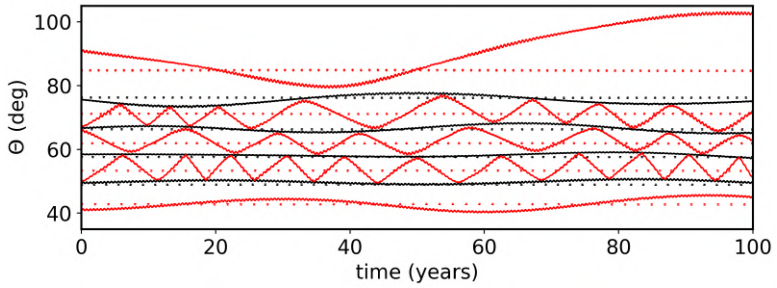

(b)

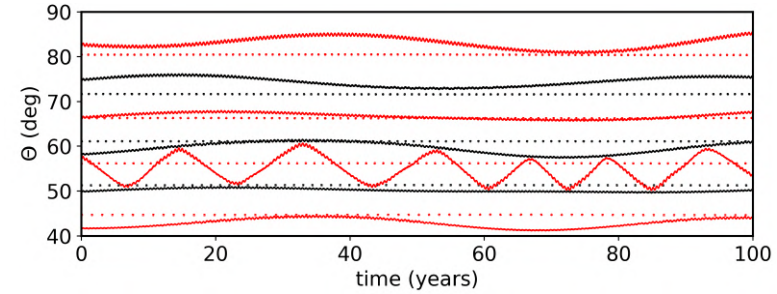

(c)

Figure 40 – Temporal variation of the azimuthal angle of moonlets (black lines) and particles (red lines) for a) P_1 configuration with 1+3 co-orbital satellites, b) P_1 configuration with 1+4 co-orbital satellites, and c) P_2 configuration with 1+4 co-orbital satellites. The full lines correspond to the case with Galatea, and the dotted lines are the trajectories for the case without the satellite.

of the trojan can be estimated as

$$m_{\rm lr} = 0.5 - 0.6\left(\frac{Q}{Q_*} - 1\right) m_{\rm tro}. \tag{4}$$

From these relations we find, for example, that a kinetic energy $Q/Q_* = 1.4$ and an impactor of $R_{\rm imp} \approx 100$ m are needed for the trojan to be destroyed, and its largest remnant has the mass $m_{\rm lr} = m_{\rm tro}/4$.

Neptune's sphere of influence is regularly crossed by comets from the Kuiper belt. It was proposed by Colwell e Esposito (1992) that such objects were responsible for catastrophic disruptions of original moons. These events would be the sources of ancient rings around the planet. Levison et al. (2000) calculated the comet impact rate in the Neptune region as $3.5 \times 10^{-4}{\rm yr}^{-1}$. Taking into account the gravitational focusing (LEVISON; DUNCAN, 1997; STERN; MCKINNON, 2000), we obtain that a comet reaches the Adams ring region every $\sim 10^5$ yrs. Since these comets have typical sizes (LEVISON et al., 2000) larger than $R_{\rm imp}$, it seems that a trojan disruption, caused by impacts with

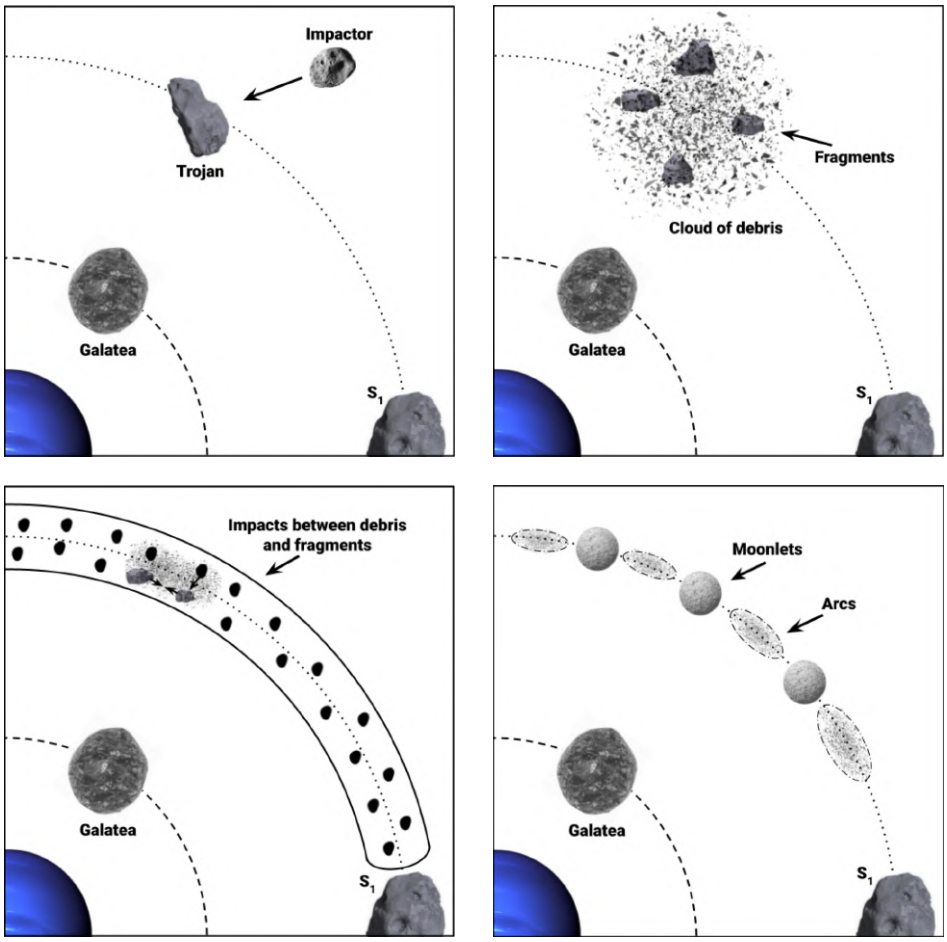

Figure 41 – Steps from the formation of co-orbital moonlets: a) After a collisional event, b) an ancient body located at the Lagrangian point of S_1 disrupts into fragments and debris. c) The fragments collide and form moonlets and arc material that d) settle in the equilibrium positions.

such comets, is possible.

If we assume that the arcs are composed of particles with physical radius s ranging from $1\ \mu\mathrm{m}$ to $1\ \mathrm{m}$, following a numerical distribution given by $dN \propto s^{-3.5}ds$ (COLWELL; ESPOSITO, 1992), we get a total mass of $\sim 4 \times 10^{10}$ kg for the structures (SFAIR; GIULIATTI-WINTER, 2012; GIULIATTI-WINTER; MADEIRA; SFAIR, 2020). This value is an order of magnitude greater than the mass of the ongoing object, which means that a 100 m-sized impactor does not contain the material needed to fill the observed arcs, requiring additional material production mechanisms. We will discuss some of these processes in the next section.

A disruption is an extreme event, responsible for producing numerous fragments. However, the rupture of an object of a few kilometres due to an impact of $\sim\ \mathrm{km/s}$ usually gives rise to a limited number of larger fragments with the same mass order (kilometric fragments), while producing a large amount of material with sizes ranging from micrometres to metres (MICHEL; BENZ; RICHARDSON, 2004; STEWART; LEINHARDT, 2009; JUTZI; BENZ, 2017). In this section, we stick to calculate the evolution of these larger fragments, while some comments on the smaller fragments are addressed in Section 4.5.

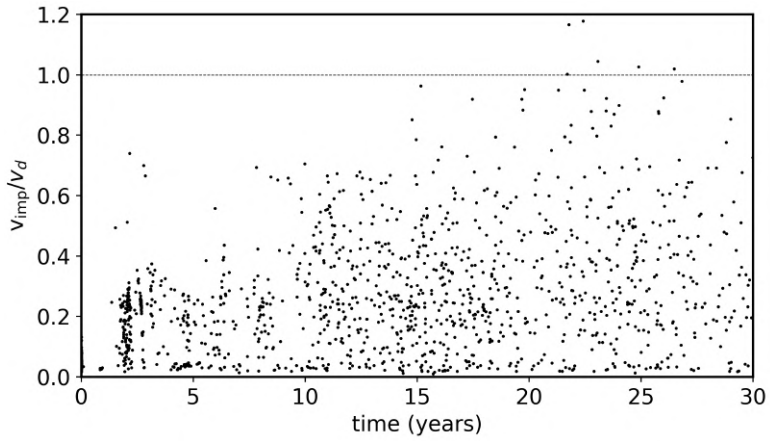

Figure 42 – Fraction between impact velocity and cut-off velocity as a function of the time the impacts occurred. The dotted vertical line provides the boundary between constructive and disruptive collisions.

4.4.2 Simulations of a representative case

To assess whether the trojan disruption generates a family of co-orbital satellites, we performed a set of simplistic numerical simulations starting right after the trojan disruption. For this, we use the MERCURY package (CHAMBERS, 1999), with the Bulirsch–Stoer algorithm. The dynamical system is composed of Neptune and its gravitational coefficients (J_2 and J_4), Galatea, the moon S_1, and the major fragments of the disruption. We also include the non-conservative term for carrying the fragments to the equilibrium positions.

Next, we present the results obtained in 3000 numerical simulations for a representative case with $\nu = 10^{-4}$ yr^{-1} and four fragments of same mass $\mathrm{m_{fra}} = 10^{-2}\mathrm{m_{S_1}}$ ($R_{\mathrm{fra}} \approx 1.1$ km). The fragments are distributed at the vertices of a regular polygon with four sides centred on the L_4 point. The length of the polygon sides is $l = 2R_{\mathrm{fra}} + 100$ m, and its angular orientation with the radial direction (φ) is given randomly in the range 0 deg-180 deg (Figure 41b).

From Figure 15 of Benz e Asphaug (1999), we obtain that fragments with mass $m_{\mathrm{tro}}/4$ are ejected with radial velocities ~ 0.4 m/s. With that in mind, we get randomly chosen ejection velocities from 0.36 m/s to 0.73 m/s. For velocities below 0.36 m/s, the relative velocity between the fragments is very low, and they collide right at the beginning of the simulation. For velocities larger than 0.73 m/s, the fragments leave the horseshoe region.

The MERCURY package treats collisions as inelastic events with conservation of linear momentum and mass. To ensure the validity of this treatment, we compare the impact velocity v_{imp} between the fragments with a cut-off velocity v_d for which a collision can be considered as constructive, given by (STEWART; LEINHARDT, 2012; TREFFENSTÄDT; MOURÃO; WINTER, 2015)

$$v_d = \sqrt{2Q_*\mu_{\mathrm{fra}}} \tag{5}$$

where the values of Q_* are taken from Fig. 11 of Stewart e Leinhardt (2012) and μ_{fra} is the mass ratio between the fragments ($\mu_{\mathrm{fra}} \geq 1$). Figure 42 shows v_{imp}/v_d as a function of time for our 3000 numerical simulations. As can be seen, only a small part of impacts ($< 1\%$) have velocities above the cut-off limit, showing that collisions can be, in general, treated as constructive events

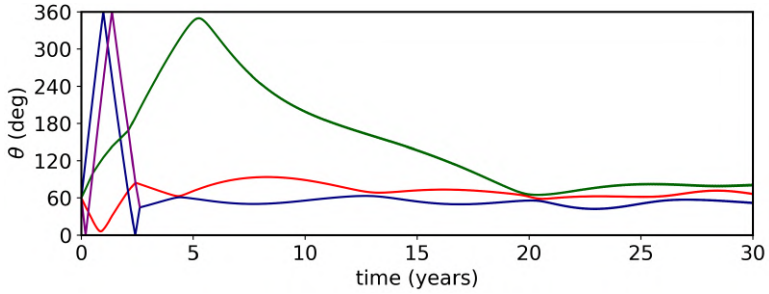

(a)

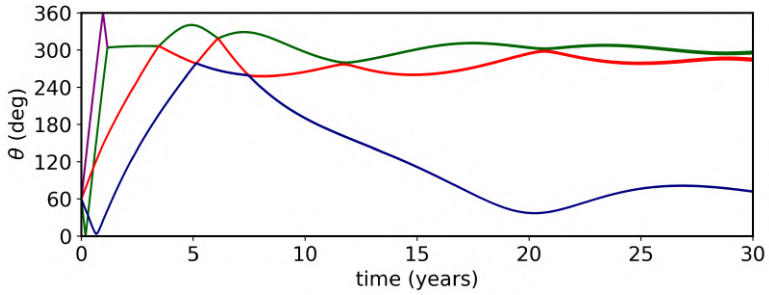

(b)

Figure 43 – Angular evolution of fragments in two systems that form 1+3 co-orbital satellites. In both systems, two fragments collide, giving rise to a moonlet with mass $2\mathrm{m_{fra}}$ and a pair of moonlets with masses $\mathrm{m_{fra}}$. We got a $\mathrm{P_1}$ final configuration in panel (a) and a $\mathrm{P_2}$ configuration in panel (b). The $2\mathrm{m_{fra}}$ mass moonlet is shown in blue and green line in panel (a) and (b), respectively.

Despite this, the impacts have relatively high velocities, v_{imp} ∼m/s (an order of magnitude higher than the ejection velocity). This fact is a result of the forced eccentricity gradient caused by the resonance with Galatea, as discussed in works such as Porco et al. (1995), Foryta e Sicardy (1996) and Renner et al. (2014). The high impact velocities, especially those in the last years of simulation, indicate that the impacts are not always perfect merging, but events with partial merging or erosion, presenting themselves as possible sources for the arcs. Some comments about it are addressed in Section 4.5.

We obtained that about 13% and 19% of the systems give rise to 1+1 and 1+2 co-orbital satellites, respectively (Figure 44). About 49% of the simulations form 1+3 co-orbital satellites, while in $\sim$ 19% of the simulations the fragments do not collide and form 1+4 satellites. We classify the formed systems in relation to their final equilibrium configurations through the classifications given in Figure 31-Figure 34. The 42:43 LER angle librates for all moonlets at the end of the simulations. Figure 43 shows examples of the formation of 1+3 co-orbital satellite systems, where in panel (a) is a $\mathrm{P_1}$ configuration while in panel (b) is presented a $\mathrm{P_2}$ configuration.

Despite having the same $\mathrm{P_i}$ configuration, two systems can be dynamically different, depending on the moonlets mass distribution. For example, a $\mathrm{P_1}$ configuration with 1+3 co-orbital satellites is obtained if a fragment collides with S_1 – forming three moonlets with masses $\mathrm{m_{fra}}$ – or if two fragments collide with each other – forming two moonlets with masses $\mathrm{m_{fra}}$ and one with $2\mathrm{m_{fra}}$. The latter can correspond to three different dynamical systems depending on the position of the moonlet with mass $2\mathrm{m_{fra}}$, resulting in a total of four degeneracies for the same $\mathrm{P_1}$ configuration with 1+3 co-orbital satellites. However, our results showed that these different mass distributions are only responsible

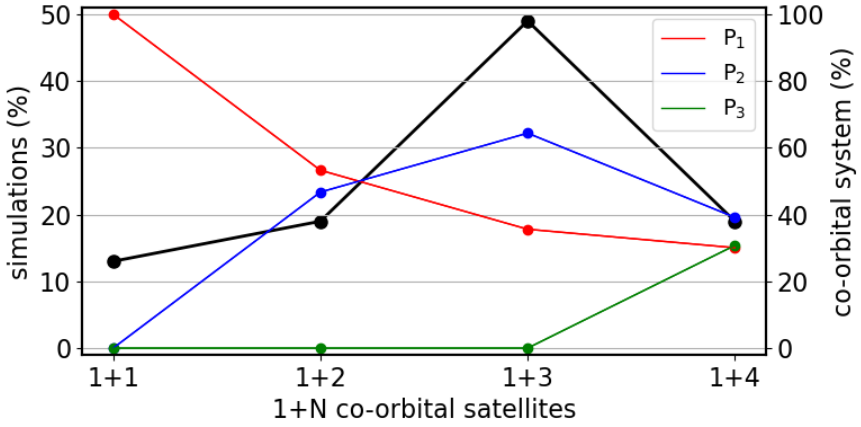

Figure 44 – Left y-axis gives the fraction of 1+N co-orbital satellites obtained in the 3,000 numerical simulations (black line) while the fractions of systems in $\mathrm{P_i}$ configuration relative to each set of 1+N co-orbital satellite system (N =1, 2, 3, and 4) are given on the right y-axis (coloured lines). The dynamical system includes four fragments of same mass ($\mathrm{m_{fra}} = 10^{-2}\mathrm{m_{S_1}}$), Neptune and its gravitational coefficients, Galatea, S_1, and a non-conservative term $\nu = 10^{-4}$ yr^{-1}.

for producing small differences in the orbital evolution of the moonlets. Equilibrium positions are approximately the same for all the degenerate cases.

The fractions of numerical simulations that produce 1+N co-orbital satellite systems are given in Figure 44 by the black line, whose values are given on the left y-axis. The figure also shows by coloured lines the fractions of systems in $\mathrm{P_i}$ configuration. The values of the coloured lines are given on the right y-axis and are relative to the number of simulations with 1+N co-orbital satellites, for N =1, 2, 3, and 4. For example, 19% of the simulations produce systems with 1+2 co-orbital satellites (570 simulations), $\sim$ 54% of this set corresponding to systems in $\mathrm{P_1}$ configuration (red line, 309 simulations) and $\sim$ 46% in $\mathrm{P_2}$ configuration (blue line, 261 simulations).

As a rule, we obtain a predominance of systems with moonlets distributed on each side of the moon than system with moonlets clustered near L_4/L_5 point. For example, for 1+4 co-orbital satellites, configurations with three moonlets near L_4 and one near L_5 are more common than configurations with all moonlets near L_4 but less common than the case with two moonlets near L_4 and two near L_5.

In our case of interest, we need at least three moonlets near L_4/L_5 to azimuthally confine the four arcs of Neptune. This condition is met by $\mathrm{P_1}$ configuration for the 1+3 co-orbital system, and $\mathrm{P_1}$ and $\mathrm{P_2}$ configurations for the 1+4 co-orbital system. These cases correspond to about 31% of our numerical simulations, and therefore, our representative case has approximately one in three chances of producing a system of moonlets that can confine Neptune arcs.

Given this, we performed new numerical simulations by varying the mass and number of fragments to verify the robustness of our statistics. Given the simplicity of our numerical simulations, we cannot make strong claims about the formation of 1+N co-orbital satellite systems. However, with the new simulations, we intend to analyse, at least in a first approximation (TREFFENSTÄDT; MOURÃO; WINTER, 2015), how common is the formation of systems capable of confining the arcs. The results of the new simulations are presented below.

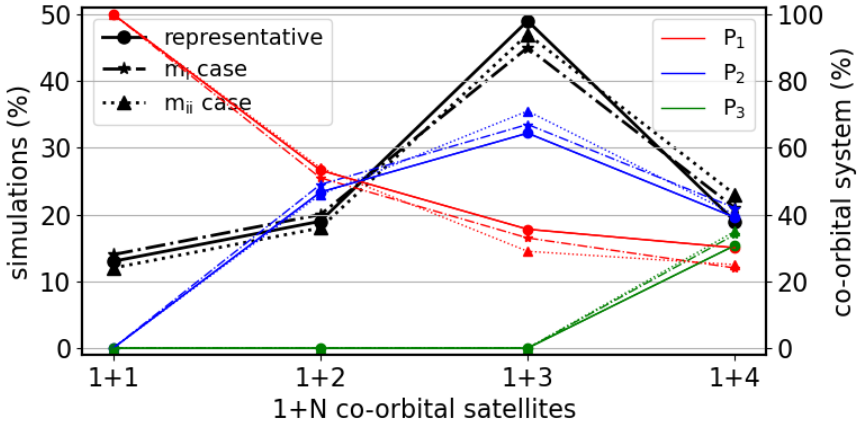

Figure 45 – Fractions of 1+N co-orbital satellite system and $\mathrm{P_i}$ configurations for initial fragments with masses $m_{\rm frac} = m_{\rm tro}/4$, $m_{\rm tro}/4$, $m_{\rm tro}/4$, $m_{\rm tro}/4$ (representative case, solid line with dots), $m_{\rm frac} = m_{\rm tro}/8$, $m_{\rm tro}/8$, $3m_{\rm tro}/8$, $3m_{\rm tro}/8$ (*m_i* case, dashed line with stars), and $m_{\rm frac} = 3m_{\rm tro}/16$, $3m_{\rm tro}/16$, $5m_{\rm tro}/16$, $5m_{\rm tro}/16$ (*m_ii* case, dotted line with triangles). The black lines give the fraction of systems with 1+N co-orbital satellites at the end of simulations, with values given on the left y-axis. The coloured lines show the fraction of simulations in $\mathrm{P_i}$ configuration for each 1+N co-orbital satellite system set, these values being given on the right y-axis.

4.4.3 Varying the mass of fragments

To evaluate the effect of the relative mass of the fragments on the results, we performed simulations assuming the following sets of fragments: *m_i)* a set varying by 50% the mass of the fragments in relation to the representative case – two fragments with mass $m_{\rm tro}/8$ and two with mass $3m_{\rm tro}/8$ – and *m_ii)* a set varying the mass of the fragments by 25% – two pairs of fragments with masses $3m_{\rm tro}/16$ and $5m_{\rm tro}/16$. Note that the total mass in fragments is $m_{\rm tro}$ in all simulations. Fragments with the same mass are initially placed at opposite vertices of the polygon in order to conserve the linear momentum after disruption. The length of the polygon is $l = 2R^{>}_{\rm fra} + 100$ m, where $R^{>}_{\rm fra}$ is the radius of the largest fragment. We performed 300 numerical simulations for each set of fragments.

Figure 45 provides the fractions obtained for the representative case (solid line with dots) and the cases *m_i* (dashed line with stars) and *m_ii* (dotted line with triangles). The values relative to the black lines are those given on the left y-axis and correspond to the fraction of simulations that result in 1+N co-orbital satellites systems. The coloured lines correspond to the fractions of $\mathrm{P_i}$ configurations obtained in the systems with 1+N co-orbital satellites, with values given on the right y-axis.

The fractions for the cases *m_i* and *m_ii* show small variations in relation to the representative case, indicating that variations in the mass of fragments have a small effect on the evolution of the system. The orbital evolution of the fragments is mainly defined by the azimuthal confinement due to S_1. As we are assuming fragments with masses two orders of magnitude smaller than the moon, we have that such a result is somehow expected.

Assuming different masses for the fragments, we obtain moonlets with a greater variety of mass in relation to the representative case. Consequently, the equilibrium positions will not be strictly the same in all systems with the same $\mathrm{P_i}$ configuration. However, we find that the azimuthal differences with respect to the cases shown in Figure 31-Figure 34 are less than 1 deg for all simulations. Next, we vary the initial number of fragments.

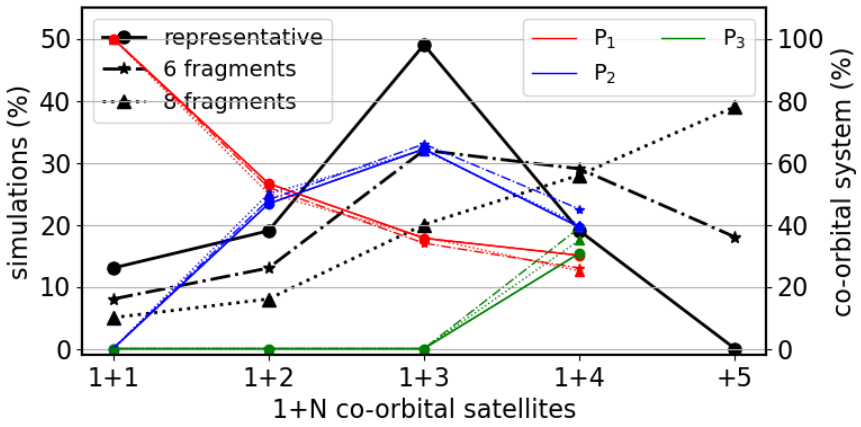

Figure 46 – Fractions of 1+N co-orbital satellite system and $\mathrm{P_i}$ configurations for cases with 4 (representative case, solid line with dots), 6 (dashed line with stars) and 8 fragments (dotted line with triangles). The coloured lines are the fraction of systems in $\mathrm{P_i}$ configuration, for $N = 1$, 2, 3, and 4 (right y-axis). The black lines give the fraction of simulations that produce N moonlets (left y-axis). Position "+5" on x-axis corresponds to systems with 5 moonlets or more.

4.4.4 Varying the number of fragments

We performed sets of 300 numerical simulations with N_{fra} fragments of the same mass $m_{\mathrm{tro}}/N_{\mathrm{fra}}$. The fragments are distributed in a regular polygon with N_{fra} vertices and length $l = 2R + 100$ m. In Figure 46, we show the same fractions as in Figure 45 for the representative case (solid line with dots) and for the cases with 6 (dashed line with stars) and 8 fragments (dotted line with triangles).

As a rule, cases with N_{fra} fragments give rise to systems with up to N_{fra} moonlets, and we obtain that the main effect of the number of fragments is to change the fractions of systems with 1+N co-orbital satellites. The fraction of systems in $\mathrm{P_i}$ configuration for $N \leq 4$ is almost the same for all cases. In the case with $N_{\mathrm{fra}} = 6$, 18% of the simulations result in systems with 5 or 6 moonlets, reducing the fraction of systems with 3 or 4 moonlets compared to the representative case. However, systems with 1+3 co-orbital satellites remain the most common outcome of the simulations. For $N_{\mathrm{fra}} = 8$, 39% of the systems have more than 5 co-orbital satellites.

In section 4.3, we obtained different equilibrium configurations with 1+3 and 1+4 co-orbital satellites that can confine the Neptune arcs. The characteristic that defines whether a configuration can confine four arcs is the presence of at least three moonlets near to the moon's L_4/L_5, which is met for all equilibrium configurations with more than 5 co-orbital satellites. Although the fraction of systems with 3 and 4 moonlets decreases when the number of fragments increases, the fractions of systems that can confine the four arcs are greater than that obtained in our representative case (31%). Therefore, the case with four fragments can be interpreted as a lower bound in our analysis of how common is the formation of a system capable of confining the arcs. In the next section, we cover the production of debris in the system.

4.5 COMMENTS ON ARC FORMATION

The origin of Neptune arcs remains a topic of debate among planetary scientists. In light of the confinement model of Porco (1991), it was proposed that the arcs would originate from dust ejected by

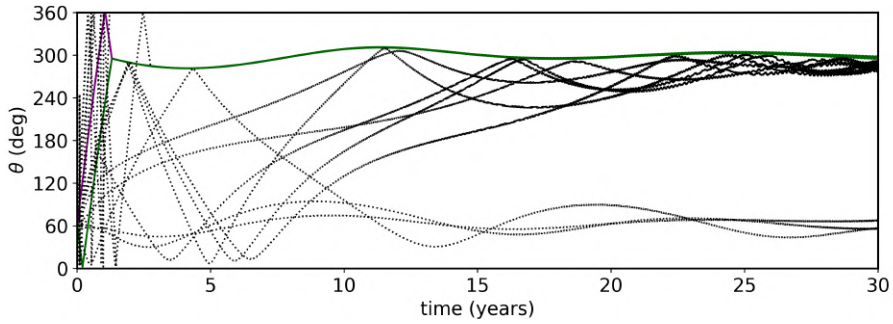

Figure 47 – Longitudinal evolution of four fragments (coloured lines) and a set of particles (black lines) initially distributed in the circle circumscribing the polygon of the fragments. The moonlet settles in the L_5 point and two arcs are formed, near L_4 and L_5 points.

immersed satellites in resonances with Galatea. However, we now know that this confinement model is not applicable to the arcs (SICARDY; ROQUES; BRAHIC, 1991; DUMAS et al., 2002), being required a different origin for them.

Several works propose that collisions between macroscopic particles are the source of the dust content observed in the Neptune arcs (SMITH et al., 1989; COLWELL; ESPOSITO, 1990a; PORCO et al., 1995; SALO; HANNINEN, 1998). It is an attractive proposition given the observational evidence for the existence of metric bodies immersed in the arc Fraternité (PATER et al., 2005). In the context of their confinement model, Renner et al. (2014) propose a hierarchical scenario where a previously accreted satellite gathers material at its Lagrangian point, forming the moonlets and the arcs. Furthermore, the hypothesis that the structures originate from the breakup of a parent satellite is mentioned in Pater et al. (2018).

Generally speaking, the Neptune arcs are likely composed of material produced by different processes. In the context of the scenario proposed in Section 4.4, we envision the production of material in three different stages of the system: At the disruption of trojan moon, in the later stage, in which the fragments are evolving to form the moonlets and after the formation of the 1+N co-orbital satellite system. Below, we discuss the mechanisms involved in each stage. We need to emphasize that collisions are complex events that are not yet well understood, and the formation of Neptune arcs requires a careful study that is beyond the scope of our work. We do not intend here to reproduce the arcs, but only to comment on possible sources for them.

4.5.1 Moon disruption stage

The disruption of objects with a few kilometres in radius due to a ∼km/s impact simultaneously produces a set of larger fragments and a large amount of debris with sizes ranging from micrometres to metres (BENZ; ASPHAUG, 1999; MICHEL; BENZ; RICHARDSON, 2004). The former were assumed by us as the building blocks of the moonlets, while the latter may have contributed to the formation of the arcs. As shown in Gallardo et al. (2020), the dust material in the Adams ring region has a short lifetime due to solar radiation and plasma drag, so macroscopic debris are the most likely to have contributed to the formation of the arcs.

To analyse the evolution of such particles, we redid some numerical simulations of the representative case, distributing 500 massless particles randomly in the circle that circumscribes the fragments'

polygon, with randomly chosen radial ejection velocities of $0.36 - 0.73$ m/s. The non-conservative term was also applied to the particles. The simulation with the highest particle survival rate is presented in Figure 47, where the fragments give rise to 1+1 co-orbital satellites in P_1 configuration. After impacts in the first years of simulation, the moonlet settle in the equilibrium position in less than 10 years and particles are confined azimuthally to two of the three particle equilibrium positions of the system.

In general, we obtain a low particle survival, with more than 70% of the set colliding with the fragments in five years of simulation. We do not verify particle survival in the cases of our interest (1+3 and 1+4 co-orbital satellite systems), whereas up to 5% of the particles survive in the 1+1 and 1+2 co-orbital satellite systems. These results seem to indicate that the debris formed in the disruption does not directly contribute to the arcs, or only contributes with a small amount of material. However, the relatively high impact velocities ($\sim$ m/s) indicate erosive events (STEWART; LEINHARDT, 2012). Therefore, they should give rise to a second generation of debris that contribute to the arcs, as will be discussed ahead.

4.5.2 Moonlets formation stage

Azimuthal confinement due to S_1 and Galatea's gravitational effect increase collisions between debris, which can be a significant source of material to the arcs. Just as a proof of concept, we assume the total debris mass as $m_{\mathrm{tro}}/4$, following a distribution given by $N \propto s^{-2.4}$ (KRIVOV et al., 2003) ($\mathrm{s} = 1\ \mu\mathrm{m} - 1$ m) and we calculate the rate of mass-produced due to impacts between debris. This can be estimated for soft target-ejecta as (COLWELL; ESPOSITO, 1990a)

$$\dot{M}_{\mathrm{coll}} = 4 \times 10^{-8} \frac{\Omega}{A} \sum_{s_i > s_j} N_i \sum_{s_j} N_j K_j (s_i + s_j)^2 \tag{6}$$

where Ω is the orbital frequency, A is the area of the region, and $N_{i,j}$ is the number of debris with radius $s_{i,j}$. K_j is the kinetic energy of the impactor particle, where we have assumed impacts with mean velocities of $\mathrm{v}_{\mathrm{imp}} = 1$ m/s.

As a result, we obtain that impacts can populate the four arcs in $T \sim 10^4$ years (optical depth of $\tau = 0.1$), showing that such events can be the source of the arcs. Using $\dot{M}_{\mathrm{coll}}$, we made a rough estimate comparing the cross-section of the debris with that of the fragment and found that the production, due to debris-fragment impacts, can reduce the time T by one order of magnitude.

As we showed in Section 4.4, some impacts between fragments are likely to be events with partial merging or erosion and therefore will also give rise to a second generation of debris that can contribute to the arcs. Based on Canup e Esposito (1995a), Sun, Schmidt e Spahn (2015) assume that 12% of a moon's regolith layer is released in a collision between two moonlets. As an estimate only, we made the humblest assumption that 1% of a fragment's mass is released in a collision between two fragments, giving an output of 6×10^{10} kg per collision. This amount of material exceeds the estimated mass of the arcs (4×10^{10} kg). Therefore, if completely confined, the material produced in just one impact between fragments is sufficient to reproduce the optical depth of the four arcs.

In order to analyse the evolution of the second generation debris, we redid some numerical

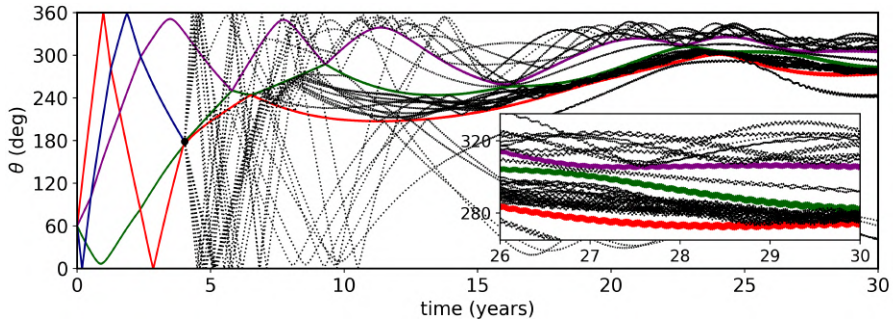

Figure 48 – Evolution of a set of particles produced by the collision of two fragments in a simulation initially with four fragments that give rise to a system in P_1 configuration with 1+3 co-orbital satellites. The particles are initially in a disk around the moonlet formed after the collision. The instant of the collision (~ 4 yr) is set by the black dot. We only show the surviving particles (black dotted lines), which are about 8% of the initial set. Fragments that give rise to the satellites are the solid coloured lines.

simulations, distributing 500 massless particles in a disk around the moonlet formed right after a collision. The particles are influenced by the non-conservative term, and the distance of each particle to the moonlet is chosen randomly in the range $1.0 - 1.5\ \mathrm{R_b}$, where $\mathrm{R_b}$ is the physical radius of the body. The radial velocity is chosen randomly in the range $1 - 3\ \mathrm{v_{esc}}$. For higher velocities, particles leave the horseshoe region.

Most particles collide in the first few years after being added to the system. However, the fraction that eventually survives is greater than in the case of particles produced in the disruption. This was to be expected, as particles are added later in the system, sometimes when satellites are already in tadpole-like orbits. In 15% of the numerical simulations in P_1 configuration with 1+3 co-orbital satellites, at lest one arc with material is obtained at the end of the simulation.

Figure 48 shows a case where all particle equilibrium positions are populated by material at the end of simulation, with a particle survival rate of 8%. As can be seen, four arcs are obtained near the L_5 point of the moon. This case is an exception, in most simulations only two arcs were produced, but it serves our purpose to demonstrate that collisions between fragments can be the origin of at least some of the arcs.

4.5.3 Post-formation stage

After the moonlets are formed, they can suffer impacts of interplanetary dust particles (IDPs) or meteoroids originating mainly from the Kuiper Belt (POPPE, 2016; POPPE et al., 2019). These impacts can provide material for the Adams ring and also be part of the source of Neptune arcs. IDPs have a typical radius of order $100\ \mu\mathrm{m}$, while meteoroids can be up to a few metres in size. At the end of the section, we briefly discuss different sizes of material produced by these two different populations of impactors.

We distributed 500 particles in a disk around the moonlets. The distance of particles to the moonlet is chosen randomly in the range $1.0 - 1.5\ \mathrm{R_b}$ and their radial velocities are chosen randomly in the range $1 - 3\ \mathrm{v_{esc}}$. Figure 49 shows the evolution of the particles in black dotted lines for a P_1 configuration with 1+3 co-orbital satellites. Each panel corresponds to a different simulation, where particles are initially around a different moonlet of the system. The moonlet which produces the

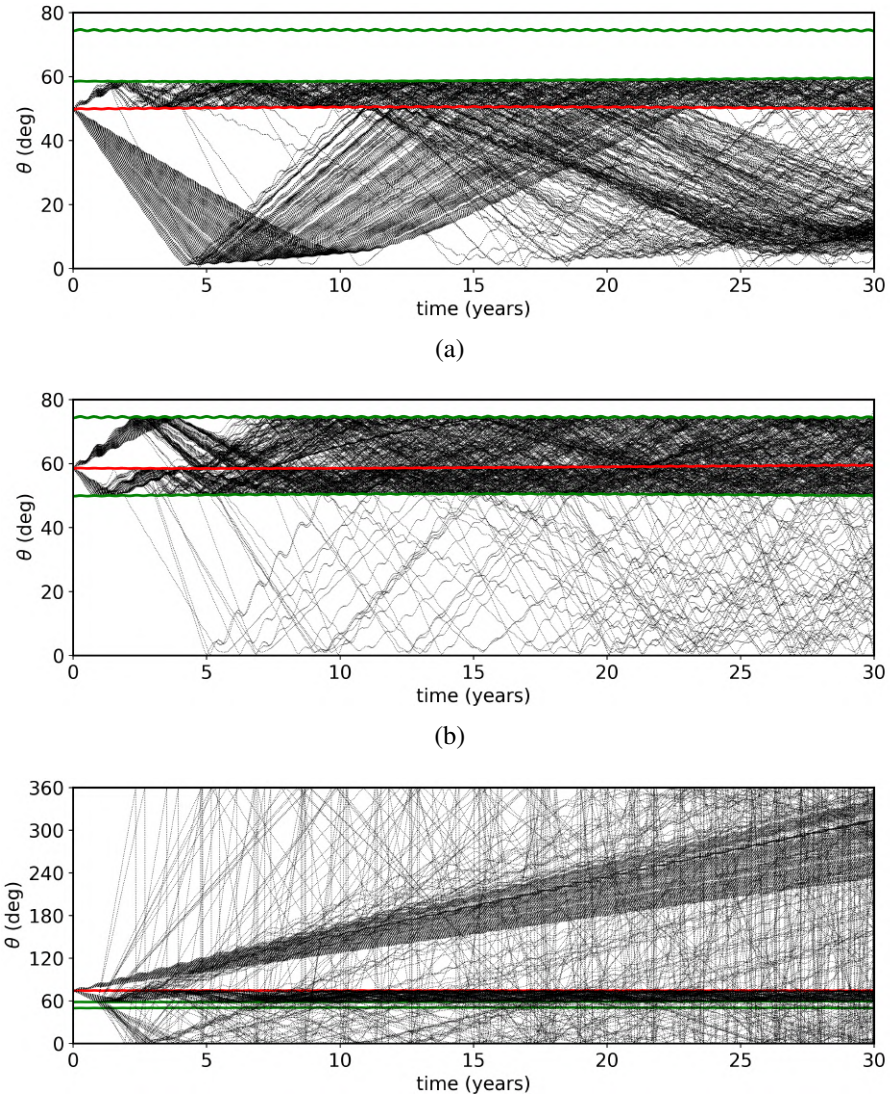

Figure 49 – Temporal evolution of particles produced by impacts of external bodies for a P_1 configuration with 1+3 co-orbital satellites. We show in separate panels the particles (black dotted lines) that originated from different moonlets. The moonlets are shown in coloured lines. The one that produces the material is the red line, and other moonlets are the green lines. We refer to the moonlets from bottom to top as S_2, S_3, and S_4.

particles is shown in red, while the others are in green. We found that $< 10\%$ of the particles collide in all the simulations.

As expected, the particles are confined by a pair of moonlets, as we can see for example in Figure 48b, where most of the particles launched by S_3 are confined between $S_2 - S_3$ and $S_3 - S_4$. A few particles leave the confinement of the pair $S_2 - S_3$, becoming confined by the pair $S_1 - S_2$; these particles correspond to the transient particles classified by Giuliatti-Winter, Madeira e Sfair (2020).

We emphasize that the type of impactor influences the sizes of the launched particles. The impacts of IDPs produce micrometre particles ($1 - 100\ \mu$m) that suffer the effects of dissipative forces, such as the solar radiation force and plasma drag (GALLARDO et al., 2020). Giuliatti-Winter, Madeira e Sfair (2020) showed that the lifetime of micrometre particles in the arcs under the effects of the solar radiation force is less than 50 years and that moonlets cannot replenish the arcs by IDP impacts.

On the other hand, meteoroid collisions can produce from micrometre particles up to metric-sized debris. For centimetre or larger bodies, the effects of the dissipative forces can be disregarded and the orbital evolution of the bodies is represented by Figure 49. Giuliatti-Winter, Madeira e Sfair (2020) showed that larger bodies survive for more than 1,000 years in the arcs, making meteoroid impacts a possible source for the arcs. The arcs' formation due to meteoroid impacts is an intricate problem, as collisions cannot disturb the stability of co-orbital satellites while they must produce an amount of material that reproduces the system.

4.6 DISCUSSION

In this work, we analyse through a set of numerical simulations the formation and orbital evolution of 1+N co-orbital satellite systems that could confine the arcs of Neptune. Revisiting the work of Renner e Sicardy (2004), we obtain that the equilibrium configurations obtained by them are not altered when we consider the moonlets in an orbit with the estimated eccentricity of particles located at the Adams ring (RENNER et al., 2014). It turns out that the 42:43 LER with Galatea does not destroy the equilibrium configurations, but only shifts the equilibrium positions by a few degrees.

We obtained a total of three distinct equilibrium configurations that can reproduce the angular width of the arcs – P_1 configuration with 1+3 co-orbital satellites and the P_1 and P_2 configurations with 1+4 co-orbital satellites. We also have that small variations in the mass of the moonlets do not alter the equilibrium configurations (RENNER et al., 2014). These results are interesting, as they demonstrate that different set of masses, longitudes, and number of moonlets can confine the arcs, giving robustness to the model proposed by Renner et al. (2014).

The origin of these moonlets and arcs is still unknown, being discussed in Renner et al. (2014) a scenario in which an ancient satellite gathered material around its L_4/L_5 point, forming the moonlets. The arcs would be the residual material of this process. Although mechanisms such as the one proposed by Izidoro, Winter e Tsuchida (2010) show the formation of moons at the triangular points of satellites, it is not clear which process would lead to the formation of some moonlets and not just one. It is also unclear how these moonlets would reach the equilibrium configuration. Satellite formation simulations in circumplanetary disks show the formation of pairs of co-orbitals (MADEIRA; IZIDORO; GIULIATTI-WINTER, 2021), but not of systems with more than two co-orbitals. Such results indicate that the moonlets, if they exist, probably have formed by a process other than simple accretion.

We propose the formation of moonlets by the disruption of an ancient body due to an impact with an ongoing object. This is a possible scenario since many objects originating in the Kuiper belt crosses the Neptune region (COLWELL; ESPOSITO, 1992; LEVISON et al., 2000). We are aware that our treatment is very simplistic. A more realistic model requires the study of the disruption itself, which depends on the physical parameters of target and impactor, impact parameter and velocity. It also requires studying the post-evolution of fragments and debris, considering mechanisms such as growth due to collisions with smaller debris and Adams ring material.

Nevertheless, our simulations varying the mass of fragments result in variation in the fractions lower than 10%, showing a self-consistency. In these simulations, we obtain that a disruption has a

probability of $\sim 30\%$ of producing a system capable of confining the four arcs. When we assume the formation of more than four fragments in the disruption, these values increase due to the possible formation of a system with more than 5 moonlets. These results place the scenario studied here, at least in a first approximation, as a possible scenario for the formation of the moonlets.

Our simulations include an artificial non-conservative term responsible for varying the system's energy and carrying the moonlets to equilibrium positions. In our representative case, this term was adjusted to generate the equilibrium configuration over an arbitrary period of 30 years, and we also performed simulations with timespans of 300 and 3000 years. In the real system, a series of mechanisms act by varying the energy of the system, such as inelastic collisions with disruption debris and the Adams ring material, and resonant torques due to Galatea. However, such effects work over long timescales, indicating that the moonlets formed and settled at equilibrium positions over timescales longer than the ones considered by us.

Changes in brightness and longitude of the arcs (PATER et al., 2005) and the disappearance of the arcs Liberté and Courage (PATER et al., 2018) seem to indicate that the dust population of the arcs is recent. Giuliatti-Winter, Madeira e Sfair (2020) support this assumption by obtaining lifetimes of a few decades for the dust material in the arcs. GIULIATTI-WINTER; MADEIRA; SFAIR also found that the disappearance of two arcs can be explained if they are composed of particles with typical sizes different from the arcs that still remain.

In our scenario, these differences in the particle sizes between the arcs can be obtained if they originated at different stages. In particular, our crude analysis shows that micrometre-sized material is possibly originated from impacts between the disruption outcomes (fragments and debris). Meteoroid impacts with the already formed moonlets is another possible source. However, it is likely that several processes act to produce the arcs, such as impacts, fragmentation, and erosion.

4.7 CONCLUSION

We have explored, by numerical simulations, the confinement model for Neptune arcs proposed in Renner et al. (2014). The model proves to be possible, as different sets of moonlets, in number, mass, and location, can roughly reproduce the width of the four arcs. However, further investigation and refinements are needed to explain the interesting evolution shown by the arcs since their discovery. If these co-orbital satellites exist, we show that the disruption of an ancient body at a triangular point of a moon is a possible model for their formation. In such a scenario, the arcs may have been formed by different processes such as collisions, fragmentation, re-accretion, external impacts, among others. We find that impacts between fragments and debris and meteoroid impacts with the moonlets are attractive possibilities. The arcs may have been formed in different stages, with the arcs composed only of dust particles being the final stage of the arc life.

5 DYNAMICS AROUND A SPHERICAL BODY WITH MASS ANOMALY

The discovery of satellites and rings around non-planetary bodies and recent space missions designed to visit small bodies have boosted the study of dynamics around non-spherical bodies. An example of an object that has recently caught the the attention of the scientific community is the TNO Chariklo, which hosts two narrow rings. The shape of such an object is not well known, being a triaxial ellipsoid, Jacobi ellipsoid and a spherical body with high topographic features possibilities for its shape (LEIVA et al., 2017; SICARDY, 2020). Here, we study the dynamics around a spherical body with a mass anomaly, motivated by the last possible shape for Chariklo. The classic pendulum model is modified in order to obtain the width of the spin-orbit resonances raised by non-asymmetric gravitational terms of the central object. The Poincaré surface of section technique is adopted to confront our analytical results.

The content of this chapter was published as: Gustavo Madeira et al. "Dynamics around non-spherical symmetric bodies–I. The case of a spherical body with mass anomaly."Monthly Notices of the Royal Astronomical Society 510.1 (2022): 1450-1469 (MADEIRA et al., 2022).

5.1 INTRODUCTION

In the last three decades, the acquisition of data on the shape of small heliocentric bodies, by ground and space-based observations (HUDSON; OSTRO, 1995; HANUŠ; MARCHIS; ĎURECH, 2013; HANUŠ et al., 2017) and by space-mission explorations – such as OSIRIS-REx and Hayabusa spacecraft (YOSHIKAWA et al., 2015; LAURETTA et al., 2017) – fostered the study of the dynamics around these bodies. This class of objects, which involves asteroids, trans-Neptunian objects, Centaurs, and comets, characteristically have diameters of less than 1000 km (JORDA et al., 2016). Due to their small sizes, these bodies do not have enough mass to reach hydrostatic equilibrium, showing irregular and asymmetric shapes.

The development of space-missions was a strong motivation for the search of equilibrium regions around irregular bodies, as accomplished, e.g., by Scheeres, Williams e Miller (2000) which obtained stable orbits around the asteroid 433 Eros for the spacecraft NEAR-Shoemaker (PROCKTER et al., 2002). Some other works with such purpose are Yu e Baoyin (2012), Shang, Wu e Cui (2015), Wang, Li e Gong (2016), Winter et al. (2020), Moura et al. (2020). The discovery of satellites and rings around this class of objects were also justifications for the interest in the stability of irregular bodies systems (CHAPMAN et al., 1995; MERLINE et al., 2002; BRAGA-RIBAS et al., 2014; ORTIZ et al., 2017).

When investigating the motion around irregular bodies, it is essential to consider the gravitational field generated by their odd shape. One method used for this is to approximate the irregular shape to a symmetric one – such as a MacLaurin spheroid or a triaxial ellipsoid – which allows studying the system theoretically or through low-cost simulations. Another course of action is to decompose the irregular body into a set of regular polyhedra (Polyhedron Shape Model) (WERNER, 1994) or mass

points (Mascon Model) (GEISSLER et al., 1996). Despite the high level of accuracy, this methodology has a higher computational cost.

Here, we are interested in the dynamics around a class of objects classified by us as Non-Spherical Symmetric Bodies (NSSBs): contact binaries, triaxial ellipsoids with uniform density, and spherical bodies with a mass anomaly. The motion around NSSBs has already been studied in some articles, such as Lages, Shepelyansky e Shevchenko (2017) which analysed the stability around contact binaries through a generalized Kepler map technique (MEISS, 1992; SHEVCHENKO, 2011), obtaining chaotic gravitational zones around the central body, similar to those found for symmetrical elongated bodies (MYSEN; OLSEN; AKSNES, 2006; MYSEN; AKSNES, 2007). Their results are appliable to the asteroids 243 Ida and 25143 Itokawa (LAGES; SHEPELYANSKY; SHEVCHENKO, 2017).

Lages, Shevchenko e Rollin (2018) also use the Kepler map technique to study the chaotic region around cometary nuclei of dumb-bell shape, obtaining that such region is responsible for engulfing most of the Hill sphere of Comet 1P/Halley. Amarante e Winter (2020) studied the dynamics around 486958 Arrokoth, an object similar to a contact binary, using a Polyhedron Shape Model and found an unstable zone in the equatorial region of the asteroid. Rollin, Shevchenko e Lages (2021) obtain that the particles in the equatorial plane of 486958 Arrokoth are lost due to the chaotic diffusion of the orbits, which results in collisions or particle ejection. Interestingly, Rollin, Shevchenko e Lages (2021) also obtain theoretical dumb-bell-shaped objects with certain combinations of mass and spin period that host, not a complete chaotic zone, but a chaotic ring.

The dynamics around triaxial ellipsoids were previously studied by Scheeres (1994), Vantieghem (2014), and in particular by Winter, Borderes-Motta e Ribeiro (2019) which analysed the motion around 136108 Haumea, an ellipsoidal-shape object. This dwarf planet is particularly interesting due to its complex system that includes a pair of satellites, Hi'iaka and Namaka, and a ring (RAGOZZINE; BROWN, 2009; ORTIZ et al., 2017). The non-asymmetric terms of the gravitational field of the NSSBs create strong resonances between the orbital period of the ring particles and the spin of the central body. Ortiz et al. (2017) propose that the Haumea ring would be associated with the 1:3 resonance. However, Winter, Borderes-Motta e Ribeiro (2019) using Poincaré surface of sections showed that this resonance is doubled, generating a large chaotic region in the resonance separatrix. Consequently, the ring is not associated with the 1:3 resonance but probably with first kind periodic orbits.

10199 Chariklo is another irregular body with a complex system involving a pair of narrow rings and possibly small satellites (BRAGA-RIBAS et al., 2014; BÉRARD et al., 2017). The shape of Chariklo is still not well known. Observational data suggest triaxial and Jacobi ellipsoid shapes for the object (LEIVA et al., 2017). Sicardy (2020) discuss the possibility of Chariklo to be a sphere with topographical features of a few kilometres, i.e., an object with a mass anomaly. Assuming a spherical Chariklo with a mass anomaly, Sicardy et al. (2019), Sicardy et al. (2020) show that particles inside the corotation radius migrate onto the body, and the outer material is pushed beyond the 1:2 resonance.

Here, we apply some well-known techniques to study the dynamics around a spherical body with a mass anomaly. Relations for the width and location of the spin-orbit resonances, a.k.a., sectoral resonances are presented. The dependence of resonances on the central body parameters are analysed. Poincaré surface of section technique is also applied to the system for analysing the stability of the

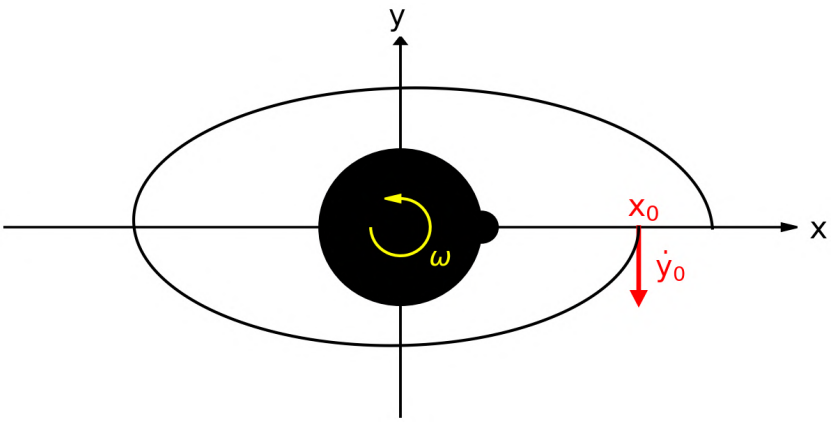

Figure 50 – Schematic diagram of the trajectory of a particle around a spherical object with a mass anomaly at its equator. The trajectory is fixed in the rotating frame with the central body's angular velocity ω. x_0 is the initial position of the particle, and the red arrow indicates the initial velocity.

particles. We advance the reader the existence of a chaotic region near the object with a mass anomaly. This region extension is measured, and an adjusted equation is obtained as a function of the system parameters.

5.2 DYNAMICAL SYSTEM

In the present work, we analyse the dynamics of particles orbiting a hypothetical spherical object of mass M and radius R, with a mass anomaly m_a at its equator (Figure 50). We assume the object with an uniform mass distribution, where the masses M and m_a have the same bulk density ($\rho = 1$ g/cm^3). The object is also assumed to rotate with constant angular velocity ω ($\omega = 2\pi/T$, where T is the rotation period) without wobbling motion. For simplicity, we will express our physical quantities in the following units: $GM = 1$, while $R = 1$ is the distance between the system centre and the mass anomaly. We also define as a unit the Keplerian frequency of the mass anomaly, scaled by the density ρ of the object:

$$\omega_k = \sqrt{\frac{GM}{R^3}} = \sqrt{\frac{4\pi G\rho}{3}} = 1. \tag{1}$$

Two dimensionless parameters will define our dynamic system: the normalized mass anomaly $\mu = m_a/M$ and the rotating rate $\lambda = \omega/\omega_k$.

Equations of motion in a frame Oxy rotating with the same period as the central body's spin are given by (SCHEERES et al., 1996)

$$\ddot{x} - 2\lambda\dot{y} = \lambda^2 x + U_x \tag{2}$$

and

$$\ddot{y} + 2\lambda\dot{x} = \lambda^2 y + U_y, \tag{3}$$

where U_x and U_y stand for the partial derivatives of the gravitational potential.

The potential acting on a particle with position-vector $\vec{r} = x\hat{x} + y\hat{y}$ ($r = |\vec{r}|$) in the rotating frame is obtained by adding the gravitational potential of the spherical portion of the object – at the centre of

the system – with the gravitational potential of the mass anomaly, located at $\vec{R} = \hat{x}$ (SICARDY et al., 2019):

$$U(r) = -\frac{1}{r} - \frac{\mu}{|\vec{r} - \hat{x}|} + \lambda^2 \mu (\vec{r} \cdot \hat{x}). \tag{4}$$

Note that the potential given in Equation 4 differs from that acting on a particle in the RP3BP (MURRAY; DERMOTT, 1999) by the rotating parameter λ^2 in the indirect term. While the secondary mass in RP3BP surrounds the central body with Keplerian velocity ω_k, here the mass anomaly rotates with angular velocity $\lambda\omega_k$. We introduced the rotating parameter to correct this difference.

Similar to the dynamics of a particle in the RP3BP with a disturbing internal body, we obtain the expansion of the potential U for the lowest order terms in eccentricity (e) as:

$$U = -\frac{1}{r} - \sum_{j=0}^{\infty} \sum_{m=-\infty}^{\infty} \mu e^j \left[\alpha F_j b_{1/2}^{(m-j)}(\alpha) + \frac{\lambda^2}{\alpha} f_j \delta_{|m|,1} \right] \cos\phi, \tag{5}$$

where $\alpha = 1/a < 1$ (a=semi-major axis of the particle), $b_{1/2}^{(m)}$ is the Laplace coefficient, f_j and F_j are linear operators, $\delta_{|m|,1}$ is the Kronecker delta and ϕ is a characteristic angle of the system relating the rotation of the central object with the longitudes of the particle. The linear operators F_j for $j \leq 5$ are given by (MURRAY; DERMOTT, 1999; ELLIS; MURRAY, 2000)

$$F_1 = \frac{1}{2} \left[(-1 + 2m) + \alpha D \right], \tag{6}$$

$$F_2 = \frac{1}{8} \left[\left(2 - 7m + 4m^2\right) + (-2 + 4m)\, \alpha D + \alpha^2 D \right], \tag{7}$$

$$\begin{aligned} F_3 =& \frac{1}{48}[(-6 + 29m - 30m^2 + 8m^3)] + \\ &+ \frac{1}{48}[(6 - 21m + 12m^2)\alpha D + (-3 + 6m)\alpha^2 D + \alpha^3 D^3], \end{aligned} \tag{8}$$

$$\begin{aligned} F_4 =& \frac{1}{384}[(24 - 146m + 211m^2 - 104m^3 + 16m^4)] + \\ &+ \frac{1}{384}[(-24 + 116m - 120m^2 + 32m^3)\alpha D] + \\ &+ \frac{1}{384}[(12 - 42m + 24m^2)\alpha^2 D + (-4 + 8m)\alpha^3 D^3 + \alpha^4 D^4], \end{aligned} \tag{9}$$

and

$$\begin{aligned} F_5 =& \frac{1}{3840}[(-120 + 874m - 1595m^2 + 1110m^3 - 320m^4 + 32m^5)] + \\ &+ \frac{1}{3840}[(120 - 730m + 1055m^2 - 520m^3 + 80m^4)\alpha D] + \\ &+ \frac{1}{3840}[(-60 - 290m - 300m^2 + 80m^3)\alpha^2 D] + \\ &+ \frac{1}{3840}[(20 - 70m + 40m^2)\alpha^3 D^3 + (5 + 10m)\alpha^4 D^4 + \alpha^5 D^5] \end{aligned} \tag{10}$$

where D is the derivative operator D=d/dα. The operators f_j are (MURRAY; DERMOTT, 1999; ELLIS; MURRAY, 2000)

$$f_1 = -\frac{1}{2}, \tag{11}$$

$$f_2 = -\frac{3}{8}, \tag{12}$$

$$f_3 = -\frac{1}{3}, \tag{13}$$

$$f_4 = -\frac{125}{384}, \tag{14}$$

and

$$f_5 = -\frac{27}{80} \tag{15}$$

The characteristic angle associated with the sectoral resonances is presented in Section 5.3.

In conservative systems, such as those analysed in this work, the Jacobi constant C_J is a conserved quantity used to obtain the Poincaré surface of sections. It is expressed here in the units $R^2\omega_k^2$ and is given by (SCHEERES et al., 1996)

$$C_J = \lambda^2(x^2 + y^2) + 2U(x, y) - \dot{x}^2 - \dot{y}^2. \tag{16}$$

5.3 SECTORAL RESONANCES

At the planar limit, a pair of fundamental frequencies describe the motion of a particle: the synodic and radial epicyclic frequencies. The first, $n - \omega$ (n= angular frequency of the particle), corresponds to the frequency of the particle's return to a fixed position on the rotating frame. The second, $\kappa = n - \dot{\varpi}$, is the frequency of the particle's return to its pericentre, being $\dot{\varpi}$ the derivative of the particle's longitude of pericentre. If these frequencies are commensurable, the particle is in a sectoral resonance – spin-orbit resonance – with the central body. Once in resonance, the orbital evolution of the particle will be modelled by the energy balance provided by the resonant configuration. Sectoral resonances with real non-spherical bodies were studied in Borderes-Motta e Winter (2018) and Winter, Borderes-Motta e Ribeiro (2019) for the asteroid 4179 Toutatis and the dwarf planet Haumea, respectively.

A particle at the centre of a m:$(m - j)$ resonance satisfies the resonance condition (SICARDY et al., 2019)

$$m\omega - (m - j)n - j\dot{\varpi} = 0, \tag{17}$$

where m and j are integers responsible for giving the commensurability of the frequencies. For $j = 0$, the particle is in corotation resonance, while for $j = m$, we have the apsidal resonances. Both cases are out of the scope of this work (SICARDY et al., 2019) and here we will focus on resonances with $j \geq 1$, where the numerical value of j gives the order of the resonance.

When a particle is in a m:$(m - j)$ resonance, the characteristic angle ϕ – also called resonant angle – librates with an amplitude lower than $360°$. The angle is given by

$$\phi = m\omega t - (m - j)\lambda_p - j\varpi, \tag{18}$$

where λ_p is the mean longitude of the particle. For simplicity, we ignore variations in the mean longitude of epoch.

5.3.1 Resonance Location

The angular and radial epicyclic frequencies are given by (CHANDRASEKHAR, 1942)

$$n^2 = \frac{1}{r}\frac{dU_0}{dr} \tag{19}$$

and

$$\kappa^2 = \frac{1}{r^3}\frac{d(r^4 n^2)}{dr}, \tag{20}$$

where U_0 is the axisymmetric part of the gravitational potential ($j = m = 0$).

From Equation 5, we obtain:

$$U_0 = -\frac{1}{r} - \frac{\mu}{2r} b^{(0)}_{1/2}(\alpha)\,. \tag{21}$$

Expanding the Laplace coefficient up to second order in α,

$$\frac{1}{2} b^{(0)}_{1/2}(\alpha) = 1 + \frac{1}{4}\alpha^2, \tag{22}$$

we obtain the axisymmetric part of the gravitational potential for the spherical body with a mass anomaly:

$$U_0 = -\frac{1}{r}\left(1 + \mu + \frac{\mu}{4}\alpha^2\right). \tag{23}$$

Keeping the lowest order terms in μ in Equations 19 and 20, we obtain

$$n^2 = \frac{1}{r^3}\left(1 + \mu + \frac{3\mu}{4}\alpha^2\right) \tag{24}$$

and

$$\kappa^2 = \frac{1}{r^3}\left(1 + \mu - \frac{3\mu}{4}\alpha^2\right). \tag{25}$$

The location of the resonances can be obtained by numerical methods, such as the Newton-Raphson method (PRESS et al., 1989; RENNER; SICARDY, 2006), by applying Equations 24 and 25 in the resonance condition (Equation 17). Table 5 shows the location of the resonances in the ranges $-4 \leq m \leq 4$ and $j \leq 5$ (up to fifth-order resonances). The central body is a Chariklo-type body with

Table 5 – The location of the m:$(m-j)$ resonances in the ranges $-4 \leq m \leq 4$ and $j \leq 5$. We assumed a central body with parameters based on the centaur Chariklo, with $\lambda = 0.471$ and $\mu = 10^{-3}$ (reference object). The resonances marked "inside" occur within the physical radius of the central body and, therefore, do not exist in the considered system. The resonances marked as "apsidal" are out of the scope of this work.

j	m →	-4	-3	-2	-1	1	2	3	4
1	resonance	5:6	4:5	3:4	2:3	1:2	1:0	2:1	3:2
	a/R	1.909	1.993	2.156	2.612	apsidal	inside	1.256	1.358
2	resonance	5:7	4:6	3:5	2:4	1:3	1:-1	2:0	3:1
	a/R	2.156	2.313	2.612	3.423	inside	apsidal	inside	inside
3	resonance	5:8	4:7	3:6	2:5	1:4	1:-2	2:-1	3:0
	a/R	2.389	2.612	3.031	4.146	inside	inside	apsidal	inside
4	resonance	4:8	3:7	2:6	1:5	1:-3	2:-2	3:-1	4:0
	a/R	2.612	2.895	3.423	4.811	inside	inside	inside	apsidal
5	resonance	4:9	3:8	2:7	1:6	1:-4	2:-3	3:-2	4:-1
	a/R	2.825	3.164	3.793	5.433	inside	inside	inside	inside

$\mu = 10^{-3}$ and $\lambda = 0.471$ ($M = 6.3 \times 10^{18}$ kg and $T = 7.004$ hr) (LEIVA et al., 2017), defined as our reference object. We assume $\mu = 10^{-3}$ as a reference value because it is small enough for the centre of the system to be approximately the physical centre of the spherical portion and large enough for the effects of the mass anomaly to be observed.

5.3.2 Resonance Width

In this section, we follow the classical approach of the pendulum model, presented in Winter e Murray (1997a) and Murray e Dermott (1999), to obtain the resonance width for our case of interest. A particle is in a m:$(m-j)$ sectoral resonance when its resonant angle ϕ librates, which means that the particle oscillates in the rotating frame around the central position of the resonance (Equation 17). We can evaluate the maximum amplitude of a resonant particle through the temporal variations of ϕ:

$$\dot{\phi} = m\omega - (m-j)n - j\dot{\varpi} \tag{26}$$

and

$$\ddot{\phi} = -(m-j)\dot{n} - j\ddot{\varpi}. \tag{27}$$

Considering only the lowest order terms in eccentricity (e), we obtain using the Lagrange's equations (MURRAY; DERMOTT, 1999):

$$\dot{n} = -3nC_r(m-j)e^j \sin\phi \tag{28}$$

and

$$\dot{\varpi} = je^{j-2}C_r \cos\phi, \tag{29}$$

where

$$C_r = \mu \frac{n}{\alpha} \left[\alpha F_j b_{1/2}^{(m-j)} + \frac{\lambda^2}{\alpha} f_j \delta_{|m|,1} \right]. \tag{30}$$

From Equation 29, we obtain that the second derivative of ϖ is

$$\ddot{\varpi} = j(j-2)e^{j-3}\dot{e}C_r \cos\phi - je^{j-2}C_r \sin\phi\dot{\phi}, \tag{31}$$

where the time variation of eccentricity ($\dot{e}$) obtained through Lagrange's equations is $\dot{e} = -je^{j-1}C_r \sin\phi$.

It can be shown that

$$\ddot{\varpi} = j^2 e^{2(j-2)} C_r^2 \sin j\phi - je^{j-2}C_r(m\omega - (m-j)n)\sin\phi. \tag{32}$$

Therefore,

$$\ddot{\phi} = -j^3 e^{2(j-2)} C_r^2 \sin 2\phi + 3nC_r(m-j)^2 e^j \sin\phi + j^2 e^{j-2} C_r (m\omega - (m-j)n)\sin\phi. \tag{33}$$

By inspection, we can evaluate the contribution of each term of Equation 33. The C_r function is proportional to μ, a value lower than one. In fact, for high values of mass anomaly ($\mu \gtrsim 10^{-2}$), we can not assume the centre of mass of the system as the physical centre of the spherical object, and Equation 5 is no longer applied – this range of μ defines another NSSB, the contact binary. Since $\mu << 1$, the term that depends on C_r will dominate those dependent on C_r^2, in principle. For first-order resonances ($j = 1$), the first and third terms in Equation 33 are proportional to $1/e^2$ and $1/e$, respectively – e is a small value – and dominate over the second term, proportional to e.

5.3.2.1 Second and higher-order resonances

For second and higher-order resonances, the eccentricity exponents in Equation 33 are positive, and we can approximate the equation to

$$\ddot{\phi} + \omega_0^2 \sin\phi = 0, \tag{34}$$

where $\omega_0^2 = 3n|C_r|(m-j)^2 e^j$. To obtain this result, we have assumed $m\omega - (m-j)n \approx 0$ since the particle is in resonance.

From Equation 34, we can see that a resonant particle is confined in a pendulum motion around an equilibrium position of the resonance. The number of equilibrium positions of a m:$(m-j)$ sectoral resonance is j. Analogous to the simple pendulum problem, the particle reduced energy in the rotating frame is

$$E = \frac{\dot{\phi}^2}{2} + 2\omega_0^2 \sin^2\frac{\phi}{2}. \tag{35}$$

The maximum possible energy of the pendulum ($\dot{\phi} = 0$ deg and $\phi = 90$ deg) defines the separatrix between libration and circulation of the resonant angle. That is, the separatrix corresponds to the boundary between bounded and unbounded motions. The energy of such trajectory is $E = 2\omega_0^2$, and the temporal variation of the resonant angle is $\dot{\phi} = \pm 2\omega_0 \cos(\phi/2)$.

Relating ϕ and n:

$$dn = \frac{\dot{n}}{\dot{\phi}} d\phi = \pm\sqrt{3n|C_r|e^j}\sin\frac{\phi}{2}d\phi, \tag{36}$$

we obtain, by integration, the range of angular frequency in which a particle is in a $m{:}(m-j)$ sectoral resonance:

$$n = n_0 \pm \sqrt{12n|C_r|e^j}\cos\frac{\phi}{2}, \tag{37}$$

where n_0 is the central angular frequency of the resonance.

Therefore, a particle is in a second or higher-order resonance if its semi-major axis meets the relation:

$$a = a_0 \pm \left(\frac{16}{3}\frac{|C_r|}{n}e^j\right)^{1/2} a_0, \tag{38}$$

where a_0 is the central semi-major axis of the resonance (Section 5.3.1).

5.3.2.2 First-order resonances

For $m{:}(m-1)$ resonances, none of the terms in Equation 33 can be disregarded, requiring a different solution than the one obtained. As *ansatz*, we assume a solution similar to Equation 37, $n = n_0 + k\cos(\phi/2)$, where k is an as-yet-unknown constant. By integrating Equation 33, we obtain the kinetic energy of the system

$$\frac{1}{2}\dot{\phi}^2 = \int \ddot{\phi}d\phi = \frac{C_r^2}{e^2}\left(2\cos^2\frac{\phi}{2} + \cos^2\phi\right) - 6nC_r(m-1)^2 e\cos^2\frac{\phi}{2} + \frac{4}{3}\frac{C_r}{e}(m-1)k\cos^3\frac{\phi}{2}, \tag{39}$$

where the constant arising from the integration was determined considering $\phi = 0$ deg and $\phi = 180$ deg.

Applying $n = n_0 + k\cos(\phi/2)$ to Equation 26 and assuming that the particle is exactly at the centre of the resonance ($\phi = 0$ deg and $\phi = 180$ deg), we find that $m\omega - (m-1)n_0 = -C_r/e$. From Equation 26, we get

$$\frac{1}{2}\dot{\phi}^2 = \frac{1}{2}\frac{C_r^2}{e^2}(1+\cos\phi)^2 + \frac{1}{2}(m-1)^2k^2\cos^2\frac{\phi}{2} + \frac{C_r}{e}(1+\cos\phi)(m-1)k\cos\frac{\phi}{2}. \tag{40}$$

Taking Equations 39 and 40 as equal and assuming $\phi = 0$ deg:

$$(m-1)^2k^2 + \frac{4}{3}\frac{C_r}{e}(m-1)k + 12nC_r(m-1)^2 e = 0. \tag{41}$$

Therefore, the boundaries of the angular frequency and semi-major axis in which a particle is in a first-order resonance are, respectively:

$$n = n_0 \pm \sqrt{12|C_r|ne}\left(1 + \frac{1}{27(m-1)^2e^3}\frac{|C_r|}{n}\right)^{1/2} - \frac{|C_r|}{3(m-1)e} \tag{42}$$

and

$$a = a_0 \pm \left(\frac{16}{3}\frac{|C_r|}{n}e^j\right)^{1/2}\left(1 + \frac{1}{27(m-1)^2e^3}\frac{|C_r|}{n}\right)^{1/2} a_0 + \frac{2}{9(m-1)e}\frac{|C_r|}{n}a_0. \tag{43}$$

5.4 POINCARÉ SURFACES OF SECTION

Poincaré surface of section technique is usually applied in studies of the RP3BP (HÉNON, 1965a; HÉNON, 1965b; HENON, 1966; HÉNON, 1966; HÉNON, 1969; JEFFERYS, 1971; Winter; Murray, 1994a; Winter; Murray, 1994b), to analyse the dynamics of the third body, providing information such as the location and size of stable and chaotic regions, including the mean motion resonance regions. In RP3BP, the problem is considered in a rotating system where the primary and secondary bodies are fixed, and only the third body describes a free motion. Some works have also adopted the Poincaré surface of section to study dynamical systems composed of two bodies, with a non-spherical central object. Scheeres et al. (1996) applied this technique to find periodic orbits around the asteroid 4769 Castalia. This technique was also applied by Borderes-Motta e Winter (2018) and Winter, Borderes-Motta e Ribeiro (2019) to study the region around Toutatis and Haumea, respectively.

This work also applies the Poincaré surface of section to a two-body problem composed of a massive central body and a massless particle. Instead of the orbital motion between the primary and secondary bodies, the rotation of the central body gives the motion of the rotating frame. The Poincaré surface of section applied to the two-body problem with a mass anomaly provides information about stability and resonances. However, in this case, there are spin-orbit resonances instead of mean motion resonances.

Poincaré surface of sections are maps generated in the phase space through the intersection points of the particle orbits with a fixed section in the system. These maps are generated for fixed values of the Jacobi constant (Equation 16). In Figure 51, we see an example of this map for a system composed of a massive central body with a mass anomaly. The Poincaré surface of section was defined in the plane $y = 0$ around our reference object and for the fixed value of the Jacobi constant $\mathrm{C_J} = 2.032\ \mathrm{R}^2\omega_\mathrm{k}^2$. We distributed the initial conditions on the x-axis.

In Figure 51, the different sets of closed curves, called stability islands, delimit the stable regions of the system. Each stability island is formed by a single quasi-periodic orbit that is named because it does not have a defined orbital period. At the centre of the stability islands, we have periodic orbits. The latter crosses the Poincaré surface of section always at the same points and can be classified into two kinds (POINCARÉ, 1893): those not associated with resonances are the first kind, and those associated with resonance are the second kind.

The point in the centre of all black closed curves is a first kind periodic orbit. In contrast, the points in the centres of the blue and green islands are the second kind orbits associated with the 1:3 and 2:7 resonances, respectively (Figure 51). A single stability island identifies periodic orbits of first kind, while one or more stability islands can identify the orbits of second one. The number of islands for the second kind orbits is related to the order of the resonance (WINTER; MURRAY, 1997b). For example, the pair of blue islands in Figure 51 is formed by quasi-periodic orbits that librate around the periodic orbit associated with the 1:3 resonance, a second-order resonance. In the same vein, each particle in the 2:7 resonance – a fifth-order resonance – generates five islands on the surface of section.

A set of first and second kind orbits belonging to the same resonance usually appears in a continuous Jacobi constant range and defines a family of orbits. The families present evolution in structure and position in the Poincaré surface of section during the variation of the Jacobi constant. In addition to the

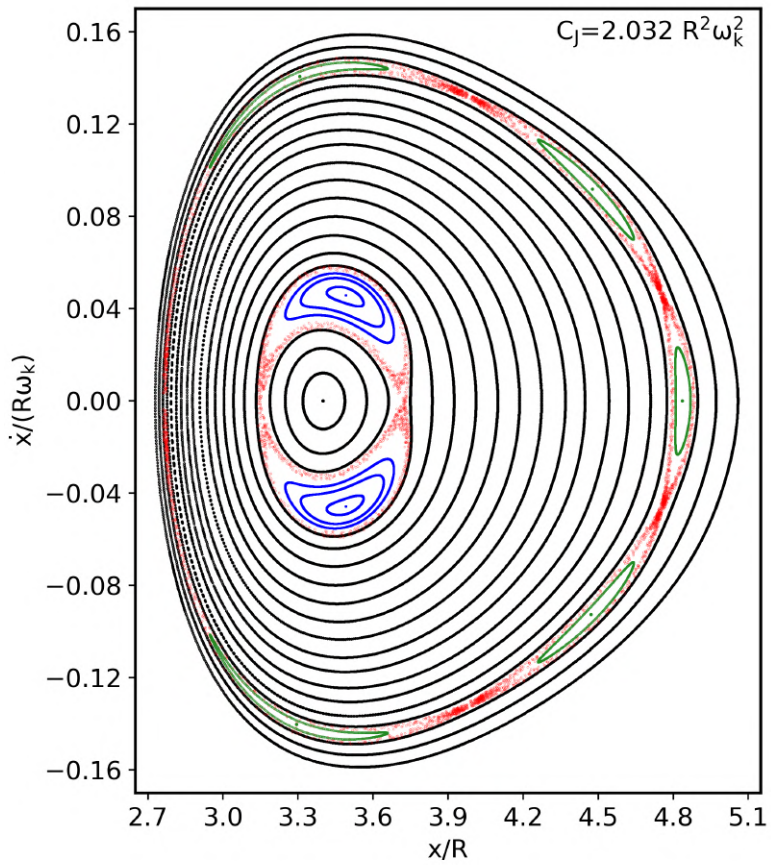

Figure 51 – Poincaré surface of section for $C_J = 2.032\ R^2\omega_k^2$ around an object with $\mu = 10^{-3}$ and $\lambda = 0.471$. The black islands are quasi-periodic orbits associated with the periodic orbit of first kind. Blue islands are associated with the 1:3 resonance and the green ones with the 2:7 resonance. The red points are chaotic orbits that cross the phase plane irregularly.

stability region delimited by the islands, there are also unstable regions filled with scattered red points in the figure, created by chaotic orbits. These chaotic regions are seen around the stability islands associated with the periodic orbits of 1:3 and 2:7 resonances. They are associated with the resonance separatrix and do not enter the stable regions, as we can see in Figure 51. A stable region bounded by quasi-periodic orbits (black curves) separates the two chaotic regions.

In the following sections, we use Poincaré surface of section to explore the stability around bodies with a mass anomaly by varying the central body parameters.

5.5 SYSTEM OVERVIEW

We studied the dynamics around our object by simulating a set of particles with pericentre distance q and eccentricity in the ranges $1 < q/R \leq q_f$ and $0 \leq e \leq 0.5$, respectively ($\Delta e = 0.05$ and $\Delta q/R = 0.01$). q_f is a given value of q for which all particles survive. The particles were simulated for 10,000 orbits. We assumed the parameters λ and μ in the ranges $0.01 \leq \lambda \leq 1$ and $10^{-6} \leq \mu \leq 5 \times 10^{-3}$, respectively. Except for the near-Earth asteroids, we have that the vast majority of small heliocentric bodies have $\omega > \omega_k$ (WARNER; HARRIS; PRAVEC, 2009), justifying the fact that we do not focus on cases with $\lambda > 1$.

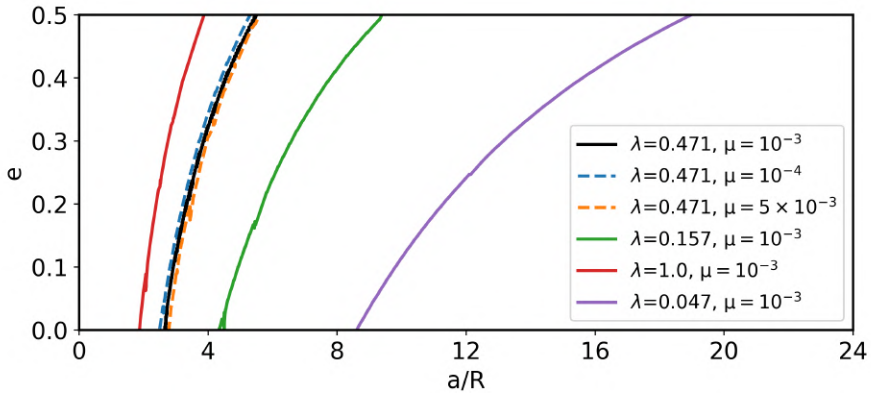

Figure 52 – Boundary curves between the chaotic (on the left) and stable (on the right) regions. The solid black line corresponds to the reference object, while the coloured solid and dashed lines are the cases in which we varied the parameters λ and μ, respectively.

We verified in all numerical simulations the existence of a chaotic region just outside the central body in which particles collide or are ejected from the system. Beyond the chaotic region, there is a stable region, and the boundaries between them are shown in Figure 52. Particles with semi-major axis and eccentricity in the region bounded by the curve (on the left side of the figure) will be lost, while those outside the boundary will survive for at least 10,000 orbits. The solid black line correspond to our reference object, while the solid coloured and dashed lines provide the boundary curves for systems where we vary λ and μ, respectively.

The successive close-encounters of the particle with the mass anomaly are responsible for exchanges of energy and angular momentum, resulting in the variation of the particles' orbital elements. Particles with sufficiently small semi-major axis show orbital evolution with chaotic diffusive character (ROLLIN; SHEVCHENKO; LAGES, 2021). In general, eccentricities in the chaotic region tend to increase, resulting in occasional collisions or until the orbit becomes hyperbolic.

Figure 53 shows a) the trajectory in the rotating frame and b) eccentricity of a pair of particles initially in circular orbits around a central body with parameters $\lambda = 0.471$ and $\mu = 5 \times 10^{-3}$. The semi-major axis of the innermost (red line) and outermost (blue line) particles are $1.74\ R$ and $3.48\ R$, respectively. We observe that the eccentricity shows a secular increase for the innermost particle, reaching values up to 0.15. The particle collides with the central body after about $3.5\omega_k^{-1}$ or ~ 12 spin periods. The eccentricity shows periodic variations for the outermost particle, and the particle remains stable around the central body.

The boundary curves are robust against the final simulation period and are preserved when we extend the simulations to 100,000 orbits. Lages, Shepelyansky e Shevchenko (2017) analyse through the Lyapunov exponent the stability of particles around a contact binary, obtaining a chaotic region coherent with ours. Our boundary curve is also coherent with the region where the particles are lost in the numerical simulations for a Chariklo with a mass anomaly performed by Sicardy et al. (2019).

The boundary between chaotic and stable regions has only a slight dependence on the relative mass anomaly. Although the increase of μ generates only a small swell of the chaotic region, it produces larger increments in eccentricity and the particles are lost more quickly. The extension of the chaotic region is mainly affected by the parameter λ. Decreasing in 10 times the rotating rate, we obtain that

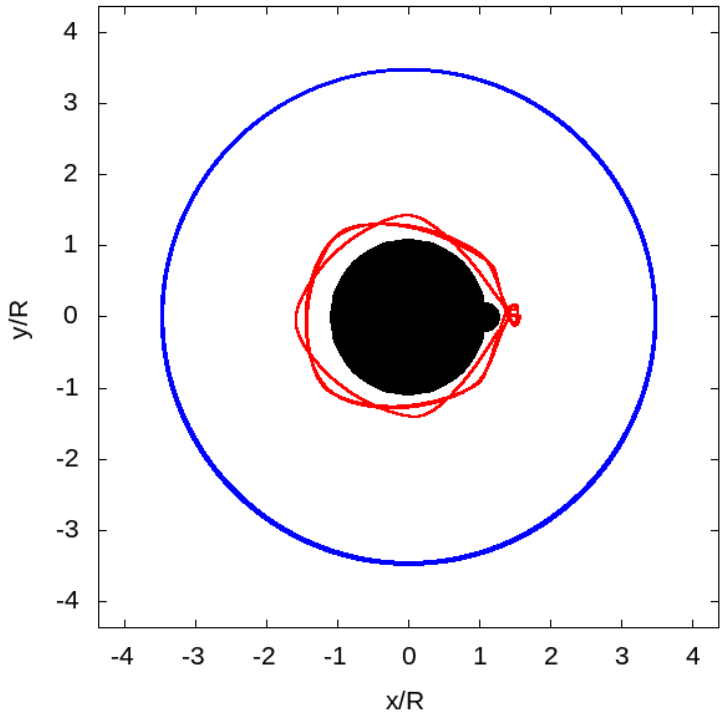

(a)

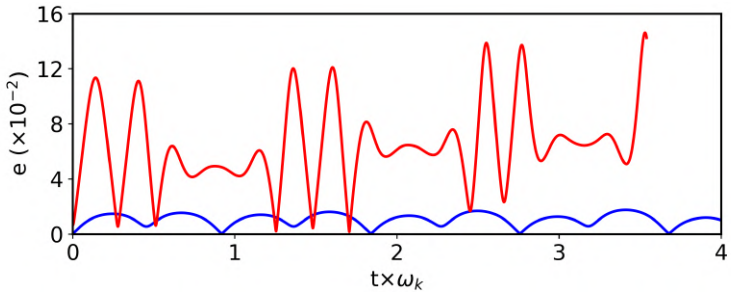

(b)

Figure 53 – a) Trajectory in the rotating frame and b) temporal evolution of the eccentricity. The innermost particle (red line) is at $1.74\ R$ and the outermost one (blue line) at $3.48\ R$, and both are initially in circular orbits. The parameters of the central body are $\lambda = 0.471$ and $\mu = 5 \times 10^{-3}$.

the chaotic region is more than doubled, a result also obtained by Lages, Shepelyansky e Shevchenko (2017).

In order to crudely evaluate the extension of the chaotic region, we calculate for a set of systems the semi-major axis at which a particle in circular orbit will survive for up to 10,000 orbits – the threshold semi-major axis (a_t). The curve fitted from the numerical results is given by

$$\frac{a_t}{R} = \left[1.298 - 0.007\mathcal{M} + 0.006\mathcal{M}^2 + 0.674\lambda^{-0.75}\right], \tag{44}$$

where $\mathcal{M} = -\log\mu$. Physically, we can interpret the threshold semi-major axis as the minimum semi-major axis, beyond which rings and satellites can exist around a body with a mass anomaly.

Figure 54 shows the threshold semi-major axis obtained in the numerical simulations. The x-axis gives the normalized mass anomaly of each simulation, and different colours and markers show the different rotating rates. The solid lines correspond to the curves given by Equation 44 (the colour of

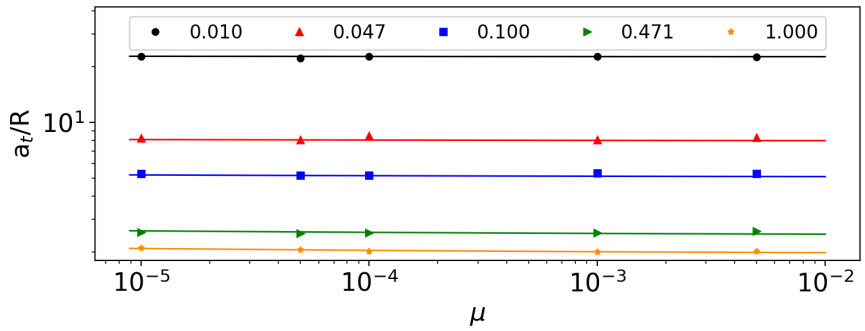

Figure 54 – Threshold semi-major axis obtained in selected numerical simulations (markers) and through Equation 44 (solid lines). The x-axis gives the normalized mass anomalies, and the different colours and markers give the rotating rates.

the lines matches the colour of the markers for the same λ).

Figure 55 shows the position and width of the sectoral resonances, obtained theoretically (Section 5.3), where each panel corresponds to a different normalized mass anomaly, while the rotating rate is fixed as $\lambda = 0.471$. The vertical black line in each panel corresponds to the corotation radius a_c of the system ($a_c = \lambda^{-2/3}$), and the coloured lines give the boundaries of the resonances. The white region on the left provides the initial conditions of particles with pericentre within the central body, and the white area on the right is the stable region. The grey area places the chaotic region.

Since the sectoral resonances are spin-orbit resonances, we have that μ has a minor effect on their locations, as seen in the figure. However, the resonance width will depend on μ, as an increase in the mass anomaly will enhance the gravitational perturbation felt by the particles, allowing larger regions to be connected to the resonance equilibrium points. As we increase the numerical value of m, the resonances approach the corotation radius. The first-order resonances with $|m| > 4$ overlap for the case with $\mu = 10^{-4}$ (Figure 55a). For $\mu = 10^{-3}$ (Figure 55b), we see that additional first-order resonances, such as 4:5 and 3:4, overlap for high eccentricities, while for $\mu = 5 \times 10^{-3}$ (Figure 55c) the overlap is intensified, covering the 2:3 resonance.

The overlap of first-order resonances is generally responsible for eliminating stable regions associated with the resonance (WISDOM, 1980; WINTER; MURRAY, 1997a; WINTER; MURRAY, 1997b). Thus, they should contribute to the chaotic behaviour verified in the systems. It is not by chance that the region surrounding the corotation radius is always chaotic. However, while the overlap helps to carve the chaotic region around the central object, it is not the primary source of chaoticity for the system. Such a fact can be seen in Figure 56a, where the chaotic region covers a region where there is no overlap of first-order resonances. As already mentioned, encounters with the mass anomaly produce chaotic diffusion of the orbits, clearing an entire region that extends beyond the corotation radius. In our numerical simulations, we did not find stable particles in internal resonances.

Analogously to Figure 55, we present in Figure 56 the resonances and chaotic and stable regions around an object with a mass anomaly, now keeping μ constant and varying λ. As we can see in the figure, the parameter affects both the location and the width of the resonances (Equations 17 and 30). When λ is increased by one order, resonances move more than four times closer to the body, while chaotic regions approach it by only a factor of two. So, by changing λ, we change which resonances will be in the stable region.

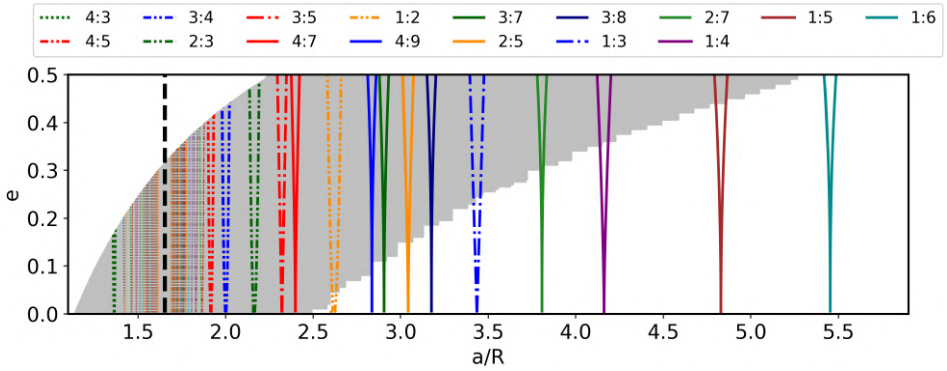

(a) $\mu = 10^{-4}$

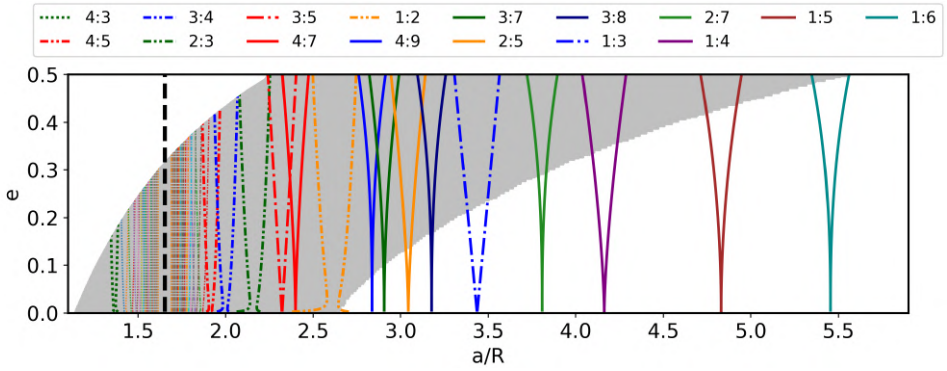

(b) $\mu = 10^{-3}$

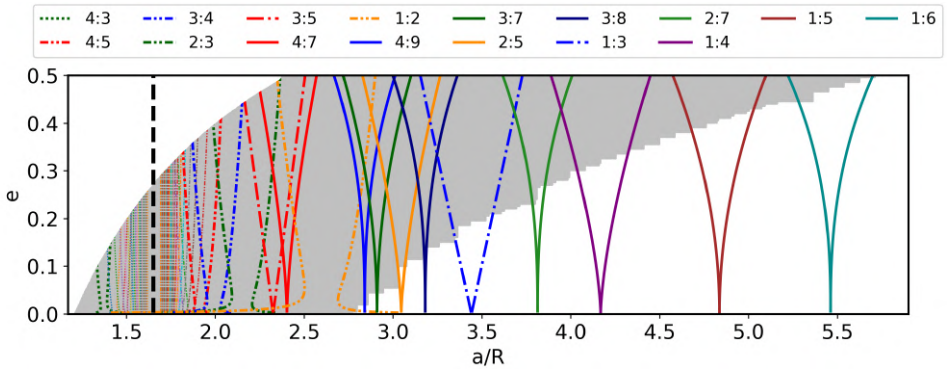

(c) $\mu = 5 \times 10^{-3}$

Figure 55 – Semi-major axis (a/R) versus eccentricity (e) for systems, with $\lambda = 0.471$ and a) $\mu = 10^{-4}$, b) $\mu = 10^{-3}$, and c) $\mu = 5 \times 10^{-3}$. Particles with initial a/R and initial e in the left white region have pericentre within the central body and collide. Particles in the grey area collide with the central body or are ejected, and those in the right white one remain in the system for more than 10,000 orbits. The dashed black lines correspond to the corotation radius, and the coloured lines provide the theoretical boundaries of the resonances. Coloured lines not referenced on the label and close to the corotation radius correspond to first order resonances with $|m| > 4$.

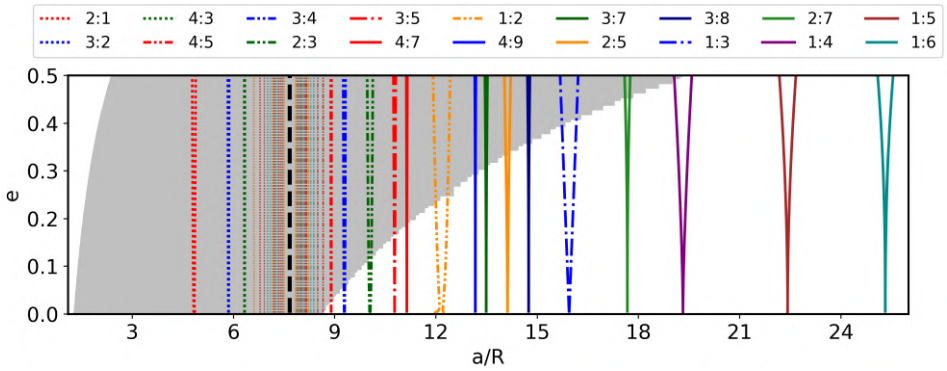

(a) $\lambda = 0.047$

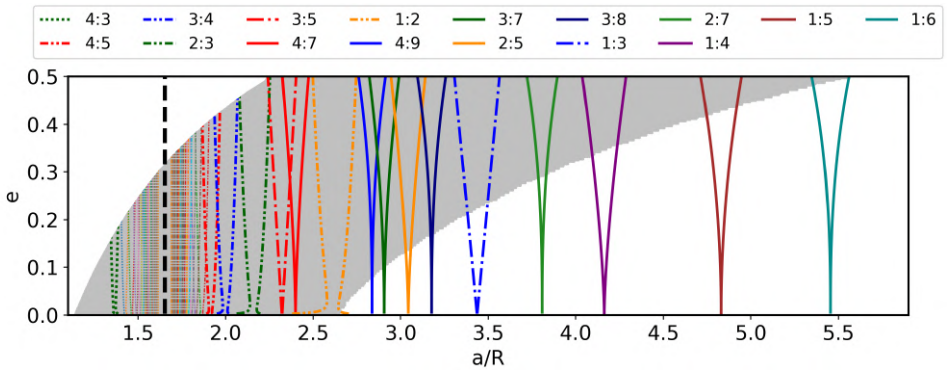

(b) $\lambda = 0.471$

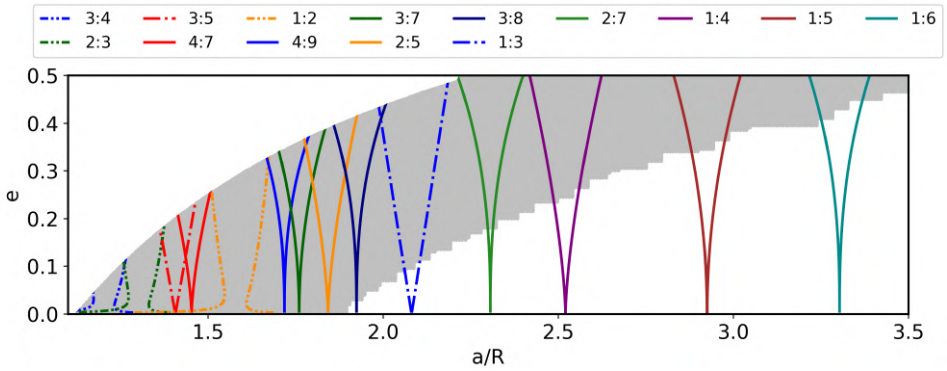

(c) $\lambda = 1.000$

Figure 56 – Semi-major axis (a/R) versus eccentricity (e) of systems with $\mu = 10^{-3}$ and rotating rate λ given in the caption of each panel. Particles with initial conditions in the white region on the left have pericentre within the central body and collide, while those in the grey area show chaotic behaviour. The white region on the right is the stable region. The dashed black line provides the corotation radius, and the coloured lines give the theoretical boundaries of the resonances. Coloured lines not referenced on the label and close to the corotation radius correspond to first order resonances with $|m| > 4$.

In the case shown in Figure 56c, the rotation frequency is equal to the Keplerian one, which places the corotation radius on the surface of the spherical portion of the body. Consequently, the internal resonances and some external ones reside within the central body, with only a few resonances in the stable region. Assuming objects with even faster rotation, we get a narrower chaotic region with fewer resonances outside the object, corresponding to unattractive cases. In the hypothetical case where the spin frequency tends to infinity, it would be not sectoral resonances or chaotic region since it falls in the case of a non-rotating spherical object with a ridge at its equator.

In Section 5.6, we analyse the evolution of the stable region and the external resonances using Poincaré surfaces of section.

5.6 STABLE REGION

In Section 5.5, we have shown the existence of two distinct regions around a spherical body with a mass anomaly: a chaotic region where particles collide or are ejected, and a stable region, which will be our focus in this section. First, we compare the resonance widths obtained by numerical simulations with those predicted by the analytical model described in Section 5.3. We then analyse the motion of test particles in the vicinity of external resonances.

We put our analytical model to the test using the following methodology: i) for a given resonance, we theoretically calculate its central position (Section 5.3.1) and the Jacobi constant (Equation 16), initially assuming a circular orbit; ii) we generate Poincaré surface of section of a broad region around the central position; iii) by visual inspection, we obtain the position of the stable fixed point of the resonance – which corresponds to the real central position of the resonance – and the limits of the widest island surrounding the point – the width of the resonance; iv) then, we successively increase the eccentricity by 10^{-2} and repeat the previous steps until the islands disappear or until we reach $e = 0.5$.

Figure 57 shows the resonance widths obtained theoretically and through the Poincaré surfaces of sections, for our reference object and an object with $\lambda = 0.157$ and $\mu = 10^{-3}$. We found that numerical data agree reasonably well with the analytical model, indicating that the pendulum model with necessary adaptations applies to our system. In general, we obtain that the largest divergences occur for larger eccentricities ($e \gtrsim 0.2$). It is expected, since we assumed first-order approximations in eccentricity in the development of the pendulum model.

We verify that the innermost resonances present the largest displacements in the central position for the reference case. These same displacements are verified for the case with $\lambda = 0.157$ (Figure 57b) in which resonances are at least twice as far from the central body. As a rule, we obtain that displacements depend on the distance a_t/a_c from the resonance to the corotation radius. The central positions we obtained differ by less than 5% from those theoretically obtained, demonstrating the robustness of the analytical method.

After the validity of the analytical model is attested, we turn our attention to the resonance dynamics. Figure 58a shows Poincaré surface of section of the region around the 2:5 resonance for the reference object and $C_J = 1.964\ \mathrm{R}^2\omega_\mathrm{k}^2$. In the figure, we can identify four types of motion in the stable region: periodic motion of first kind, quasi-periodic motion associated with the latter, resonant and chaotic motion – which is not stable despite being within the region defined by us as stable. The single black

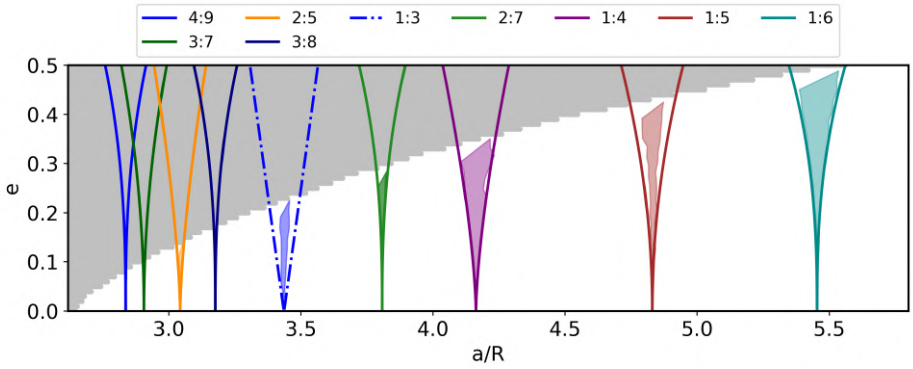

(a) $\lambda = 0.471$ and $\mu = 10^{-3}$

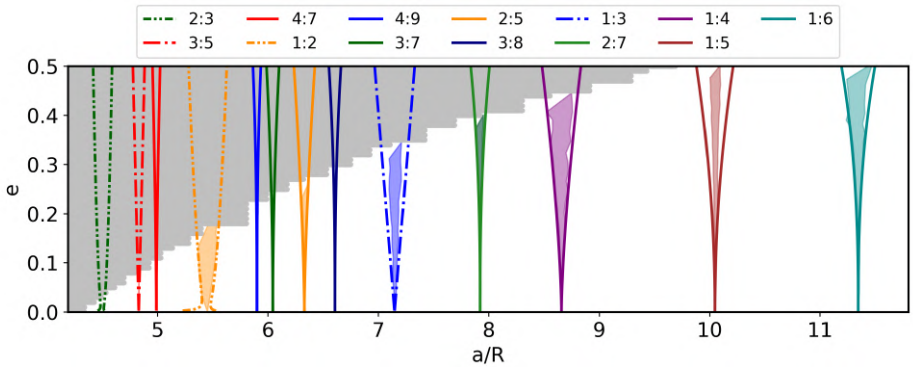

(b) $\lambda = 0.157$ and $\mu = 10^{-3}$

Figure 57 – The width of the external sectoral resonances in the stable region for a) an object with $\lambda = 0.471$ and $\mu = 10^{-3}$ and b) for an object with $\lambda = 0.157$ and $\mu = 10^{-3}$. The solid and dashed lines give the widths predicted by the analytical model, and the coloured filled regions delimit the obtained numerically widths. The grey region corresponds to the chaotic region near the central body.

dot at $x_0/R = 3$ corresponds to the orbit classified as periodic of first kind. Periodic orbits in a Poincaré surface of section divide the x-axis positions into pericentric positions – at smaller x – and apocentric positions – at larger x. Seeing the right part of the figure, we have particles with higher initial eccentricity, forming black closed curves surrounding the periodic orbit. They are quasi-periodic orbits and define regions where particles remain indefinitely in stable motion without other effects.

The orange islands correspond to orbits associated with the 2:5 resonance, where every single dot in the centre of an island is a stable fixed point of the resonance. All three orange dots in the figure correspond to a single periodic orbit of second kind. Due to energy exchanges between the central body and resonant particles, the latter can remain stable even in the presence of other effects, depending on the system conditions.

The red dots show the chaotic zone between the resonant and quasi-periodic orbits. Section 5.7 shows Poincaré surfaces of section of the resonances found around the reference object. As one can see, the chaotic zones at the resonances separatrices are always narrow, showing that the region we named the "stable region" has in fact a few very small strips of confined chaotic motion. Moving to the right in Figure 58a, there is another region with quasi-periodic orbits that extends up to $x_0/R = 3.57$. After this limit, we have the chaotic region, where the red dot at $x_0/R = 3.65$ corresponds to a particle that collides with the central body.

In Figure 58b, we present the evolution of the 2:5 resonance, showing the largest stable orbit of the

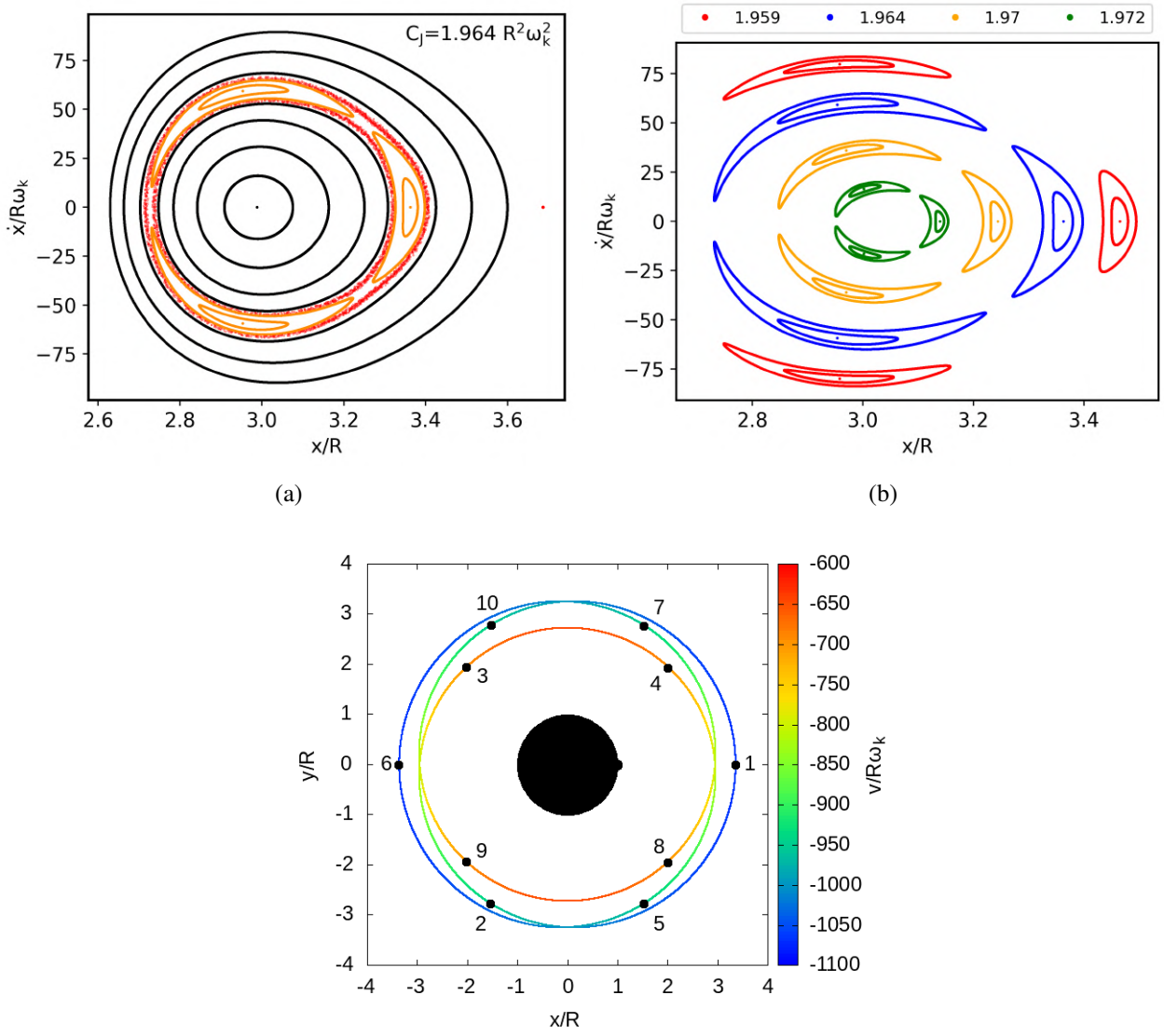

Figure 58 – a) Poincaré surface of section for $C_J = 1.964\ \mathrm{R}^2\omega_\mathrm{k}^2$, with $\lambda = 0.471$ and $\mu = 10^{-3}$. We assume initial conditions with $3.15 \leq x_0/R \leq 3.84$. The black curves are the periodic and quasi-periodic orbits of first kind, and the orange curves are orbits associated with the 2:5 resonance. Red dots correspond to chaotic orbits. b) Evolution of the 2:5 resonance islands, where the colours of the dots correspond to values of C_J given on the figure's label. c) Central orbit of the 2:5 resonance for $C_J = 1.964\ \mathrm{R}^2\omega_\mathrm{k}^2$ in the rotating frame. The temporal evolution of the orbit is given by numbers and dots equally spaced in time, while the colour-coding gives the velocity in the rotating frame.

resonance, an intermediate one, and the central orbit, for different values of the Jacobi constant. Since the 2:5 resonance is a third-order resonance ($j = 3$), each initial condition produces three distinct islands in Poincaré surfaces of section. Except for the case with $C_J = 1.959\ \mathrm{R}^2\omega_\mathrm{k}^2$, we see that the three islands shrink and get closer as the value of C_J increases. The Jacobi constant and the eccentricity are inversely proportional, so the latter decreases from right to left in the figure. The resonance width decreases with the eccentricity, and the resonant orbits tend towards the periodic orbit of the first kind, explaining why the islands shrink until they disappear.

To understand why the largest red island is smaller than the largest blue island (Figure 58b), we present in Figure 59a the Poincaré surfaces of section for $C_J = 1.959\ \mathrm{R}^2\omega_\mathrm{k}^2$, and in Figure 59b, the theoretical and numerical boundaries of the 2:5 resonance. The red dashed line places the case with $C_J = 1.959\ \mathrm{R}^2\omega_\mathrm{k}^2$ and the grey area is the chaotic region. For this value of Jacobi constant, the resonance is at the edge between the stable and chaotic regions. As a result, the particles most bounded to the resonance - closer to the stable fixed point – remains stable (in orange), while particles closer to the resonance boundaries initially follow the pattern expected for resonant particles. However, they are showing the stickiness phenomenon behaviour mimicking the resonant behaviour, but they are lost from the system at some point.

The eccentricity of one of these less bounded particles is shown in Figure 59c by the solid red line, while the eccentricity of the central resonant orbit is the solid orange line. Both particles show a periodic variation in eccentricity. However, the eccentricity of the less bounded particle also shows an increase, reaching $e \sim 0.145$.

Figure 58c shows, in the rotating frame, the periodic orbit of the second kind seen in Figure 58a, where the colour-coding gives the velocity. Since the particle is at the stable fixed point of the resonance, the orbit is closed. Also, the orbit is retrograde ($v < 0$) because the resonance is beyond the corotation radius. As the central body is symmetric, there will always be at least one axis that divides the orbit into two symmetric parts. For example, for the orbit shown in Figure 58c, this axis corresponds to $y = 0$.

Sicardy (2020) discusses some additional symmetries expected for the trajectory of a particle in a $m : m - j$ sectoral resonance. The orbit is invariant by a rotation of $360/|m|$ deg, and it has a total of $|m|(j - 1)$ self-crossing. For the 2:5 case ($j = 3$ and $m = -2$), we see that the orbit is invariant by a rotation of 180 deg and has four self-crossing.

A peculiarity of our system is the positions of the particle pericentre and apocentre. In RP3BP, in which the disturbing body is at $x_0/R = 1$ and the particle is initially at $x_0/R < 1$, the gravitational effect felt by the particle is weaker (stronger) when it is on the x-axis at $x/R > 0$ ($x/R < 0$). Consequently, the particle starts at the pericentre, the apocentre being in the opposite direction. In our case, we have the opposite scenario. The orbit position where a particle feels the strongest gravitational effect is on the x-axis at $x/R > 0$ – where the modulus of gravitational force is the sum of the forces of the two portions of the central body. Thus, a particle initially on the x-axis ($x/R > 0$) starts at its apocentre (minimum velocity), as we can see from the dot labelled “1” in Figure 58.

Figure 60 shows a) the Poincaré surface of section for $C_J = 2.087\ \mathrm{R}^2\omega_\mathrm{k}^2$, b) the whole evolution of the islands of the 1:4 resonance, and c) the trajectory of a particle at a stable fixed point of the

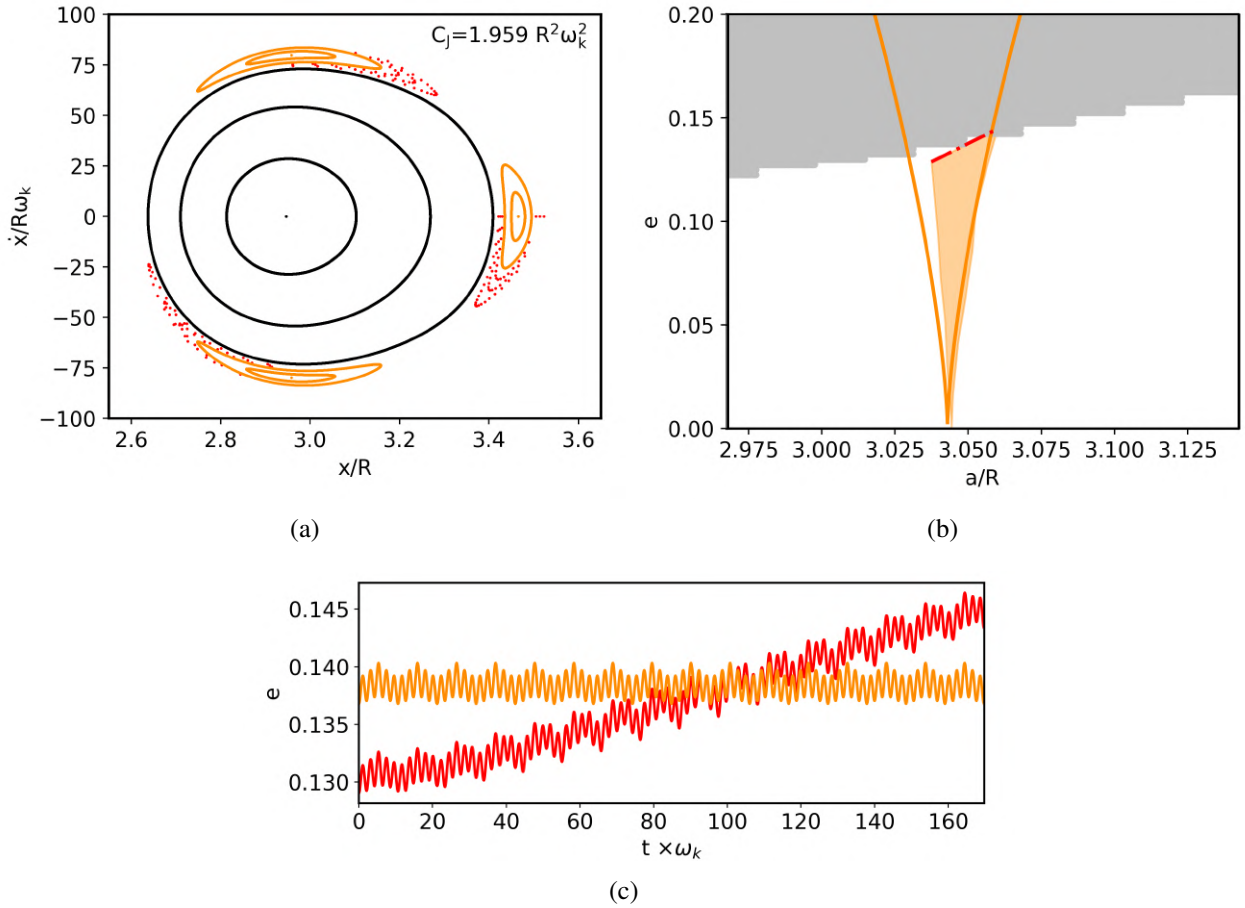

Figure 59 – a) Poincaré surface of section for $C_J = 1.959\ \mathrm{R}^2\omega_\mathrm{k}^2$ where the periodic/quasi-periodic orbits of first kind are in black, the 2:5 resonance islands are in orange, and the particles in the chaotic region are in red. b) Theoretical boundaries of the 2:5 resonance are shown by the solid orange lines. In contrast, the filled orange and grey regions are regions numerically obtained for the 2:5 resonance and the chaotic region, respectively. The red dashed line gives the initial conditions of the simulation with $C_J = 1.959\ \mathrm{R}^2\omega_\mathrm{k}^2$. c) Eccentricity of a pair of particles: the one that remains in the system is orange, and the unstable one is red.

resonance. As shown in Figure 60a, the overview of the resonance neighbourhood is similar to the 2:5 resonance, with a narrow, chaotic region at the resonance boundaries, surrounded by a region with periodic/quasi-periodic orbits. A crucial difference, however, is obtained in the resonance islands. While the 2:5 resonance has three stable fixed points, we obtained in Figure 60a six stable points for the 1:4 resonance.

To understand the dynamics of the resonance, we colour green (Figure 60a) the trajectory of a particle near one of these points. The particle is responsible for forming three islands around three of the stable fixed points (in green in the figure). This fact leads us to conclude that the resonance is the 1:4 (of third-order) and not the 2:8 (of sixth-order) as we would obtain in the ellipsoidal problem. The islands produced by the particle have the particularity of being asymmetric in relation to the x-axis – we say that the particle is in asymmetric libration (BEAUGÉ, 1994; WINTER; MURRAY, 1997b).

In Figure 60b, we highlight the Poincaré surface of section islands of some particles by plotting them in black, intending to show the asymmetric libration. Each island produced by a particle in asymmetric libration has a mirror image obtained from the motion of a different particle in asymmetric

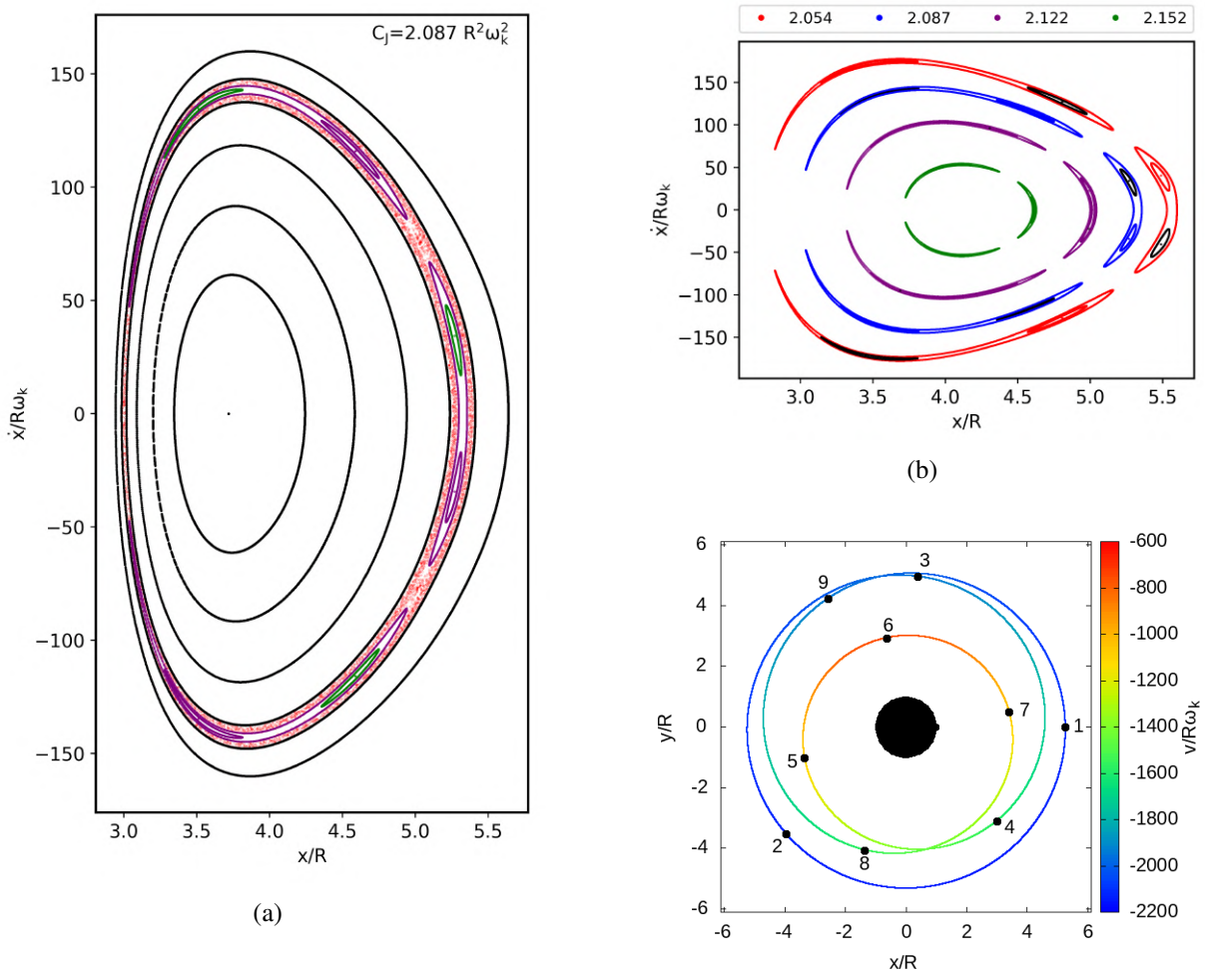

Figure 60 – a) Poincaré surface of section for $C_J = 2.087\ \mathrm{R}^2\omega_\mathrm{k}^2$, with $\lambda = 0.471$ and $\mu = 10^{-3}$. We assumed initial conditions with $3.70 \leq x_0/R \leq 5.97$ and separated the distinct types of orbits by colour: the periodic/quasi-periodic orbits of first kind are in black, the 1:4 resonance orbits are in purple and green and chaotic ones in red. b) Resonance islands for different values of C_J. The label on the panel gives the colour of the largest island for each value of C_J. c) Central orbit in the rotating frame of one of the families associated with the 1:4 resonance (in green in the top panel) for $C_J = 2.087\ \mathrm{R}^2\omega_\mathrm{k}^2$. The numbers and colours on the panel provide time evolution and velocity in the rotating frame, respectively.

libration. Closer to the resonance boundaries, we also get "horseshoe fashion" orbits encompassing pairs of fixed points of two different trajectories.

When we refer to asymmetric resonance or libration, we refer to the symmetry of the trajectory in Poincaré surface of section and not in the xy-plane. As already mentioned, the trajectory in the xy-plane of the resonant particles has a symmetry axis due to the symmetric mass distribution in the central body. For example, in Figure 60c, the axis of symmetry would correspond to the axis connecting the point "6" to the centre of the system.

Several works such as Message (1970), Frangakis (1973b), Frangakis (1973a), Taylor et al. (1978), Bruno (1994), Beaugé (1994) and Winter e Murray (1997b) have studied asymmetric periodic orbits in the context of RP3BP, showing that these orbits are characteristics of $1:1+p$ resonances and are obtained only for particles with eccentricities above a critical value. Similar to particles in $m:m-j$

resonance with $m \neq -1$, the ones with eccentricity lower than this threshold value present symmetric libration in Poincaré surface of section. We obtained these same results for the case with mass anomaly. In Figure 60b, the critical eccentricity is reached somewhere between the Jacobi constants $2.122\ \mathrm{R}^2\omega_\mathrm{k}^2$ and $2.152\ \mathrm{R}^2\omega_\mathrm{k}^2$. Carrying out a set of Poincaré surface of section in this interval, we obtain that the critical eccentricity for the 1:4 resonance is $e \sim 0.167$ ($2.136\ \mathrm{R}^2\omega_\mathrm{k}^2$).

Figure 61a shows one island of the 1:4 resonance for the critical eccentricity ($2.136\ \mathrm{R}^2\omega_\mathrm{k}^2$, in green), for $2.133\ \mathrm{R}^2\omega_\mathrm{k}^2$ (in purple) and $2.139\ \mathrm{R}^2\omega_\mathrm{k}^2$ (in blue). For the highest value of Jacobi constant (smallest eccentricity), we see a single stable point in the figure related to a single family of resonant orbits. The critical eccentricity is reached by decreasing the Jacobi constant, and the stable point bifurcates into two points (the stars in the figure). Each of the points gives rise to an independent family of resonant orbits. The x-axis, which previously allocated the single stable point, now allocates the unstable equilibrium point after the bifurcation, corresponding to the inflexion position of the "horseshoe fashion" orbits.

Figure 61b shows the trajectories of the stable points given by stars in Figure 61a. The orbits are mirror versions of each other. The same is obtained for eccentricities in Figure 61c, in which the red curve is the mirror version of the black one with respect to time $t \approx 4.2\omega_k^{-1}$ (pericentre passage time). As discussed in Bruno (1994), the bifurcation of the stable points is related to the indirect term of the disturbing function, which differs from zero only for $1 : 1 + p$ resonances (Equation 5).

We show another example of particles in asymmetric libration in Figure 62. This figure shows a) Poincaré surface of section of the region of 1:2 resonance for a central body with $\lambda = 0.157$ and $\mu = 10^{-3}$, b) the whole evolution of the resonance, and c) the trajectory of a particle in a stable fixed point of the resonance. As in the reference case, chaotic behaviour is seen only in a narrow region in the separatrices, with a large regular region of periodic/quasi-periodic orbits of first kind around the resonances. For the 1:2 resonance, we have a low critical eccentricity ($e \sim 10^{-2}$), with symmetric libration only in the cases where the resonance islands are tiny.

Trajectories of particles in 1:2 resonance are the only ones without self-crossings in the rotating frame, as we can see in Figure 62c. Such fact has implications for the temporal evolution of a ring of particles, as self-crosses increase collisions between particles. In this context, a ring with particles into the 1:2 resonance or in periodic/quasi-periodic orbits of first kind – which do not show self-crossing either – should have a lower rate of collisions than a ring with particles in other resonances, disregarding other external effects. The particles shown in Figure 60c and Figure 62c do not start at the apocentre of the orbit because they are not initially with $\dot{x} = 0$. A particle around a body with mass anomaly will start at its apocentre only when that condition is met.

5.7 POINCARÉ SURFACES OF SECTION FOR THE REFERENCE OBJECT

For completeness, we present here Poincaré surface of sections of the remaining resonances in the stable region of the reference case – $\lambda = 0.471$ and $\mu = 10^{-3}$. All figures have three panels, following the pattern:

a) panel (a) shows the Poincaré surface of section of a broad region, with the value of C_J given

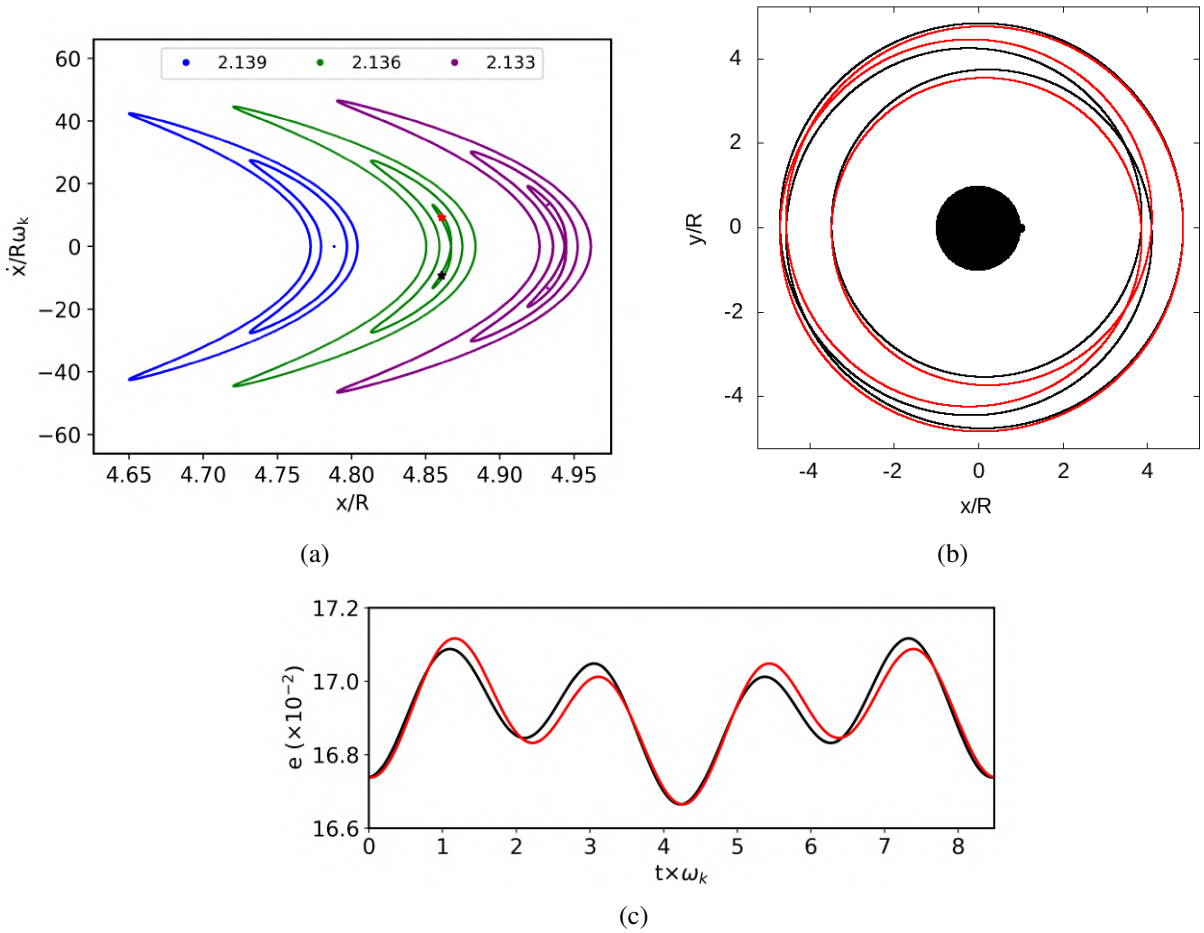

Figure 61 – a) Poincaré surface of section of one island of the 1:4 resonance for $C_J = 2.133$, 2.136, and 2.139 $\mathrm{R}^2\omega_\mathrm{k}^2$ (in purple, green, and blue, respectively). The black and red stars are the stable points obtained after bifurcation. b) Trajectories and c) eccentricities of the stable points given by stars in panel (a), where the colour of the solid lines coincides with the colour of the star for the same stable point.

in the upper right corner of the figure. Black closed curves are periodic/quasi-periodic orbits of first kind. In red is the chaotic motion. Closed coloured curves correspond to islands of the resonance given on the figure label. In the case of $1{:}1 + p$ resonances, we plot some islands with different colours to show the asymmetric libration of the resonance.

b) panel (b) shows the entire evolution of the resonance. The label at the top gives the colour of the largest island for each C_J value. In the case of $1 : 1 + p$ resonances, we plotted some islands in black to highlight the asymmetric libration observed in such resonances.

c) panel (c) shows the trajectory of the central orbit of the resonance in the rotating frame. The value of C_J is the same as panel (a). We show the temporal evolution of the orbit by numbers and dots equally spaced in time, while colour-coding gives the velocity in the rotating frame.

The pattern above was not followed only for the 4:9 resonance, for which we do not show the panel (b). We got only one value of C_J in the stable region for this resonance. Figures are given from the resonance closest to the central body to the farthest. Figure 63-Figure 69 correspond to 4:9, 3:7, 3:8, 1:3, 2:7, 1:5, and 1:6 resonances, respectively.

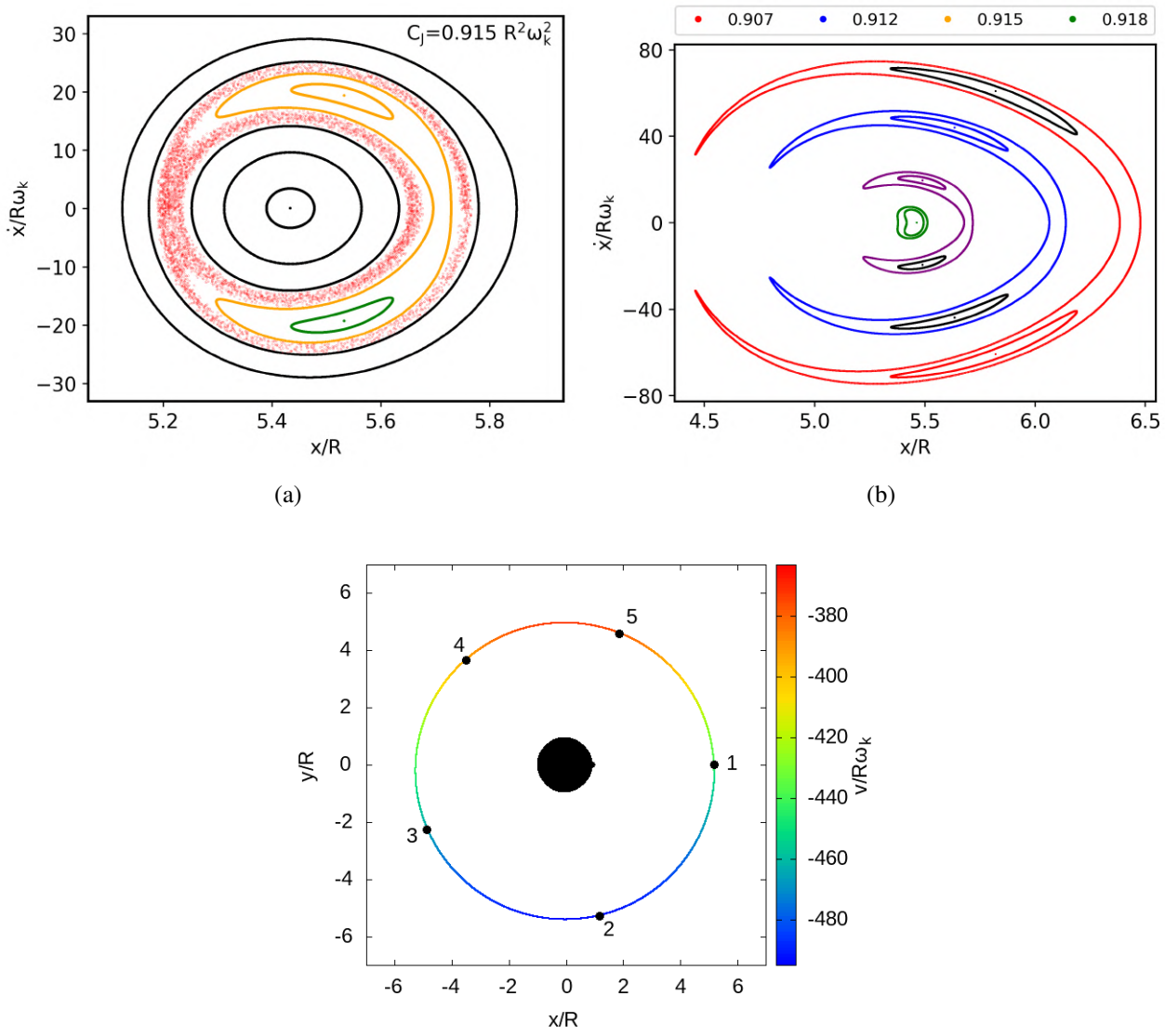

Figure 62 – a) Poincaré surface of section for $C_J = 0.915\ \mathrm{R}^2\omega_\mathrm{k}^2$, with $\lambda = 0.157$ and $\mu = 10^{-3}$. The non-resonant orbits are in black. Particles in 1:2 resonance and chaotic orbits are in orange and green and red, respectively. b) Poincaré surface of section for some particles in 1:2 resonance, with $C_J = 0.907$, 0.912, 0.915, and $0.918\ \mathrm{R}^2\omega_\mathrm{k}^2$. Different colours of the islands involved by the same "horseshoe fashion" orbit correspond to different particles. c) Trajectory of a stable fixed point shown in orange in the top panel, where the colour-coding gives the velocity and the numbers and dots, the time evolution of the orbit.

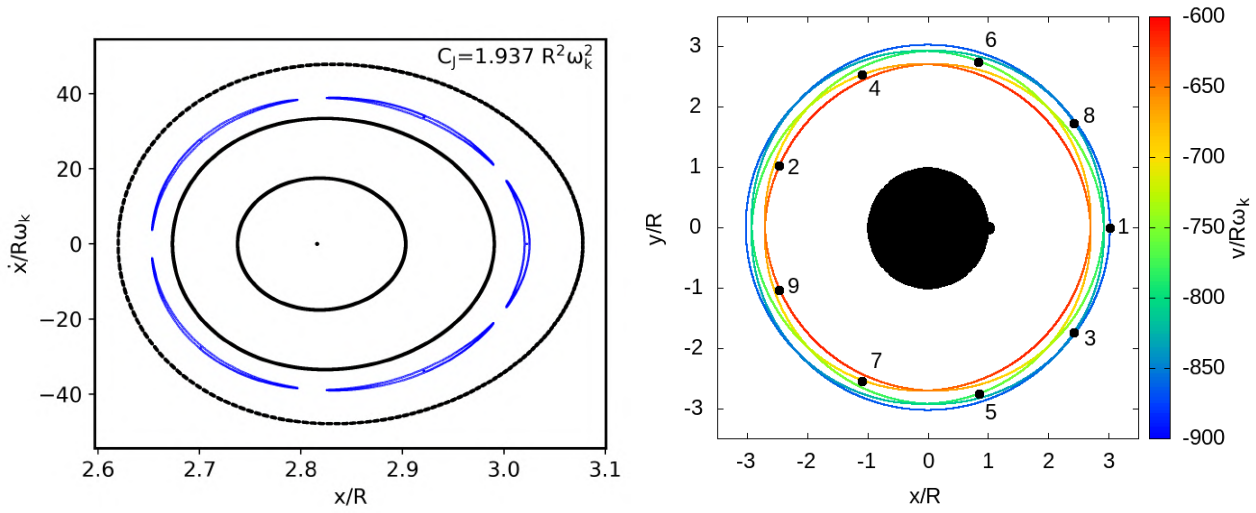

(a) (b)

Figure 63 – a) Poincaré surface of section for $C_J = 1.937\ \mathrm{R}^2\omega^2$ in which the black curves are the periodic and quasi-periodic orbits of first kind and the blue curves are orbits associated with the 4:9 resonance. b) Central orbit of the 4:9 resonance for $C_J = 1.937\ \mathrm{R}^2\omega^2 2$ in the rotating frame. The temporal evolution of the orbit is given by numbers and dots equally spaced in time, while the colour-coding gives the velocity in the rotating frame.

5.8 APPLICATION TO THE CHARIKLO SYSTEM

Leiva et al. (2017) using stellar occultation data, investigated the shape of Chariklo, obtaining four distinct shapes models for the object: a sphere, a MacLaurin spheroid, a triaxial ellipsoid, and a Jacobi ellipsoid. According to Sicardy et al. (2019), observational data suggest the presence of topographic features of typical heights of 5 km in the spherical solution. This fact places Chariklo as a possible body with a mass anomaly. In this section, we briefly study the dynamics around Chariklo, in particular in the region of the ring. The rings have orbital radii of 391 km and 405 km, with radial widths of 7 km and 3 km, respectively (BÉRARD et al., 2017).

We performed numerical simulations adopting the spherical Chariklo given by Leiva et al. (2017), $\lambda = 0.471$, with a mass anomaly of $\mu = 7 \times 10^{-6} = (5\ \mathrm{km}/(2 \times 129\ \mathrm{km}))^3$. Figure 70 shows the width of the resonances and the location of the chaotic region. The vertical dashed line gives the corotation radius and the central location of the rings by the vertical dotted lines. We obtained a threshold semi-major axis of $a_t/R = 2.5$ in the numerical simulation. This result is in good agreement with our adjusted equation (Equation 44) which returns $a_t/R = 2.6$. The 1:2 resonance is the only first-order resonance beyond the chaotic region. The region beyond the chaotic one is essentially stable, hosting the rings and possibly moons, depending on their eccentricity.

Leiva et al. (2017) propose that the inner ring is associated with the 1:3 spin-orbit resonance. Therefore, we studied this resonance in detail, as it is close to both rings. Figure 71a shows Poincaré surface of section for the largest Jacobi constant obtained by us for the 1:3 resonance ($C_J = 2.038\ \mathrm{R}^2\omega_\mathrm{k}^2$). For this value of C_J, the resonance has not reached the critical eccentricity, and we obtain only a single symmetric periodic orbit. A narrow, chaotic region surrounds the islands of resonance, but the whole set is surrounded by a stable region associated with periodic/quasi-periodic orbits of first kind.

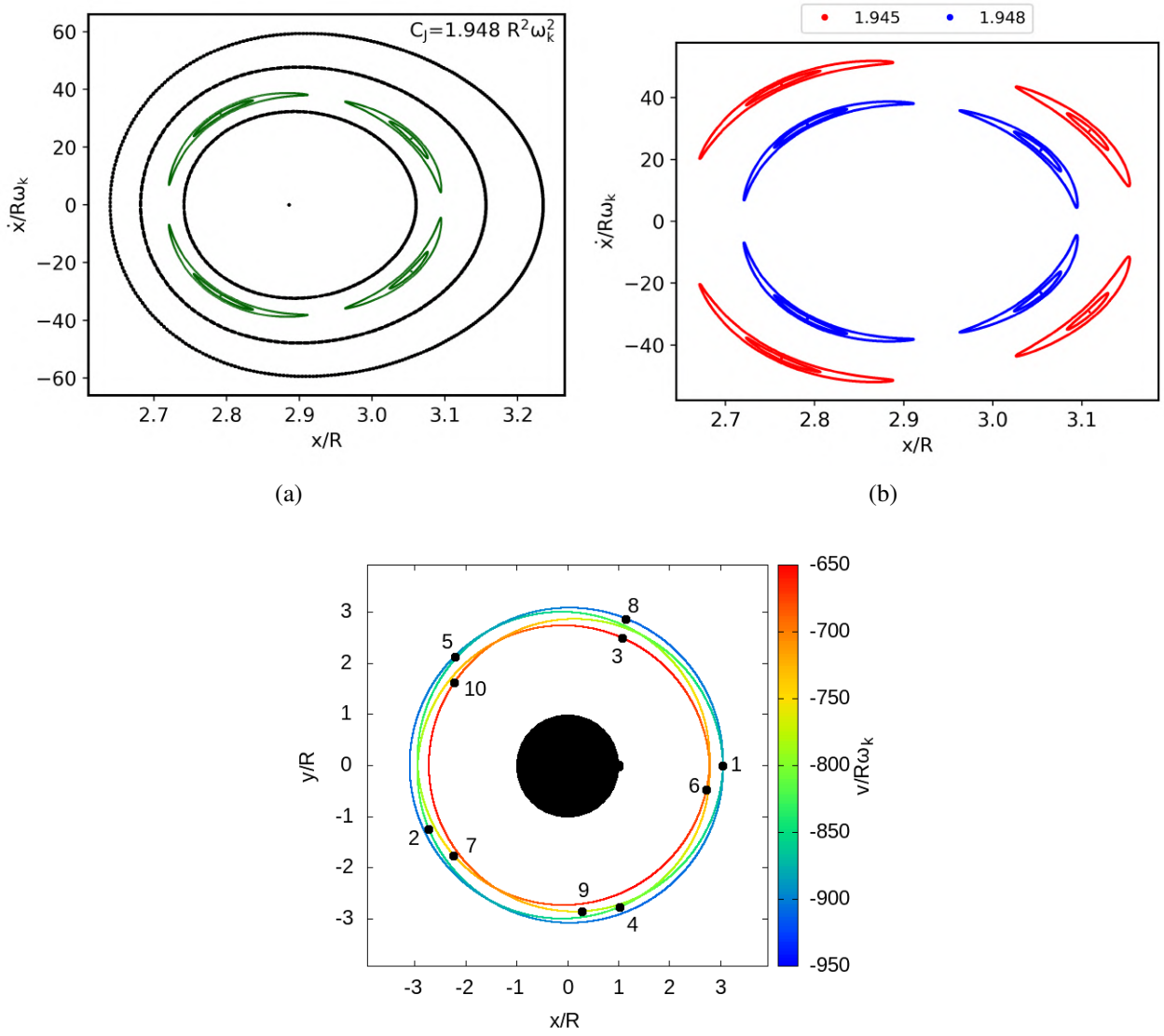

(a) (b)

(c)

Figure 64 – a) Poincaré surface of section for $C_J = 1.948\ \mathrm{R}^2\omega^2$ in which the periodic/quasi-periodic orbits of first kind are in black and the 3:7 resonance orbits are in green. b) Resonance islands for different values of C_J given in the label of the figure. c) Central orbit of the 3:7 resonance for $C_J = 1.948\ \mathrm{R}^2\omega^2$. The numbers and colours on the panel provide time evolution and the velocity in the rotating frame, respectively.

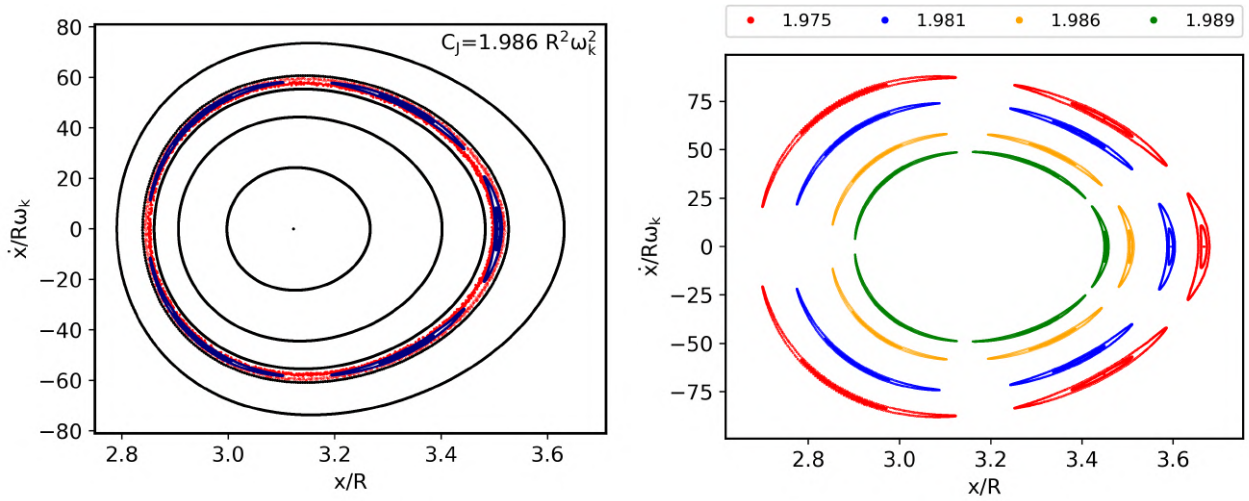

(a) (b)

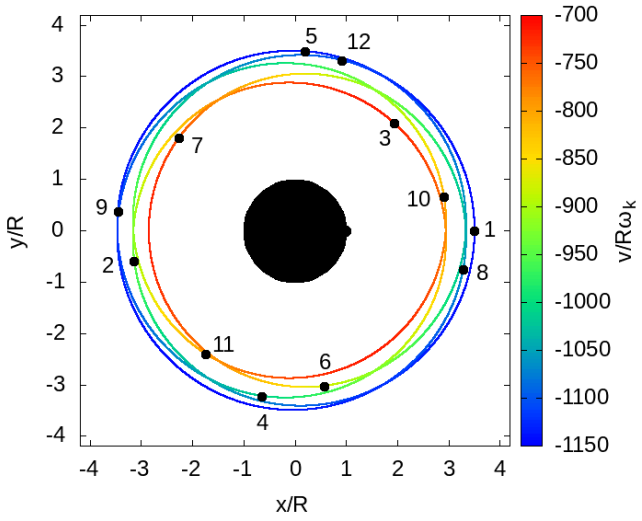

(c)

Figure 65 – a) Poincaré surface of section for $C_J = 1.986\ \mathrm{R}^2\omega^2$. Black curves are periodic and quasi-periodic orbits of first kind, and blue curves are orbits associated with the 3:8 resonance. Red dots correspond to chaotic orbits. b) Evolution of the 3:8 resonance islands, where the colours of the dots correspond to values of C_J given on the label of the figure. c) Central orbit of the 3:8 resonance for $C_J = 1.986\ \mathrm{R}^2\omega^2$ in the rotating frame. The temporal evolution of the orbit is given by numbers and dots equally spaced in time, while the colour coding gives the velocity in the rotating frame.

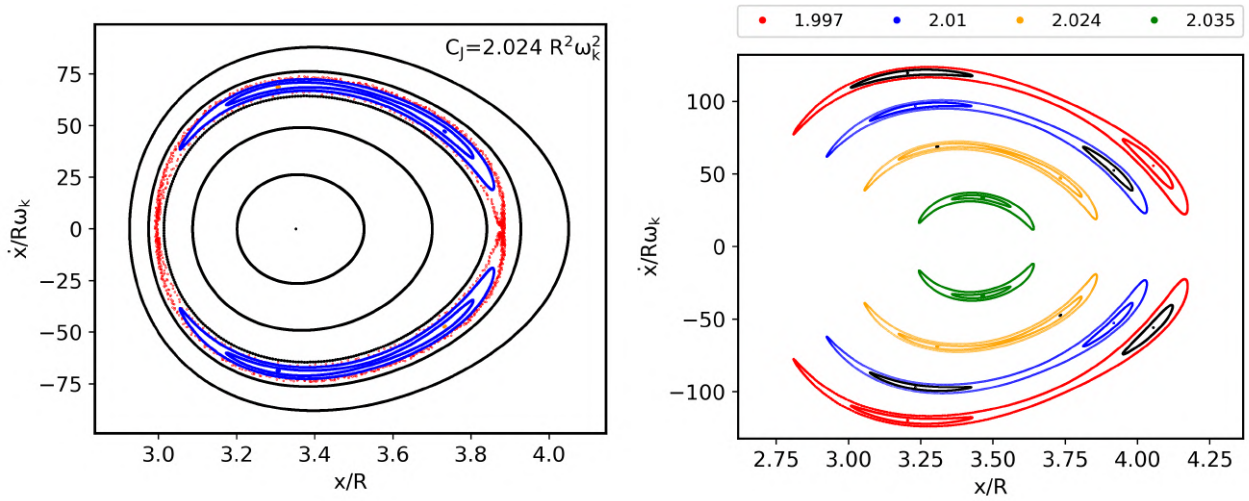

(a) (b)

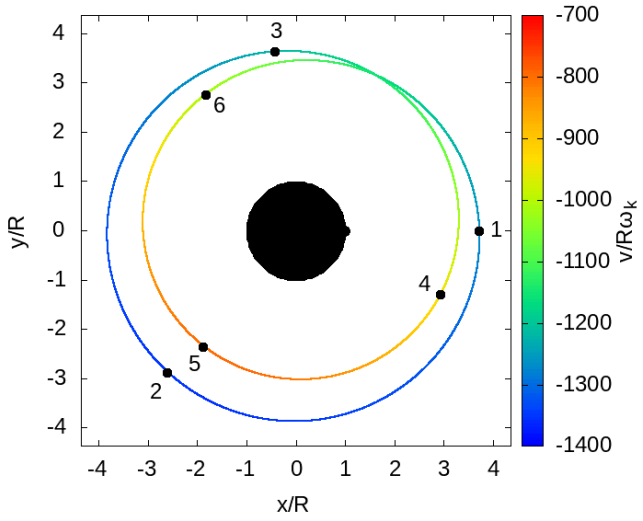

(c)

Figure 66 – a) Poincaré surface of section for $C_J = 2.024\ \mathrm{R}^2\omega^2$. Periodic/quasi-periodic orbits of first kind are in black, the 1:3 resonance orbits are in blue and orange and chaotic ones in red. b) Resonance islands for different values of C_J. The label on the panel gives the colour of the largest island for each value of C_J. c) Central orbit in the rotating frame of one of the families associated with the 1:3 resonance (in blue in panel a) for $C_J = 2.024\ \mathrm{R}^2\omega^2$. The numbers and colours on the panel provide time evolution and the velocity in the rotating frame, respectively.

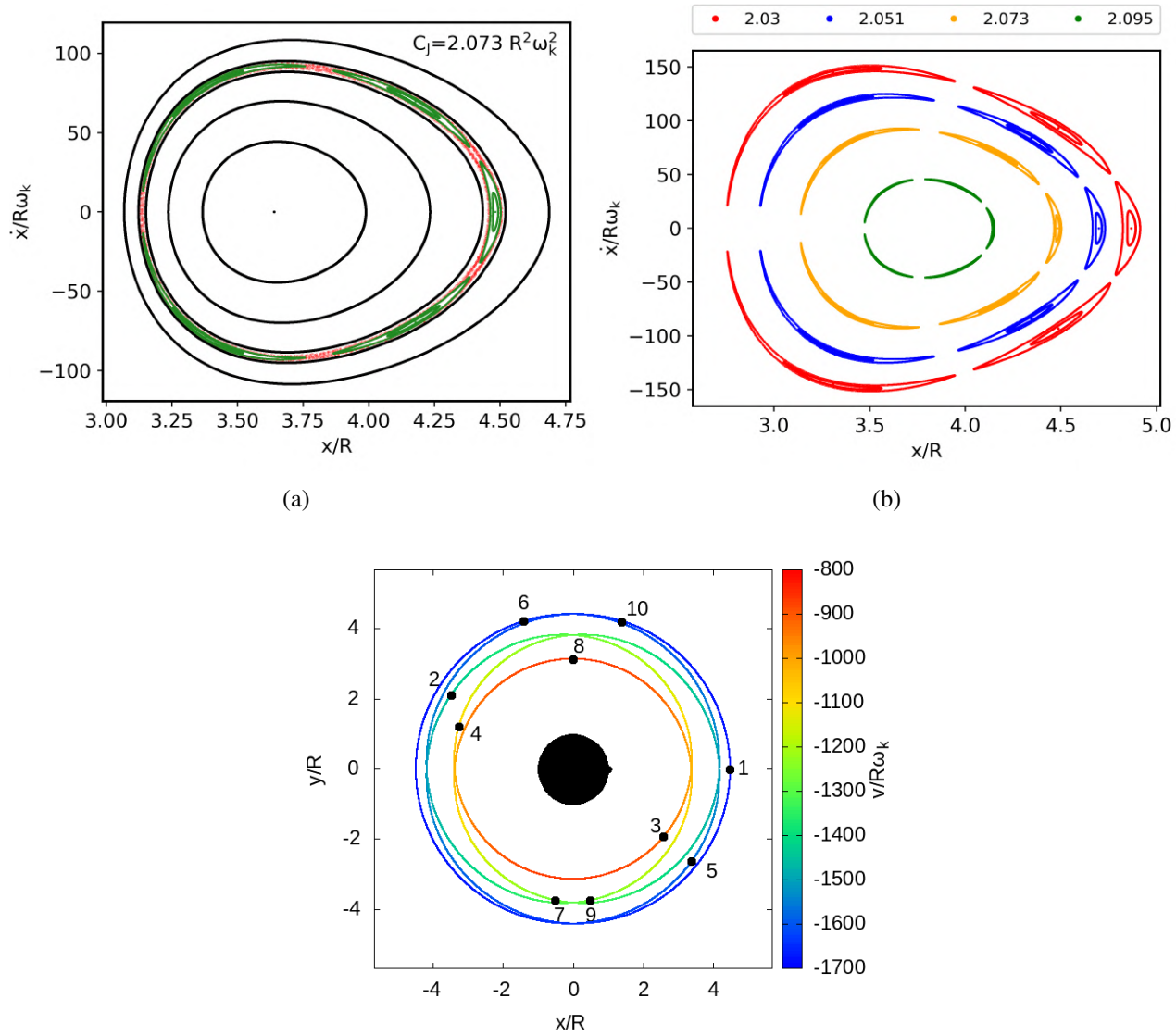

(a) (b)

(c)

Figure 67 – a) Poincaré surface of section for $C_J = 2.073\ \mathrm{R}^2\omega_\mathrm{k}^2$. Black curves are periodic and quasi-periodic orbits of first kind, and green curves are orbits associated with the 2:7 resonance. Red dots correspond to chaotic orbits. b) Evolution of the 2:7 resonance islands, where the colours of the dots correspond to the values of C_J given on the label of the figure. c) Central orbit of the 2:7 resonance for $C_J = 2.073\ \mathrm{R}^2\omega_\mathrm{k}^2$ in the rotating frame. The temporal evolution of the orbit is given by numbers and dots equally spaced in time, while the colour coding gives the velocity in the rotating frame.

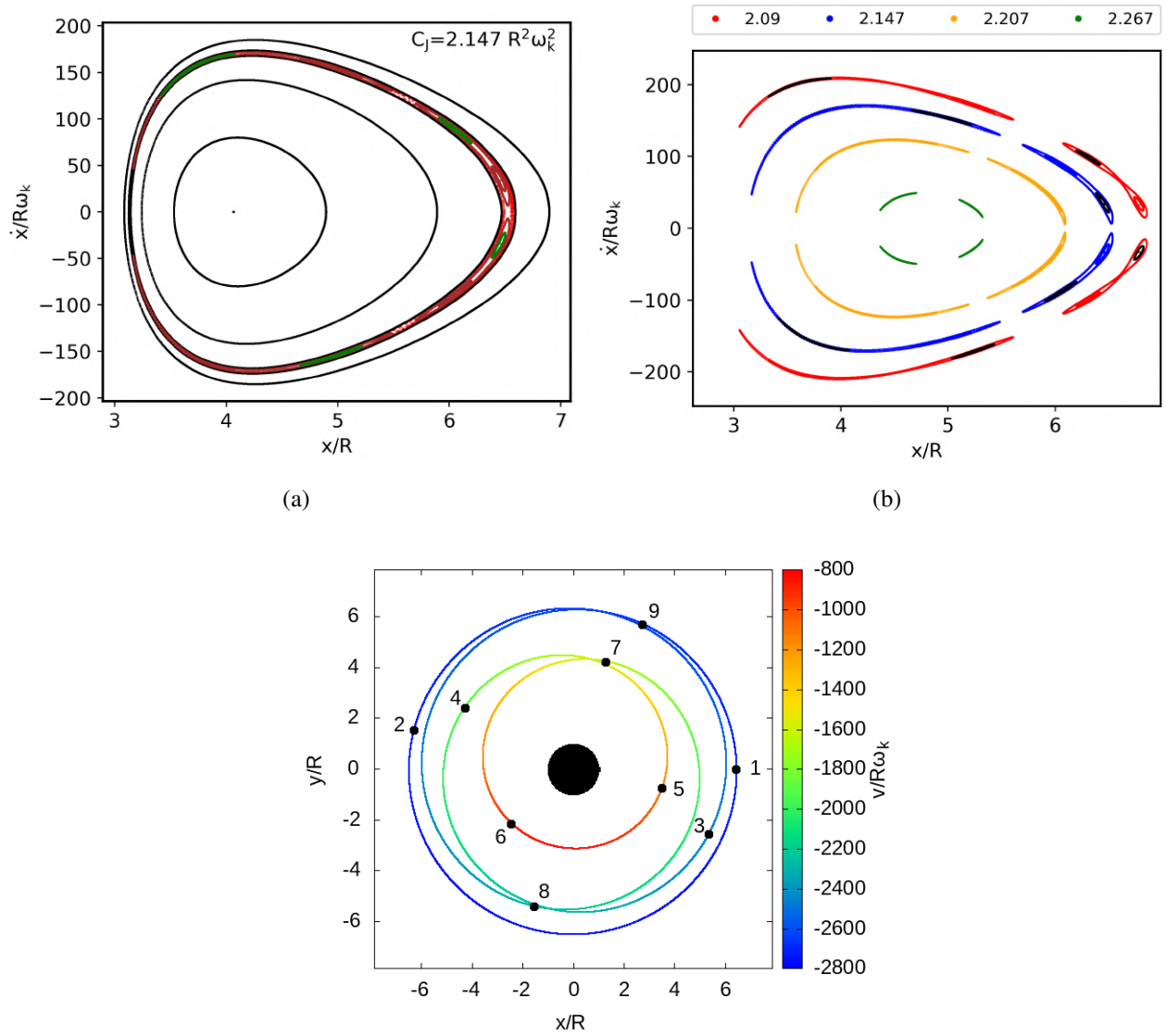

(a) (b)

(c)

Figure 68 – a) Poincaré surface of section for $C_J = 2.147\ \mathrm{R}^2\omega_\mathrm{k}^2$. The periodic/quasi-periodic orbits of first kind are in black, the 1:5 resonance orbits are in brown and green and chaotic ones in red. b) Resonance islands for different values of C_J. The label on the panel gives the colour of the largest island for each value of C_J. c) Central orbit in the rotating frame of one of the families associated with the 1:5 resonance (in brown in panel a) for $C_J = 2.147\ \mathrm{R}^2\omega_\mathrm{k}^2$. The numbers and colours on the panel provide time evolution and the velocity in the rotating frame, respectively.

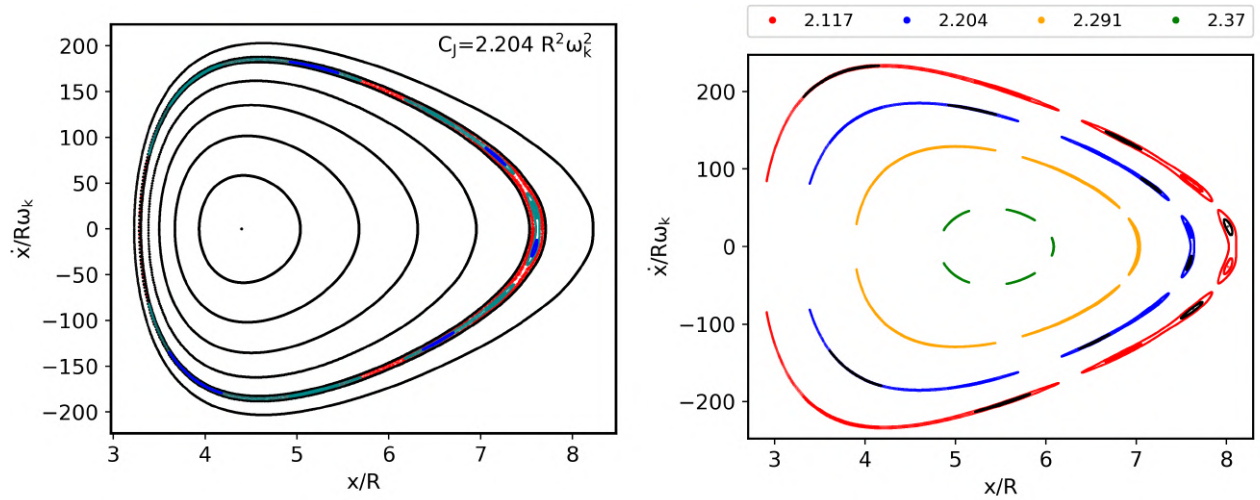

(a) (b)

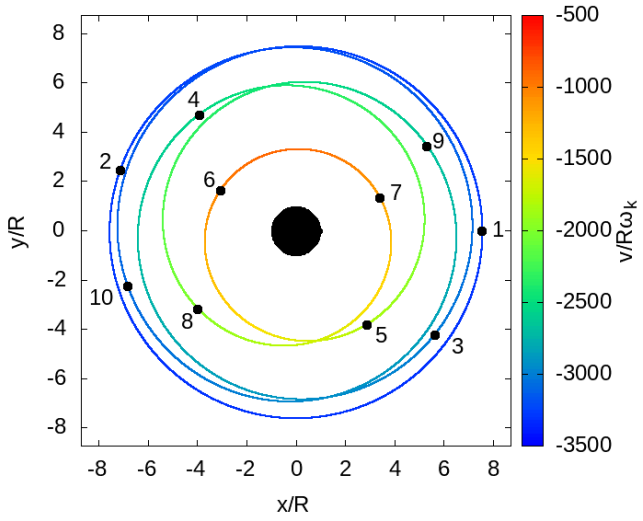

(c)

Figure 69 – a) Poincaré surface of section for $C_J = 2.204\ \mathrm{R}^2\omega_\mathrm{k}^2$. The periodic/quasi-periodic orbits of first kind are in black, the 1:6 resonance orbits are in cyan and blue and chaotic ones in red. b) Resonance islands for different values of C_J. The label on the panel gives the colour of the largest island for each value of C_J. c) Central orbit in the rotating frame of one of the families associated with the 1:6 resonance (in cyan in panel a) for $C_J = 2.204\ \mathrm{R}^2\omega_\mathrm{k}^2$. The numbers and colours on the panel provide time evolution and the velocity in the rotating frame, respectively.

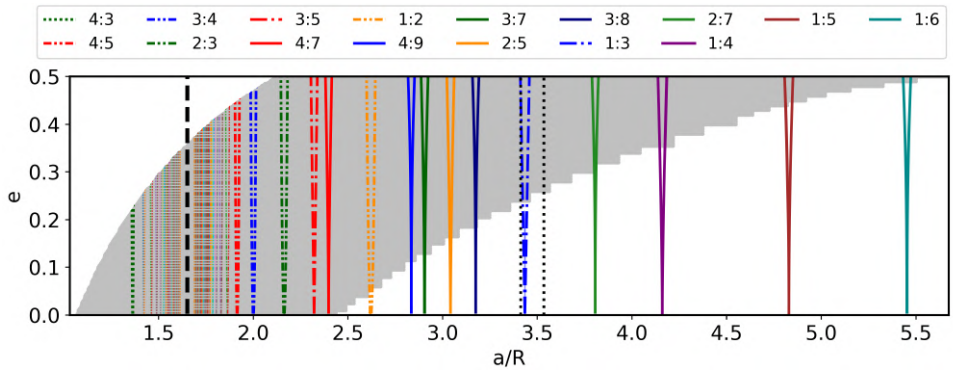

Figure 70 – Semi-major axis versus eccentricity for Chariklo system, where coloured lines place the sectoral resonances, and the grey area corresponds to the chaotic region. Coloured lines not referenced on the label, between $1.4 - 1.8$, correspond to first order resonances with $|m| > 4$. A vertical dashed line at $a/R \approx 1.7$ gives the corotation radius, while vertical dotted lines give the central location of the rings.

Figure 71b shows the motion in the rotating frame of the periodic orbits given in Figure 71a, in which the colour of the orbits matches those given in panel (a), and the green regions correspond to the location of the rings. For clarity, we only show the portions of the orbits with $y > 0$. We show the radial variation of the orbits in Figure 71c.

The 1:3 resonance orbit has one self-crossing at $y = 0$ and a period of almost $6.4\omega_k^{-1}$. In contrast, the trajectory of the first kind follows the Chariklo shape, with a period of almost $3.2\omega_k^{-1}$. As one can see in the figure, both orbits are initially in the inner ring – near its outer edge. However, only the first kind of periodic orbit remains within the ring throughout the simulation, while the resonant orbit crosses the ring edges and reaches the outer ring.

The difference in radial variation is due to the different nature of the orbits. Periodic orbits of first kind correspond to nearly circular orbits, while those of second kind are intrinsically eccentric, explaining why the latter has a significantly larger radial variation. Here, when we refer to eccentricity, we are referring to osculating elements defined in the context of the classical 2-body problem. We refer the reader to the work of Ribeiro et al. (2021) for a detailed discussion regarding the orbital elements in the context of NSSBs.

The results discussed in the last paragraph lead us to question whether the inner ring is associated with the 1:3 resonance. To verify this, we present in Figure 72 a diagram with the semi-major axis versus eccentricity for a range of values corresponding to the rings (in green). We also show the orbital elements obtained for the periodic orbits of first and second kinds (black and blue lines, respectively). The region filled in blue shows the 1:3 resonance boundaries obtained in the Poincaré surface of sections.

The largest possible eccentricity for a particle to remain within the boundaries of the inner ring is $e = 9 \times 10^{-3}$, which is smaller than the smallest eccentricity obtained for the resonant orbits ($e = 10^{-2}$). In addition, the resonant periodic orbits and the ring are displaced, indicating that the ring is not confined by such resonance.

Meanwhile, periodic orbits of first kind cover a broad region and encompass both rings. The entire region shown in Figure 72, which is not associated with the 1:3 resonance (blue region), is composed of periodic/quasi-periodic orbits of first kind, including the ring region. Therefore, we conclude that

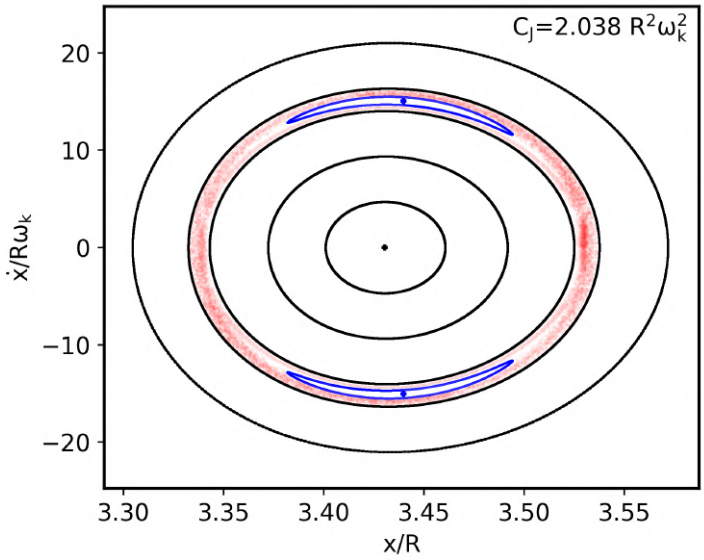

(a)

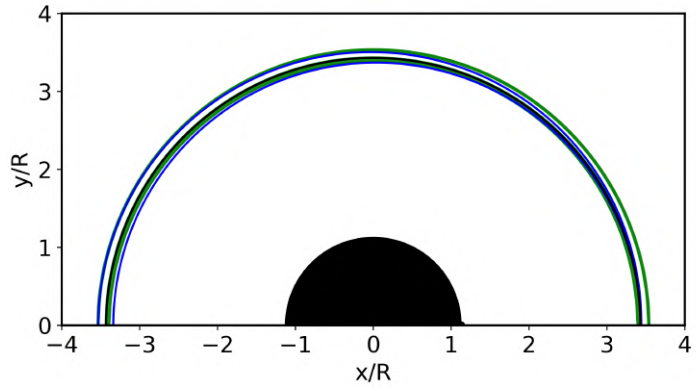

(b)

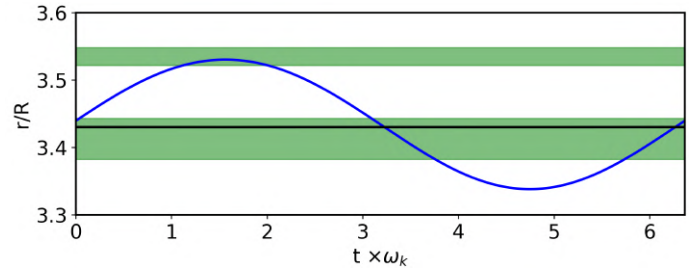

(c)

Figure 71 – a) Poincaré surface of section of Chariklo system for $C_J = 2.038\ \mathrm{R}^2\omega_\mathrm{k}^2$. We show different orbits by different colours: the non-resonance orbits are black, the 1:3 resonant orbits are blue, and the chaotic ones are red. b) motion in the rotating frame for $y > 0$ and c) radial variation of periodic orbits shown in panel a). The orbits of the first and second kind are given by black and blue lines, respectively, and the green regions correspond to the positions of Chariklo rings.

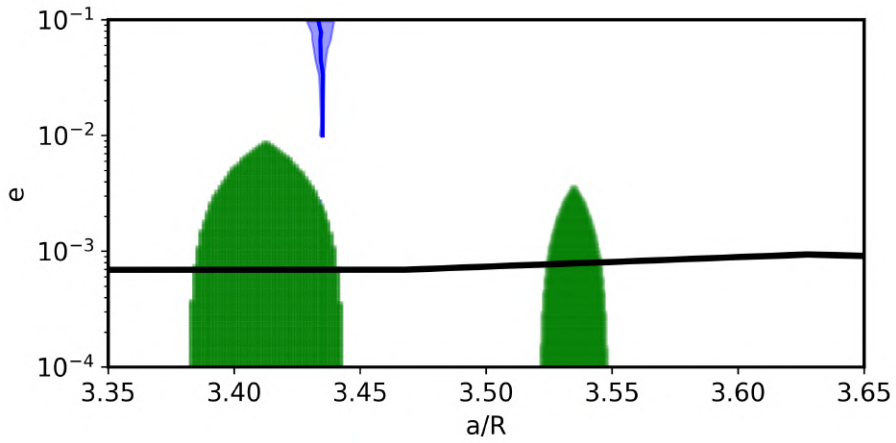

Figure 72 – Diagram of the semi-major axis versus eccentricity. The green regions show the range of values that corresponds to the location of the rings. The blue line shows the orbital elements obtained for the central orbit of the 1:3 resonance, and the blue filled regions give the boundaries of the resonance. The black line gives the periodic orbits of first kind.

Chariklo rings are associated with first kind orbits and not with the 1:3 resonance, as proposed by Leiva et al. (2017). Similar results were obtained by Winter, Borderes-Motta e Ribeiro (2019) for the Haumea ring.

5.9 CONCLUSIONS AND DISCUSSION

Here, we have attempted to perform a general analysis of the dynamics of particles around a spherical body with a mass anomaly. For this, we used well-known techniques of the 3-body problem study, varying the parameters of the central object. We can summarise our overall results as follows:

- The pendulum model with the necessary adaptations and the Poincaré surface of section proved to apply to the mass anomaly problem. We verified a strong agreement between the results by comparing both techniques.
- There is a chaotic region near the central object where particles collide or are ejected due to chaotic diffusion caused by successive close-encounters with the mass anomaly. Mysen, Olsen e Aksnes (2006), Mysen e Aksnes (2007) and Lages, Shepelyansky e Shevchenko (2017) also obtains chaotic regions near the central object for elongated bodies and contact binaries, respectively.
- For the set of parameters analysed by us, the chaotic region extends beyond the corotation radius. This fact indicates a lack of stable internal sectoral and corotation resonances in the mass anomaly system.
- Resonances location is mainly affected by the mass of the spherical portion and the spin period. In contrast, the masses of the spherical and anomalous portions of the body and spin period are responsible for determining the width of the resonances.

- Beyond the chaotic region, there is a region where the motion of the particles is dynamically stable. In such a region, there is chaotic behaviour only in a narrow region in the separatrices of the resonances.

- The behaviour of the particles in the external sectoral resonances is similar to those obtained for the mean motion resonances in the RP3BP (WINTER; MURRAY, 1997a; WINTER; MURRAY, 1997b). Similar to RP3BP, we verify the existence of asymmetric periodic orbits associated with $1:1+p$ resonances.

Although objects with the shape assumed in this work are unknown so far, the completely irregular shapes known for some asteroids lead us to speculate that such a class of object might exist. We emphasize that bodies with mass anomaly are perfectly reasonable outputs from a collision of a satellite that spirals towards the central body due to tidal dissipation or a collision between two objects at low velocity, with partial accretion (LEINHARDT; STEWART, 2011).

Sicardy et al. (2019) discuss the possibility of Chariklo having a spherical shape with topographic feature with $\mu \sim 10^{-5}$, which places the Centaur as a first candidate to integrate the class of mass anomaly objects. We studied the dynamics around a Chariklo with mass anomaly and found that 1:3 resonant particles present radial variations too large for the radial extension of the inner ring. On the other hand, particles in periodic/quasi-periodic first kind orbits show radial motions that match the extension of the two rings of Chariklo. Consequently, the ring must be associated with these orbits and not with orbits of second kind as proposed by Leiva et al. (2017). With the constant increase in data on small heliocentric bodies, we believe that objects with shapes similar to bodies with mass anomalies may soon be detected.

It is essential to point out that in the current study, we limited ourselves to analyse the dynamics of an isolated particle around a NSSB, disregarding the effects associated with the ring particles, such as collisions between them, local viscous, and self-gravity effects. We also disregard external effects that modulate the dynamics of small particles, such as solar radiation pressure and Poynting-Robertson drag. Nevertheless, the location and width of resonances and the chaotic region are general results and should remain almost unchanged in the presence of other effects. Therefore, our work presents some tools and first general results for studies on dynamics of mass anomaly systems.

6 CONCLUSION

There are some processes that result in the formation of satellites and rings. The largest satellites of the giant planets are believed to have formed in circumplanetary disks, while mid-sized and small satellites may have formed through accretion in rings or debris disks, disruption of older satellites, or captures. On the other hand, rings can be produced by the ejection of material from satellites and planets, destruction or splitting of satellites, or dissipation of the gas content of a circumplanetary disk. In this thesis, we studied the formation and evolution of different systems of satellites and rings of the Solar System, using different numerical and mathematical methods.

The first system we analyzed is the Galilean satellites system, their formation in a circumplanetary disk being studied in Chapter 2. we propose that the Galilean satellites formed through the mutual impacts of satellitesimals captured from the circumstellar disk and pebble accretion. It is assumed that the pebbles result from the ablation of material from the circumstellar disk. This scenario is appealing because it invokes a single mechanism to explain the origin of satellitesimals and pebbles in the disk. The mathematical modeling was done using the `MERCURY` package (CHAMBERS, 1999), responsible for computing the gravitational interaction between physical bodies in its original version. They are Jupiter and the satellitesimals in my case. We implemented in the package the gas drag, type I migration, eccentricity and inclination damping, and growth by pebble accretion.

The formation process was studied through 120 numerical simulations assuming different numbers of satellitesimals and pebble fluxes. Collisions between satellitesimals always occur in the disk, which means that more than four satelitesimals are needed to form the Galilean satellites. Satellitesimals grow via pebble accretion and migrate to the disk inner edge. When they approach this location, dynamical instabilities and orbital crossing promote further growth via impacts. After 2 Myr, we get a set of satellites anchored at the disk's inner edge, forming a resonant chain. Larger pebble fluxes are responsible for forming systems with few very massive satellites, while smaller fluxes form systems with more satellites of lower mass. In the latter case, the systems are also more compact. The flux responsible for forming a system analogous to the Galilean one is 1.5×10^{-9} $\mathrm{M_J}$/yr. Unlike current Galilean satellites, all satellites are formed in 2:1 MMR with the adjacent satellite and have eccentricities ~ 0.1.

Analyzing the long-term evolution of the system, we found that the effects of the classic tidal migration are not capable of forming Galilean satellites dynamically compatible with the current ones. This is because the Callisto would need to migrate faster than the inner satellites in order to break the Ganymede-Callisto resonance. Callisto's faster migration is only possible considering the recent dynamical tidal theory (FULLER; LUAN; QUATAERT, 2016). After the publication of Madeira, Izidoro e Giuliatti-Winter (2021), dynamical tidal effects were verified on Jupiter (IDINI; STEVENSON, 2021). These results seem to imply that the Galilean satellites did, in fact, form in a circumplanetary disk during the last stages of Jupiter's formation. They also suggest that Callisto was originally locked in resonance, leaving it via divergent migration and that the eccentricities of Galilean satellites were much higher in the past.

In Chapter 3, the formation of Phobos in the recycling material model is explored using the hybrid code HYDRORINGS (CHARNOZ; SALMON; CRIDA, 2010; SALMON et al., 2010), developed to study the formation of satellites from the viscous spreading of rings. The numerical simulations begin with Mars and a disk of material within the martian Roche limit. The disk is considered as a set of one-dimensional bins. It is assumed that material spreading out of the Roche limit coagulates to form rubble-pile satellites. Satellites migrate due to disk and tidal torques and can be destroyed due to tides. The exploration was carried out by performing 180 numerical simulations with disks of different masses and particle sizes, and assuming different locations where satellites are destroyed.

We verify through a theoretical study (HOLSAPPLE; MICHEL, 2006; HOLSAPPLE; MICHEL, 2008) that the location where the satellites will be destroyed depends on the mass, when they are in the "strength regime". Seen that, we propose that satellites may not be totally destroyed upon reaching the disruption location, but may be eroded by tides, in a process called "tidal downsizing". The simulation were carried out assuming both scenario: the one in which the satellites are completely destroyed and the scenario in which tidal downsizing occurs. An interesting result is that tidal downsizing effects almost do not affect the formation of Phobos, as only satellites with similar or smaller masses than Phobos are in the strength regime. However, tidal downsizing may be important for the post-evolution of Phobos, and it is possible that the satellite is under this effect today (depending on its friction angle).

In the recycling model, Phobos is formed after a few cycles of satellite destruction and re-accretion. In general, the cycles give rise to a satellite that migrates towards the planet and is destroyed by tides, forming a ring that will restart the formation process. At every cycle, material is deposited onto Mars and, as a consequence, the satellite formed will be smaller from one cycle to the next, the mass of Phobos being reached after a certain number of cycles. The formed satellites confine the ring due to Lindblad resonances and thus hold material in the ring region. Because of this, a ring coexisting with Phobos is always obtained.

We obtain that the ring coexisting with Phobos would be visible for all parameter combinations we simulated, demonstrating a caveat in the recycling model. The model also predicts that the formation of the debris disk would need to be much more recent than the observational evidence seems to indicate. The ring problem could be solved by including a dissipative effect in the system. Here we have included the Yarkovsky effects, obtaining systems where Phobos is formed without a ring. However, as dissipative forces act to remove material from the system, it follows that the formation of the debris disk would need to be even faster than in the case without these effects. This demonstrates that Phobos is not formed through the process of material recycling, although this may have occurred at some point around Mars. Phobos must not be a rubble-pile satellite but very cohesive, or must have formed outside the region where the recycling process would take place.

In Chapter 4, we first study via N-body simulations with MERCURY package the confinement of particles due to families of co-orbital satellites. As result, we obtain that the Neptune's four arcs can be confined by any configuration of 1+N co-orbital satellites with at least three moonlets around the point L_4 or L_5 of a moon. This gives robustness to the confinement model of Neptune arcs proposed by Renner et al. (2014). In Chapters 2 and 3, satellite formation is studied assuming accretion processes. In Chapter 4, we propose the formation of co-orbital satellites through a different process, not by

accretion, but by disruption.

We propose that the Neptune arc system formed from the disruption of an object confined at a Lagrangian point of a moon. Such an object would be disrupted due to an impact on some large fragments and a cluster of debris, which remain in the moon's horseshoe region. The large fragments collide with each other forming moonlets that reach an equilibrium configuration. Debris, in turn, are expected to contribute to the formation of the arcs. We performed 4200 numerical simulations, including the fragments, Neptune, and the moon, and varied the number and mass of fragments and ejection velocities. Assuming the disruption in four fragments, it is obtained that almost one third of the formed systems can confine the Neptune arcs. This rate increases if the number of fragments is greater. These numbers demonstrate that the formation of a co-orbital satellite system through the disruption of an object is an attractive possibility.

In this scenario, the formation of material can happen in three different stages of the system: in the disruption of the object, in the collisions between fragments and debris, and due to the impact of meteoroids with the formed moonlets. Despite the difficulty in analyzing the amount of material produced in these different stages, which would require more adequate and much slower numerical tools, we analyzed the dynamic evolution of test particles in the system. Most of the material formed in the disruption collides with the fragments, while the material formed in the last two stages can survive and be confined in the region of the arcs. Thus, the proposed model becomes more attractive, as it manages to explain the formation of the material of the arcs and the satellites that confine them by one single disruptive event.

Finally, based on the recent discovery of rings around bodies that are not planets, we analyze the dynamics and stability around a spherical body with a mass anomaly, that is, a body with asymmetrical distribution of mass. The system was normalized based on the normalization of the two-body problem and numerically evolved by solving the equations of motion with the Burlish-Stoer method. The rotating rate and body mass anomaly were varied. We used the Poincaré surface of section technique in the analysis. We identify structures remarkably similar to those of the classical restrict and planar 3-body problem in the Poincaré surface of sections, including the 1:1+p resonances, which show asymmetric periodic behavior. Additionally, we obtained an chaotic region near the central body, in which the eccentricity of the particles increases until they are lost from the system. The chaotic region extends beyond the corotation orbit, so there are no internal spin-orbit resonance in the case of the mass anomaly.

Assuming that Chariklo is a spherical body with a mass anomaly, it is obtained that the chaotic region is very internal to the rings, meaning that this region is not responsible for the confinement of the inner edge of the ring system. Also, it is verified that the 1:3 resonance is not in the region of the rings, with no relation between such a resonance and the inner ring being verified, contrary to what was proposed by Leiva et al. (2017). We conclude that the ring particles are related to quasi-periodic orbits of first kind, corresponding to stable and non-resonant elliptical orbits.

As shown in this work, the formation of satellites and rings is a complex subject, involving different mechanisms and physical processes, depending on the environment and the instant in which the formation occurs. This thesis aimed to study the formation of different systems of satellites and rings of

the Solar System, through different numerical techniques. In special, we tried to address the symbiotic relationship between satellites and particulative sets of material, whether in the context of disks of material or planetary rings. Given what has been presented here, we conclude that satellites and rings seem to correspond to the same geological system, seen at different times.

REFERENCES

ABALAKIN, V. et al. Report of the iau/iag working group on cartographic coordinates and rotational elements of the planets and satellites: 2000. **Celestial Mechanics and Dynamical Astronomy**, Springer, v. 82, n. 1, p. 83–111, 2002.

ADACHI, I.; HAYASHI, C.; NAKAZAWA, K. The gas drag effect on the elliptic motion of a solid body in the primordial solar nebula. **Progress of Theoretical Physics**, Oxford University Press, v. 56, n. 6, p. 1756–1771, 1976.

ALBEE, A. L. et al. Overview of the mars global surveyor mission. **Journal of Geophysical Research: Planets**, Wiley Online Library, v. 106, n. E10, p. 23291–23316, 2001.

ALBERT, R. et al. Maximum angle of stability in wet and dry spherical granular media. **Physical Review E**, APS, v. 56, n. 6, p. R6271, 1997.

ALTOBELLI, N. et al. Characterisation of the outer solar system dust by cassini-cda. In: **European Planetary Science Congress**. [S.l.: s.n.], 2018. p. EPSC2018–199.

AMARANTE, A.; WINTER, O. Surface dynamics, equilibrium points and individual lobes of the kuiper belt object (486958) arrokoth. **Monthly Notices of the Royal Astronomical Society**, Oxford University Press, v. 496, n. 4, p. 4154–4173, 2020.

ANDREWS-HANNA, J. C.; ZUBER, M. T.; BANERDT, W. B. The borealis basin and the origin of the martian crustal dichotomy. **Nature**, Nature Publishing Group, v. 453, n. 7199, p. 1212–1215, 2008.

ARMITAGE, P. J.; EISNER, J. A.; SIMON, J. B. Prompt planetesimal formation beyond the snow line. **The Astrophysical Journal Letters**, IOP Publishing, v. 828, n. 1, p. L2, 2016.

ATAIEE, S. et al. How much does turbulence change the pebble isolation mass for planet formation? **Astronomy & Astrophysics**, EDP Sciences, v. 615, p. A110, 2018.

A'HEARN, J. A.; HEDMAN, M. M.; HAMILTON, D. P. Modeling saturn's d68 clumps as a co-orbital satellite system. **The Planetary Science Journal**, IOP Publishing, v. 2, n. 2, p. 74, 2021.

BAGHERI, A. et al. Dynamical evidence for phobos and deimos as remnants of a disrupted common progenitor. **Nature Astronomy**, Nature Publishing Group, v. 5, n. 6, p. 539–543, 2021.

BARR, A. C.; CANUP, R. M. Constraints on gas giant satellite formation from the interior states of partially differentiated satellites. **Icarus**, Elsevier, v. 198, n. 1, p. 163–177, 2008.

BARR, A. C.; CANUP, R. M. Origin of the ganymede–callisto dichotomy by impacts during the late heavy bombardment. **Nature Geoscience**, Nature Publishing Group, v. 3, n. 3, p. 164–167, 2010.

BATH, G.; PRINGLE, J. The evolution of viscous discs–i. mass transfer variations. **Monthly Notices of the Royal Astronomical Society**, Oxford University Press Oxford, UK, v. 194, n. 4, p. 967–986, 1981.

BATYGIN, K. Capture of planets into mean-motion resonances and the origins of extrasolar orbital architectures. **Monthly Notices of the Royal Astronomical Society**, Oxford University Press, v. 451, n. 3, p. 2589–2609, 2015.

BATYGIN, K. On the terminal rotation rates of giant planets. **The Astronomical Journal**, IOP Publishing, v. 155, n. 4, p. 178, 2018.

BATYGIN, K.; MORBIDELLI, A. Formation of giant planet satellites. **The Astrophysical Journal**, IOP Publishing, v. 894, n. 2, p. 143, 2020.

BEAUGÉ, C. Asymmetric librations in exterior resonances. **Celestial mechanics and Dynamical astronomy**, Springer, v. 60, n. 2, p. 225–248, 1994.

BEAUGÉ, C.; MICHTCHENKO, T.; FERRAZ-MELLO, S. Planetary migration and extrasolar planets in the 2/1 mean-motion resonance. **Monthly Notices of the Royal Astronomical Society**, The Royal Astronomical Society, v. 365, n. 4, p. 1160–1170, 2006.

BELENKAYA, E.; COWLEY, S.; ALEXEEV, I. Saturn's aurora in the january 2004 events. In: COPERNICUS GMBH. **Annales Geophysicae**. [S.l.], 2006. v. 24, n. 6, p. 1649–1663.

BELL, K. et al. The fu orionis outburst as a thermal accretion event: Observational constraints for protostellar disk models. **The Astrophysical Journal**, v. 444, p. 376–395, 1995.

BENZ, W.; ASPHAUG, E. Catastrophic disruptions revisited. **Icarus**, Elsevier, v. 142, n. 1, p. 5–20, 1999.

BÉRARD, D. et al. The structure of chariklo's rings from stellar occultations. **The Astronomical Journal**, IOP Publishing, v. 154, n. 4, p. 144, 2017.

BIERSON, C. J.; NIMMO, F. Explaining the galilean satellites' density gradient by hydrodynamic escape. **The Astrophysical Journal Letters**, IOP Publishing, v. 897, n. 2, p. L43, 2020.

BITSCH, B. et al. Pebble-isolation mass: Scaling law and implications for the formation of super-earths and gas giants. **Astronomy & Astrophysics**, EDP Sciences, v. 612, p. A30, 2018.

BITSCH, B. et al. Formation of planetary systems by pebble accretion and migration: growth of gas giants. **Astronomy & Astrophysics**, EDP Sciences, v. 623, p. A88, 2019.

BLACK, B. A.; MITTAL, T. The demise of phobos and development of a martian ring system. **Nature Geoscience**, Nature Publishing Group, v. 8, n. 12, p. 913–917, 2015.

BLUM, J.; WURM, G. Experiments on sticking, restructuring, and fragmentation of preplanetary dust aggregates. **Icarus**, Elsevier, v. 143, n. 1, p. 138–146, 2000.

BORDERES-MOTTA, G.; WINTER, O. C. Poincaré surfaces of section around a 3d irregular body: the case of asteroid 4179 toutatis. **Monthly Notices of the Royal Astronomical Society**, Oxford University Press, v. 474, n. 2, p. 2452–2466, 2018.

BOTTKE, W. et al. The effect of yarkovsky thermal forces on the dynamical evolution of asteroids and meteoroids. **Asteroids III**, this volume. Univ. of Arizona, Tucson, v. 395, p. 408, 2002.

BOTTKE, W. F.; ANDREWS-HANNA, J. C. A post-accretionary lull in large impacts on early mars. **Nature Geoscience**, Nature Publishing Group, v. 10, n. 5, p. 344–348, 2017.

BRAGA-RIBAS, F. et al. A ring system detected around the centaur (10199) chariklo. **Nature**, Nature Publishing Group, v. 508, n. 7494, p. 72–75, 2014.

BRAHIC, A. Systems of colliding bodies in a gravitational field. i-numerical simulation of the standard model. **Astronomy and Astrophysics**, v. 54, p. 895–907, 1977.

BRASSER, R.; DUNCAN, M.; LEVISON, H. Embedded star clusters and the formation of the oort cloud: Ii. the effect of the primordial solar nebula. **Icarus**, Elsevier, v. 191, n. 2, p. 413–433, 2007.

BRASSER, R.; MOJZSIS, S. The partitioning of the inner and outer solar system by a structured protoplanetary disk. **Nature Astronomy**, Nature Publishing Group, v. 4, n. 5, p. 492–499, 2020.

BROWN, E. W. Orbits, periodic, on a new family of periodic orbits in the problem of three bodies. **Monthly Notices of the Royal Astronomical Society**, v. 71, p. 438–454, 1911.

BRUNO, A. D. **The restricted 3-body problem: plane periodic orbits**. [S.l.]: Walter de Gruyter, 1994.

BURNS, J. A. Contradictory clues as to the origin of the martian moons. **Mars**, p. 1283–1301, 1992.

BURNS, J. A.; LAMY, P. L.; SOTER, S. Radiation forces on small particles in the solar system. **Icarus**, Elsevier, v. 40, n. 1, p. 1–48, 1979.

BURNS, J. A. et al. Lorentz resonances and the structure of the jovian ring. **Nature**, Nature Publishing Group, v. 316, n. 6024, p. 115–119, 1985.

BURNS, J. A. et al. The formation of jupiter's faint rings. **Science**, American Association for the Advancement of Science, v. 284, n. 5417, p. 1146–1150, 1999.

CANUP, R.; SALMON, J. Origin of phobos and deimos by the impact of a vesta-to-ceres sized body with mars. **Science advances**, American Association for the Advancement of Science, v. 4, n. 4, p. eaar6887, 2018.

CANUP, R. M. Origin of saturn's rings and inner moons by mass removal from a lost titan-sized satellite. **Nature**, Nature Publishing Group, v. 468, n. 7326, p. 943–946, 2010.

CANUP, R. M.; ESPOSITO, L. W. Accretion in the roche zone: Coexistence of rings and ringmoons. **Icarus**, Elsevier, v. 113, n. 2, p. 331–352, 1995.

CANUP, R. M.; ESPOSITO, L. W. Accretion in the roche zone: Coexistence of rings and ringmoons. **Icarus**, Elsevier, v. 113, n. 2, p. 331–352, 1995.

CANUP, R. M.; WARD, W. R. Formation of the galilean satellites: Conditions of accretion. **The Astronomical Journal**, IOP Publishing, v. 124, n. 6, p. 3404, 2002.

CANUP, R. M.; WARD, W. R. A common mass scaling for satellite systems of gaseous planets. **Nature**, Nature Publishing Group, v. 441, n. 7095, p. 834–839, 2006.

CANUP, R. M.; WARD, W. R. Origin of europa and the galilean satellites. **Europa**, University of Arizona Press Tucson, p. 59–83, 2009.

CASSIDY, T.; JOHNSON, R. Collisional spreading of enceladus' neutral cloud. **Icarus**, Elsevier, v. 209, n. 2, p. 696–703, 2010.

CHAMBERS, J. E. A hybrid symplectic integrator that permits close encounters between massive bodies. **Monthly Notices of the Royal Astronomical Society**, Blackwell Science Ltd Oxford, UK, v. 304, n. 4, p. 793–799, 1999.

CHANDRASEKHAR, S. **Principles of stellar dynamics**. [S.l.]: Courier Corporation, 1942.

CHANDRASEKHAR, S. Ellipsoidal figures of equilibrium. New Haven Yale Univ. Press, 1969.

CHAPMAN, C. et al. Discovery and physical properties of dactyl, a satellite of asteroid 243 ida. **Nature**, Nature Publishing Group, v. 374, n. 6525, p. 783–785, 1995.

CHAPMAN, S.; BARTELS, J. Geomagnetism, vol. i: Geomagnetic and related phenomena. **Geomagnetism**, 1940.

CHARNOZ, S. et al. The origin of planetary ring systems. **arXiv preprint arXiv:1703.09741**, 2017.

CHARNOZ, S. et al. Accretion of saturn's mid-sized moons during the viscous spreading of young massive rings: Solving the paradox of silicate-poor rings versus silicate-rich moons. **Icarus**, Elsevier, v. 216, n. 2, p. 535–550, 2011.

CHARNOZ, S.; SALMON, J.; CRIDA, A. The recent formation of saturn's moonlets from viscous spreading of the main rings. **Nature**, Nature Publishing Group, v. 465, n. 7299, p. 752–754, 2010.

CHEN, W.-F.; HAN, D.-J. **Plasticity for structural engineers**. [S.l.]: J. Ross Publishing, 2007.

CHRISTENSEN, E. J. .; WILLIAMS, B. G. . Mars gravity field derived from viking-1 and viking-2: The navigation result. **Journal of Guidance and Control**, v. 2, n. 3, p. 179–183, 1979.

CHRISTIAENS, V. et al. Evidence for a circumplanetary disk around protoplanet pds 70 b. **The Astrophysical Journal Letters**, IOP Publishing, v. 877, n. 2, p. L33, 2019.

CILIBRASI, M. et al. Satellites form fast & late: A population synthesis for the galilean moons. **Monthly Notices of the Royal Astronomical Society**, Oxford University Press, v. 480, n. 4, p. 4355–4368, 2018.

CITRON, R. I.; GENDA, H.; IDA, S. Formation of phobos and deimos via a giant impact. **Icarus**, Elsevier, v. 252, p. 334–338, 2015.

COLEMAN, G. A.; NELSON, R. P. On the formation of planetary systems via oligarchic growth in thermally evolving viscous discs. **Monthly Notices of the Royal Astronomical Society**, The Royal Astronomical Society, v. 445, n. 1, p. 479–499, 2014.

COLOMBO, G.; LAUTMAN, D. A.; SHAPIRO, I. I. The earth's dust belt: Fact or fiction?: 2. gravitational focusing and jacobi capture. **Journal of Geophysical research**, Wiley Online Library, v. 71, n. 23, p. 5705–5717, 1966.

COLWELL, J. E.; ESPOSITO, L. W. A model of dust production in the neptune ring system. **Geophysical research letters**, Wiley Online Library, v. 17, n. 10, p. 1741–1744, 1990.

COLWELL, J. E.; ESPOSITO, L. W. A model of dust production in the neptune ring system. **Geophysical research letters**, Wiley Online Library, v. 17, n. 10, p. 1741–1744, 1990.

COLWELL, J. E.; ESPOSITO, L. W. A numerical model of the uranian dust rings. **Icarus**, Elsevier, v. 86, n. 2, p. 530–560, 1990.

COLWELL, J. E.; ESPOSITO, L. W. Origins of the rings of uranus and neptune: 1. statistics of satellite disruptions. **Journal of Geophysical Research: Planets**, Wiley Online Library, v. 97, n. E6, p. 10227–10241, 1992.

CRADDOCK, R. A. The origin of phobos and deimos. In: **Lunar and Planetary Science Conference**. [S.l.: s.n.], 1994. v. 25, p. 293.

CRADDOCK, R. A. Are phobos and deimos the result of a giant impact? **Icarus**, Elsevier, v. 211, n. 2, p. 1150–1161, 2011.

CRESSWELL, P.; NELSON, R. P. Three-dimensional simulations of multiple protoplanets embedded in a protostellar disc. **Astronomy & Astrophysics**, EDP Sciences, v. 482, n. 2, p. 677–690, 2008.

CRIDA, A.; CHARNOZ, S. Formation of regular satellites from ancient massive rings in the solar system. **Science**, American Association for the Advancement of Science, v. 338, n. 6111, p. 1196–1199, 2012.

ĆUK, M. et al. Evidence for a past martian ring from the orbital inclination of deimos. **The Astrophysical Journal Letters**, IOP Publishing, v. 896, n. 2, p. L28, 2020.

DAISAKA, H.; TANAKA, H.; IDA, S. Viscosity in a dense planetary ring with self-gravitating particles. **Icarus**, Elsevier, v. 154, n. 2, p. 296–312, 2001.

DECK, K. M.; BATYGIN, K. Migration of two massive planets into (and out of) first order mean motion resonances. **The Astrophysical Journal**, IOP Publishing, v. 810, n. 2, p. 119, 2015.

DERMOTT, S. Dynamics of narrow rings. In: **IAU Colloq. 75: Planetary Rings**. [S.l.: s.n.], 1984. p. 589–637.

DERMOTT, S. F.; MURRAY, C. D. The dynamics of tadpole and horseshoe orbits: Ii. the coorbital satellites of saturn. **Icarus**, Elsevier, v. 48, n. 1, p. 12–22, 1981.

DIKAREV, V. et al. The new esa meteoroid model. **Advances in Space Research**, Elsevier, v. 35, n. 7, p. 1282–1289, 2005.

DIVINE, N. Five populations of interplanetary meteoroids. **Journal of Geophysical Research: Planets**, Wiley Online Library, v. 98, n. E9, p. 17029–17048, 1993.

DMITROVSKII, A. A. et al. Constraints on the interior structure of phobos from tidal deformation modeling. **Icarus**, Elsevier, v. 372, p. 114714, 2022.

DOBROVOLSKIS, A. R. Tidal disruption of solid bodies. **Icarus**, Elsevier, v. 88, n. 1, p. 24–38, 1990.

DONES, L.; TREMAINE, S. On the origin of planetary spins. **Icarus**, Elsevier, v. 103, n. 1, p. 67–92, 1993.

DOWNEY, B. G.; NIMMO, F.; MATSUYAMA, I. Inclination damping on callisto. **Monthly Notices of the Royal Astronomical Society**, Oxford University Press, v. 499, n. 1, p. 40–51, 2020.

DRAŻKOWSKA, J.; SZULÁGYI, J. Dust evolution and satellitesimal formation in circumplanetary disks. **The Astrophysical Journal**, IOP Publishing, v. 866, n. 2, p. 142, 2018.

DUMAS, C. et al. Astrometry and near-infrared photometry of neptune's inner satellites and ring arcs. **The Astronomical Journal**, IOP Publishing, v. 123, n. 3, p. 1776, 2002.

DURANTE, D. et al. Jupiter's gravity field halfway through the juno mission. **Geophysical Research Letters**, Wiley Online Library, v. 47, n. 4, p. e2019GL086572, 2020.

DUXBURY, T. C.; OCAMPO, A. C. Mars: Satellite and ring search from viking. **Icarus**, Elsevier, v. 76, n. 1, p. 160–162, 1988.

DWYER, C. et al. The influence of imperfect accretion and radial mixing on ice: rock ratios in the galilean satellites. **Icarus**, Elsevier, v. 225, n. 1, p. 390–402, 2013.

D'ANGELO, G.; PODOLAK, M. Capture and evolution of planetesimals in circumjovian disks. **The Astrophysical Journal**, IOP Publishing, v. 806, n. 2, p. 203, 2015.

ELLIS, K. M.; MURRAY, C. D. The disturbing function in solar system dynamics. **Icarus**, Elsevier, v. 147, n. 1, p. 129–144, 2000.

ELROD, M. K. et al. Seasonal and radial trends in saturn's thermal plasma between the main rings and enceladus. **Icarus**, Elsevier, v. 242, p. 130–137, 2014.

ESTRADA, P. R.; MOSQUEIRA, I. A gas-poor planetesimal capture model for the formation of giant planet satellite systems. **Icarus**, Elsevier, v. 181, n. 2, p. 486–509, 2006.

ESTRADA, P. R. et al. **Formation of Jupiter and conditions for accretion of the Galilean satellites**. [S.l.]: University of Arizona Press Tucson, 2009.

FENDYKE, S. M.; NELSON, R. P. On the corotation torque for low-mass eccentric planets. **Monthly Notices of the Royal Astronomical Society**, The Royal Astronomical Society, v. 437, n. 1, p. 96–107, 2014.

FERRAZ-MELLO, S.; BEAUGE, C.; MICHTCHENKO, T. Evolution of migrating planet pairs in resonance. **Celestial Mechanics and Dynamical Astronomy**, Springer, v. 87, n. 1, p. 99–112, 2003.

FERRAZ-MELLO, S.; TSUCHIDA, M.; KLAFKE, J. On symmetrical planetary corotations. **Celestial Mechanics and Dynamical Astronomy**, Springer, v. 55, n. 1, p. 25–45, 1993.

FORYTA, D. W.; SICARDY, B. The dynamics of the neptunian adams ring's arcs. **Icarus**, Elsevier, v. 123, n. 1, p. 129–167, 1996.

FRAEMAN, A. et al. Analysis of disk-resolved omega and crism spectral observations of phobos and deimos. **Journal of Geophysical Research: Planets**, Wiley Online Library, v. 117, n. E11, 2012.

FRANGAKIS, C. Numerical exploration of commensurable periodic solutions of the restricted problem of three bodies and their stability. **Astrophysics and Space Science**, Springer, v. 23, n. 1, p. 17–42, 1973.

FRANGAKIS, C. Phase plane analysis of the commensurable restricted three-body problem. **Astrophysics and Space Science**, Springer, v. 22, n. 2, p. 421–440, 1973.

FRENCH, R. G. et al. Noncircular features in saturn's rings iv: Absolute radius scale and saturn's pole direction. **Icarus**, Elsevier, v. 290, p. 14–45, 2017.

FUJIMOTO, M.; TASKER, E. J. Unveiling the secrets of a habitable world with jaxa's small-body missions. **Nature Astronomy**, Nature Publishing Group, v. 3, n. 4, p. 284–286, 2019.

FUJITA, T. et al. Capture of planetesimals by gas drag from circumplanetary disks. **The Astronomical Journal**, IOP Publishing, v. 146, n. 6, p. 140, 2013.

FULLER, J.; LUAN, J.; QUATAERT, E. Resonance locking as the source of rapid tidal migration in the jupiter and saturn moon systems. **Monthly Notices of the Royal Astronomical Society**, Oxford University Press, v. 458, n. 4, p. 3867–3879, 2016.

GALLARDO, D. G. et al. Analysing the region of the rings and small satellites of neptune. **Astrophysics and Space Science**, Springer, v. 365, n. 1, p. 1–10, 2020.

GAO, P.; STEVENSON, D. J. Nonhydrostatic effects and the determination of icy satellites' moment of inertia. **Icarus**, Elsevier, v. 226, n. 2, p. 1185–1191, 2013.

GASLAC-GALLARDO, D. et al. Analysing the region of the rings and small satellites of neptune. **Astrophysics and Space Science**, Springer, v. 365, n. 1, p. 1–10, 2020.

GEISSLER, P. et al. Erosion and ejecta reaccretion on 243 ida and its moon. **Icarus**, Elsevier, v. 120, n. 1, p. 140–157, 1996.

GENDA, H.; KOKUBO, E.; IDA, S. Merging criteria for giant impacts of protoplanets. **The Astrophysical Journal**, IOP Publishing, v. 744, n. 2, p. 137, 2011.

GENIO, A. D. D. et al. Albedos, equilibrium temperatures, and surface temperatures of habitable planets. **The Astrophysical Journal**, IOP Publishing, v. 884, n. 1, p. 75, 2019.

GILLON, M. et al. Seven temperate terrestrial planets around the nearby ultracool dwarf star trappist-1. **Nature**, Nature Publishing Group, v. 542, n. 7642, p. 456–460, 2017.

GIULIATTI-WINTER, S.; MADEIRA, G.; SFAIR, R. Neptune's ring arcs confined by coorbital satellites: dust orbital evolution through solar radiation. **Monthly Notices of the Royal Astronomical Society**, Oxford University Press, v. 496, n. 1, p. 590–597, 2020.

GOLDREICH, P.; SCHLICHTING, H. E. Overstable librations can account for the paucity of mean motion resonances among exoplanet pairs. **The Astronomical Journal**, IOP Publishing, v. 147, n. 2, p. 32, 2014.

GOLDREICH, P.; SOTER, S. Q in the solar system. **Icarus**, Elsevier, v. 5, n. 1-6, p. 375–389, 1966.

GOLDREICH, P.; TREMAINE, S.; BORDERIES, N. Towards a theory for neptune's arc rings. **The Astronomical Journal**, v. 92, p. 490–494, 1986.

GRAF, J. E. et al. The mars reconnaissance orbiter mission. **Acta Astronautica**, Elsevier, v. 57, n. 2-8, p. 566–578, 2005.

GREENBERG, R. Evolution of satellite resonances by tidal dissipation. **The Astronomical Journal**, v. 78, p. 338, 1973.

GREENBERG, R. Orbit-orbit resonances in the solar system: Varieties and similarities. **Vistas in Astronomy**, v. 21, n. 3, p. 209–239, 1977.

GRUN, E.; MORFILL, G. E.; MENDIS, D. A. Dust-magnetosphere interactions. In: **IAU Colloq. 75: Planetary Rings**. [S.l.: s.n.], 1984. p. 275–332.

GRÜN, E. et al. Collisional balance of the meteoritic complex. **Icarus**, Elsevier, v. 62, n. 2, p. 244–272, 1985.

HALL, A. Discovery of satellites of mars. **Monthly Notices of the Royal Astronomical Society**, v. 38, p. 205–209, 1878.

HAMILTON, D. P. Motion of dust in a planetary magnetosphere: Orbit-averaged equations for oblateness, electromagnetic, and radiation forces with application to saturn's e ring. **Icarus**, Elsevier, v. 101, n. 2, p. 244–264, 1993.

HAMILTON, D. P.; BURNS, J. A. Origin of saturn's e ring: Self-sustained, naturally. **Science**, American Association for the Advancement of Science, v. 264, n. 5158, p. 550–553, 1994.

HAMILTON, D. P.; KRIVOV, A. V. Circumplanetary dust dynamics: Effects of solar gravity, radiation pressure, planetary oblateness, and electromagnetism. **Icarus**, Elsevier, v. 123, n. 2, p. 503–523, 1996.

HANSEN, B. M. A dynamical context for the origin of phobos and deimos. **Monthly Notices of the Royal Astronomical Society**, Oxford University Press, v. 475, n. 2, p. 2452–2466, 2018.

HANUŠ, J.; MARCHIS, F.; ĎURECH, J. Sizes of main-belt asteroids by combining shape models and keck adaptive optics observations. **Icarus**, Elsevier, v. 226, n. 1, p. 1045–1057, 2013.

HANUŠ, J. et al. Shape model of asteroid (130) elektra from optical photometry and disk-resolved images from vlt/sphere and nirc2/keck. **Astronomy & Astrophysics**, EDP Sciences, v. 599, p. A36, 2017.

HARTMANN, W. K. Impact experiments: 1. ejecta velocity distributions and related results from regolith targets. **Icarus**, Elsevier, v. 63, n. 1, p. 69–98, 1985.

HAY, H. C.; TRINH, A.; MATSUYAMA, I. Powering the galilean satellites with moon-moon tides. **Geophysical Research Letters**, Wiley Online Library, v. 47, n. 15, p. e2020GL088317, 2020.

HAYASHI, C. Structure of the solar nebula, growth and decay of magnetic fields and effects of magnetic and turbulent viscosities on the nebula. **Progress of Theoretical Physics Supplement**, Oxford Academic, v. 70, p. 35–53, 1981.

HEDMAN, M. et al. Aegaeon (saturn liii), a g-ring object. **Icarus**, Elsevier, v. 207, n. 1, p. 433–447, 2010.

HEDMAN, M. et al. Photometric analyses of saturn's small moons: Aegaeon, methone, and pallene are dark; helene and calypso are bright. **The Astronomical Journal**, IOP Publishing, v. 159, n. 4, p. 129, 2020.

HEDMAN, M. et al. Three tenuous rings/arcs for three tiny moons. **Icarus**, Elsevier, v. 199, n. 2, p. 378–386, 2009.

HÉNON, M. Exploration numérique du problème restreint. i. masses égales; orbites périodiques. In: **Annales d'Astrophysique**. [S.l.: s.n.], 1965. v. 28, p. 499.

HÉNON, M. Exploration numérique du problème restreint. ii. masses égales, stabilité des orbites périodiques. In: **Annales d'Astrophysique**. [S.l.: s.n.], 1965. v. 28, p. 992.

HÉNON, M. Numerical exploration of the restricted three-body problem. In: **The Theory of Orbits in the Solar System and in Stellar Systems**. [S.l.: s.n.], 1966. v. 25, p. 157.

HENON, M. Sur la topologie des lignes de courant dans un cas particulier. **Comptes Rendus Acad. Sci. Paris A**, v. 262, p. 312–314, 1966.

HÉNON, M. Numerical exploration of the restricted problem, v. **Astronomy and Astrophysics**, v. 1, p. 223–238, 1969.

HESSELBROCK, A. J.; MINTON, D. A. An ongoing satellite–ring cycle of mars and the origins of phobos and deimos. **Nature Geoscience**, Nature Publishing Group, v. 10, n. 4, p. 266–269, 2017.

HESSELBROCK, A. J.; MINTON, D. A. Three dynamical evolution regimes for coupled ring-satellite systems and implications for the formation of the uranian satellite miranda. **The Astronomical Journal**, IOP Publishing, v. 157, n. 1, p. 30, 2019.

HOLSAPPLE, K. On equilibrium shapes of solid solar system bodies. In: **Lunar and Planetary Science Conference**. [S.l.: s.n.], 2001. p. 1992.

HOLSAPPLE, K. A.; MICHEL, P. Tidal disruptions: A continuum theory for solid bodies. **Icarus**, Elsevier, v. 183, n. 2, p. 331–348, 2006.

HOLSAPPLE, K. A.; MICHEL, P. Tidal disruptions: Ii. a continuum theory for solid bodies with strength, with applications to the solar system. **Icarus**, Elsevier, v. 193, n. 1, p. 283–301, 2008.

HORÁNYI, M.; JUHÁSZ, A.; MORFILL, G. E. Large-scale structure of saturn's e-ring. **Geophysical Research Letters**, Wiley Online Library, v. 35, n. 4, 2008.

HSU, H.-W. et al. Stream particles as the probe of the dust-plasma-magnetosphere interaction at saturn. **Journal of Geophysical Research: Space Physics**, Wiley Online Library, v. 116, n. A9, 2011.

HUBBARD, W. B. et al. Occultation detection of a neptunian ring-like arc. **Nature**, Nature Publishing Group, v. 319, n. 6055, p. 636–640, 1986.

HUDSON, R. S.; OSTRO, S. J. Shape and non-principal axis spin state of asteroid 4179 toutatis. **Science**, American Association for the Advancement of Science, v. 270, n. 5233, p. 84–86, 1995.

HYODO, R. et al. On the impact origin of phobos and deimos. i. thermodynamic and physical aspects. **The Astrophysical Journal**, IOP Publishing, v. 845, n. 2, p. 125, 2017.

HYODO, R. et al. On the impact origin of phobos and deimos. iv. volatile depletion. **The Astrophysical Journal**, IOP Publishing, v. 860, n. 2, p. 150, 2018.

HYODO, R. et al. Challenges in forming phobos and deimos directly from a splitting of an ancestral single moon. **The Planetary Science Journal**, IOP Publishing, v. 3, n. 8, p. 204, 2022.

HYODO, R. et al. Transport of impact ejecta from mars to its moons as a means to reveal martian history. **Scientific reports**, Nature Publishing Group, v. 9, n. 1, p. 1–6, 2019.

HYODO, R.; OHTSUKI, K.; TAKEDA, T. Formation of multiple-satellite systems from low-mass circumplanetary particle disks. **The Astrophysical Journal**, IOP Publishing, v. 799, n. 1, p. 40, 2015.

HYODO, R. et al. On the impact origin of phobos and deimos. ii. true polar wander and disk evolution. **The Astrophysical Journal**, IOP Publishing, v. 851, n. 2, p. 122, 2017.

HYODO, R.; USUI, T. Searching for life on mars and its moons. **Science**, American Association for the Advancement of Science, v. 373, n. 6556, p. 742–742, 2021.

IDA, S.; GUILLOT, T.; MORBIDELLI, A. The radial dependence of pebble accretion rates: A source of diversity in planetary systems-i. analytical formulation. **Astronomy & Astrophysics**, EDP Sciences, v. 591, p. A72, 2016.

IDINI, B.; STEVENSON, D. J. Dynamical tides in jupiter as revealed by juno. **The Planetary Science Journal**, IOP Publishing, v. 2, n. 2, p. 69, 2021.

IRVINE, W. M. Light scattering by spherical particles: Radiation pressure, asymmetry factor, and extinction cross section. **Journal of the Optical Society of America**, Optical Society of America, v. 55, n. 1, p. 16–21, 1965.

ISELLA, A. et al. Detection of continuum submillimeter emission associated with candidate protoplanets. **The Astrophysical Journal Letters**, IOP Publishing, v. 879, n. 2, p. L25, 2019.

IZIDORO, A. et al. Formation of planetary systems by pebble accretion and migration-hot super-earth systems from breaking compact resonant chains. **Astronomy & Astrophysics**, EDP Sciences, v. 650, p. A152, 2021.

IZIDORO, A. et al. Planetesimal rings as the cause of the solar system's planetary architecture. **Nature Astronomy**, Nature Publishing Group, v. 6, n. 3, p. 357–366, 2022.

IZIDORO, A. et al. Breaking the chains: hot super-earth systems from migration and disruption of compact resonant chains. **Monthly Notices of the Royal Astronomical Society**, Oxford University Press, v. 470, n. 2, p. 1750–1770, 2017.

IZIDORO, A.; WINTER, O.; TSUCHIDA, M. Co-orbital satellites of saturn: congenital formation. **Monthly Notices of the Royal Astronomical Society**, The Royal Astronomical Society, v. 405, n. 4, p. 2132–2140, 2010.

JACOBSON, R.; LAINEY, V. Martian satellite orbits and ephemerides. **Planetary and space science**, Elsevier, v. 102, p. 35–44, 2014.

JACOBSON, R. et al. Revised orbits of saturn's small inner satellites. **The Astronomical Journal**, IOP Publishing, v. 135, n. 1, p. 261, 2007.

JEFFERYS, W. H. An atlas of surfaces of section for the restricted problem of three bodies. **Publications Department of Astronomy**, 1971.

JOHANSEN, A. et al. The multifaceted planetesimal formation process. **arXiv preprint arXiv:1402.1344**, 2014.

JOHNSON, T. V. The galilean satellites of jupiter: four worlds. **Annual Review of Earth and Planetary Sciences**, Annual Reviews 4139 El Camino Way, PO Box 10139, Palo Alto, CA 94303-0139, USA, v. 6, n. 1, p. 93–125, 1978.

JORDA, L. et al. The global shape, density and rotation of comet 67p/churyumov-gerasimenko from preperihelion rosetta/osiris observations. **Icarus**, Elsevier, v. 277, p. 257–278, 2016.

JOURNAUX, B. et al. Large ocean worlds with high-pressure ices. **Space Science Reviews**, Springer, v. 216, n. 1, p. 7, 2020.

JR, E. S.; JOHNSON, R. E. Dust plasma environment between saturn's rings and mimas' l shell. In: **AGU Fall Meeting Abstracts**. [S.l.: s.n.], 2015. v. 2015, p. P43E–08.

JUTZI, M.; BENZ, W. Formation of bi-lobed shapes by sub-catastrophic collisions-a late origin of comet 67p's structure. **Astronomy & Astrophysics**, EDP Sciences, v. 597, p. A62, 2017.

KARJALAINEN, R. Aggregate impacts in saturn's rings. **Icarus**, Elsevier, v. 189, n. 2, p. 523–537, 2007.

KAULA, W. M. Tidal dissipation by solid friction and the resulting orbital evolution. **Reviews of geophysics**, Wiley Online Library, v. 2, n. 4, p. 661–685, 1964.

KEMPF, S. et al. The e ring in the vicinity of enceladus: I. spatial distribution and properties of the ring particles. **Icarus**, Elsevier, v. 193, n. 2, p. 420–437, 2008.

KEMPF, S.; BECKMANN, U.; SCHMIDT, J. How the enceladus dust plume feeds saturn's e ring. **Icarus**, Elsevier, v. 206, n. 2, p. 446–457, 2010.

KENYON, S.; HARTMANN, L. Spectral energy distributions of t tauri stars-disk flaring and limits on accretion. **The Astrophysical Journal**, v. 323, p. 714–733, 1987.

KLEY, W. Mass flow and accretion through gaps in accretion discs. **Monthly Notices of the Royal Astronomical Society**, Blackwell Science Ltd Oxford, UK, v. 303, n. 4, p. 696–710, 1999.

KOKUBO, E.; GENDA, H. Formation of terrestrial planets from protoplanets under a realistic accretion condition. **The Astrophysical Journal Letters**, IOP Publishing, v. 714, n. 1, p. L21, 2010.

KOKUBO, E.; IDA, S. On runaway growth of planetesimals. **Icarus**, Elsevier, v. 123, n. 1, p. 180–191, 1996.

KOKUBO, E.; IDA, S. Formation of protoplanets from planetesimals in the solar nebula. **Icarus**, Elsevier, v. 143, n. 1, p. 15–27, 2000.

KOOTEN, E. M. V. et al. Isotopic evidence for primordial molecular cloud material in metal-rich carbonaceous chondrites. **Proceedings of the National Academy of Sciences**, National Acad Sciences, v. 113, n. 8, p. 2011–2016, 2016.

KOSCHNY, D.; GRÜN, E. Impacts into ice–silicate mixtures: Crater morphologies, volumes, depth-to-diameter ratios, and yield. **Icarus**, Elsevier, v. 154, n. 2, p. 391–401, 2001.

KRETKE, K.; LEVISON, H. Challenges in forming the solar system's giant planet cores via pebble accretion. **The Astronomical Journal**, IOP Publishing, v. 148, n. 6, p. 109, 2014.

KRIVOV, A. V. et al. Impact-generated dust clouds around planetary satellites: spherically symmetric case. **Planetary and Space Science**, Elsevier, v. 51, n. 3, p. 251–269, 2003.

KRÜGER, H.; KRIVOV, A. V.; GRÜN, E. A dust cloud of ganymede maintained by hypervelocity impacts of interplanetary micrometeoroids. **Planetary and Space Science**, Elsevier, v. 48, n. 15, p. 1457–1471, 2000.

KRUIJER, T. S. et al. Age of jupiter inferred from the distinct genetics and formation times of meteorites. **Proceedings of the National Academy of Sciences**, National Acad Sciences, v. 114, n. 26, p. 6712–6716, 2017.

KURAMOTO, K. et al. Martian moons exploration mmx: sample return mission to phobos elucidating formation processes of habitable planets. **Earth, Planets and Space**, SpringerOpen, v. 74, n. 1, p. 1–31, 2022.

LAGES, J.; SHEPELYANSKY, D. L.; SHEVCHENKO, I. I. Chaotic zones around rotating small bodies. **The Astronomical Journal**, IOP Publishing, v. 153, n. 6, p. 272, 2017.

LAGES, J.; SHEVCHENKO, I. I.; ROLLIN, G. Chaotic dynamics around cometary nuclei. **Icarus**, Elsevier, v. 307, p. 391–399, 2018.

LAINEY, V. et al. Strong tidal dissipation in io and jupiter from astrometric observations. **Nature**, Nature Publishing Group, v. 459, n. 7249, p. 957–959, 2009.

LAINEY, V. et al. New constraints on saturn's interior from cassini astrometric data. **Icarus**, Elsevier, v. 281, p. 286–296, 2017.

LAMBRECHTS, M.; JOHANSEN, A. Rapid growth of gas-giant cores by pebble accretion. **Astronomy & Astrophysics**, EDP Sciences, v. 544, p. A32, 2012.

LAMBRECHTS, M.; JOHANSEN, A. Forming the cores of giant planets from the radial pebble flux in protoplanetary discs. **Astronomy & Astrophysics**, EDP Sciences, v. 572, p. A107, 2014.

LAMBRECHTS, M. et al. Quasi-static contraction during runaway gas accretion onto giant planets. **Astronomy & Astrophysics**, EDP Sciences, v. 630, p. A82, 2019.

LANDGRAF, M. et al. Origins of solar system dust beyond jupiter. **The Astronomical Journal**, IOP Publishing, v. 123, n. 5, p. 2857, 2002.

LAPLACE, P. S. **Exposition du système du monde**. [S.l.]: Bachelier, 1798.

LARI, G.; SAILLENFEST, M.; FENUCCI, M. Long-term evolution of the galilean satellites: the capture of callisto into resonance. **Astronomy & Astrophysics**, EDP Sciences, v. 639, p. A40, 2020.

LAURETTA, D. et al. Osiris-rex: sample return from asteroid (101955) bennu. **Space Science Reviews**, Springer, v. 212, n. 1, p. 925–984, 2017.

LECACHEUX, J. et al. A new satellite of saturn: Dione b. **Icarus**, Elsevier, v. 43, n. 1, p. 111–115, 1980.

LEINHARDT, Z. M.; STEWART, S. T. Collisions between gravity-dominated bodies. i. outcome regimes and scaling laws. **The Astrophysical Journal**, IOP Publishing, v. 745, n. 1, p. 79, 2011.

LEIVA, R. et al. Size and shape of chariklo from multi-epoch stellar occultations. **The Astronomical Journal**, IOP Publishing, v. 154, n. 4, p. 159, 2017.

LELEU, A. et al. Six transiting planets and a chain of laplace resonances in toi-178. **Astronomy & Astrophysics**, EDP Sciences, v. 649, p. A26, 2021.

LEVISON, H. F.; DUNCAN, M. J. From the kuiper belt to jupiter-family comets: The spatial distribution of ecliptic comets. **Icarus**, Elsevier, v. 127, n. 1, p. 13–32, 1997.

LEVISON, H. F. et al. Planetary impact rates from ecliptic comets. **Icarus**, Elsevier, v. 143, n. 2, p. 415–420, 2000.

LEVISON, H. F.; KRETKE, K. A.; DUNCAN, M. J. Growing the gas-giant planets by the gradual accumulation of pebbles. **Nature**, Nature Publishing Group, v. 524, n. 7565, p. 322–324, 2015.

LEVISON, H. F.; KRETKE, K. A.; DUNCAN, M. J. Growing the gas-giant planets by the gradual accumulation of pebbles. **Nature**, Nature Publishing Group, v. 524, n. 7565, p. 322–324, 2015.

LIANG, Y.; HYODO, R. Giga-year dynamical evolution of particles around mars. **Icarus**, Elsevier, v. 391, p. 115335, 2023.

LIN, D. N.; PAPALOIZOU, J. On the tidal interaction between protoplanets and the primordial solar nebula. ii-self-consistent nonlinear interaction. **The Astrophysical Journal**, v. 307, p. 395–409, 1986.

LIN, D. N.; PAPALOIZOU, J. On the tidal interaction between protoplanets and the protoplanetary disk. iii-orbital migration of protoplanets. **The Astrophysical Journal**, v. 309, p. 846–857, 1986.

LISSAUER, J. J. Shepherding model for neptune's arc ring. **Nature**, Springer, v. 318, n. 6046, p. 544–545, 1985.

LIU, B.; ORMEL, C. W. Catching drifting pebbles-i. enhanced pebble accretion efficiencies for eccentric planets. **Astronomy & Astrophysics**, EDP Sciences, v. 615, p. A138, 2018.

LIU, X. et al. Dynamics and distribution of jovian dust ejected from the galilean satellites. **Journal of Geophysical Research: Planets**, Wiley Online Library, v. 121, n. 7, p. 1141–1173, 2016.

LIU, X.; SCHMIDT, J. Configuration of the martian dust rings: shapes, densities, and size distributions from direct integrations of particle trajectories. **Monthly Notices of the Royal Astronomical Society**, Oxford University Press, v. 500, n. 3, p. 2979–2985, 2021.

LONGARETTI, P.-Y. Theory of narrow rings and sharp edges. **Planetary Ring Systems. Properties, Structure, and Evolution, Edited by MS Tiscareno and CD Murray.**, p. pp–225, 2018.

LUBOW, S.; SEIBERT, M.; ARTYMOWICZ, P. Disk accretion onto high-mass planets. **The Astrophysical Journal**, IOP Publishing, v. 526, n. 2, p. 1001, 1999.

LUNINE, J. I.; STEVENSON, D. J. Formation of the galilean satellites in a gaseous nebula. **Icarus**, Elsevier, v. 52, n. 1, p. 14–39, 1982.

LYNDEN-BELL, D.; PRINGLE, J. E. The evolution of viscous discs and the origin of the nebular variables. **Monthly Notices of the Royal Astronomical Society**, The Royal Astronomical Society, v. 168, n. 3, p. 603–637, 1974.

MADEIRA, G.; GIULIATTI-WINTER, S. M. Effects of immersed moonlets in the ring arc particles of saturn. **The European Physical Journal Special Topics**, Springer, v. 229, n. 8, p. 1527–1543, 2020.

MADEIRA, G.; GIULIATTI-WINTER, S. M. Numerical analysis of processes for the formation of moonlets confining the arcs of neptune. **Monthly Notices of the Royal Astronomical Society**, Oxford University Press, v. 513, n. 1, p. 297–309, 2022.

MADEIRA, G.; IZIDORO, A.; GIULIATTI-WINTER, S. M. Building the galilean moons system via pebble accretion and migration: A primordial resonant chain. **Monthly Notices of the Royal Astronomical Society**, Oxford University Press, v. 504, n. 2, p. 1854–1872, 2021.

MADEIRA, G. et al. Production and fate of the g ring arc particles due to aegaeon (saturn liii). **Monthly Notices of the Royal Astronomical Society**, Oxford University Press on behalf of the Royal Astronomical Society, v. 475, n. 4, p. 5474, 2018.

MADEIRA, G. et al. Dynamics around non-spherical symmetric bodies–i. the case of a spherical body with mass anomaly. **Monthly Notices of the Royal Astronomical Society**, Oxford University Press, v. 510, n. 1, p. 1450–1469, 2022.

MARINOVA, M. M.; AHARONSON, O.; ASPHAUG, E. Mega-impact formation of the mars hemispheric dichotomy. **Nature**, Nature Publishing Group, v. 453, n. 7199, p. 1216–1219, 2008.

MASE, R. A. et al. Mars odyssey navigation experience. **Journal of spacecraft and rockets**, v. 42, n. 3, p. 386–393, 2005.

MCKINNON, W. B. Differentiation of the galilean satellites: It's different out there. **LPICo**, v. 1335, p. 66–67, 2006.

MEISS, J. Symplectic maps, variational principles, and transport. **Reviews of Modern Physics**, APS, v. 64, n. 3, p. 795, 1992.

MELITA, M. D. et al. Assessment of different formation scenarios for the ring system of (10199) chariklo. **Astronomy & Astrophysics**, EDP Sciences, v. 602, p. A27, 2017.

MERLINE, W. J. et al. Asteroids do have satellites. **Asteroids III**, this volume. Univ. of Arizona, Tucson, v. 1, p. 289–312, 2002.

MESSAGE, P. On asymmetric periodic solutions of the plane restricted problem of three bodies. In: SPRINGER. **Periodic Orbits, Stability and Resonances: Proceedings of a Symposium Conducted by the University of São Paulo, the Technical Institute of Aeronautics of São José Dos Campos, and the National Observatory of Rio De Janeiro, at the University of São Paulo, São Paulo, Brasil, 4–12 September, 1969**. [S.l.], 1970. p. 19–32.

MEYER-VERNET, N.; SICARDY, B. On the physics of resonant disk-satellite interaction. **Icarus**, Elsevier, v. 69, n. 1, p. 157–175, 1987.

MICHEL, P.; BENZ, W.; RICHARDSON, D. C. Catastrophic disruption of pre-shattered parent bodies. **Icarus**, Elsevier, v. 168, n. 2, p. 420–432, 2004.

MIGNARD, F. Effects of radiation forces on dust particles in planetary rings. In: **IAU Colloq. 75: Planetary Rings**. [S.l.: s.n.], 1984. p. 333–366.

MIGUEL, Y.; IDA, S. A semi-analytical model for exploring galilean satellites formation from a massive disk. **Icarus**, Elsevier, v. 266, p. 1–14, 2016.

MILLS, S. M. et al. A resonant chain of four transiting, sub-neptune planets. **Nature**, Nature Publishing Group, v. 533, n. 7604, p. 509–512, 2016.

MISHCHENKO, M. I. et al. Bidirectional reflectance of flat, optically thick particulate layers: an efficient radiative transfer solution and applications to snow and soil surfaces. **Journal of Quantitative Spectroscopy and Radiative Transfer**, Elsevier, v. 63, n. 2-6, p. 409–432, 1999.

MISHCHENKO, M. I.; TRAVIS, L. D.; LACIS, A. A. **Scattering, absorption, and emission of light by small particles**. [S.l.]: Cambridge university press, 2002.

MORAES, R. A.; KLEY, W.; NETO, E. V. Growth and evolution of satellites in a jovian massive disc. **Monthly Notices of the Royal Astronomical Society**, Oxford University Press, v. 475, n. 1, p. 1347–1362, 2018.

MORBIDELLI, A. et al. The great dichotomy of the solar system: Small terrestrial embryos and massive giant planet cores. **Icarus**, Elsevier, v. 258, p. 418–429, 2015.

MORBIDELLI, A. et al. Meridional circulation of gas into gaps opened by giant planets in three-dimensional low-viscosity disks. **Icarus**, Elsevier, v. 232, p. 266–270, 2014.

MORFILL, G.; GRÜN, E. The motion of charged dust particles in interplanetary space—i. the zodiacal dust cloud. **Planetary and Space Science**, Elsevier, v. 27, n. 10, p. 1269–1282, 1979.

MORFILL, G.; HAVNES, O.; GOERTZ, C. Origin and maintenance of the oxygen torus in saturn's magnetosphere. **Journal of Geophysical Research: Space Physics**, Wiley Online Library, v. 98, n. A7, p. 11285–11297, 1993.

MORGADO, B. et al. A stellar occultation by the transneptunian object (50000) quaoar observed by cheops. **Astronomy & Astrophysics**, EDP Sciences, v. 664, p. L15, 2022.

MORGADO, B. et al. Refined physical parameters for chariklo's body and rings from stellar occultations observed between 2013 and 2020. **Astronomy & Astrophysics**, EDP Sciences, v. 652, p. A141, 2021.

MOSQUEIRA, I.; ESTRADA, P.; TURRINI, D. Planetesimals and satellitesimals: formation of the satellite systems. **Space Science Reviews**, Springer, v. 153, n. 1-4, p. 431–446, 2010.

MOSQUEIRA, I.; ESTRADA, P. R. Formation of the regular satellites of giant planets in an extended gaseous nebula i: subnebula model and accretion of satellites. **Icarus**, Elsevier, v. 163, n. 1, p. 198–231, 2003.

MOSQUEIRA, I.; ESTRADA, P. R. Formation of the regular satellites of giant planets in an extended gaseous nebula ii: satellite migration and survival. **Icarus**, Elsevier, v. 163, n. 1, p. 232–255, 2003.

MOURA, T. et al. Dynamical environment and surface characteristics of asteroid (16) psyche. **Monthly Notices of the Royal Astronomical Society**, Oxford University Press, v. 491, n. 3, p. 3120–3136, 2020.

MOUTAMID, M. E.; SICARDY, B.; RENNER, S. Coupling between corotation and lindblad resonances in the presence of secular precession rates. **Celestial Mechanics and Dynamical Astronomy**, Springer, v. 118, n. 3, p. 235–252, 2014.

MUÑOZ-GUTIÉRREZ, M. A. et al. Long-term dynamical evolution of pallene (saturn xxxiii) and its diffuse, dusty ring. **Monthly Notices of the Royal Astronomical Society**, Oxford University Press, v. 511, n. 3, p. 4202–4222, 2022.

MURRAY, C. D.; DERMOTT, S. F. **Solar system dynamics**. [S.l.]: Cambridge university press, 1999.

MYSEN, E.; AKSNES, K. On the dynamical stability of the rosetta orbiter. ii. **Astronomy & Astrophysics**, EDP Sciences, v. 470, n. 3, p. 1193–1199, 2007.

MYSEN, E.; OLSEN, Ø.; AKSNES, K. Chaotic gravitational zones around a regularly shaped complex rotating body. **Planetary and Space Science**, Elsevier, v. 54, n. 8, p. 750–760, 2006.

NESVORNỲ, D. et al. Cometary origin of the zodiacal cloud and carbonaceous micrometeorites. implications for hot debris disks. **The Astrophysical Journal**, IOP Publishing, v. 713, n. 2, p. 816, 2010.

NESVORNỲ, D. et al. Evidence for very early migration of the solar system planets from the patroclus–menoetius binary jupiter trojan. **Nature Astronomy**, Nature Publishing Group, v. 2, n. 11, p. 878–882, 2018.

NICHOLSON, P. D. et al. Noncircular features in saturn's rings ii: The c ring. **Icarus**, Elsevier, v. 241, p. 373–396, 2014.

NICHOLSON, P. D. et al. Observations of saturn's ring-plane crossings in august and november 1995. **Science**, American Association for the Advancement of Science, v. 272, n. 5261, p. 509–515, 1996.

NIMMO, F. et al. The thermal and orbital evolution of enceladus: observational constraints and models. **Enceladus and the icy moons of Saturn**, University of Arizona Press Tucson, v. 475, p. 79–94, 2018.

NIMMO, F. et al. Implications of an impact origin for the martian hemispheric dichotomy. **Nature**, Nature Publishing Group, v. 453, n. 7199, p. 1220–1223, 2008.

NORTHROP, T.; BIRMINGHAM, T. Adiabatic charged particle motion in rapidly rotating magnetospheres. **Journal of Geophysical Research: Space Physics**, Wiley Online Library, v. 87, n. A2, p. 661–669, 1982.

OBERTI, P.; VIENNE, A. An upgraded theory for helene, telesto, and calypso. **Astronomy & Astrophysics**, EDP Sciences, v. 397, n. 1, p. 353–359, 2003.

OGIHARA, M.; IDA, S. N-body simulations of satellite formation around giant planets: origin of orbital configuration of the galilean moons. **The Astrophysical Journal**, IOP Publishing, v. 753, n. 1, p. 60, 2012.

OGIHARA, M.; KOBAYASHI, H. Condition for capture into first-order mean motion resonances and application to constraints on the origin of resonant systems. **The Astrophysical Journal**, IOP Publishing, v. 775, n. 1, p. 34, 2013.

ORMEL, C.; KLAHR, H. The effect of gas drag on the growth of protoplanets-analytical expressions for the accretion of small bodies in laminar disks. **Astronomy & Astrophysics**, EDP Sciences, v. 520, p. A43, 2010.

ORMEL, C. W.; LIU, B. Catching drifting pebbles-ii. a stochastic equation of motion for pebbles. **Astronomy & Astrophysics**, EDP Sciences, v. 615, p. A178, 2018.

ORTIZ, J. et al. Possible ring material around centaur (2060) chiron. **Astronomy & Astrophysics**, EDP Sciences, v. 576, p. A18, 2015.

ORTIZ, J. L. et al. The size, shape, density and ring of the dwarf planet haumea from a stellar occultation. **Nature**, Nature Publishing Group, v. 550, n. 7675, p. 219–223, 2017.

OWEN, W.; VAUGHAN, R.; SYNNOTT, S. Orbits of the six new satellites of neptune. **The Astronomical Journal**, v. 101, p. 1511–1515, 1991.

O'ROURKE, J. G.; STEVENSON, D. J. Stability of ice/rock mixtures with application to a partially differentiated titan. **Icarus**, Elsevier, v. 227, p. 67–77, 2014.

PAARDEKOOPER, S.-J. et al. A torque formula for non-isothermal type i planetary migration–i. unsaturated horseshoe drag. **Monthly Notices of the Royal Astronomical Society**, Blackwell Publishing Ltd Oxford, UK, v. 401, n. 3, p. 1950–1964, 2010.

PAARDEKOOPER, S.-J.; BARUTEAU, C.; KLEY, W. A torque formula for non-isothermal type i planetary migration–ii. effects of diffusion. **Monthly Notices of the Royal Astronomical Society**, The Royal Astronomical Society, v. 410, n. 1, p. 293–303, 2011.

PAJOLA, M. et al. Spectrophotometric investigation of phobos with the rosetta osiris-nac camera and implications for its collisional capture. **Monthly Notices of the Royal Astronomical Society**, Blackwell Science Ltd Oxford, UK, v. 427, n. 4, p. 3230–3243, 2012.

PAJOLA, M. et al. Phobos as a d-type captured asteroid, spectral modeling from 0.25 to 4.0 μm. **The Astrophysical Journal**, IOP Publishing, v. 777, n. 2, p. 127, 2013.

PANG, K. D. et al. The composition of phobos: Evidence for carbonaceous chondrite surface from spectral analysis. **Science**, American Association for the Advancement of Science, v. 199, n. 4324, p. 64–66, 1978.

PASCU, D.; HARRINGTON, R.; SEIDELMANN, P. Satellites of saturn. **International Astronomical Union Circular**, v. 3534, p. 1, 1980.

PATER, I. D. et al. The rings of neptune. **in Planetary Ring Systems (eds Tiscareno M. S. & Murray C. D.), 112-124, Cambridge Univ. Press**, 2018.

PATER, I. de et al. The dynamic neptunian ring arcs: evidence for a gradual disappearance of liberté and resonant jump of courage. **Icarus**, Elsevier, v. 174, n. 1, p. 263–272, 2005.

PÄTZOLD, M. et al. Phobos mass determination from the very close flyby of mars express in 2010. **Icarus**, Elsevier, v. 229, p. 92–98, 2014.

PEALE, S. Origin and evolution of the natural satellites. **Annual Review of Astronomy and Astrophysics**, Annual Reviews 4139 El Camino Way, PO Box 10139, Palo Alto, CA 94303-0139, USA, v. 37, n. 1, p. 533–602, 1999.

PEALE, S.; CASSEN, P. Contribution of tidal dissipation to lunar thermal history. **Icarus**, Elsevier, v. 36, n. 2, p. 245–269, 1978.

PEALE, S.; LEE, M. H. A primordial origin of the laplace relation among the galilean satellites. **Science**, American Association for the Advancement of Science, v. 298, n. 5593, p. 593–597, 2002.

PERSOON, A. et al. Evidence for a seasonally dependent ring plasma in the region between saturn's a ring and enceladus' orbit. **Journal of Geophysical Research: Space Physics**, Wiley Online Library, v. 120, n. 8, p. 6276–6285, 2015.

PERSOON, A. et al. Distribution in saturn's inner magnetosphere from 2.4 to 10 rs: A diffusive equilibrium model. **Journal of Geophysical Research: Space Physics**, Wiley Online Library, v. 125, n. 3, p. e2019JA027545, 2020.

PICHIERRI, G.; MORBIDELLI, A.; CRIDA, A. Capture into first-order resonances and long-term stability of pairs of equal-mass planets. **Celestial Mechanics and Dynamical Astronomy**, Springer, v. 130, n. 8, p. 1–32, 2018.

PINEDA, J. E. et al. High-resolution alma observations of hd 100546: Asymmetric circumstellar ring and circumplanetary disk upper limits. **The Astrophysical Journal**, IOP Publishing, v. 871, n. 1, p. 48, 2019.

PIQUETTE, M. et al. Student dust counter: status report at 38 au. **Icarus**, Elsevier, v. 321, p. 116–125, 2019.

PIQUETTE, M. R. **In-situ observations of the interplanetary dust population from Earth to the Edgeworth-Kuiper Belt**. Tese (Doutorado) — University of Colorado at Boulder, 2019.

POINCARÉ, H. **Les méthodes nouvelles de la mécanique céleste**. [S.l.]: Gauthier-Villars et fils, imprimeurs-libraires, 1893. v. 2.

POPPE, A.; JAMES, D.; HORÁNYI, M. Measurements of the terrestrial dust influx variability by the cosmic dust experiment. **Planetary and Space Science**, Elsevier, v. 59, n. 4, p. 319–326, 2011.

POPPE, A. et al. Constraining the solar system's debris disk with in situ new horizons measurements from the edgeworth–kuiper belt. **The Astrophysical Journal Letters**, IOP Publishing, v. 881, n. 1, p. L12, 2019.

POPPE, A. R. An improved model for interplanetary dust fluxes in the outer solar system. **Icarus**, Elsevier, v. 264, p. 369–386, 2016.

PORCO, C. et al. Cassini imaging science: Initial results on saturn's rings and small satellites. **science**, American Association for the Advancement of Science, v. 307, n. 5713, p. 1226–1236, 2005.

PORCO, C. et al. Neptune's ring system. In: **Neptune and Triton**. [S.l.: s.n.], 1995. p. 703–804.

PORCO, C. C. An explanation for neptune's ring arcs. **Science**, The American Association for the Advancement of Science, v. 253, n. 5023, p. 995, 1991.

PORCO, C. C.; GOLDREICH, P. Shepherding of the uranian rings. i-kinematics. ii-dynamics. **The Astronomical Journal**, v. 93, p. 724–737, 1987.

PORCO, C. C. et al. Saturn's small inner satellites: Clues to their origins. **science**, American Association for the Advancement of Science, v. 318, n. 5856, p. 1602–1607, 2007.

POSTBERG, F. et al. The e-ring in the vicinity of enceladus: Ii. probing the moon's interior—the composition of e-ring particles. **Icarus**, Elsevier, v. 193, n. 2, p. 438–454, 2008.

PRESS, W. H. et al. **Numerical recipes 3rd edition: The art of scientific computing**. [S.l.]: Cambridge university press, 1989.

PROCKTER, L. et al. The near shoemaker mission to asteroid 433 eros. **Acta Astronautica**, Elsevier, v. 51, n. 1-9, p. 491–500, 2002.

RAGOZZINE, D.; BROWN, M. E. Orbits and masses of the satellites of the dwarf planet haumea (2003 el61). **The Astronomical Journal**, IOP Publishing, v. 137, n. 6, p. 4766, 2009.

RAMSLEY, K. R.; HEAD, J. W. The stickney crater ejecta secondary impact crater spike on phobos: Implications for the age of stickney and the surface of phobos. **Planetary and Space Science**, Elsevier, v. 138, p. 7–24, 2017.

RAYMOND, S. N.; IZIDORO, A. Origin of water in the inner solar system: Planetesimals scattered inward during jupiter and saturn's rapid gas accretion. **Icarus**, Elsevier, v. 297, p. 134–148, 2017.

REIN, H.; LIU, S.-F. Rebound: an open-source multi-purpose n-body code for collisional dynamics. **Astronomy & Astrophysics**, EDP Sciences, v. 537, p. A128, 2012.

RENNER, S.; SICARDY, B. Stationary configurations for co-orbital satellites with small arbitrary masses. **Celestial Mechanics and Dynamical Astronomy**, Springer, v. 88, n. 4, p. 397–414, 2004.

RENNER, S.; SICARDY, B. Use of the geometric elements in numerical simulations. **Celestial Mechanics and Dynamical Astronomy**, Springer, v. 94, n. 2, p. 237–248, 2006.

RENNER, S. et al. Neptune's ring arcs: Vlt/naco near-infrared observations and a model to explain their stability. **Astronomy & Astrophysics**, EDP Sciences, v. 563, p. A133, 2014.

RIBEIRO, T. et al. Quasi circular orbits around prolate bodies. **Monthly Notices of the Royal Astronomical Society**, 2021.

ROLLIN, G.; SHEVCHENKO, I. I.; LAGES, J. Dynamical environments of mu69 and similar objects. **Icarus**, Elsevier, v. 357, p. 114178, 2021.

RONNET, T.; JOHANSEN, A. Formation of moon systems around giant planets-capture and ablation of planetesimals as foundation for a pebble accretion scenario. **Astronomy & Astrophysics**, EDP Sciences, v. 633, p. A93, 2020.

RONNET, T.; MOUSIS, O.; VERNAZZA, P. Pebble accretion at the origin of water in europa. **The Astrophysical Journal**, IOP Publishing, v. 845, n. 2, p. 92, 2017.

RONNET, T. et al. Saturn's formation and early evolution at the origin of jupiter's massive moons. **The Astronomical Journal**, IOP Publishing, v. 155, n. 5, p. 224, 2018.

ROSENBLATT, P.; CHARNOZ, S. On the formation of the martian moons from a circum-martian accretion disk. **Icarus**, Elsevier, v. 221, n. 2, p. 806–815, 2012.

ROSENBLATT, P. et al. Accretion of phobos and deimos in an extended debris disc stirred by transient moons. **Nature Geoscience**, Nature Publishing Group, v. 9, n. 8, p. 581–583, 2016.

RUBINCAM, D. P. On the secular decrease in the semimajor axis of lageos's orbit. **Celestial mechanics**, Springer, v. 26, n. 4, p. 361–382, 1982.

RUBINCAM, D. P. Saturn's rings, the yarkovsky effects, and the ring of fire. **Icarus**, Elsevier, v. 184, n. 2, p. 532–542, 2006.

RUBINCAM, D. P. The thermal expansion of particles and their secular orbital evolution as they circle a planet. **Icarus**, Elsevier, v. 239, p. 96–104, 2014.

SAFRONOV, V. Ejection of bodies from the solar system in the course of the accumulation of the giant planets and the formation of the cometary cloud. In: CAMBRIDGE UNIVERSITY PRESS. **Symposium-International Astronomical Union**. [S.l.], 1972. v. 45, p. 329–334.

SALMON, J.; CANUP, R. M. Accretion of saturn's inner mid-sized moons from a massive primordial ice ring. **The Astrophysical Journal**, IOP Publishing, v. 836, n. 1, p. 109, 2017.

SALMON, J. et al. Long-term and large-scale viscous evolution of dense planetary rings. **Icarus**, Elsevier, v. 209, n. 2, p. 771–785, 2010.

SALO, H.; HANNINEN, J. Neptune's partial rings: Action of galatea on self-gravitating arc particles. **Science**, American Association for the Advancement of Science, v. 282, n. 5391, p. 1102–1104, 1998.

SALO, H.; YODER, C. The dynamics of coorbital satellite systems. **Astronomy & Astrophysics**, v. 205, p. 309–327, 1988.

SAMUEL, H. et al. The rheology and thermal history of mars revealed by the orbital evolution of phobos. **Nature**, Nature Publishing Group, v. 569, n. 7757, p. 523–527, 2019.

SÁNCHEZ, P. Asteroid evolution: role of geotechnical properties. **Proceedings of the International Astronomical Union**, Cambridge University Press, v. 10, n. S318, p. 111–121, 2015.

SASAKI, T.; STEWART, G. R.; IDA, S. Origin of the different architectures of the jovian and saturnian satellite systems. **The Astrophysical Journal**, IOP Publishing, v. 714, n. 2, p. 1052, 2010.

SCHEERES, D.; WILLIAMS, B. G.; MILLER, J. K. Evaluation of the dynamic environment of an asteroid: Applications to 433 eros. **Journal of Guidance, Control, and Dynamics**, v. 23, n. 3, p. 466–475, 2000.

SCHEERES, D. J. Dynamics about uniformly rotating triaxial ellipsoids: applications to asteroids. **Icarus**, Elsevier, v. 110, n. 2, p. 225–238, 1994.

SCHEERES, D. J. et al. Orbits close to asteroid 4769 castalia. **Icarus**, Elsevier, v. 121, n. 1, p. 67–87, 1996.

SCHELLER, E. L.; EHLMANN, B. L. Composition, stratigraphy, and geological history of the noachian basement surrounding the isidis impact basin. **Journal of Geophysical Research: Planets**, Wiley Online Library, v. 125, n. 7, p. e2019JE006190, 2020.

SCHMEDEMANN, N. et al. The age of phobos and its largest crater, stickney. **Planetary and Space Science**, Elsevier, v. 102, p. 152–163, 2014.

SCHUBERT, G. et al. Interior composition, structure and dynamics of the galilean satellites. **Jupiter: The planet, satellites and magnetosphere**, Cambridge University Press Cambridge, UK, v. 1, p. 281–306, 2004.

SCHULIK, M. et al. On the structure and mass delivery towards circumplanetary discs. **Astronomy & Astrophysics**, EDP Sciences, v. 642, p. A187, 2020.

SEARLS, M. L.; BANERDT, W. B.; PHILLIPS, R. J. Utopia and hellas basins, mars: Twins separated at birth. **Journal of Geophysical Research: Planets**, Wiley Online Library, v. 111, n. E8, 2006.

SFAIR, R.; GIULIATTI-WINTER, S. The role of mab as a source for the μ ring of uranus. **Astronomy & Astrophysics**, EDP Sciences, v. 543, p. A17, 2012.

SHAKURA, N. I.; SUNYAEV, R. A. Black holes in binary systems. observational appearance. **Astronomy and Astrophysics**, v. 24, p. 337–355, 1973.

SHANG, H.; WU, X.; CUI, P. Periodic orbits in the doubly synchronous binary asteroid systems and their applications in space missions. **Astrophysics and Space Science**, Springer, v. 355, n. 1, p. 69–87, 2015.

SHARPLESS, B. P. Secular accelerations in the longitudes of the satellites of mars. **Astronomical Journal, Vol. 51, p. 185-186 (1945)**, v. 51, p. 185–186, 1945.

SHEVCHENKO, I. I. The kepler map in the three-body problem. **New Astronomy**, Elsevier, v. 16, n. 2, p. 94–99, 2011.

SHIBAIKE, Y. et al. The galilean satellites formed slowly from pebbles. **The Astrophysical Journal**, IOP Publishing, v. 885, n. 1, p. 79, 2019.

SHOWALTER, M. R.; HAMILTON, D. P.; NICHOLSON, P. D. A deep search for martian dust rings and inner moons using the hubble space telescope. **Planetary and Space Science**, Elsevier, v. 54, n. 9-10, p. 844–854, 2006.

SHOWALTER, M. R. et al. The neptune system revisited: New results on moons and rings from the hubble space telescope. In: **AAS/Division for Planetary Sciences Meeting Abstracts**. [S.l.: s.n.], 2013. v. 45.

SICARDY, B. Resonances in nonaxisymmetric gravitational potentials. **The Astronomical Journal**, IOP Publishing, v. 159, n. 3, p. 102, 2020.

SICARDY, B. et al. Ring dynamics around non-axisymmetric bodies with application to chariklo and haumea. **Nature Astronomy**, Nature Publishing Group, v. 3, n. 2, p. 146–153, 2019.

SICARDY, B.; LISSAUER, J. J. Dynamical models of the arcs in neptune's 63k ring (1989n1r). **Advances in Space Research**, Elsevier, v. 12, n. 11, p. 81–95, 1992.

Sicardy, B. et al. The dynamics of rings around centaurs and trans-neptunian objects. In: **The Trans-Neptunian Solar System**. [S.l.]: Elsevier, 2020. p. 249–269.

SICARDY, B. et al. Images of neptune's ring arcs obtained by a ground-based telescope. **Nature**, Nature Publishing Group, v. 400, n. 6746, p. 731–733, 1999.

SICARDY, B.; ROQUES, F.; BRAHIC, A. Neptune's rings, 1983–1989: Ground-based stellar occultation observations: I. ring-like arc detections. **Icarus**, Elsevier, v. 89, n. 2, p. 220–243, 1991.

SIMON, J. B. et al. The mass and size distribution of planetesimals formed by the streaming instability. i. the role of self-gravity. **The Astrophysical Journal**, IOP Publishing, v. 822, n. 1, p. 55, 2016.

SIMON, J. B. et al. The mass and size distribution of planetesimals formed by the streaming instability. i. the role of self-gravity. **The Astrophysical Journal**, IOP Publishing, v. 822, n. 1, p. 55, 2016.

SINGER, S. Origin of phobos and deimos: a new capture model. In: **Sixth International Conference on Mars**. [S.l.: s.n.], 2003. p. 3063.

SMITH, B. et al. Saturn's inner co-orbital satellites. In: **Bulletin of the American Astronomical Society**. [S.l.: s.n.], 1980. v. 12, p. 727.

SMITH, B. A. et al. Voyager 2 at neptune: Imaging science results. **Science**, American Association for the Advancement of Science, v. 246, n. 4936, p. 1422–1449, 1989.

SPAHN, F. et al. E ring dust sources: Implications from cassini's dust measurements. **Planetary and Space Science**, Elsevier, v. 54, n. 9-10, p. 1024–1032, 2006.

SPAHN, F. et al. Circumplanetary dust populations. **Space Science Reviews**, Springer, v. 215, n. 1, p. 1–54, 2019.

SPITALE, J. et al. The orbits of saturn's small satellites derived from combined historic and cassini imaging observations. **The Astronomical Journal**, IOP Publishing, v. 132, n. 2, p. 692, 2006.

SRAMA, R. et al. Constraints for a saturn dust environment model based on in-situ data of the cda instrument. In: **European Planetary Science Congress**. [S.l.: s.n.], 2020. p. EPSC2020–1012.

SRIDHAR, S.; TREMAINE, S. Tidal disruption of viscous bodies. **Icarus**, Elsevier, v. 95, n. 1, p. 86–99, 1992.

STERN, S. A.; MCKINNON, W. B. Triton's surface age and impactor population revisited in light of kuiper belt fluxes: Evidence for small kuiper belt objects and recent geological activity. **The Astronomical Journal**, IOP Publishing, v. 119, n. 2, p. 945, 2000.

STEWART, S. T.; LEINHARDT, Z. M. Velocity-dependent catastrophic disruption criteria for planetesimals. **The Astrophysical Journal Letters**, IOP Publishing, v. 691, n. 2, p. L133, 2009.

STEWART, S. T.; LEINHARDT, Z. M. Collisions between gravity-dominated bodies. ii. the diversity of impact outcomes during the end stage of planet formation. **The Astrophysical Journal**, IOP Publishing, v. 751, n. 1, p. 32, 2012.

SUETSUGU, R.; OHTSUKI, K. Distribution of captured planetesimals in circumplanetary gas disks and implications for accretion of regular satellites. **The Astrophysical Journal**, IOP Publishing, v. 839, n. 1, p. 66, 2017.

SUETSUGU, R.; OHTSUKI, K.; FUJITA, T. Orbital characteristics of planetesimals captured by circumplanetary gas disks. **The Astronomical Journal**, IOP Publishing, v. 151, n. 6, p. 140, 2016.

SUN, K.-L.; SCHMIDT, J.; SPAHN, F. Particle dynamics in the central ringlet of saturn's encke gap. **arXiv preprint arXiv:1510.07730**, 2015.

SUN, K.-L. et al. Dust in the arcs of methone and anthe. **Icarus**, Elsevier, v. 284, p. 206–215, 2017.

SYNNOTT, S. Evidence for the existence of additional small satellites of saturn. **Icarus**, Elsevier, v. 67, n. 2, p. 189–204, 1986.

SZETO, A. M. Orbital evolution and origin of the martian satellites. **Icarus**, Elsevier, v. 55, n. 1, p. 133–168, 1983.

SZULÁGYI, J.; CILIBRASI, M.; MAYER, L. In situ formation of icy moons of uranus and neptune. **The Astrophysical Journal Letters**, IOP Publishing, v. 868, n. 1, p. L13, 2018.

SZULÁGYI, J. et al. Circumplanetary disc or circumplanetary envelope? **Monthly Notices of the Royal Astronomical Society**, Oxford University Press, v. 460, n. 3, p. 2853–2861, 2016.

SZULÁGYI, J. et al. Accretion of jupiter-mass planets in the limit of vanishing viscosity. **The Astrophysical Journal**, IOP Publishing, v. 782, n. 2, p. 65, 2014.

TANAKA, H.; TAKEUCHI, T.; WARD, W. R. Three-dimensional interaction between a planet and an isothermal gaseous disk. i. corotation and lindblad torques and planet migration. **The Astrophysical Journal**, IOP Publishing, v. 565, n. 2, p. 1257, 2002.

TANIGAWA, T.; OHTSUKI, K.; MACHIDA, M. N. Distribution of accreting gas and angular momentum onto circumplanetary disks. **The Astrophysical Journal**, IOP Publishing, v. 747, n. 1, p. 47, 2012.

TAYLOR, D. et al. On asymmetric periodic solutions of the plane restricted problem of three bodies, and bifurcations of families. In: CAMBRIDGE UNIVERSITY PRESS. **International Astronomical Union Colloquium**. [S.l.], 1978. v. 41, p. 319–323.

TEAGUE, R.; BAE, J.; BERGIN, E. A. Meridional flows in the disk around a young star. **Nature**, Nature Publishing Group, v. 574, n. 7778, p. 378–381, 2019.

THOMAS, P. Gravity, tides, and topography on small satellites and asteroids: application to surface features of the martian satellites. **Icarus**, Elsevier, v. 105, n. 2, p. 326–344, 1993.

THOMAS, P. et al. The inner small satellites of saturn: A variety of worlds. **Icarus**, Elsevier, v. 226, n. 1, p. 999–1019, 2013.

THOMMES, E. W.; DUNCAN, M. J.; LEVISON, H. F. Oligarchic growth of giant planets. **Icarus**, Elsevier, v. 161, n. 2, p. 431–455, 2003.

TOOMRE, A. On the gravitational stability of a disk of stars. **The Astrophysical Journal**, v. 139, p. 1217–1238, 1964.

TREFFENSTÄDT, L. L.; MOURÃO, D. C.; WINTER, O. C. Formation of the janus-epimetheus system through collisions. **Astronomy & Astrophysics**, EDP Sciences, v. 583, p. A80, 2015.

TSENG, W.-L.; IP, W.-H. An assessment and test of enceladus as an important source of saturn's ring atmosphere and ionosphere. **Icarus**, Elsevier, v. 212, n. 1, p. 294–299, 2011.

TSENG, W.-L. et al. The structure and time variability of the ring atmosphere and ionosphere. **Icarus**, Elsevier, v. 206, n. 2, p. 382–389, 2010.

USOL'TSEVA, O. et al. Laboratory studies of geomechanical properties of deep-level rocks. In: IOP PUBLISHING. **IOP Conference Series: Earth and Environmental Science**. [S.l.], 2019. v. 262, n. 1, p. 012081.

VANTIEGHEM, S. Inertial modes in a rotating triaxial ellipsoid. **Proceedings of the Royal Society A: Mathematical, Physical and Engineering Sciences**, The Royal Society Publishing, v. 470, n. 2168, p. 20140093, 2014.

WANG, X.; LI, J.; GONG, S. Bifurcation of equilibrium points in the potential field of asteroid 101955 bennu. **Monthly Notices of the Royal Astronomical Society**, Oxford University Press, v. 455, n. 4, p. 3724–3734, 2016.

WARD, W. R.; CANUP, R. M. Circumplanetary disk formation. **The Astronomical Journal**, IOP Publishing, v. 140, n. 5, p. 1168, 2010.

WARNER, B. D.; HARRIS, A. W.; PRAVEC, P. The asteroid lightcurve database. **Icarus**, Elsevier, v. 202, n. 1, p. 134–146, 2009.

WEBER, P. et al. Characterizing the variable dust permeability of planet-induced gaps. **The Astrophysical Journal**, IOP Publishing, v. 854, n. 2, p. 153, 2018.

WEIDENSCHILLING, S. Aerodynamics of solid bodies in the solar nebula. **Monthly Notices of the Royal Astronomical Society**, The Royal Astronomical Society, v. 180, n. 2, p. 57–70, 1977.

WERNER, R. A. The gravitational potential of a homogeneous polyhedron or don't cut corners. **Celestial Mechanics and Dynamical Astronomy**, Springer, v. 59, n. 3, p. 253–278, 1994.

WILLNER, K.; SHI, X.; OBERST, J. Phobos' shape and topography models. **Planetary and Space Science**, Elsevier, v. 102, p. 51–59, 2014.

WINTER, O.; BORDERES-MOTTA, G.; RIBEIRO, T. On the location of the ring around the dwarf planet haumea. **Monthly Notices of the Royal Astronomical Society**, Oxford University Press, v. 484, n. 3, p. 3765–3771, 2019.

WINTER, O.; MURRAY, C. Resonance and chaos: I. first-order interior resonances. **Astronomy and Astrophysics**, p. 290–304, 1997.

WINTER, O.; MURRAY, C. Resonance and chaos: Ii. exterior resonances and asymmetric libration. **Astronomy and Astrophysics**, p. 399–408, 1997.

WINTER, O. et al. Asteroid triple-system 2001 sn263: surface characteristics and dynamical environment. **Monthly Notices of the Royal Astronomical Society**, Oxford University Press, v. 492, n. 3, p. 4437–4455, 2020.

Winter, O. C.; Murray, C. D. **Atlas of the Planar, Circular, Restricted Three-Body Problem. I. Internal Orbits**. [S.l.]: QMW Maths Notes, London, 1994.

Winter, O. C.; Murray, C. D. **Atlas of the Planar, Circular, Restricted Three-Body Problem. II. External Orbits**. [S.l.]: QMW Maths Notes, London, 1994.

WISDOM, J. The resonance overlap criterion and the onset of stochastic behavior in the restricted three-body problem. **The Astronomical Journal**, v. 85, p. 1122–1133, 1980.

WITASSE, O. et al. Mars express investigations of phobos and deimos. **Planetary and Space Science**, Elsevier, v. 102, p. 18–34, 2014.

YANG, C.-C.; JOHANSEN, A.; CARRERA, D. Concentrating small particles in protoplanetary disks through the streaming instability. **Astronomy & Astrophysics**, EDP Sciences, v. 606, p. A80, 2017.

YANG, J.; LUO, X. The critical state friction angle of granular materials: does it depend on grading? **Acta Geotechnica**, Springer, v. 13, n. 3, p. 535–547, 2018.

YE, S.-Y. et al. Electron density inside enceladus plume inferred from plasma oscillations excited by dust impacts. **Journal of Geophysical Research: Space Physics**, Wiley Online Library, v. 119, n. 5, p. 3373–3380, 2014.

YE, S.-Y. et al. Properties of dust particles near saturn inferred from voltage pulses induced by dust impacts on cassini spacecraft. **Journal of Geophysical Research: Space Physics**, Wiley Online Library, v. 119, n. 8, p. 6294–6312, 2014.

YODER, C. et al. Theory of motion of saturn's coorbiting satellites. **Icarus**, Elsevier, v. 53, n. 3, p. 431–443, 1983.

YODER, C. F. Tidal rigidity of phobos. **Icarus**, Elsevier, v. 49, n. 3, p. 327–346, 1982.

YOSHIKAWA, M. et al. Hayabusa sample return mission. **Asteroids IV**, University of Arizona Press Tucson, AZ, v. 1, p. 397–418, 2015.

YOUDIN, A. N.; GOODMAN, J. Streaming instabilities in protoplanetary disks. **The Astrophysical Journal**, IOP Publishing, v. 620, n. 1, p. 459, 2005.

YOUDIN, A. N.; LITHWICK, Y. Particle stirring in turbulent gas disks: Including orbital oscillations. **icarus**, Elsevier, v. 192, n. 2, p. 588–604, 2007.

YU, Y.; BAOYIN, H. Orbital dynamics in the vicinity of asteroid 216 kleopatra. **The Astronomical Journal**, IOP Publishing, v. 143, n. 3, p. 62, 2012.

ZHANG, H.; ZHANG, C.-Z. The q values of the galilean satellites and their tidal contributions to the deceleration of jupiter's rotation. **Chinese Journal of Astronomy and Astrophysics**, IOP Publishing, v. 4, n. 5, p. 499, 2004.

ZHANG, Y.; MICHEL, P. Tidal distortion and disruption of rubble-pile bodies revisited-soft-sphere discrete element analyses. **Astronomy & Astrophysics**, EDP Sciences, v. 640, p. A102, 2020.

ZHU, Z. et al. Dust filtration by planet-induced gap edges: implications for transitional disks. **The Astrophysical Journal**, IOP Publishing, v. 755, n. 1, p. 6, 2012.

APÊNDICE A – ORIGIN AND DYNAMIC EVOLUTION OF THE PALLENE RING

Anthe, Methone, and Pallene are kilometer-sized moons embedded in Saturn's E ring (HEDMAN et al., 2009). The first two objects are immersed in arcs of dust material, as in Aegaeon, a tiny moon immersed in the G ring (HEDMAN et al., 2010). Pallene, in turn, shares its orbit with an inclined ring composed mostly of micrometer-sized dust. Due to their small size, it has been proposed that these satellites maintain their associated arcs/ring by ejecting material due to interplanetary dust projectile impacts. Madeira et al. (2018), Madeira e Giuliatti-Winter (2020) compute the material production for Aegaeon, Anthe, and Methone, finding that solar radiation pressure removes arc material faster than the satellites replenish material. Thus, the arcs must be emptied of dust material in a few decades. Here, the mass production computation is done for Aegaeon, Anthe, Methone, and Pallene considering the most recent data on Saturn and the production due to E-ring impactors, an effect not considered by Madeira et al. (2018), Madeira e Giuliatti-Winter (2020). The orbital evolution of the Pallene ring particles is studied including the non-gravitational forces acting in the region, in order to confront the mass loss and production in the ring.

The content of this chapter was published as a section of the article: MA Muñoz-Gutiérrez et al. "Long-term dynamical evolution of Pallene (Saturn XXXIII) and its diffuse, dusty ring."Monthly Notices of the Royal Astronomical Society 511.3 (2022): 4202-4222.

A.1 INTRODUCTION

Pallene (Saturn XXXIII) is a satellite of only 2.23 km in radius (THOMAS et al., 2013), orbiting Saturn at an average distance of $\sim 212\,283$ km, with an eccentricity of ~ 0.004, and a relatively large inclination of $\sim 0.18^{\circ}$ (SPITALE et al., 2006; JACOBSON et al., 2007). This small Saturnian moon was first observed in a single photograph of the *Voyager 2* spacecraft. It was reported, together with a preliminary orbital and physical characterisation, by Synnott (1986). Pallene was then rediscovered in 2005 by the *Cassini* Imaging Science team (PORCO et al., 2005) and positively identified as the S/1981 S14 object from *Voyager 2*.

The satellite shares its orbit with a diffuse ring of micrometre-sized dust, first reported by Hedman et al. (2009). The complete dusty ringlet was observed by *Cassini* images in high phase angle, while a concentration of large particles ($\gtrsim 100\ \mu m$) was detected in other phase angle images (HEDMAN et al., 2009). These data indicate that the ring is composed of micrometre-sized particles and denser bodies. Hedman et al. (2009) found that the ring has a radial full-width of ∼2500 km and a vertical profile with a full-width at half-maximum (FWHM) of ∼50 km, that is, the ring is vertically thin. More recently, Spahn et al. (2019) measured the FWHM of the Gaussian vertical profile as ∼270 km while obtaining the same radial full-width as Hedman et al. (2009). Spahn et al. (2019) also found that the radial mean position of the ring is shifted radially outwards by ∼1100 km.

The resupply of the Pallene's ring material is expected to come from impact debris, expelled from the satellite's surface by collisions between interplanetary dust particles (IDPs) and the moon. A similar mechanism has been proposed and explored in order to explain the existence of Aegaeon's ring

arc inside the G ring (HEDMAN et al., 2010; MADEIRA et al., 2018), the ring arcs of Methone and Anthe (SUN et al., 2017; MADEIRA; GIULIATTI-WINTER, 2020), as well as the Neptune rings and arcs (GASLAC-GALLARDO et al., 2020; GIULIATTI-WINTER; MADEIRA; SFAIR, 2020). In this work, we perform a characterisation of the evolution of Pallene's ring, by considering all the relevant non-gravitational forces that affect small particles.

We study the evolution of the diffuse ring through two distinct scenarios: (a) particles initially co-orbital to the satellite and (b) by considering the temporal evolution of particles launched from Pallene's surface. The study is performed considering the system's gravitational effects and also non-gravitational forces acting in the region (solar radiation force, plasma drag, and the electromagnetic force).

A.2 PALLENE'S MASS PRODUCTION BY IMPACTS

In theory, satellites of a few kilometres in radius are efficient sources of debris for rings and arcs due to their reasonably large cross-section and low escape velocity (POPPE, 2016). However, Madeira et al. (2018) and Madeira e Giuliatti-Winter (2020) found that Saturn's three smallest moons (Aegaeon, Anthe, and Methone) do not replenish the material lost by their associated arcs due to non-gravitational forces. It raises the question of whether Pallene can maintain its diffuse ring in a steady state, as proposed by Hedman et al. (2009). In this section, we compute the amount of debris ejected from Pallene and analyse the fate of the ejecta in Section A.5.

The production of material by Pallene is the result of energetic collisions between the surface of the satellite and fluxes of interplanetary dust projectiles (IDPs) (GRÜN et al., 1985; DIVINE, 1993). Typically, IDPs are supplied by families of comets (Jupiter-family, Halley-type, and Oort-Cloud comets) (DIKAREV et al., 2005; NESVORNÝ et al., 2010; POPPE; JAMES; HORÁNYI, 2011) and by the Edgeworth-Kuiper Belt (EKB) (LANDGRAF et al., 2002). Data obtained by the Student Dust Counter (SDC) on board the New Horizons spacecraft indicate that the Saturn neighbourhood is dominated by EKB dust (PIQUETTE et al., 2019; POPPE et al., 2019) corresponding to the population that reaches the orbits of Saturn's satellites.

In addition to the impacts with IDPs, Pallene may produce material due to impacts with the E ring particles (ERPs). The icy-dust emission from Enceladus's volcanism is the principal source of the E ring (SPAHN et al., 2006; KEMPF; BECKMANN; SCHMIDT, 2010), producing a dense population of debris that impacts the surface of satellites immersed in the E ring (SPAHN et al., 2006). The mass production rate by Pallene (or any other satellite) is given by (KRIVOV et al., 2003):

$$M^{+} = \pi R_m^2 (F_{\mathrm{IDP}} Y_{\mathrm{IDP}} + F_{\mathrm{ERP}} Y_{\mathrm{ERP}}) \tag{1}$$

where R_m is the satellite radius, F_{IDP} and F_{ERP} are the mass flux of impactors due to IDPs and ERPs, respectively, and Y_{IDP} and Y_{ERP} are the ejecta yields associated to each projectile-type.

The ejecta yield is the ratio between the mass produced during the impact and the impactor's mass. This quantity is calculated using the empirical prescription obtained by Koschny e Grün (2001) for

pure-ice satellites:

$$Y = \frac{6.69 \times 10^{-8}}{2^{1.23}\ \mathrm{kg/m^3}} \left(\frac{1}{927\ \mathrm{kg/m^3}}\right)^{-1} \left(\frac{m_{\mathrm{imp}}}{\mathrm{kg}}\right)^{0.23} \left(\frac{v_{\mathrm{imp}}}{\mathrm{m/s}}\right)^{2.46} \tag{2}$$

where m_{imp} and v_{imp} are the mass and velocity of the impactor, respectively.

Pallene, Aegaeon, Anthe, and Methone are likely porous satellites (HEDMAN et al., 2020), with bulk densities ρ_m lower than the density of ice (ρ_{ice}=927 kg/m^3). Since an impact on a porous body is expected to generate more material than an impact on a non-porous surface, we artificially modified Equation 2 by introducing a porosity ratio of $\alpha_{\mathrm{p}} = \rho_{\mathrm{m}}/\rho_{\mathrm{ice}}$:

$$Y_p = \frac{(6.69 \times 10^{-8})^{\alpha_p}}{2^{1.23}\ \mathrm{kg/m^3}} \left(\frac{\alpha_p}{927\ \mathrm{kg/m^3}}\right)^{-1} \left(\frac{m_{\mathrm{imp}}}{\mathrm{kg}}\right)^{0.23} \left(\frac{v_{\mathrm{imp}}}{\mathrm{m/s}}\right)^{2.46}. \tag{3}$$

We must point out that Equation 2 is theoretical, and there is no experimental evidence that it actually rules the yield for a porous body. In this work, we will use Equation 2 only as an artifice to demonstrate the uncertainties related to the collision yield. The parameters assumed for the two projectile populations are presented below.

A.2.1 Interplanetary Dust Projectiles

In Saturn's vicinity, the (unfocused) IDP mass flux is estimated to be $F_{\mathrm{IDP}}^{(\infty)} = 10^{-16}$ kgm^{-2}s^{-1} (ALTOBELLI et al., 2018; PIQUETTE, 2019). We assume the IDPs' velocity near Saturn as the median speed of EKB grains, $v_{\mathrm{imp}}^{(\infty)} = 3.1$ km/s (POPPE, 2016) and the mass of the impactors as $m_{\mathrm{imp}} = 10^{-8}$ kg. When IDPs enter Saturn's Hill sphere, the planet's gravitational force is responsible for enhancing the flux and velocity of the projectiles (KRIVOV et al., 2003). Respectively, the mass flux and velocity of IDPs at an orbital radius r are (COLOMBO; LAUTMAN; SHAPIRO, 1966; KRIVOV et al., 2003):

$$\frac{F_{\mathrm{imp}}}{F_{\mathrm{imp}}^{(\infty)}} = \frac{1}{2}\left(\frac{v_{\mathrm{imp}}}{v_{\mathrm{imp}}^{(\infty)}}\right)^2 + \frac{1}{2}\frac{v_{\mathrm{imp}}}{v_{\mathrm{imp}}^{(\infty)}}\left[\left(\frac{v_{\mathrm{imp}}}{v_{\mathrm{imp}}^{(\infty)}}\right)^2 - \left(\frac{R_{\mathrm{S}}}{r}\right)^2\left(1 + \frac{2GM_S}{R_{\mathrm{S}}(v_{\mathrm{imp}}^{(\infty)})^2}\right)\right]^{1/2}, \tag{4}$$

and

$$\frac{v_{\mathrm{imp}}}{v_{\mathrm{imp}}^{(\infty)}} = \sqrt{1 + \frac{2GM_S}{r\left(v_{\mathrm{imp}}^{(\infty)}\right)^2}}. \tag{5}$$

A.2.2 E Ring Impactors

We assume that the E ring is composed of sub-micrometric ejecta from Enceladus onto highly eccentric orbits (NICHOLSON et al., 1996; KEMPF et al., 2008; POSTBERG et al., 2008; YE et al., 2014a). The average mass of impactors is assumed to be $m_{\mathrm{imp}} = 2.3 \times 10^{-15}$ kg (0.65 μm) (SPAHN

et al., 2006) and the impact velocity is given by (HAMILTON; BURNS, 1994; SPAHN et al., 2006):

$$v_{\rm imp} = \frac{1}{2}\sqrt{\frac{GM_S}{r}} \tag{6}$$

The flux of impactors on the equator plane is assumed to be $F_{\rm ERP} = m_{\rm imp} v_{\rm imp} N_{\rm ERP}$, where $N_{\rm ERP}$ is the particle number density in the E ring, extracted from the Cosmic Dust Analyser data (KEMPF et al., 2008):

$$N_{\rm ERP}(r) = N_0 \exp\left(-\frac{z_0(r)^2}{2\sigma(r)^2}\right) \begin{cases} \left(\frac{r}{3.98\ R_{\rm S}}\right)^{50} & \text{for } r \leq 3.98\ R_{\rm S} \\ \left(\frac{r}{3.98\ R_{\rm S}}\right)^{-20} & \text{for } r > 3.98\ R_{\rm S}, \end{cases} \tag{7}$$

with

$$\sigma(r) = 1826\ {\rm km} + (r - 3.98\ R_{\rm S}) \begin{cases} -\frac{467\ {\rm km}}{0.82\ R_{\rm S}} & \text{for } r \leq 3.98\ R_{\rm S} \\ \frac{510\ {\rm km}}{0.77\ R_{\rm S}} & \text{for } r > 3.98\ R_{\rm S}, \end{cases} \tag{8}$$

and,

$$z_0(r) = \begin{cases} -1220 \left(\frac{r - 3.98\ R_{\rm S}}{0.82\ R_{\rm S}}\right)\ {\rm km} & \text{for } r \leq 3.98\ R_{\rm S} \\ 0 & \text{for } r > 3.98\ R_{\rm S}, \end{cases}, \tag{9}$$

where N_0 is the maximum particle number density – near Enceladus' radius – set as $N_0 = 1\ {\rm m}^{-3}$ (YE et al., 2014b).

A.2.3 Mass Production Rate of Aegaeon, Anthe, Methone, and Pallene

Following the prescription described in Sections A.2.1 and A.2.2 and using Equation 2, we estimate the mass production rate of Pallene as

$$M^+ \sim 7.4 \times 10^{-4}\ {\rm kg/s}. \tag{10}$$

In order to determine whether Pallene can maintain the ring, we need to estimate the mass of the structure and compare it with the lifetime of the ejected material, which is obtained by N-body numerical simulations in Section A.5. If the time $\mathcal{T}$ for Pallene to produce the amount of mass observed in the ring is shorter than the particles' lifetime, then the satellite is an efficient source for the ring and the structure will be in a steady state. On the other hand, if $\mathcal{T}$ is longer than the lifetime of the particles, the ring will disappear unless another source keeps it in a steady-state.

The time for the satellite to produce the observed mass of the ring is (MADEIRA; GIULIATTI-WINTER, 2020)

$$\mathcal{T} = M_{\rm Ring}/M^+, \tag{11}$$

where $M_{\rm Ring}$ is the mass of a ring (or arc) given by (SFAIR; GIULIATTI-WINTER, 2012):

$$M_{\rm Ring} = A\left(\frac{4}{3}\pi\rho_{\rm ice}\right)\int_{0.1\ \mu m}^{100\ \mu m} C\pi s^{3-q} ds, \tag{12}$$

where s is the physical radius of the particles, C is a constant, and q is the slope of the size distribution of the particles. The surface area is $A = r\Delta\theta\Delta r/2$ (MADEIRA; GIULIATTI-WINTER, 2020), where

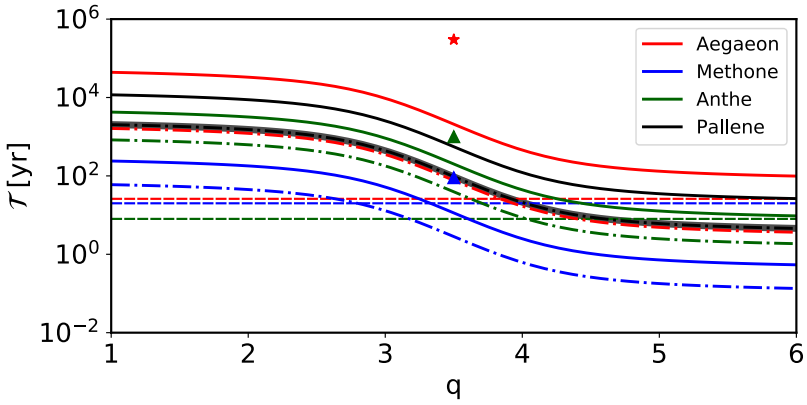

Figure 73 – Estimated time $\mathcal{T}$ for Aegaeon, Methone, Anthe, and Pallene to produce the mass of their associated arc/ring as a function of the slope q of the particle radius distribution. The solid and dashed lines correspond to the time calculated following the prescription given in A.2. The solid (dash-dotted) black line corresponds to Pallene's system assuming a non-porous (porous) satellite and the grey area gives the error in the calculation of $\mathcal{T}$ due to the uncertainties in Pallene's bulk density. The coloured red, blue, and green lines correspond to the arcs of Aegaeon, Methone, and Anthe, respectively. The arc lifetime is given by different coloured dashed lines. The red star gives $\mathcal{T}$ obtained for Aegaeon by Madeira et al. (2018) and the triangles the times obtained for Methone (blue) and Anthe (green) by Madeira e Giuliatti-Winter (2020).

$\Delta\theta$ is the angular width of the ring/arc in radians and Δr is the radial width. The constant C can be obtained from the observed optical depth τ (SFAIR; GIULIATTI-WINTER, 2012)

$$\tau = \int_{0.1\ \mu m}^{100\ \mu m} C\pi s^{2-q} ds. \tag{13}$$

The distribution of particles in Pallene's ringlet is not constrained by observational data. However, the data regarding the size distribution of the E ring provides us a range of possible slopes q for the ringlet, with values ranging from 1.9 to 5 (HORÁNYI; JUHÁSZ; MORFILL, 2008; KEMPF et al., 2008; YE et al., 2014a; SRAMA et al., 2020). For instance, Horányi, Juhász e Morfill (2008) estimated from numerical simulations that the grain density in the E ring follows a power law distribution with $q = 2.5$, while Kempf et al. (2008) obtained slopes between 4 and 5 for $s > 0.9$ μm from Cassini data. The slopes reported by Ye et al. (2014a) vary between 3 and 4 for $s > 10$ μm. To cover all possible values of q, we assume slopes between 1 and 6.

Figure 73 shows the time $\mathcal{T}$ for Pallene to produce the ringlet mass (solid black line) for slopes between 1 and 6, assuming a non-porous satellite (Equation 2). The figure also shows the time for the moons Aegaeon, Methone, and Anthe to produce the material of their associated arcs (solid coloured lines). Meanwhile, the dash-dotted lines provide the estimated production time $\mathcal{T}$ assuming that the satellites are porous. For Aegaeon, Anthe, and Methone, we assume a bulk density of 500 kg/m^3, while for Pallene this value is 250 kg/m^3. The filled region surrounding the dashed black line gives the $\mathcal{T}$ calculated using the minimum and maximum bulk densities estimated for Pallene ($\rho_{\rm Pal}$=190-340 kg/m^3). The mass production rate depends only on the cross-section of the satellite, so if we assume a non-porous Pallene, the uncertainties regarding its bulk density do not affect the mass production, since the physical radius of the satellite is constrained by observational data (HEDMAN et al., 2009).

Table 6 – Radial width (Δr), angular width ($\Delta\theta$), and optical depth (τ) assumed for the systems of Aegaeon, Methone, Anthe, and Pallene (HEDMAN et al., 2009; HEDMAN et al., 2010; HEDMAN et al., 2020; SUN et al., 2017; SPAHN et al., 2019). The table shows the fractions of yield Y, flux F, and mass rate M^+ between the IDP and ERP, and the total mass rate production in kg/s.

	Aegaeon	Methone	Anthe	Pallene
Δr [km]	250	1000	1000	2500
$\Delta\theta$ [°]	60	10	20	360
τ	10^{-5}	10^{-6}	10^{-6}	10^{-6}
$Y_{\rm IDP}/Y_{\rm ERP}$	–	447	448	449
$F_{\rm IDP}/F_{\rm ERP}$	–	10	4	10^{-1}
$M^+_{\rm IDP}/M^+_{\rm ERP}$	–	4×10^{3}	2×10^{3}	50
M^+[kg/s]	2.6×10^{-5}	3.7×10^{-4}	4.2×10^{-5}	7.4×10^{-4}

Madeira et al. (2018) and Madeira e Giuliatti-Winter (2020) estimated $\mathcal{T}$ following a simple prescription assuming production due to IDP impacts of cometary origin (with lower focused fluxes and velocities than the EKB grains), and assumed a single slope, $q = 3.5$. The prescription here presented goes a step further in relation to their model because it incorporates recent data and the production due to ERP impacts. The time $\mathcal{T}$ obtained in Madeira et al. (2018) for the arc of Aegaeon is shown by the red star in Figure 73 and the times obtained in Madeira e Giuliatti-Winter (2020) for the arcs of Methone and Anthe are the triangles with matching colours. The dashed lines correspond to the lifetime of 10 μm-sized particles, obtained by Madeira et al. (2018) and Madeira e Giuliatti-Winter (2020).

Our times are shorter than those estimated in previous works. Madeira et al. (2018) obtained that Aegaeon's arc will most likely disappear if it is composed exclusively of micrometre-sized grains. Here, we also obtained that a non-porous Aegaeon cannot replenish the arc material when we disregard other sources in the arcs,[1] since $\mathcal{T}$ is at least an order of magnitude higher than the lifespan of the particles. However, if we mimic the effect of porosity on the yield, the satellite can maintain the arc for $q \gtrsim 4$. Unlike Madeira e Giuliatti-Winter (2020), Methone can replenish the arc material for $q > 3.3$ regardless of its porosity. Although the lifetime of the particles in Anthe's arc is shorter than our $\mathcal{T}$ for the non-porous case, the radial width of the arc is unknown [2] and we cannot be sure if the satellite can produce by itself the amount of material necessary to keep the arc in a steady-state or not. Assuming a porous limit, the Anthe arc seems to be in a steady-state for $q \gtrsim 4$.

Table 6 summarises the initial ring (arc) parameters and the estimated fraction of yield, flux, and mass production between the IDP and ERP populations. We also include the total mass production for Aegaeon, Methone, Anthe, and Pallene for the non-porous case. Ejecta production due to IDP impacts is the most efficient for all systems. For the arcs of Aegaeon, Methone, and Anthe, production due to ERPs can be disregarded because the M^+ due to IDP impacts is more than 1000 times higher than for ERPs. The production due to ERPs corresponds to 2% of the total amount produced by Pallene.

[1] We do not compute production due to ERPs because Aegaeon is immersed in the G ring.

[2] We assume the same radial width as Methone's arc due to the proximity of the systems and the similar evolution of the particles under the effects of the 14:15 and 10:11 corotation resonance.

A.3 DYNAMICAL MODEL

We study the evolution and fate of Pallene's ringlet by analysing the temporal evolution of two distinct sets of particles: i) particles initially co-orbital to the satellite (A.4) and ii) particles ejected from Pallene's surface (A.5). The first set corresponds to a scenario in which the ringlet, and perhaps Pallene, would have formed by a disruption of an ancient satellite, while the second mimics the evolution of the material produced by impacts onto the satellite (A.2).

The numerical simulations were performed using the `MERCURY` (CHAMBERS, 1999) package with the Bulirsch-Stoer algorithm. We used 5,000 particles with micrometric sizes ranging from 0.1 μm to 100 μm, and integrated the system until either all particles collide with Mimas, Pallene, or Enceladus or migrate outwards beyond the orbit of Enceladus. We adopted the collision detection treatment between particles and satellites as implemented in the package (CHAMBERS, 1999; LIU et al., 2016).

Micrometre-sized particles are affected by non-gravitational forces that decrease their lifetimes. Thus it is necessary to include these effects in the system. In our simulations, the particles are under the effect of a total force,

$$\vec{\mathrm{F}} = \vec{\mathrm{F}}_{\mathrm{SR}} + \vec{\mathrm{F}}_{\mathrm{PD}} + \vec{\mathrm{F}}_{\mathrm{EM}} + \vec{\mathrm{F}}_{\mathrm{G}}, \tag{14}$$

where $\vec{\mathrm{F}}_{\mathrm{SR}}$ is the solar radiation force, $\vec{\mathrm{F}}_{\mathrm{PD}}$ is the plasma drag force, $\vec{\mathrm{F}}_{\mathrm{EM}}$ is the electromagnetic force, and $\vec{\mathrm{F}}_{\mathrm{G}}$ corresponds to the sum of the gravitational forces of the system: Saturn (including its gravitational coefficients), Mimas, Enceladus, Tethys, Dione, Rhea, Titan, and Pallene. The initial conditions of Saturn and the satellites are given in Muñoz-Gutiérrez et al. (2022).

A.3.1 Non-Gravitational Forces

The solar radiation force ($\vec{\mathrm{F}}_{\mathrm{SR}}$) includes two components (BURNS; LAMY; SOTER, 1979; MIGNARD, 1984): the radiation pressure (RP) caused by collisions of solar radiation on the dust grain,

$$\vec{\mathrm{F}}_{\mathrm{RP}} = \frac{\Phi \pi s^2}{c} Q_{pr} \frac{\vec{r}_{sp}}{r_{sp}}, \tag{15}$$

and the Poynting-Robertson drag (PR), caused by the re-emission of the solar radiation absorbed by the particles,

$$\vec{\mathrm{F}}_{\mathrm{PR}} = -\frac{\Phi \pi s^2}{c} Q_{pr} \left\{ \frac{\vec{V}_P + \vec{V}}{c} + \left[\left(\frac{\vec{V}_P}{c} + \frac{\vec{V}}{c} \right) \cdot \frac{\vec{r}_{sp}}{r_{sp}} \right] \frac{\vec{r}_{sp}}{r_{sp}} \right\}, \tag{16}$$

where c is the speed of light, Φ is the solar flux (BURNS; LAMY; SOTER, 1979), and $\vec{V}$ is the velocity vector of the particle relative to the planet. The solar radiation pressure efficiency Q_{pr} (in Equations 15 and 16) depends on the radius of the particle and is computed from Mie theory (IRVINE, 1965; MISHCHENKO et al., 1999; MISHCHENKO; TRAVIS; LACIS, 2002) assuming spherical ice grains. The particle is in a circumplanetary orbit $\vec{r}$ ($r = |\vec{r}|$), and the planet in a circular heliocentric orbit. The heliocentric position of Saturn $\vec{r}_{sp}$ ($r_{sp} = |\vec{r}_{sp}|$) and the magnitude of the planet's velocity $\vec{V}_P$ are considered constants. We also assume that Saturn shields particles from solar radiation when the planet eclipses the Sun from the particle's perspective, i.e., the solar radiation force is neglected when

the particle is in the planet's shadow, which happens when $\vec{r} \cdot \vec{r}_{sp} < 0$ and $(r^2 - R_S^2) r_{sp} - |\vec{r} \cdot \vec{r}_{sp}|^2 < 0$ (LIU et al., 2016).

The principal source of plasma for Saturn's magnetosphere in the E ring region is the ionisation of neutrals provided by the Enceladus plume. The E ring region is dominated by water group ions, i.e., O^+, OH^+, H_2O^+, and H_3O^+, the O^+ ion being the most abundant (CASSIDY; JOHNSON, 2010; TSENG et al., 2010; TSENG; IP, 2011; JR; JOHNSON, 2015). Direct collision of the plasma with the ring particles is responsible for a drag force ($\vec{F}_{PD}$) (MORFILL; GRÜN, 1979; MORFILL; HAVNES; GOERTZ, 1993; HORÁNYI; JUHÁSZ; MORFILL, 2008), given by

$$\vec{F}_{PD} = \pi s^2 m_i N_i a^2 (n - \Omega_S)^2 \hat{u}_t, \tag{17}$$

where n is the mean motion of the particle, m_i and N_i are the mass and number density of the plasma ions, respectively, and $\hat{u}_t$ is the unit vector in the tangential direction to the osculating orbit of the particle. *Cassini* measurements have shown seasonal variations in ion densities ranging from $N_i \sim 40\ \mathrm{cm}^{-3}$ to $N_i \sim 120\ \mathrm{cm}^{-3}$ in Pallene's vicinity (ELROD et al., 2014; PERSOON et al., 2015; PERSOON et al., 2020). For simplicity, we assume that the plasma in the Pallene region is only composed of O^+ ions (molecular mass of 16 a.m.u.) with constant number density $N_i = 65.9\ \mathrm{cm}^{-3}$ (PERSOON et al., 2015). Moreover, we neglect the indirect Coulomb interaction between charged ring particles and the plasma material, since this effect is at least two orders of magnitude weaker than the direct collisions (NORTHROP; BIRMINGHAM, 1982; GRUN; MORFILL; MENDIS, 1984; SUN; SCHMIDT; SPAHN, 2015).

The ring particles are also influenced by Saturn's magnetosphere due to the charging of the particles by the ambient plasma and electrons photoemission (solar UV). Therefore, the electromagnetic force ($\vec{F}_{EM}$) (NORTHROP; BIRMINGHAM, 1982; BURNS et al., 1985), is included in our simulations as

$$\vec{F}_{EM} = \frac{4\pi\epsilon_0 s V}{c} \left\{ \left[\vec{V} - \Omega_S (\hat{u}_n \times \vec{r}) \right] \times \vec{B} \right\}, \tag{18}$$

where $\epsilon_0 = 8.8542 \times 10^{-12}$ F/m is the vacuum permittivity (CHAPMAN; BARTELS, 1940), V is the electric potential, $\vec{B}$ is the magnetic field vector, and $\hat{u}_n$ is the unit vector perpendicular to the planet's equatorial plane. We adopt an equilibrium potential of $V = -3$ V for the Pallene region, as determined by Hsu et al. (2011) in their investigation of the dynamics of the Saturnian stream particles.

We assumed the Saturnian magnetic field as a composition of an aligned dipole and a quadrupole (CHAPMAN; BARTELS, 1940; HAMILTON, 1993):

$$\vec{B} = g_{1.0} R_S^3 \vec{\nabla} \left(\frac{\cos\zeta}{r^2} \right) + \frac{g_{2.0}}{2} R_S^4 \vec{\nabla} \left(\frac{3\cos^2\zeta - 1}{r^3} \right) \tag{19}$$

where $g_{1.0} = 0.21$ G is the Saturnian dipole momentum and $g_{2.0} = 0.02$ G, the quadrupole momentum (HAMILTON, 1993; BELENKAYA; COWLEY; ALEXEEV, 2006); ζ is the angle between $\hat{u}_n$ and $\vec{r}$.

A.3.2 Orbital elements of one representative particle

The non-gravitational forces are responsible for variations in the shape and orientation of the orbits, affecting the temporal evolution of the particles. The mean temporal variations of the osculating orbital elements of a particle with mass m are (MIGNARD, 1984; HAMILTON, 1993; MADEIRA; GIULIATTI-WINTER, 2020)

$$\dot{a} = -\frac{2na^2\alpha_{\rm r}}{c}\frac{5+\cos^2 I}{6} + \frac{2|\vec{F}_{\rm PD}|}{mn}\sqrt{1-e^2}, \tag{20}$$

$$\begin{aligned}\dot{e} = \alpha_{\rm r}\sqrt{1-e^2}(\cos\Omega\sin\omega + \sin\Omega\cos\omega\cos I) + \\ -\frac{3}{2}\frac{e|\vec{F}_{\rm PD}|}{mna}\sqrt{1-e^2} - \frac{qg_{1.0}R_{\rm S}^3\Omega_{\rm S}}{4mcna^3}e\sqrt{1-e^2}\sin^2 I\sin 2\omega,\end{aligned} \tag{21}$$

$$\dot{I} = \frac{\alpha_{\rm r}e}{\sqrt{1-e^2}}\sin\Omega\cos\omega\sin I + \frac{3}{2}\frac{|\vec{F}_{\rm PD}|}{mna}\sqrt{1-e^2}\sin I + \frac{qg_{1.0}R_{\rm S}^3\Omega_{\rm S}}{8mcna^3}\frac{e^2}{\sqrt{1-e^2}}\sin 2I\sin 2\omega, \tag{22}$$

$$\begin{aligned}\dot{\Omega} = -\dot{\Omega}_{\rm obl} + \frac{\alpha_{\rm r}e}{\sqrt{1-e^2}}\sin\Omega\sin\omega - (2-e)\frac{|\vec{F}_{\rm PD}|}{mna}\cos I\sqrt{1-e^2} + \\ + \frac{qg_{1.0}R_{\rm S}^3\Omega_{\rm S}}{mcna^3}\frac{1}{\sqrt{1-e^2}}\left[\cos I - \frac{1}{(1-e^2)}\left(\frac{n}{\Omega_{\rm S}}\right)\right],\end{aligned} \tag{23}$$

and

$$\begin{aligned}\dot{\varpi} = \dot{\varpi}_{\rm obl} + \frac{\alpha_{\rm r}\sqrt{1-e^2}}{e}(\cos\Omega\cos\omega - \sin\Omega\sin\omega\cos I) + \\ + (2-e)\frac{|\vec{F}_{\rm PD}|}{mna}\sqrt{1-e^2} + \frac{qg_{1.0}R_{\rm S}^3\Omega_{\rm S}}{mcna^3}\frac{2\cos I}{(1-e^2)^{3/2}}\left(\frac{n}{\Omega_{\rm S}}\right),\end{aligned} \tag{24}$$

where

$$\alpha_{\rm r} = \frac{3\Phi\pi s^2}{2mcna}Q_{pr}. \tag{25}$$

$\dot{\Omega}_{\rm obl}$ and $\dot{\varpi}_{\rm obl}$ are the temporal variation of longitude of ascending node and argument of pericentre, respectively, due to the non-sphericity of Saturn (RENNER; SICARDY, 2006).

Figure 74 illustrates the variation of geometric orbital elements (a, e, I, Ω and ϖ) of one representative particle with 10 μm of radius due to each non-gravitational force and the total force (Equation 14). The particle is initially co-orbital to Pallene with $\lambda = \lambda_{\rm Pal} + 180°$, where λ and $\lambda_{\rm Pal}$ are the mean longitude of the particle and Pallene, respectively. As one can see in the top panel of Figure 74, the semi-major axis is affected secularly by two distinct drag effects (Equation 20): the Poynting-Robertson component that produces an inward migration, and the plasma drag, which increases the semi-major axis of the particle. We find that the plasma drag is at least one order of magnitude stronger than the Poynting-Robertson component for all particle sizes. While the electromagnetic force only induces short-term variations in the semi-major axis, the net outcome is that grains migrate outward when all the effects are included.

In the eccentricities, we have that the electromagnetic and solar radiation forces produce oscillations with constant period and amplitude for the same particle size (HAMILTON, 1993; MADEIRA et al.,

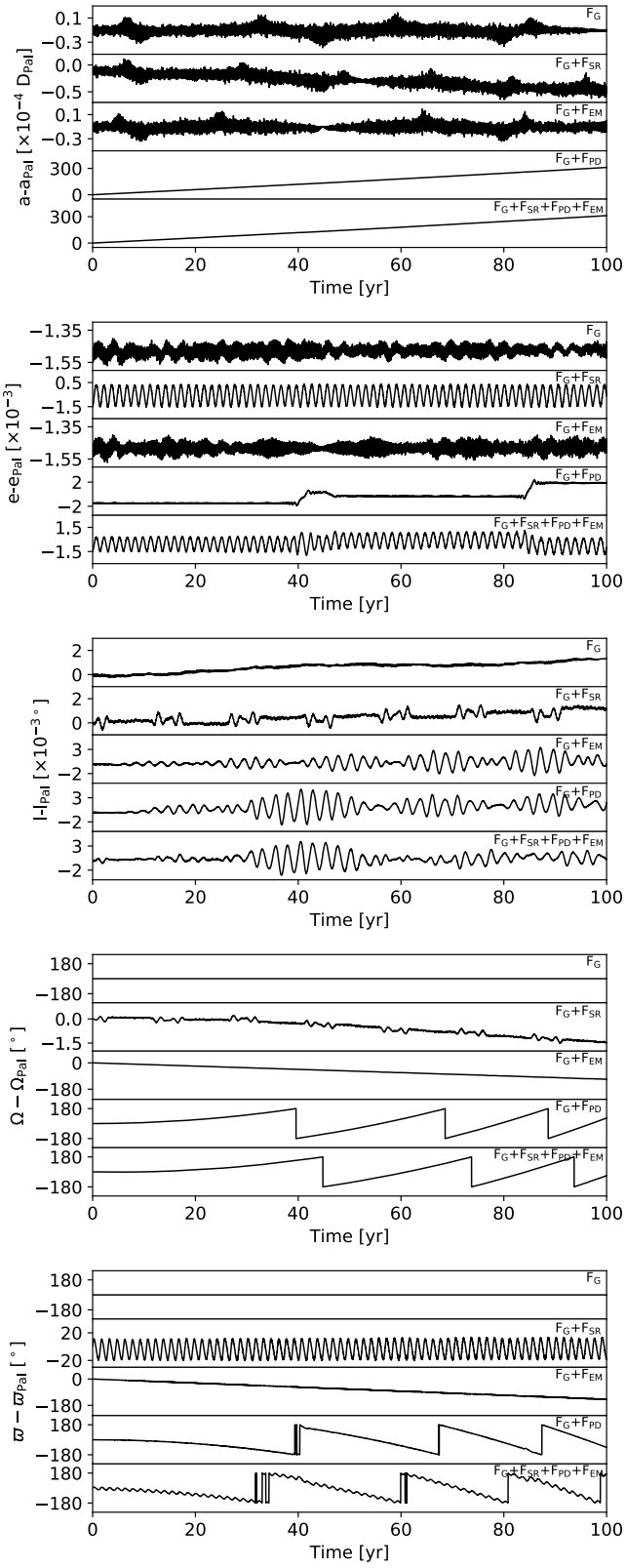

Figure 74 – From top to bottom: Geometric semi-major axis, eccentricity, inclination, longitude of ascending node, and argument of pericentre of a 10 μm-sized particle co-orbital to Pallene with displacement in the mean anomaly of 180° in relation to the satellite. The top row of each panel shows the orbital elements when only gravitational effect is included. The following rows display the evolution of the particle when different non-gravitational forces are included (i.e., solar radiation force, electromagnetic force, and plasma drag). Finally, the bottom row of each panel shows the effect of all forces.

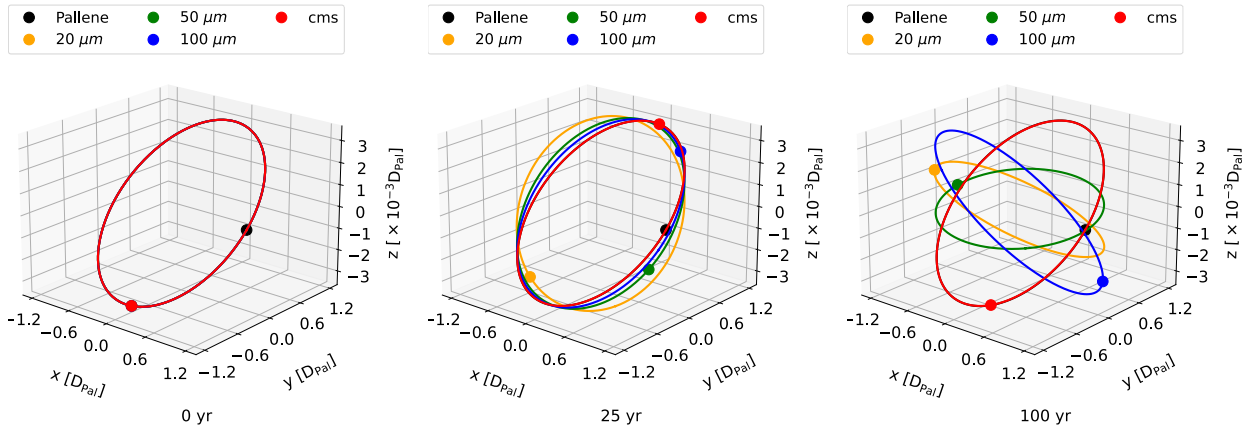

Figure 75 – Snapshots of the osculating orbit (solid lines) and spatial position (dots) of Pallene (in black) and of a co-orbital particle with $\lambda = \lambda_P + 90°$. The colour indicates the body, as labelled. We assume that the single particle has a radius of either 20 μm, 50 μm, or 100 μm. Displayed in red, we include the case solely with gravitational forces ("cms"). The orbits are provided in the rotating frame in which Pallene is stationary at $x = 1$ $\mathrm{D_{Pal}}$. An animation of this figure is available for viewing and downloading at <https://tinyurl.com/pallene>.

2018; GASLAC-GALLARDO et al., 2020). As we can see in Equation 21, the intensity of these effects depends on the radius of the particles, with $\dot{e} \propto s^{-3}$ for the electromagnetic force and $\dot{e} \propto s^{-1}$ for solar radiation. Thus, the effect of the electromagnetic force dominates over the solar radiation for smaller particles, while for larger sizes the electromagnetic force can be disregarded in relation to the solar radiation.

Plasma drag, on the other hand, produces only short-term variations in the eccentricities (MADEIRA; GIULIATTI-WINTER, 2020). The jumps of this element, seen in Figure 74, result from the crossing of the particle with resonances with Enceladus, as will be shown in A.4. For Pallene ringlet particles, the electromagnetic force dominates for $\mathrm{s} \leq 5$ μm, while the solar radiation force is the most important effect on the eccentricity of $\mathrm{s} > 5$ μm particles. We obtain that the non-perturbative forces produce only small variations in the inclination ($I \sim 10^{-3}$ deg) for the time intervals considered by us.

The longitude of ascending node and argument of pericentre are mainly affected by the plasma drag, which is responsible for the precession of the elements in relation to Pallene. Figure 75 displays snapshots of the osculating orbit (solid lines) of a representative particle (coloured dots) and Pallene (black dot). We rotate the systems on each snapshot to keep Pallene in the fixed position $x = 1$ $\mathrm{D_{Pal}}$. We show particles with radius of 20 μm, 50 μm, 100 μm, as well as with radius of centimetres, which corresponds to the case with only gravitational forces.

As we can see in Figure 75, without non-gravitational forces, the particle remains in the same orbit as Pallene and lacks vertical variation in relation to the satellite's orbital plane. When the non-gravitational forces are included, the orbit precesses, exhibiting vertical excursions in relation to Pallene's orbital plane. This phenomenon could be responsible for the observed vertical width of $\sim 10^2$ km of the ring (HEDMAN et al., 2009; SPAHN et al., 2019) indicating that the ringlet may evolve into a torus, as observed in the gossamer rings of Jupiter (BURNS et al., 1999). The formation of the torus occurs when the precession of the pericentre acts long enough to completely randomise the orientation of the particles' orbits. These results will be discussed in detail in A.4.

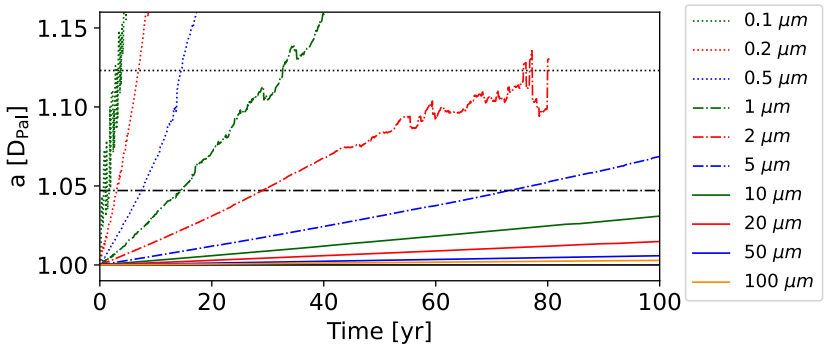

(a)

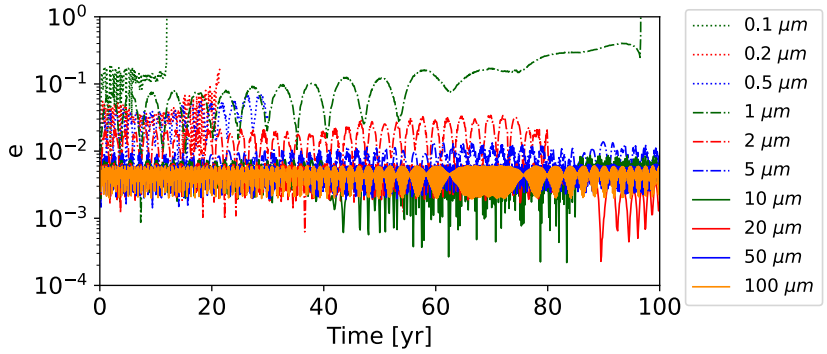

(b)

Figure 76 – a) Osculating semi-major axis and b) eccentricity of representative particles co-orbiting Pallene. The particles have a size of 0.1 μm, 0.2 μm, 0.5 μm, 1 μm, 2 μm, 5 μm, 10 μm, 20 μm, 50 μm, and 100 μm (coloured lines). The horizontal dotted line indicates Enceladus's semi-major axis, while the horizontal dot-dashed line is the maximum semi-major axis of the particle to be considered as a ringlet particle. The particles are under the effects of the solar radiation force, plasma drag, and electromagnetic force.

The osculating semi-major axis and eccentricity of a representative particle under the effects of the non-gravitational forces are presented in Figure 76. The lines correspond to numerical simulations where the physical radius of the single particle is modified (0.1 μm, 0.2 μm, 0.5 μm, 1 μm, 2 μm, 5 μm, 10 μm, 20 μm, 50 μm, and 100 μm). The solid and dotted horizontal lines indicate the orbits of Pallene and Enceladus, respectively. In this work, we consider a particle to be removed from the ringlet if it collides with a satellite or migrates outside the generous limit of $a_{\rm Pal} + 1100$ km (~ 1.05 D$_{\rm Pal}$). The latter can be seen in the figure by the horizontal dot-dashed line.

Particles with s ≤ 2 μm migrate beyond the orbit of Enceladus (horizontal dotted line) in less than 100 yr and reach $e > 10^{-2}$. In the case shown in Figure 76, the particles of 0.1 μm and 1 μm are ejected from the Saturnian system ($e > 1$) while the particles of 0.2 μm and 0.5 μm collide with a satellite outside the orbit of Enceladus. The 2 μm-sized particle collides with Enceladus in about 80 yr.

The effects of the non-gravitational forces are weaker for larger grains and particles with $s > 5$ μm remain with eccentricities of the order of 10^{-3}. These particles migrate outwards but still are considered ringlet particles according to our definition. These results roughly demonstrate that the permanence of the particles in the ring is strongly affected by non-gravitational forces and only particles with a radius of tens of micrometres or greater should have significantly long lifetimes in the ringlet (several hundreds of years). In the next sections, we perform full N-body simulations of the ring particles

evolution.

A.4 PARTICLES CO-ORBITAL TO PALLENE

In this section, we analyse Pallene's ringlet as formed by a set of 5,000 particles co-orbital to the satellite. We assume particles with the same orbital elements as Pallene, except for the mean anomaly that was randomly selected from a uniform distribution between 0° and 360°. The ring composed of co-orbital particles corresponds, e.g., to a scenario where the structure could be formed by the disruption of a proto-Pallene. In this scenario, the ring would also be composed of centimetre-sized or even larger particles. Nevertheless, we do not perform simulations for this size range since the effects of non-gravitational forces can be neglected. The orbital evolution of the centimetre-sized particles would correspond to a scenario analysed in Muñoz-Gutiérrez et al. (2022). They obtain that most of the particles initially located inside the Pallene collision region would eventually collide with the satellite, reducing the survival rate of co-orbital particles.

As a general outcome, we obtain that particles with $s \leq 10$ μm present a dynamical evolution similar to those shown in Figure 74. The particles migrate towards Enceladus and show an increase in eccentricity. However, we obtain a more complex dynamical evolution for particles with $s \geq 20$ μm caused by capture in resonances with Enceladus. Roughly speaking, a migrating particle is captured at a given resonance with a satellite if the migration timescale is shorter than the libration period of the resonance (BATYGIN, 2015). In our case, this condition is achieved for the largest particles (20 μm, 50 μm, and 100 μm) which are captured, even for a short period of time, in the 7:6, 8:7, 9:8, and 10:9 e-type MMRs with Enceladus.

Figure 77 shows the evolution of the fraction of particles with $s > 20$ μm (left column), as well as their geometric eccentricity (right column), as a function of the geometric semi-major axis. Initially, all particles have the same semi-major axis and eccentricity as Pallene (black dot). As the particles migrate outward, they cross resonances with Enceladus, increasing their eccentricities. After 200 yr, a fraction of 20 μm-sized particles is trapped in the 7:6 and 8:7 MMRs, while most of the set is located between the 8:7 and 9:8 MMRs. Particles in the 7:6 MMR are confined for a longer period of time, reaching the highest eccentricity values (≈0.05). The 20 μm-sized particles that are not in MMRs at 200 yr had their eccentricity increased during the passage through the two innermost resonances, reaching values ~ 0.01. Particles with radius of 50 μm and 100 μm have not yet crossed any resonances and remain with the same initial eccentricity.

At 750 yr, the 100 μm-sized particles have crossed the 7:6 MMR, and the 50 μm-sized particles have crossed all four resonances. Most of the 20 μm-sized particles migrated outside the limit of ≈ 1.05 $\mathrm{D_{Pal}}$, leaving only the particles confined in MMRs. A similar result is seen for 5,000 yr, when only 100 μm-sized particles in MMRs remain in the ring, indicating that capture in resonances increases their longevity. Therefore, the vicinity of MMRs would correspond to brighter regions of the ring, as will be shown later. Finally, after 8000 yr, the ring is completely depleted of μm-sized particles.

Figure 78a shows two different timescales as a function of particle radius: in blue, the time required for 50% of particles to collide with a satellite or migrate outside the limit of ~ 1.05 $\mathrm{D_{Pal}}$ – hereafter

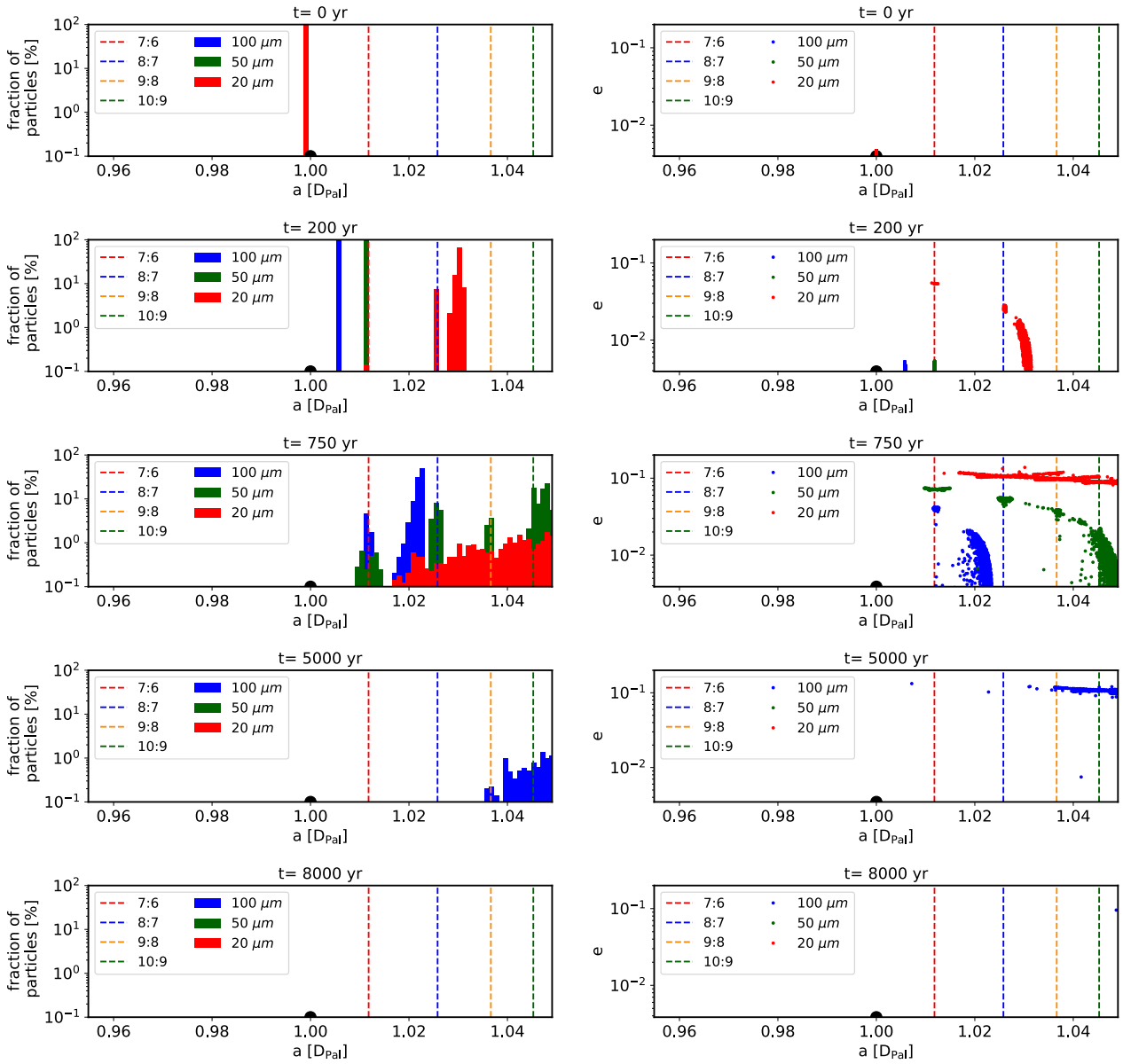

Figure 77 – Snapshots showing the percentage of particles as a function of the geometric semi-major axis (at left) and the geometric eccentricity vs. geometric semi-major axis (at right). From top to bottom, we show the data for 0, 200, 750, 5000, and 8000 yr. The 20 μm, 50 μm, and 100 μm sized particles are shown in different colours, as indicated. Pallene is represented by a black filled-circle. The locations of MMRs with Enceladus are indicated by dashed vertical lines. An animation of this figure is available for viewing and downloading at <https://tinyurl.com/pallene>.

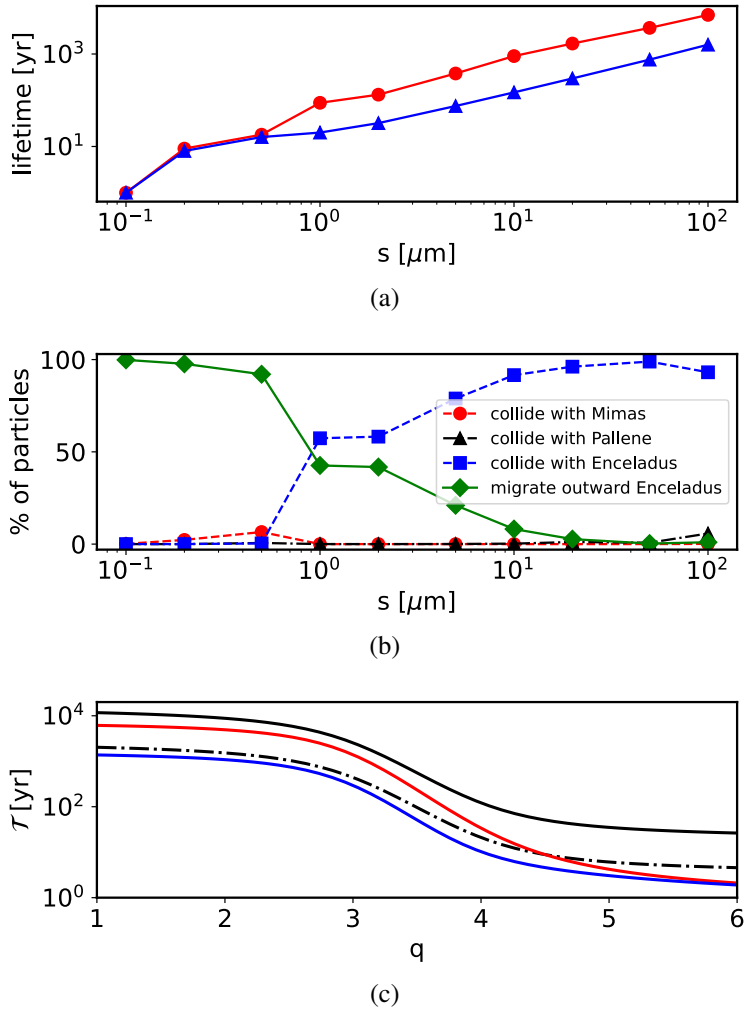

Figure 78 – a) The half-life (in blue) and the lifetime (in red) of the ring as a function of the physical radius of the co-orbital particles. b) The fraction of the particles that collides with the satellites Mimas (in red), Pallene (in black), and Enceladus (in blue), and the fraction of particles that migrates out of the orbit of Enceladus (in green). c) The time $\mathcal{T}$ for the satellite to produce the mass of the ring, assuming a non-porous (black solid line) and a porous (black dot-dashed line) Pallene. The red and blue lines give the ring's lifetime and half-life, respectively, as a function of the slope q.

referred to as the ring's half-lifetime – and in red the time required for all particles to be lost – referred as the ring's lifetime. The ring is completely depleted of sub-micrometric particles in less than a decade, while particles of radius of $1 - 10$ μm have lifetimes of the order of 10^2 yr. Particles that last longer are those with $s \geq 20$ μm, with lifetimes of $\sim 10^3$ yr – same order of the time $\mathcal{T}$ for Pallene to produce the mass of the ring (see Figure 73).

Particle sinks are shown in Figure 78b. Due to the intense migration caused by the plasma drag, almost all the sub-micrometric particles migrate beyond the orbit of Enceladus and collide with an external satellite or are ejected from the system. By increasing the radius of the particles, the slower rate of migration increases the period that the particles interact gravitationally with Enceladus in the vicinity of the satellite. Consequently, the number of collisions with Enceladus increases, as seen in Figure 78b. Also due to migration, the number of particles that collide with Pallene is less than 5% for all sizes; this rules out Pallene as an efficient secondary source of material, produced by subsequent impact with these particles.

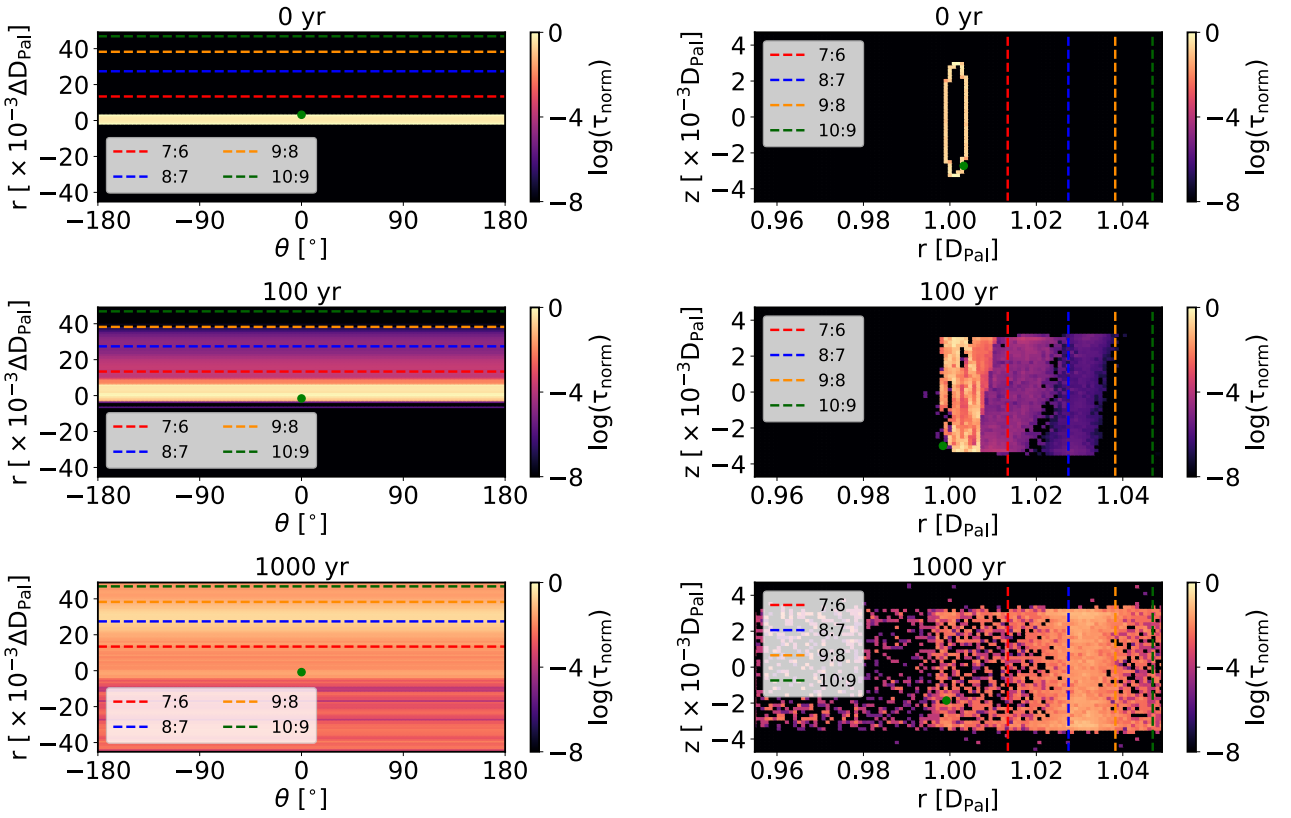

Figure 79 – Animations showing the normalised optical depth $\tau_{\rm norm}$ in the θ-r (left panels) and r-z (right panels) planes in the rotating frame for co-orbital particles. The green dot gives Pallene's position and the dashed lines indicate the MMRs with Enceladus. The upper limit of the radius in the panels corresponds to the limit 1.05 $\mathrm{D_{Pal}}$. An animation of this figure is available for viewing and downloading at <https://tinyurl.com/pallene>.

Figure 78c shows in black lines the same curves shown in Figure 73: the solid line is the time for Pallene to produce the ring mass in the non-porous case, while the dot-dashed line is the same for the porous case. The red and blue lines indicate the ring's lifetime and half-lifetime, respectively, obtained by a time-weighted average:

$$\bar{T} = \frac{\sum_s m_s \left(\frac{s\ (\mu\mathrm{m})}{100\ \mu\mathrm{m}}\right)^{-q} T_s}{\sum_s m_s \left(\frac{s\ (\mu\mathrm{m})}{100\ \mu\mathrm{m}}\right)^{-q}} \tag{26}$$

where m_s is the mass of a particle with radius s and T_s is the (half)-lifetime of the particles.

Focusing on the red curve in Figure 78c, we verify that the ring would not be in a steady-state, assuming ejection by Pallene as the only source of material. However, given the uncertainties in the yield calculation and the proximity of the values between the black and red solid curves, towards the lower values of q, we can conclude that Pallene might be able to maintain its ring if the particle distribution is given by $\mathrm{q} \lesssim 3$. Lower slope values mean that the ring has higher concentrations of larger particles, which seems to be the case of the ringlet of Pallene – given that larger particles can be captured in MMRs with Enceladus, while smaller ones have lifetimes of only a few years. If the particle distribution in the ring is given by slopes $\mathrm{q} \gtrsim 4$, Pallene by itself certainly cannot maintain the ring, since the lifetime is lower than $\mathcal{T}$ even for the porous limit.

Figure 79 shows animations of the co-orbital particle profiles in the planes θ-r (left panels) and

r-z (right panels). The colour of each pixel gives the normalised optical depth of that pixel, assuming a particle distribution with slope $q = 2.5$. The particles are initially distributed along the orbit of Pallene. In 10 yr, we can identify ring-like structures in the r-z plane, produced by the precession of the longitude of pericentre (Figure 75), where each structure is composed of particles with different radii. After 100 yr, the ring shows an asymmetrical profile, with the brightest part close to Pallene's orbit, and structures with lower brightness outside the satellite's orbit. We do not see any bright regions inside the orbit of Pallene, since outward migration is dominant for all particles.

At 400 yr, the torus structure is completely formed, and the ring has an asymmetric structure. The brightest part of the ring is in the region of the 7:6 MMR with Enceladus, but we see dimmer structures inside and outside this location, as an effect of the increased eccentricity of resonant particles. After 1000 yr, the complete structure of the ring has moved outward and the brightest region is located in the 8:7 MMR. After 4000 yr, the structure has moved further away and only a few particles have remained in the ring region.

A.5 PARTICLES EJECTED FROM PALLENE

In the numerical simulations presented in this section, 5000 particles were randomly and uniformly distributed in a spherical shell within the Hill radius of Pallene. Particles are ejected radially with random velocities that follow the normalised distribution (HARTMANN, 1985; KRIVOV et al., 2003; SUN et al., 2017):

$$f_v = \frac{1}{v_0}\left(\frac{v}{v_0}\right)^{-2}\Theta[v - v_0], \tag{27}$$

where $\Theta(x)$ denotes the Heaviside function. The minimum ejecta speed, v_0, is obtained from the transcendental equation (KRÜGER; KRIVOV; GRÜN, 2000)

$$\frac{K_e}{K_i} = Y\left(\frac{v_0}{v_{\rm imp}}\right)^2\left[\left(\frac{v_0}{v_{\rm max}}\right)^{-1} - 1\right], \tag{28}$$

where $v_{\rm max}$ is the maximum ejecta speed and K_e/K_i is the ratio between the kinetic energy partitioned to the ejecta and the impactor's kinetic energy, assumed as $K_e/K_i = 0.1$ (SUN et al., 2017).

Figure 80 is similar to Figure 79 but for the ejected particles. The temporal evolution of the ejected particles is similar to the co-orbital particles scenario. The same is true for the ring profiles, with greater distinctions only in the first years of the simulation, due to the different initial conditions. Figure 81 shows the half-lifetime and lifetime of the ring (Figure 81a), the particle sinks (Figure 81b), the times required for Pallene to produce the ring material, as well as the lifetimes as a function of the slope of the size distribution (Figure 81c). Our results are similar to those discussed in A.4. In both scenarios, Pallene could produce the material to keep the ring in a steady-state if the distribution of the particles in the ring is given by $q \lesssim 3$.

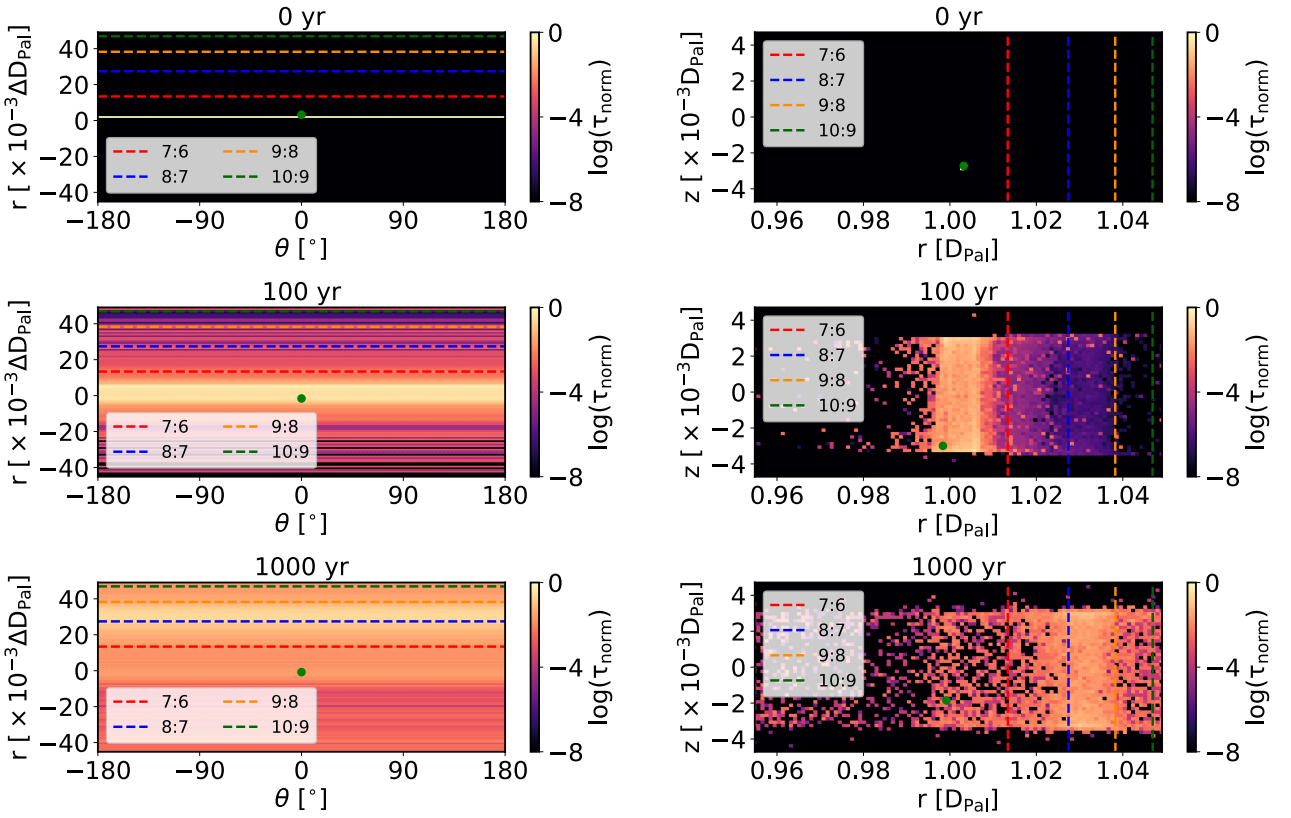

Figure 80 – Normalised optical depth $\tau_{\rm norm}$ for the ejected particles. Similarly to Figure 79, we present a cut in the θ-r and r-z planes in the rotating frame. The green dot gives Pallene's position and the vertical dashed lines are MMRs with Enceladus. An animation of this figure is available for viewing and downloading at <https://tinyurl.com/pallene>.

A.6 COMMENTS ON RING SOURCES

Similar to Madeira et al. (2018) and Madeira e Giuliatti-Winter (2020), we only computed the production due to external projectile impacts with the immersed moon. Therefore, we are analysing whether the satellite can produce the amount of material needed to keep the systems in steady-state, not whether they are in steady-state. In fact, the most likely case is that all the mentioned dusty arcs/rings are in a quasi-steady state, demonstrating that more sophisticated models are needed to understand their stability.

As we pointed out in this chapter, satellite porosity can be a factor influencing material production; however, the systems also have other sources. For example, ring particles are also impacted by external projectiles and therefore also produce material. However, following the prescription given in Dikarev et al. (2005), we obtained that such source is at least three orders of magnitude less efficient than the satellite for the systems analysed here.

The mentioned arcs/rings have the similarity of having a population of larger particles (HEDMAN et al., 2009; HEDMAN et al., 2010; SPAHN et al., 2019), which lead us to speculate whether the mutual collision of these objects or their impacts with the moon would be the main source of these systems (COLWELL; ESPOSITO, 1990b; COLWELL; ESPOSITO, 1990c). Just as a proof of concept, we will assume that in the Pallene ring is immersed a family of moonlets with radii ranging from 1 m to 100 m, following a size distribution $N \sim s^{-3.5}$ and total optical depth $\tau_{\rm mlets} = 10^{-8}$. Production

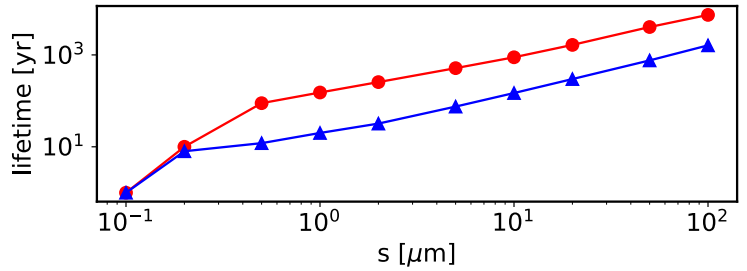

(a)

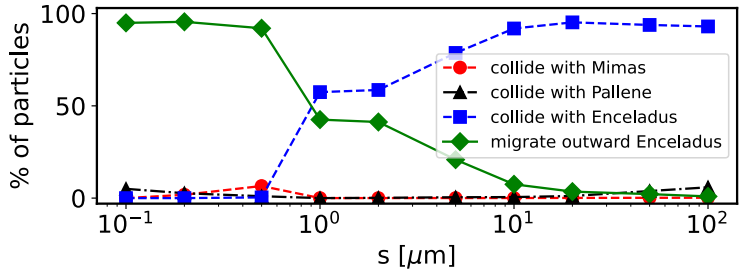

(b)

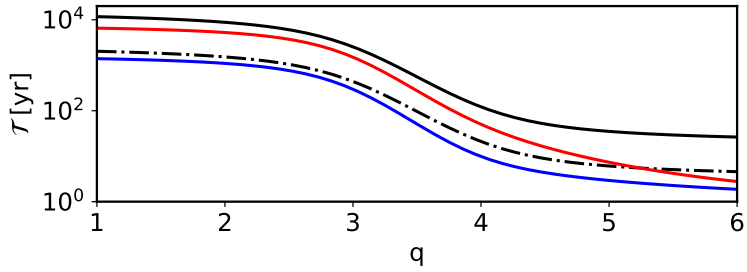

(c)

Figure 81 – a) The solid lines in blue and red show the time for 50% and 100% of the ejected particles to be removed from Pallene ring, respectively. b) The coloured lines show the fraction of particles that collide with Mimas (in red), Pallene (in black), and Enceladus (in blue), and the fraction that migrates outside the orbit of Enceladus (in green). c) The time for Pallene to produce the ring material is given by the black lines, in the non-porous (solid) and porous (dot-dashed) cases, while the ring lifetime and half-life are given by the red and blue lines, respectively.

due to impacts between the moonlets can be roughly estimated as (SUN; SCHMIDT; SPAHN, 2015)

$$\dot{M}_{\rm mlets} = 3\tau_{\rm mlets} N M_{\rm col} \tag{29}$$

where $M_{\rm col}$ is the amount of dust released per collision, assumed as $0.12 M_{\rm mlet}$ (CANUP; ESPOSITO, 1995b), and $M_{\rm mlet}$ is the total mass of the moonlet population.

As a result, we get $\dot{M}_{\rm mlets} \sim 10^{-2}$ kg/s corresponding to a value more than one order of magnitude higher than the production due to the non-porous Pallene. This shows that impacts between larger particles are an appealing possibility to keep the arcs/rings in steady-state. However, production due to impacts between centimetre-metric bodies is a very intricate problem, and is beyond the scope of this work.

A.7 DISCUSSION AND CONCLUSIONS

In this work, we explored the diffuse and dusty ring of Pallene. For this, we assumed a scenario where the particles are ejected from Pallene's surface, as well as a scenario where the material is originally co-orbital to Pallene. We found that non-gravitational forces dynamically dominate the system and the material experiences a similar dynamical evolution in both scenarios.

The outward migration due to plasma drag causes the loss of particles with radius of a few micrometres in just tens of years, while larger particles ($\gtrsim 10$ μm) can survive for a few hundred years in the ring. Spahn et al. (2019) measured the radial mean position of the ring to be more than 1000 km beyond the satellite's orbit; this is likely caused by plasma drag. Our ring profiles clearly show the formation of particle clusters beyond Pallene's orbit. Furthermore, the profiles show that the ring evolves into structures that are radially asymmetrical in relation to the satellite's orbit.

The precession of the longitude of pericentre due to non-gravitational forces produces vertical excursions of the particles in relation to Pallene's orbital plane. This could be the mechanism responsible for vertical excursions discussed in Hedman et al. (2009).

Cassini data indicate a concentration of larger particles around Pallene's orbit, which is in line with the significantly longer lifetime of the larger particles that we found. In fact, when calculating the mass production rate due to IDPs and ERPs, we find that Pallene can keep the ring in a steady-state only if it is predominantly composed of larger micrometre-sized particles ($q \lesssim 3$).

If we assume Pallene as the only source of material for the rings, we conclude that the ring would spread for $q \lesssim 4$. This corresponds to the slope range given by Kempf et al. (2008), Ye et al. (2014a) for the E ring, in which Pallene is immersed. In this scenario, our profiles show that the ring will evolve into a toroidal structure similar to the gossamer rings of Jupiter, and then it will continuously spread out, both radially and vertically, until it finally disappears. From our numerical results, we cannot constrain whether the ring originated from the material ejected from the satellite or from the disruption of an ancient proto-Pallene.

We must point out that our dynamical model is not complete; if the ring has a high concentration of larger particles, additional effects such as collisions between the particles, self-gravity, and local viscosity may be significant to the system. However, even in this case, plasma drag may dominate, and our main results would still hold valid.